Modeling Multiphysics of Traveling Wave Reactor Spent Fuel Disposal in Deep Crystalline Host Rock

by

Mariana Rodríguez Buño

S.M. in Civil and Environmental Engineering
Massachusetts Institute of Technology, 2013
Ingeniera Civil
Universidad de la República, Uruguay, 2007

Submitted to the Department of Civil and Environmental Engineering
in partial fulfillment of the requirements for the degree of

Doctor of Philosophy

at the

MASSACHUSETTS INSTITUTE OF TECHNOLOGY

February 2020

Author ..... Signature redacted
Department of Civil and Environmental Engineering
October 14, 2019

Certified by ..... Signature redacted
Herbert H. Einstein
Professor of Civil and Environmental Engineering
Thesis Supervisor

Accepted by ..... Signature redacted
Colette Heald
Professor of Civil and Environmental Engineering
Chair, Graduate Program Committee

Modeling Multiphysics of Traveling Wave Reactor Spent Fuel Disposal in Deep Crystalline Host Rock

by

Mariana Rodríguez Buño

Submitted to the Department of Civil and Environmental Engineering
on October 14, 2019, in partial fulfillment of the
requirements for the degree of
Doctor of Philosophy

Abstract

This study is the first investigation of a method to dispose of the spent fuel of the Travelling Wave Reactor (TWR), an innovative nuclear reactor design. Because significantly higher heat is produced in the central region of the rods than in conventional spent fuel, TWR spent fuel presents new challenges. This work studies the disposal of TWR high-linear-power-spent fuel in deep boreholes in crystalline host rock. The boreholes are 5 km deep, separated horizontally by 200 m, and the spent fuel is enclosed in metallic canisters placed vertically in the deposition boreholes in the bottom 2 km.

Nuclear regulators require analysis of the repository's performance for one million years. Other than human intrusion, groundwater transport is the only important mechanism for escape of radioactive material from the repository. Heat decay, combined with the natural geothermal flux, causes groundwater to flow, compromising radioactive containment. The numerical model used to study this problem must accurately predict the thermal field and induced fluid flow at different time and length scales, with strong coupling of all physics. Given these requirements, the numerical simulations of the coupled thermo-hydraulic behavior of a nuclear waste repository are computationally very expensive. To perform the repository simulations, we modified an open-source, finite element-based, fully implicit, fully coupled hydrothermal C++ code, FALCON, based on the MOOSE framework (Multiphysics Object Oriented Simulation Environment).

Our simulations show that a first local maximum temperature in the rock near the central borehole of the array occurs within 30 years of disposal (76°C), and an extended period of elevated temperatures with a larger absolute maximum (96°C) begins at 5,000 years. Neither supercritical conditions nor boiling are reached. Thermally driven fluid flow leads to particles from the waste breaking through at the surface at about 150,000 years. A comparison with nuclear waste from conventional Pressurized Water Reactors (PWR) shows that TWR spent fuel produces lower temperatures than PWR spent fuel for the first 3,200 years. After this time, TWR temperatures surpass PWR results. The flow characteristics for PWR and TWR are similar. The

breakthrough time can be extended by increasing the spacing between the boreholes.

Thesis Supervisor: Herbert H. Einstein
Title: Professor of Civil and Environmental Engineering

Acknowledgments

"Great day today!"

This is how Prof. Gilbert Strang from the Math Department began every one of his lectures at 9 am, one of the courses I took in my first term at MIT. Suddenly, somehow, I found myself at MIT in an exciting math class in front of the beautiful Charles River in a building labeled "Newton". What an adventure beyond my dreams! I feel blessed to have been able to call MIT my home for the last several years of my life. I feel so lucky to have had the chance to pursue this educational path. Not a single day was not worth effort to be here, leaving my previous life behind. I'm filled with countless memories that made this so amazing.

I made it to this point today because of my advisor, Prof. Herbert Einstein. I have no words to thank you for your constant support and encouragement, for all you did for me, for mentoring me in my research, and caring for me personally, even beyond research work. It has been a real pleasure and honor to work with you. Thank you so much for always believing in me, and helping me to cross the finish line. Thank you for teaching me what a great leader is. You taught me so much, about so many things, simply through your wordless but fiercely effective actions.

I would like to thank my PhD Committee: Prof. Ruben Juanes and Prof. John Williams for providing me with valuable comments, advice, and constant support, all of which helped me to be here today.

I also would like to thank Prof. Eduardo Kausel for all the time he spent with me discussing research and complex analytical solutions in Spanish, and for his useful advice. I am also very thankful to Prof. Heidi Nepf for her help in the final steps of the completion of this thesis.

I thank many MIT professors, Prof. John Germain, Prof. Andrew Whittle, Prof. Christopher Hill, and Dr. Jean-Michel Campin, with whom I had the chance to discuss research, science, math, computers, etc. It is something I really enjoyed, and helped me in so many ways to grow as a scientist.

In addition, I would like to express my gratitude to Prof. Michael Driscoll and

Prof. Emilio Baglietto from Nuclear Science and Engineering Department at MIT (NSE), for introducing me to nuclear science. Thank you to Prof. Baglietto for providing the computer cluster where I run my simulations. Thank you to Prof. Driscoll for your help in writing the reports to TerraPower; your interest in deep boreholes has been really inspiring to me. I am grateful to two former PhD students in NSE: Ethan Bates for sharing his knowledge in nuclear waste, and Nazar Lubchenko for his comments regarding MOOSE and numerical modeling at the early stages of this research.

This journey was enjoyable because I had amazing and admirable friends here, that I want to keep in my life. First I want to thank María José Nieves, Jorge Cañizales, Mohamed Siam, Priyanka Chatterjee, Diviya Sinha, Ivo Rosa and Alejandro Eguren for sharing with me day-to-day MIT life. Also, special thanks to my friend Juan Pablo Xandri, another Uruguayan at MIT, for being supportive and a wise source of advice. I want to also thank my research group: Wei, Bing, Omar, Rafael, Hao, and Ignacio for their friendship and support during these years. I thank my office-mate Sama for always listening to me and sharing her opinions, and my friends from Nuclear Engineering Department: Daniel Curtis for his encouragement, and Keldin Sergheyev for his friendship, for introducing me to the basics of C++ at the beginning of this research and for answering all my nuclear-related questions. I want to thank Ehsan Haghighat, post-doc of Prof. Juanes' group, for his availability to discuss my research and provide me suggestions.

I would like to acknowledge with gratitude the financial support of TerraPower, the Civil and Environmental Engineering and Nuclear Science and Engineering departments at MIT, and the Office of the Dean of Graduate Education. I am extremely thankful to Fulbright Commission US for giving me the chance to come to the United States to study. I would like to express my gratitude to Kiley and Max at CEE for their help with administrative work required for this thesis. In addition, I thank Carolyn (Prof. Einstein's secretary) for always creating a friendly environment.

Lastly, I would like to thank my family, especially my parents and brothers, Ramiro and Ricardo, for their unconditional support, love, and encouragement while

being away from home. None of this would have been possible without them.

Contents

List of Figures

List of Tables

List of Abbreviations

TWR	Traveling Wave Reactor
LWR	Light Water Reactor
PWR	Pressurized Water Reactor
BWR	Boiling Water Reactor
HLW	High Level Waste
ILW	Intermediate Level Waste
LLW	Low Level Waste
MTHM	Metric Ton of Heavy Metal
DOE	United States Department of Energy
EPA	United States Environmental Protection Agency
NRC	Nuclear Regulatory Commission
INL	Idaho National Laboratory

Chapter 1

Introduction

1.1 Objective of this Thesis

The final disposal and storage of high-level nuclear waste remains a major unresolved issue worldwide. The nuclear energy industry in the United States is hindered by the absence of a technically safe and socially acceptable permanent method of disposal of the highly radioactive spent fuel (Blue Ribbon Commission, 2012). This thesis is the first investigation of a disposal system to be used for an innovative reactor design known as the Traveling Wave Reactor (TWR), designed by TerraPower. This thesis develops the performance assessment analysis for this new type of spent nuclear fuel, when disposed of in deep boreholes of 5 km depth in a crystalline host rock.

This analysis is based on numerical modeling of the coupled physics that occur in a nuclear waste repository after emplacement for a one million year time span. Specifically, it addresses the question of whether this new type of spent fuel can be safely disposed of in a deep-borehole repository. Such a study is required for licensing of the TWR reactor design by TerraPower. In addition, this work compares the thermo-hydraulic response of a repository for Pressurized Water Reactor (PWR) spent fuel with TWR spent fuel.

1.2 Motivation of this research

1.2.1 Need for nuclear energy

The world is facing the challenge of finding new sources of energy – first, in response to fossil fuel reserves (coal, oil, and gas) depletion, and second, to reduce greenhouse gas emissions. Figure 1-1 shows the global annual concentration growth of carbon dioxide measured in parts per million. There has been a constant increase of CO_2 through the decades. To reduce global warming a reduction of greenhouse gas concentration in the atmosphere must be achieved.

The Kyoto Protocol considers six greenhouse gases: Carbon dioxide (CO_2), Methane (CH_4), Nitrous oxide (N_20), Hydrofluorocarbons (HFCs), Perfluorocarbons (PFCs), and Sulphur hexafluoride (SF_6). Carbon dioxide accounts for around three-quarters of total greenhouse gas emissions. Methane and nitrous oxide are also important sources, accounting for around 17 and 7 percent of emissions, respectively. HFC, PFC and SF_6 have a very strong warming impact per unit mass (high global warming potential), but are emitted in very small quantities and therefore make a small contribution to total warming (Ritchie & Roser, 2019).

Among all the global sources of CO_2 emissions, the energy sector is the one that contributes the most, with an increasing trend throughout the years. See Figure 1-2. A comparison of greenhouse gas emissions between different electricity generation methods is presented in Figure1-3. Coal power plants have the highest emission intensities on a lifecycle basis. Natural gas and oil have noticeably lower greenhouse gas emissions. Biomass, nuclear, hydroelectric, wind, and solar photovoltaic have lifecycle greenhouse gas emission intensities that are significantly smaller than fossil fuel based generation, with nuclear power being an almost zero greenhouse emission energy source.

Nuclear energy is generated from atomic fission, the process of splitting the nucleus of an atom into smaller lighter nuclei. The heat released by fission is used to produce steam that propels a turbine and generates electricity without any byproducts, in contrast to the CO_2 emitted in the combustion of fossil fuels.

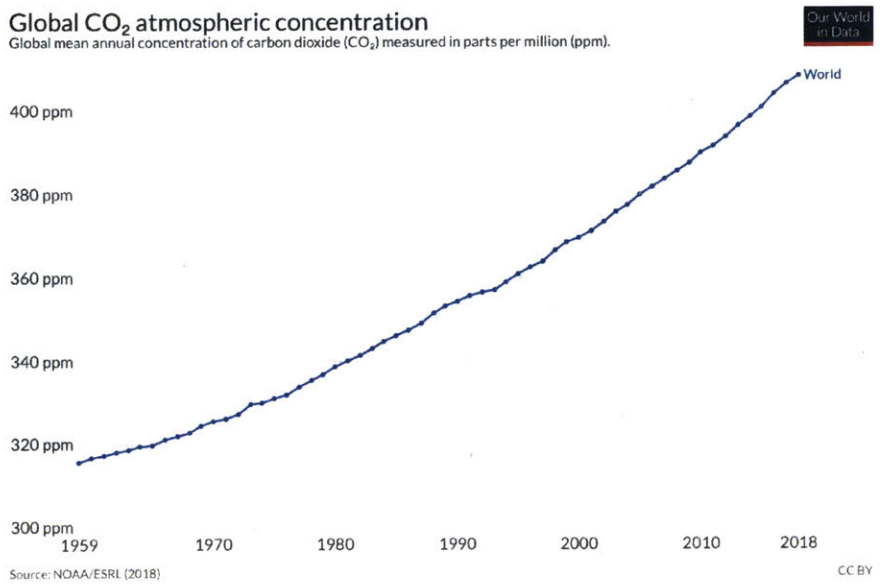

Figure 1-1: Global mean annual concentration of carbon dioxide measured in parts per million (Ritchie & Roser, 2019).

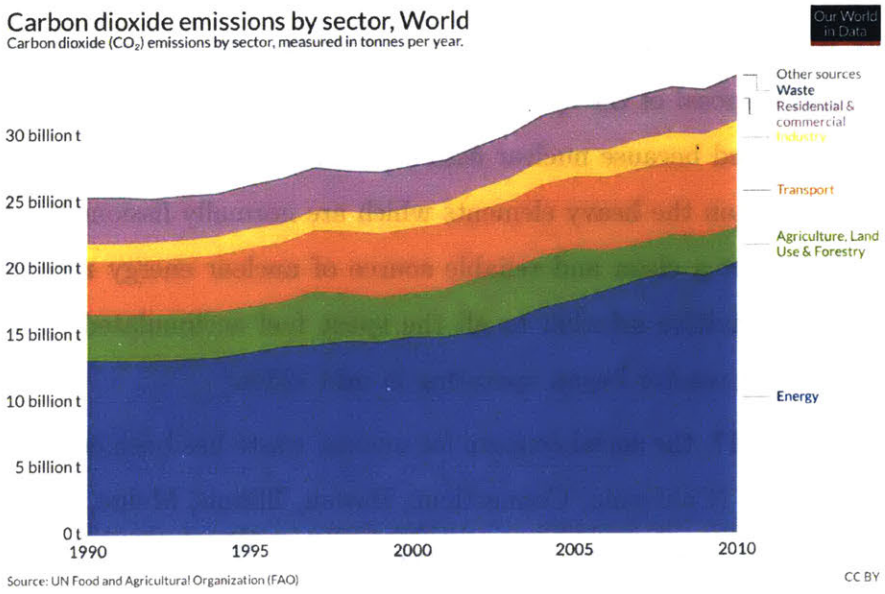

Figure 1-2: Global carbon dioxide emissions by sector measured in tonnes per year (Ritchie & Roser, 2019).

Nuclear fission is a very dense source of energy. The amount of free energy contained in nuclear fuel is millions of times the amount of free energy contained in an equal mass of refined petroleum fuel (1 kilogram of ^{235}U releases 79,390,000 MJ while 1 kilogram of standard gasoline releases 45.7 MJ). However, the expansion of nuclear

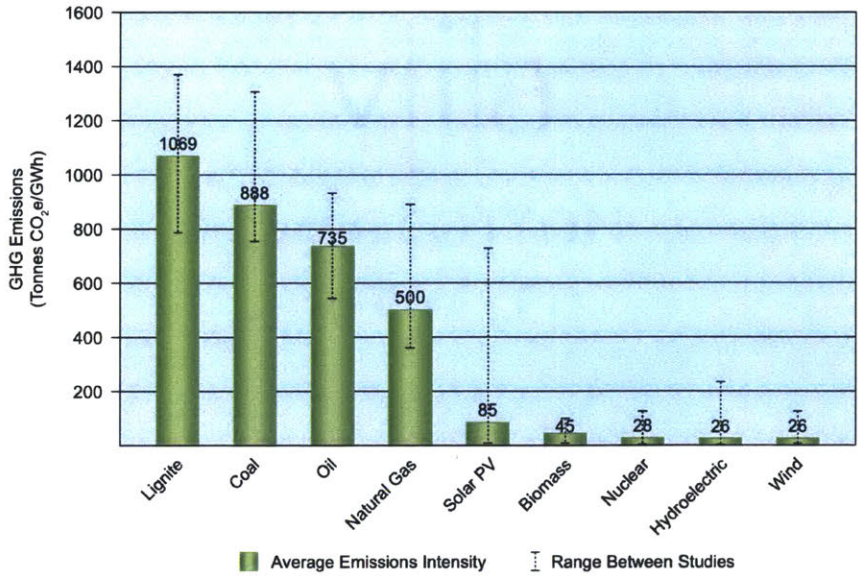

Figure 1-3: Life cycle greenhouse gas emissions intensity of electricity generation by source (World Nuclear Association, 2019a).

technology is hampered by the need for a technically safe and socially acceptable method of final disposal of the spent fuel and other radioactive byproducts. Special treatment is required because nuclear fission products are (on average) significantly more radioactive than the heavy elements which are normally fissioned as fresh fuel. The urgent need for a clean and reliable source of nuclear energy requires the development of a definitive solution to all the spent fuel accumulated since the first commercial nuclear reactor began operating in mid 1950s.[1]

In fact, since 2017, the social concern for nuclear waste has been enshrined in law. Fourteen US states (California, Connecticut, Hawaii, Illinois, Maine, Massachusetts, Minnesota, Montana, New Jersey, New York, Oregon, Rhode Island, Vermont and West Virginia) banned the construction of new nuclear power plants until a final repository is designed, there is demonstrable technology for reprocessing, or some other means for high level waste disposal (National Conference of State Legislatures, 2017).

[1]The first commercial nuclear reactor began operation in 1957 in the US (The Shippingport Atomic Power Station, 68 MW of power) and in 1954 in the USSR (Obninsk Nuclear Power Plant, 5 MW of power).

1.2.2 Radioactivity

Radioactivity is the phenomenon of emitting radiation spontaneously. An atomic nucleus, for some reason, is unstable, and releases energy to get into a more stable configuration. Excessive number of neutrons in a nucleus lead it to emit a negative beta particle, changing one of the neutrons into a proton. Excessive number of protons in a nucleus lead it to emit a positron (positively charged electron), changing a proton into a neutron. An excess of energy leads a nucleus to emit a gamma ray, which settles the nucleons into a lower energy configuration without changing any of the particles in the nucleus. An excess of mass leads a nucleus to emit an alpha particle, discarding four heavy particles (two protons and two neutrons). Radioactivity can be measured by counting how many atoms are spontaneously decaying each second.

Energy is released from the atom during each decay in the form of light and the kinetic energy of the products. These energetic products are called ionizing radiation. The atom is said to be radioactive and the nucleus it becomes is called the daughter. The set of all consecutive daughter products are called the decay chain.

There are many sources of radiation on Earth including geological, cosmogenic, and anthropogenic. Radioactive material has been always present in the Earth since the formation of the solar system. Examples include ^{40}K (half life of 1.28x10^{9} years), ^{232}Th (half life of 1.41x10^{10} years), ^{235}U (half life of 7.04x10^{8} years), and ^{238}U (half life of 4.47x10^{9} years).

Throughout the entire Earth Uranium occurs in most rocks in concentrations of 2 to 4 parts per million. All Uranium isotopes are naturally radioactive. Today, Uranium's slow decay is the main source of heat inside the Earth, which causes convection and continental drift (World Nuclear Association, 2019e). Along this decay chain, one of the elements is a naturally radioactive gas called Radon. As a gas, it can migrate from the location of the original uranium atom to the surrounding soils. On average, about two Radon atoms are emitted from every square centimeter of surface soil on the Earth every second of every day (Cohen, 1987). Humans have been exposed to Radon gas as long as they have inhabited the Earth.

Other radioactive elements are produced by the interactions of cosmic rays with atoms in the atmosphere. Examples of cosmogenic origin are: ^{3}H with half life of 12.3 years, ^{7}Be with half life of 53.28 days, and ^{14}C with half life of 5730 years (Poinssot & Geckeis, 2012).

Radioactive material is produced also by human activity, first of all from the testing of nuclear weapons, then from controlled nuclear fission in nuclear reactors and, finally, from artificially produced radionuclides for industry and medical treatment and diagnoses.

1.2.3 Nuclear fuel cycle

The nuclear fuel cycle refers to the activities associated with the fuel (i.e. uranium) utilized to generate electricity from nuclear reactions. The first step of the nuclear fuel cycle is the mining of uranium, and it ends at the disposal of nuclear waste. Uranium undergoes mining and milling, conversion, enrichment and fuel fabrication in order to be used in nuclear reactors. After spending several years in the reactor core, the uranium is deemed spent fuel, and can undergo further steps of temporary storage, or reprocessing before final disposal. Figure 1-4 schematizes all the steps of the nuclear fuel cycle. The following is a list of the steps, with the product stated for each:

1. Mining, uranium ore
2. Milling, uranium oxide (yellowcake or U_3O_8)
3. Conversion, uranium hexafluoride (UF_6)
4. Enrichment, low-enriched uranium
    - Product, depleted uranium (tails: some flow back to enrichment facility, others go to storage)
    - Storage
    - Tails re-enrichment

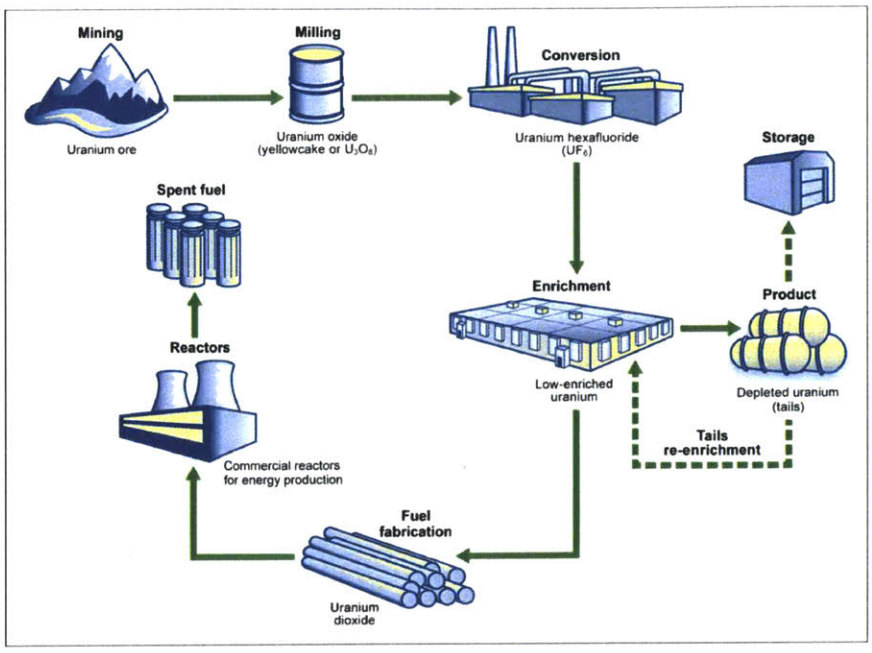

Figure 1-4: Nuclear fuel cycle (US Department of Energy, 2014)

5. Fuel fabrication, uranium dioxide

6. Reactors, commercial reactors for energy production

7. Spent fuel

1.2.4 Classification of radioactive waste

Nuclear wastes are classified by their radioactivity level as (Freiesleben, 2013):

- Very Low Level Waste (VLLW)

  It does not require high level of isolation and can be disposed of in near-surface landfills. Its radioactivity level is considered not harmful to the human environment.

- Low Level Waste (LLW)

  It contains a limited amount of long-lived radionuclides. It can be disposed of in engineered facilities near the surface, requiring robust isolation for a few

hundred years. It is produced by hospitals, industry processes and nuclear fuel cycles. It requires shielding during transport and handling. LLW can be compacted before disposal to reduce the volume. Although LLW represents 90% of the total volume of all radioactive waste, it represents only 1% of the radioactivity.

- Intermediate Level Waste (ILW)

  It contains significant amount of long-lived radionuclides, requires more containment than near-surface disposal. It comprises 7% of the volume of all radioactive waste and contains about 4% of its radioactivity. To be classified in this category, the generated heat load must not exceed 200 W/m^2 on the walls of the chamber of emplacement, producing a temperature increment smaller than 3 °K.

- High Level Waste (HLW)

  It represents more than 95% of the total radioactivity generated in the fission process in the reactors even though it represents the smallest volume of the total radioactive wastes. HLW can be classified into spent fuel itself or waste materials remaining after spent fuel is reprocessed.

1.2.5 Reasons that nuclear waste disposal is technically challenging

Spent fuel consists of assemblies of metal rods containing stacked-up fuel pellets (ceramic for PWR and metallic for TWR[2]). Before reacting, the fuel is mostly uranium. After reacting (i.e. the spent fuel), many uranium nuclei are converted into fission products.

The main reasons why nuclear waste disposal is so challenging are:

- Spent fuels are highly radioactive and contain several long-lived radionuclides,

[2]TWR and PWR stands for Traveling Wave Reactor and Pressurized Water Reactor respectively, as explained in Section 1.3.

for instance, I^{129}, T^{238}, and U^{238} with half-lives of 15.7, 14.1, and 4460 million years, respectively (NRC, 2019).

- It is at very high temperature; core inlet and outlet temperatures are 360°C and 510°C, respectively for the TWR commercial reactor (Gilleland et al., 2016a).
- It takes several years to cool down before it can be transported to a final disposal facility (Freiesleben, 2013).
- It contains fission gases that make the nuclear waste hazardous to move or otherwise handle (Knief, 2008).
- Spent fuel produces continuous heat loads for thousands of years from the radioactive decay of elements.
- It takes several years to cool down before it can be transported to a final disposal facility.
- Radioactive material is a solid that dissolves in water and therefore can spread (NRC, 2008).

1.2.6 Current solution to store nuclear waste

This section refers to conventional PWR or BWR (Boiling Water Reactors) nuclear reactors operating in the world, which are cooled with water (not to TWR, which is cooled with liquid sodium). As time progresses, fissionable U^{235} isotopes in the nuclear material can no longer be used to produce electricity in standard nuclear reactors, the fuel becomes considered "spent." After a certain number of years operating in the nuclear reactor (step 1 of Figure 1-5), about 15 years for conventional reactors, the spent fuel is removed from the reactor core and is stored in pool of water to cool down. Pool storage serves to cool spent fuel and shield against its radiation. It remains there for about 20 to 40 years (step 2 of Figure 1-5). After the spent fuel has cooled, it is encapsulated in metallic containers, which are placed into meter-thick concrete casks at nuclear reactor facilities (step 3 of Figure 1-5). Some nuclear facilities do not even

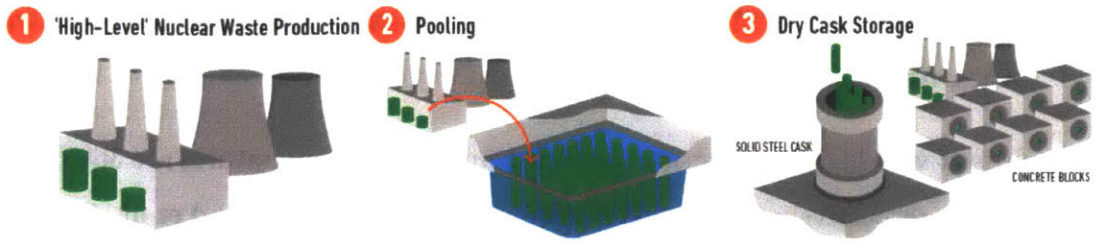

Figure 1-5: Current nuclear storage system (Stroud, 2012).

posses this dry storage system, and the spent fuel remains in the cooling pools. For almost all countries, this is the end of the fuel cycle.

A few notable countries such as Japan and France have implemented spent fuel reprocessing, which consists of chemical processes that separate plutonium and uranium from other nuclear waste contained in the spent fuel. The separated plutonium can be used to fuel reactors, but also to make nuclear weapons. Reprocessing can allow terrorists to acquire nuclear weapon materials, and for nations to develop nuclear weapon programs. In the 1970s, the United States decided not to reprocess spent fuel from power reactors based on the nuclear non-proliferation principles, and dispose of it in a deep underground geologic repositories where it would remain isolated from the human environment. However, the final disposal of this spent fuel is still a challenging and unresolved worldwide problem. To date, no country has an operating licensed disposal system for civilian High-Level Waste[3].

1.2.7 Current status of US spent nuclear fuel

Commercial Spent Nuclear Fuel (SNF) is in temporary storage at 75 reactor sites in 33 states around the US, as shown in Figure 1-6. Pool storage provides cooling and shielding of radiation. At this step, the main risk of this nuclear waste relies on loss of shielding water or cooling. Nuclear facilities pools have reached capacity limits and for this reason dry storage has been adopted. Some power plants have shut down and

[3]To date, Finland is the only country that has a HLW nuclear repository under construction, with no nuclear waste placed yet. It is the Onkalo spent nuclear fuel repository at the Olkiluoto Nuclear Plant (west coast of Finland) owned by the company Posiva. Its name means small cave, and is built in the granite bedrock. It is based on the KBS-3 method of nuclear waste burial developed in Sweden by SKB. This method will be detailed in Chapter 2.

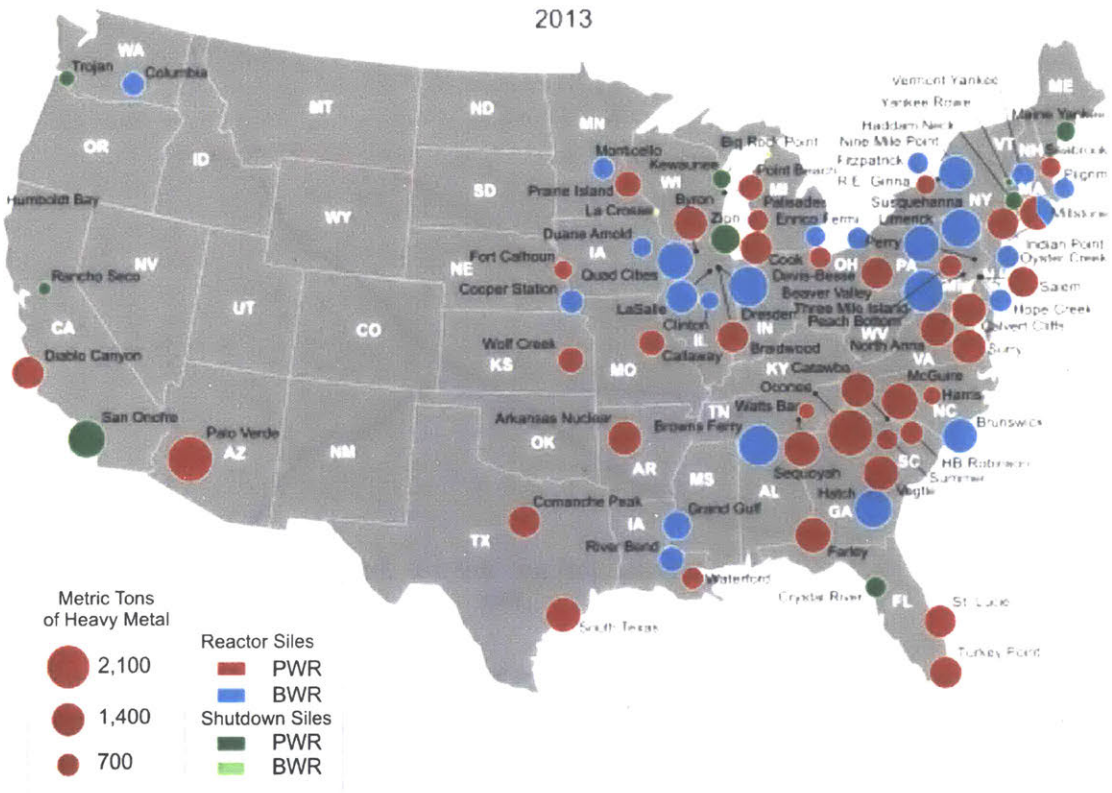

Figure 1-6: Commercial spent fuel (BRW and PWR) storage locations in US (Swift, 2017).

all that remains is "stranded" fuel at an independent spent fuel storage installation, shown as green circles in Figure 1-6.

Figure 1-7 presents the mass of spent fuel as a function of time, projected out to the year 2060. The red curve represents the total spent fuel, the blue curve represents the pool storage, and the green curve represents the dry storage. To date, there is approximately 80,150 MTHM (metric ton of heavy metal) of spent fuel in storage, of which 25,400 MTHM are in dry storage at reactor facilities, and the rest remains in the pool storage at reactors. This pool storage cannot be continued because pool storage is at full capacity now. Approximately 2,200 MTHM of spent fuel is generated, and 160 new dry storage canisters are loaded in the US each year (Swift, 2017).

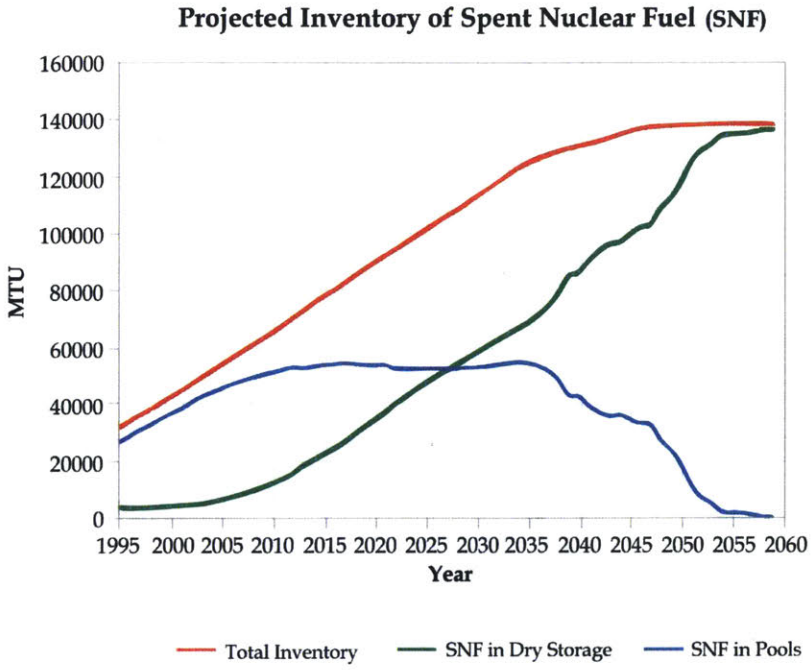

Figure 1-7: Projection of the inventory of Spent Nuclear Fuel in the US, in MTHM. This prediction assumes full license renewal and no new disposal system or reactor construction (Swift, 2017).

1.3 Traveling Wave Reactor

1.3.1 Type of nuclear reactors

To date, all commercial power reactors are based on nuclear fission. Nuclear power plants produce electricity from the heat generated when suitable atoms (such as ^{235}U) are split apart into smaller atoms. When these atoms split or fission, heat and neutrons are released. These neutrons cause subsequent fissions in a sustained chain reaction. Sustaining this chain reaction in the reactor is the key to providing reliable electricity.

Fission reactors can be categorized based on the energy of the neutrons that sustain the fission chain reaction:

- Thermal reactors

  They use slow neutrons (low kinetic energy), called thermal neutrons, to sustain

the nuclear chain reaction. Almost all current reactors are of this type. Because neutrons are born with high kinetic energy, these reactors employ neutron moderator materials that slow down neutrons until their kinetic energy reaches the thermal range. The neutrons are in thermal equilibrium with the medium they are interacting with, the reactor's fuel, moderator and structure, which is much lower energy than the fast neutrons (high kinetic energy) initially produced by fission.

Almost all nuclear power plant reactors are thermal reactors. The majority of them are Light Water Reactors (LWR). The light-water reactor uses ordinary water as its neutron moderator and coolant. The light water absorbs a large number of neutrons, which makes uranium enrichment necessary, increasing the overall costs.

There are three categories of LWR: the Pressurized Water Reactor (PWR), the Boiling Water Reactor (BWR), and the Supercritical Water Reactor (SCWR). The majority of LWRs are Pressurized Water Reactors (PWR). In a PWR, the water (coolant) is pumped at high pressure to the reactor core where it is heated by the energy released by fission. The heated water flows to a steam generator where it transfers its thermal energy to a steam generator. In the steam generator, the heat coming from the primary circuit turns the water in a secondary circuit into steam, which, in turn, spins an electric generator. Pressure in the primary coolant loop (16 MPa) prevents the water from boiling within the reactor. The less numerous of LWR are Boiling Water Reactors (BWR). The heat released in the core causes the cooling water to boil, producing steam. The steam is directly used to propel a turbine, after which it is cooled in a condenser and converted into liquid water. This water is then returned to the reactor core, closing the loop. The cooling water is maintained at about 7.6 MPa so that it boils at about 285°C in the core.

Another type of thermal reactors is the Heavy Water Reactor (HWR). It achieves moderation with heavy water, where more massive deuterium (2H) atoms re-

place protium (H) in the water molecule. Heavy water absorbs fewer neutrons and thus the fuel requires no enrichment.

- Fast neutron reactors

  This reactor uses fast neutrons to sustain the fission chain reaction in the fuel. Neutron moderators (to slow down neutrons) are thus undesirable in this reactor. Fast reactors must have a significant excess of neutrons (due to low parasitic absorption), unlike PWRs (or LWRs). On the other hand such reactors must compensate for the missing reactivity of the neutron moderator effect. Maintaining a chain reaction requires the fuel to be more highly enriched in fissile material (about 10% or more) when compared to that required for a thermal reactor due to the relatively lower probability of fission versus capture by U^{238}. Fast reactors have the potential to produce less transuranic waste because all actinides are fissionable by fast neutrons, but they are more difficult to build and more expensive to operate. Fast reactors are less common than thermal reactors. Most fast reactors have a hexagonal lattice in order to reach smaller volume ratios of coolant to fuel. Likewise, fast reactors have more compact nuclear cores than thermal reactors in order to reach required core reactivity. Combined, these factors mean that fast reactor cores exhibit higher power densities. Water cannot be used as the coolant because of its moderating properties and insufficient thermal properties. Therefore, fast reactors have used liquid sodium or lead as coolants.

1.3.2 TerraPower TWR

1.3.2.1 Background

The first conceptualization of a Traveling Wave Reactor dates from 1958, when Saveli Feinberg proposed a nuclear reactor that could breed fuel within its core, calling it a "breed and burn" reactor. Michael Driscoll at MIT carried out further research on this reactor concept in 1979. Subsequently Lev Feoktistov in 1988, Edward Teller in 1995, and Hugo Van Dam in 2000, and Hiroshi Sekimoto in 2001 published further

research on a nuclear breeding-burning wave that propagates slowly in the core's axial direction. In those years, the concept was known as the "candle reactor". The concept would eventually evolve into into TWR, presented in Figure 1-8.

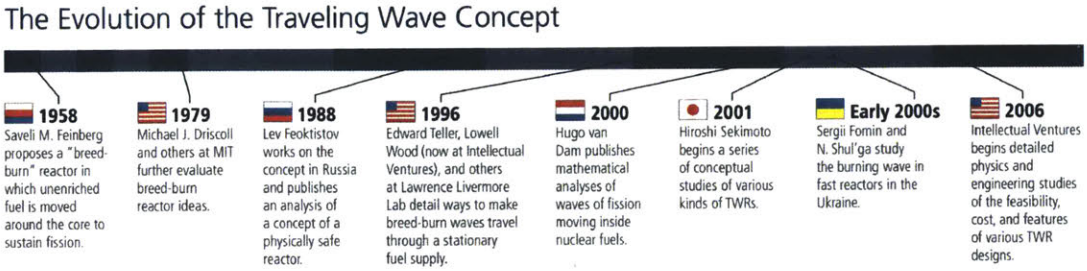

Figure 1-8: Evolution of the TWR concept (TerraPower, 2019).

In 2006, TerraPower[4] proposed a practical and innovative design for the TWR concept, a breed-and-burn fast reactor. In this design, the breed-burn wave propagates gradually from the center outward instead of from one end of the reactor to the other. Liquid sodium is used as coolant. To date, no TWR has ever been built. The TerraPower TWR is under active development, but publicly published research on its progress is limited.

1.3.2.2 Reactor design

The goal of the TWR design is to reduce risk of proliferation and to utilize low-level waste as fuel. The TWR has unique core physics that converts "fertile" material into fuel. The advantage of this reactor is that it does not have to be refueled or have its waste removed until the end of its life. In contrast, conventional light water reactors require the fuel to be replaced with fresh enriched uranium every 18 to 24 months to sustain electricity production. The TWR uses depleted uranium (^{238}U) in conjunction with an "igniter" (^{235}U), without need for refueling. TWR is capable of sustaining fission from natural or depleted uranium, which is currently a waste byproduct at enrichment plants, obtained when ^{235}U is separated from natural

[4]TerraPower is a nuclear reactor design company with headquarters in Washington, US, founded by Bill Gates in 2006.

uranium for conventional LWR fuel. Only small enrichment is needed to start fission, and no chemical reprocessing of the spent fuel is required.

The TWR design converts depleted uranium into usable fuel as it operates, with a small amount of enriched uranium initiating a slow moving wave. In fact, two parallel waves propagate through the core: the first wave creates fissionable material, and the second wave consumes the created material. This allows for more efficient fuel utilization than conventional reactors. This reaction can be continued for decades if the right conditions are achieved in the reactor. Therefore TWR generates more energy per kilogram of natural uranium, without reprocessing. The TWR requires about one-fiftieth the uranium needed by an LWR to produce the same amount of electricity (Hejzlar et al., 2013). In the long term, using waste uranium reduces the amount of waste in the overall nuclear life cycle. These features make this reactor an extremely attractive energy source. The elimination of reprocessing reduces proliferation risk, reduces the overall cost of the energy production, and becomes a sustainable source of energy by making use of a waste byproduct and reducing the production of greenhouse gases.

To summarize the design of the plant, a cylindrical rector core is submerged in liquid sodium. A continuous looping stream of liquid sodium absorbs the heat, leaves the reactor core, and then boils water to drive the steam turbine (see Figure 1-9). The major innovation in the TWR is the core. Its cylindrical geometry consists of assemblies of hexagonal cross-section, comprising a combination of assemblies of rods with enriched uranium and assemblies of rods with depleted uranium metal alloy. Figure 1-10 shows an overview of how assemblies are combined to make the core. Fuel assemblies are hexagonal ducts consisting of wire-wrapped fuel rods in a symmetric array. Assemblies are separated from one another by 5mm in the core. Assemblies with depleted uranium pins are for breeding (fertile assemblies), and fissile assemblies with fuel pins with ^{235}U (enrichment less that 20%) are needed to produce initial criticality.

Figure 1-9 presents a schematic of the TWR reactor. The reactor is placed in a vessel underground, which provides additional safety. The TWR is a pool type reac-

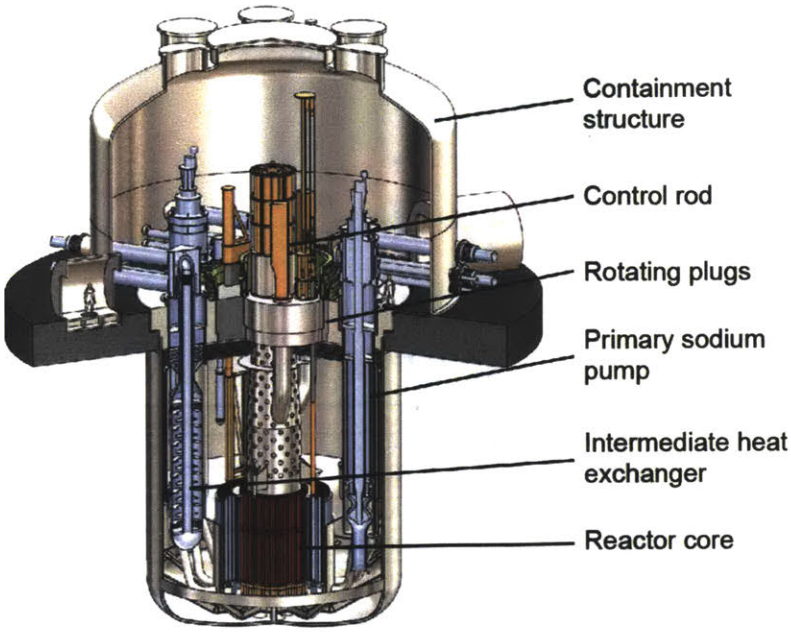

Figure 1-9: Illustration of TWR components inside the containment (Gilleland et al., 2016b).

tor. The reactor vessel contains the reactor core submerged in liquid sodium. TWR harnesses the advantages of sodium as a coolant to improve thermal performance. The figure also shows the other main reactor components: the sodium pumps, the intermediate heat exchangers, the in-vessel fuel handling machine shuffles, and control rods. Intermediate heat exchangers transfer the heat from the primary sodium pool to a secondary sodium loop, which transfers the heat to the tertiary loop containing water and steam generators. Periodically, the in-vessel fuel handling machine shuffles the fuel swapping expired fuel rods from the center of the core for fresh fuel rods from the outer edge to sustain the fission reaction. Control and safety rods are suspended above the reactor core. Control rods can be inserted into the core, adjusting the rate of the fission reaction. Safety rods can be dropped (gravity activated) into core in case of an emergency, quickly stopping the reaction altogether.

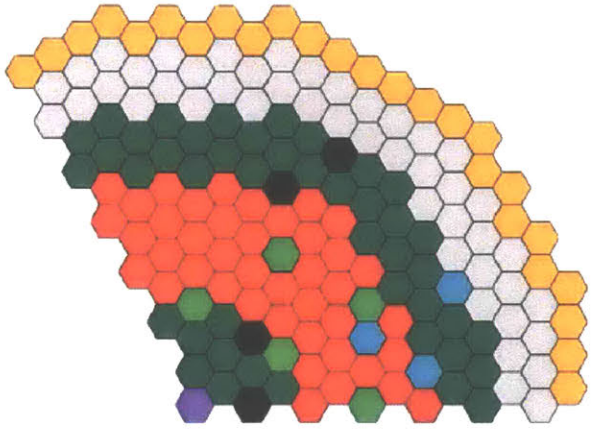

	Assembly Type	Quantity
	Driver Assemblies	126
	Feed Assemblies	132
	Control and Safety Assemblies	15
	Lead Test Assemblies I	12
	Lead Test Assemblies II	9
	Open Test Assembly	1
	Reflector Assemblies	138
	Shield Assemblies	78
	Total	**511**

Figure 1-10: TWR plain view of assemblies, known as the core map. Fuel assemblies are clustered with approximately 5mm spacing between the flats of the hexagonal ducts in a symmetric array. The core is composed of 511 assemblies. Only one third of the core is shown; the rest can be inferred from symmetry. Different colored hexagons correspond to assemblies of different functions in the TWR core. These functions are listed in the table above. For more information about these see (Hejzlar et al., 2013). Detail of an individual assembly is shown in Figure 1-13.

1.3.3 Current status of the reactor design

To date, TerraPower has achieved significant progress in the development of this advanced nuclear reactor design, and has completed the core concept design for a prototype of the TWR program. Construction of a TWR engineering simulator is still an important milestone. TerraPower continues to improve the TWR design to bring it ever closer to construction. TerraPower plans to have its prototype TWR reactor by the mid-2020s, followed by commercial distribution (TerraPower, 2013).

1.3.4 TWR spent fuel characteristics

The TWR spent fuel has distinctive characteristics that differ from conventional (PWR) spent fuel.

1.3.4.1 Dimensions

The TerraPower fuel assembly has a hexagonal cross-section, see Figure 1-11. The distance between two opposed sides of the hexagon is 16 cm. The diameter of the TWR fuel assembly is 18.47 cm. The assembly has a total height of 5.577 m, see Figures 1-12 and 1-13. The nuclear fuel is only located within 2.5 m of the total length of the rod, at the center, as seen in Figure 1-14. The TWR assembly comprises 271 pins of 8 mm outer diameter each. Each pin contains the metallic fuel. The uranium metal is alloyed with 5% to 8% zirconium. Individual fuel pins have a thin wire of 1.18 mm diameter helically wrapped around the circumference of the cladding. This wrap provides space for the coolant and mechanical stability for the assembly. The cladding, wire wrap and housing are made of ferritic-martensitic steel due to its good performance under irradiation.

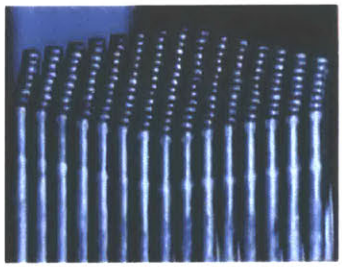

Figure 1-11: TWR assembly. The picture shows pins arranged in hexagonal cross section. Pins are made of HT-9 (High-Cr martensitic steel) (Gilleland et al., 2016a).

In contrast to LWR's spent fuel, TWR's spent fuel has smaller cross-section dimensions. PWR's assembly width is 21.4 cm and BWR's assembly width is 13.4cm, see Figure 1-15. PWR's assembly height is 4.1m.

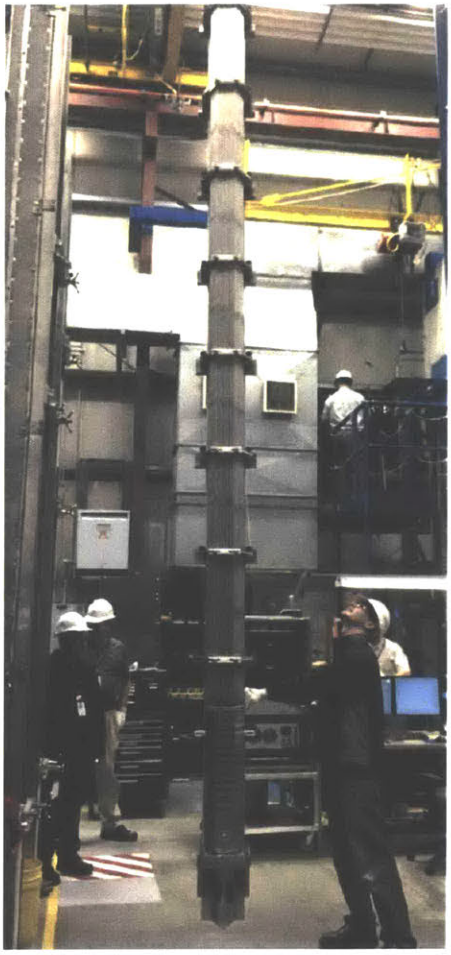

Figure 1-12: Full-size TWR proof-of-fabrication fuel assembly (Gilleland et al., 2016a).

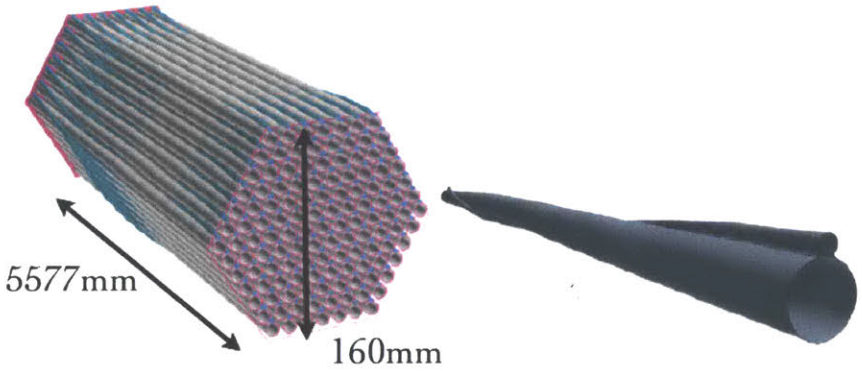

Figure 1-13: TWR assembly (Sosnovsky et al., 2015). Image at left shows dimensions of assembly. Image at right shows one rod and its wired wrap.

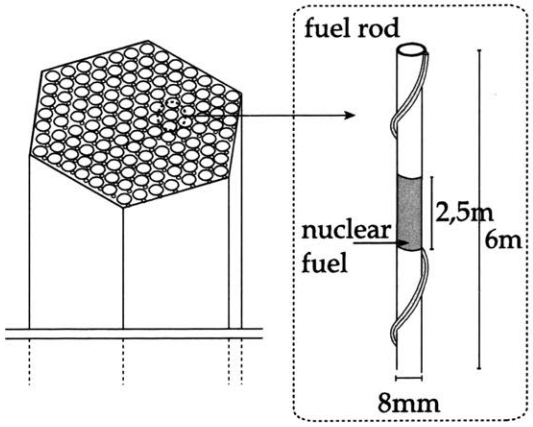

Figure 1-14: TWR assembly detail. Image at right shows one rod, its wired wrap, and the location of the nuclear fuel within the rod.

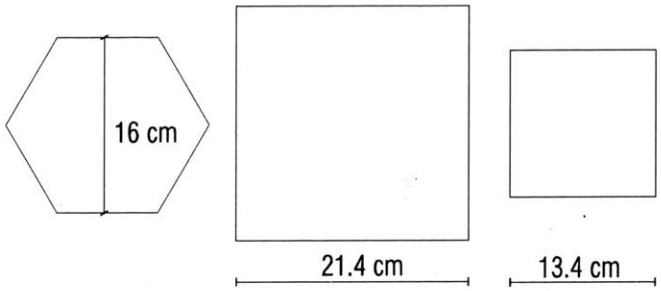

Figure 1-15: Comparison of assembly cross-sections, from left to right: TWR, PWR and BWR respectively.

1.3.4.2 Decay heat

The heat generation of the spent fuel depends on the radionuclide inventory. The radionuclide inventory present in spent fuel depends on several factors:

- reactor type
- burnup
- cooling time.

Burnup of nuclear fuel expresses the fission energy released per initial amount of heavy metal in the fuel (gigawatt-day per metric ton of heavy metal, GWd/MTHM).

After the fuel is discharged from the reactor, basically no new fission products are generated, and the radioactive nuclides start to decay. As they decay, there is an increase in the inventory of some isotopes that are daughter products of other isotopes. Figure 1-16 presents a list of the main long-lived radionuclides present in irradiated fuels and their respective half-lives. Figure 1-17 presents the composition of spent nuclear fuel for standard PWR, considering 33GWd/MTHM and 10 years of cooling time.

TerraPower has reserved information on the spent fuel inventory, but has provided us with an average decay power for the TWR spent fuel. For TWR assemblies the average linear power as a function of time, expressed in Watt per meter length of fuel, is given by:

$$\overline{q'(t)} = 458\left(\frac{10}{t_c + t}\right)^{0.575} \tag{1.1}$$

where t_c represents the post irradiation cooling time of the spent fuel t is the time since entombment in years.

The active fuel length is 2.5 m, only a fraction of the rod, considered to be centered in the rod length, see Figure 1-14. The heat production across the fuel length is not uniform. It can be approximated by $q'(z) = 740\cos(\frac{\pi z}{2.5})$, z is expressed here in m. The ratio of the maximum linear power over the average linear power is 2.4.

The heat generation of PWR spent fuel is uniform across the length. The volumetric decay heat of PWR spent fuel (57 MWd/kgHM), expressed in W/m^3 corresponds to (Malbrain, Lester, & Deutch, 1982):

$$q'''(t) = 2176\left(\frac{t_c}{t_c + t}\right)^{0.75} \tag{1.2}$$

where

t_c represents the post irradiation cooling time of the spent fuel.

Figure 1-18 presents the comparison of the average volumetric heat decay for PWR and TWR assemblies considering 25 years of cooling time, a typical proposed value of cooling time for PWR spent fuel. The graph is in logarithmic scale for both power

Radionuclide	Half-life (year)
Uranium	
^{234}U	2.46×10^{5}
^{235}U	7.04×10^{8}
^{236}U	2.34×10^{7}
^{238}U	4.47×10^{9}
Actinides (α emitters)	
^{238}Pu	87.7
^{239}Pu	24 100
^{240}Pu	6 560
^{241}Pu	14.35
^{242}Pu	3.74×10^{5}
^{237}Np	2.14×10^{6}
^{241}Am	432.7
^{243}Am	7 368
^{245}Mc	8.5×10^{3}
^{246}Mc	4.73×10^{3}
Fission products (β/ γemitters)	
^{79}Se	6.5×10^{5}
^{93}Zr	1.5×10^{6}
^{99}Tc	2.13×10^{5}
^{107}Pd	6.5×10^{6}
^{126}Sn	1×10^{5}
^{129}I	1.57×10^{7}
^{135}Cs	2.3×10^{6}
Activation products (β/ γemitters)	
^{14}C	5 715
^{59}Ni	7.6×10^{4}
^{63}Ni	100
^{93}Zr	1.53×10^{6}
^{94}Nb	2.03×10^{4}

Figure 1-16: Main long-lived or parent radionuclides present in irradiated fuels (Nuclear Energy Agency, 2009).

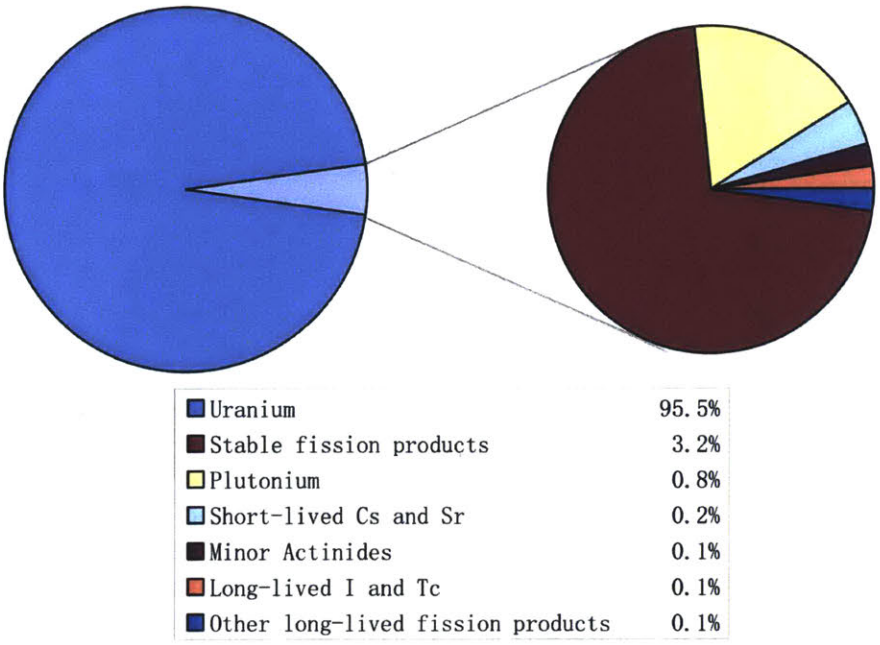

Figure 1-17: Composition of spent nuclear fuel, for standard PWR 33 GWd/MTHM and 10 year of cooling (Nuclear Energy Agency, 2006).

and time. All the simulations in this work assume this cooling time. The values in the plot are refer to volume of fuel, which means, the 2.5 m of fueled region for the TWR assembly while to the entire length for the PWR assembly. This ultimately implies that the total heat released is comparable. Figure 1-19 presents the heat decay (per unit volume of fuel) for the first 100 years, in linear scale, after 25 years of cooling time.

1.4 Thesis outline

This thesis is organized in seven chapters. Chapter 1 presents the background information necessary to understand the problem to be addressed in this thesis. Chapter 2 summarizes the methods used for geological disposal of spent fuel. This chapter describes the state of the art on nuclear waste disposal in the world and in the US. It also introduces the deep borehole concept, which is used as disposal method for the TWR spent fuel. Finally, Chapter 2 ends with introducing the time scale of analysis required by nuclear regulators. Chapter 3 presents the mathematical model of the

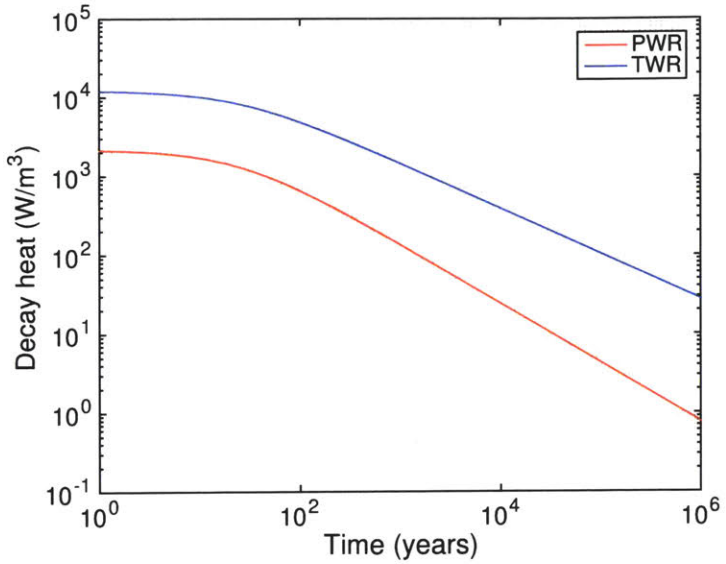

Figure 1-18: Comparison between PWR and TWR average volumetric decay heat (per unit volume of fuel) for 25 years of cooling time in log-log scale.

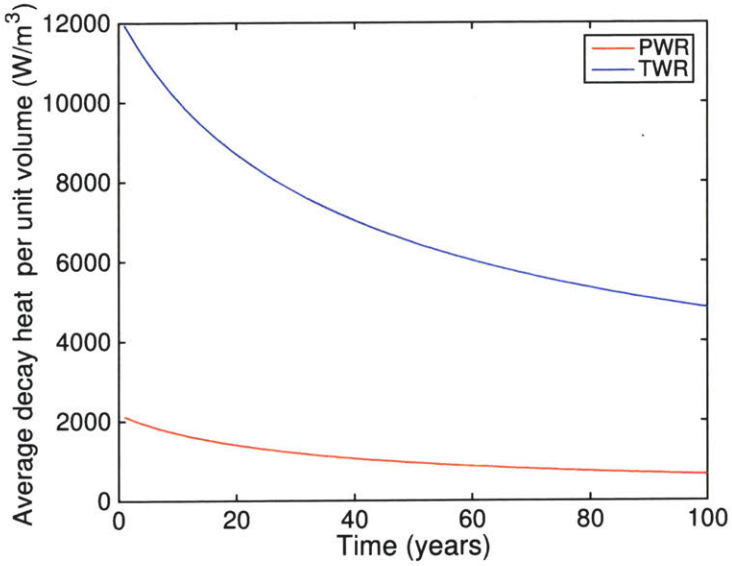

Figure 1-19: Comparison between PWR and TWR average volumetric decay heat (per unit volume of fuel) for the first 100 years after 25 years of cooling time.

physical processes that occurs in the nuclear waste repository after placing the spent fuel in deep boreholes. Chapter 4 introduces the validation cases considered for the code used. Chapter 5 presents the case studies analyzed. Chapter 6 summarizes the results of this thesis and presents the remaining work necessary for further evaluating

the performance of deep boreholes as a permanent disposal method of the TWR spent fuel.

Chapter 2

Geological Disposal

2.1 Definition

Spent nuclear fuel contains many isotopes, some of them with an extremely long half-lives (such as 4.468 billion years for ^{238}U) and high activity (release high heat, such as ^{99}Tc[1]). As a result, spent fuel needs to be deposited in a system that guarantees safety for such a time scale. To date, geological disposal remains the only long-term solution available for final disposal. The goal of the geological disposal system is to use the natural host rock as the real barrier for radionuclide isolation from the human environment. For decades, scientists worldwide have agreed that geological disposal remains the only long-term solution available for the final isolation of high-level nuclear waste. However, this has been determined to be a challenging problem, not only because of the nature of the waste and the geologic environment, but also because of the framework that rules the management of the waste.

The first investigations on underground isolation of radioactive waste began in US in the 1960s, in a salt mine near Lyons Kansas (Witherspoon & deMarsily, 1991), and in West Germany in 1965 in an underground research laboratory in a salt mine at Asse Mountains (Langer, Schneider, & Kühn, 1991). The first studies of isolation of nuclear waste in granite started in 1977 at Stripa (central Sweden) in an abandoned iron mine

[1] ^{99}Tc has low specific activity but it is produced in such quantities that its overall contribution to decay heat is large.

(Witherspoon & Degerman, 1978). An experimental tunnel of 5 meters of diameter at 300 meters depth was excavated in a mass of granite outside the underground working areas of the mine. Several investigations on underground nuclear waste isolation were performed to analyze the geological, geophysical, hydrological, geochemical, and structural effects of using a large crystalline rock mass as a geologic repository for nuclear waste. This program was sponsored by the Swedish Nuclear Power Utilities through the Swedish Nuclear Fuel Supply Company (SKBF), and the US Department of Energy (DOE) through the Lawrence Berkeley Laboratory.

In 1980, Belgium started the construction of the first underground laboratory in Europe for experimental research on geological disposal for high-level and/or long-lived radioactive waste, called HADES. It was built at a depth of 225 meters in the core of the Boom Clay formation for researching the geological disposal in clay, (Belgian Nuclear Research Centre, 2019). Switzerland in 1983 started a laboratory in crystalline rock at 450 m below Juchlistock Mountain in the Bernese Alps (McCombie & Thury, 1996). In subsequent years, several underground research laboratories were built, even for international projects such as Grimsel (crystalline rock) or Mont Terri (opalinus clay).

In any disposal system the nuclear waste is enclosed in metallic canisters to provide mechanical resistance to the assembly and to isolate the radioactive material from the human environment. Different disposal concepts emphasize different barriers:

- engineered barriers: metallic canister, filling material of the canister, and filling material of deposition holes
- natural barriers: host rock.

In contrast to the deep borehole concept, mined geological repositories, excluding salt repositories, rely more strongly on engineered systems such as the canister and the buffer materials.

The Finnish design, shown in Figure 2-1, consists of a copper canister with a cast iron insert to increase mechanical resistance. The canister of 1m diameter is designed to contain several assemblies, each with square cross-section. Figure 2-2 shows the

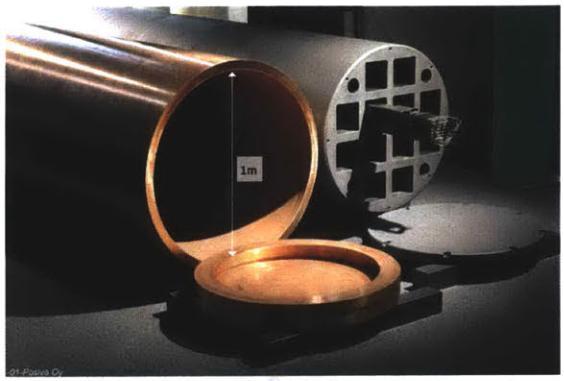

Figure 2-1: Disposal container of the spent fuel planned to be used in Finland. It consists of a copper canister with a cast iron insert to increase strength, shown at the right. In this design the canister of 1 m diameter contains several spent fuels (Posiva, 2019).

typical European design of disposal systems based on relative short boreholes that contain one canister each, filled with clay. This topic will be expanded in Sections 2.2 and 2.5.

2.2 Status around the world

Different countries have considered geological disposal in their own formations. Table 2.1 presents the status of nuclear waste disposal systems around the world. In Europe, Finland has approved the construction of a final repository for spent fuel, called Onkalo. It is a deep geological repository for the final disposal of spent nuclear fuel, the first such repository in the World (see Figures 2-3 and 2-4). Sweden has submitted an application for a repository and is under review (see Figures 2-5 and 2-6). France is planning to apply to build a final repository of HLW in the coming years (Figure 2-7). These three countries are the front-runners in developing a nuclear waste disposal method, and currently many other countries are in the process of addressing the problem of the final disposal of nuclear waste. A multinational geologic disposal facility (MGDF) has been discussed for more than 40 years (Faybishenko, Birkholzer, Sassani, & Swift, 2016a). Europe has led the development of the MGDF. This kind of repository collects the nuclear material in a central location from widespread ra-

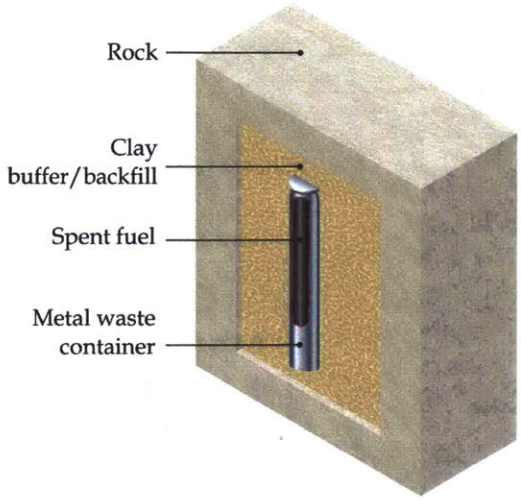

Figure 2-2: Example of multi-barrier systems which consists of a metallic canister and a clay backfill between the the metallic container and the natural host rock (Radioactive Waste Management, Government UK).

dioactive waste management programs at different stages of development, and also can include nuclear waste from countries with no nuclear waste programs. Such a repository, however, is still only a theoretical concept owing to cross-national political difficulties, differences in nuclear safety and non-proliferation and environmental policies, and public concerns.

2.3 Status in the US

In the US, the Yucca Mountain was designated by the Nuclear Waste Policy Act amendments of 1987 to be a geological repository for HLW. It is located in Nevada (130 km northwest of the Las Vegas Valley). The project was approved in 2002 by the US Congress, but federal funding for the site ended in 2011, leaving the US without any site for disposal of the HLW, currently at the nuclear power plant facilities around the country. The Yucca Mountain repository would have been the first nuclear repository operating in the World. The Yucca Mountain design consists of tunnels approximately 1000 feet below the top of Yucca Mountain and about 1000 feet above the aquifer underlying the repository, see Figures 2-8 and 2-9. Radioactive waste is

placed in deep tunnels utilizing for isolation from the human environment a combination of natural and engineered barriers. Its maximum capacity is 70,000 metric tons of spent nuclear fuel and high-level waste (Nuclear Waste Policy Act of 1982), which is less than the current total accumulated spent fuel in the US (Swift, 2017). Consequently, even if this repository were constructed, another would be needed. For non-civilian nuclear waste, the US has the Waste Isolation Pilot Plant (WIPP), which was constructed during the 1980s for the disposal of only the transuranic waste from the Department Of Energy (DOE) sites with national defense purposes (research and production of nuclear weapons). Transuranic waste consists of clothing, tools, rags, residues, debris, soil and other items contaminated with plutonium and other man-made radioactive elements. The waste is disposed of in rooms mined in an underground salt bed layer over 600 m from the surface. The WIPP facility is located 42 km east of Carlsbad, New Mexico, in the Delaware Basin, a sedimentary basin formed approximately 250 million years ago. This basin was formed by repetitive filling of an ancient shallow sea that evaporated while the basin slowly subsided, leaving an impermeable layer of evaporites, mainly salt, of 1000 m thickness, that got covered by soil and rock over time.

2.4 Previous studies on nuclear waste disposal

One can distinguish, grosso modo, two geological disposal system designs: the shallow mined repositories and the deep borehole repositories. In the first design the nuclear waste is placed within the first several hundred meters (700m) below the repository surface. This approach is mainly adopted in Europe (e.g. Onkalo in Finanld and Forsmark in Sweden). In contrast, in the deep borehole concept the nuclear waste is placed several kilometers below the repository surface.

Many researchers have studied the problem of geological disposal of nuclear waste, analyzing different problems involved in the disposal system. The majority of the published research addressed the study of shallow disposal systems. Less abundant in the literature is the investigation of deep repositories. Below are references to

Table 2.1: Geological disposal systems around the world (Faybishenko et al., 2016b).

Country	Host rock type	Status
Finland	Granitic Gneiss	Construction license granted 2015
Sweden	Granite	License application submitted 2011
France	Argillite	Disposal operations planned for 2025
Canada	Granite, sedimentary rock	Candidate sites being identified
China	Granite	Repository proposed in 2050
Russia	Granite, gneiss	Licensing planned for 2029
Germany	Salt, other	Uncertain
US	Salt (transuranic waste at the Waste Isolation Pilot Plant [WIPP]) Volcanic tuff (Yucca Mountain)	WIPP: operating Yucca Mountain: suspended

relevant studies on shallow disposal systems, which will act as reference points for deep borehole repositories presented in Section 2.5.

S. Olivella, J. Carrera, A. Gens and E. Alonso developed a numerical model to analyze nuclear waste disposal in saline rock. They proposed a general formulation for non-isothermal multi-phase flow of brine and gas through saline media (Olivella, Gens, Carrera, & Alonso, 1995). Salt rock formations (composed of salt minerals, with halite [NaCl] the most common) are considered as one of the potential medium for radioactive waste disposal. Salt repositories are considered as disposal host media given the ductile behaviour of salt rock. This allows self sealing of natural and induced defects, even closing them. By this mechanism fills and seals can reduce their porosity to reach values similar to natural salt rock. Environmental conditions strongly affect the rates of deformation. These authors proposed the macroscopic governing equations, in continuum media, for non-iosthermal multiphase flow of brine and gas through porous deformable saline media. This formulation is used to develop a numerical finite element model to handle COupled DEformation, BRIne, Gas and

Figure 2-3: ONKALO nuclear waste repository site in Olkiluoto in summer 2014. The ramp and entrance to the access tunnel are visible at the center of the picture (Faybishenko et al., 2016a).

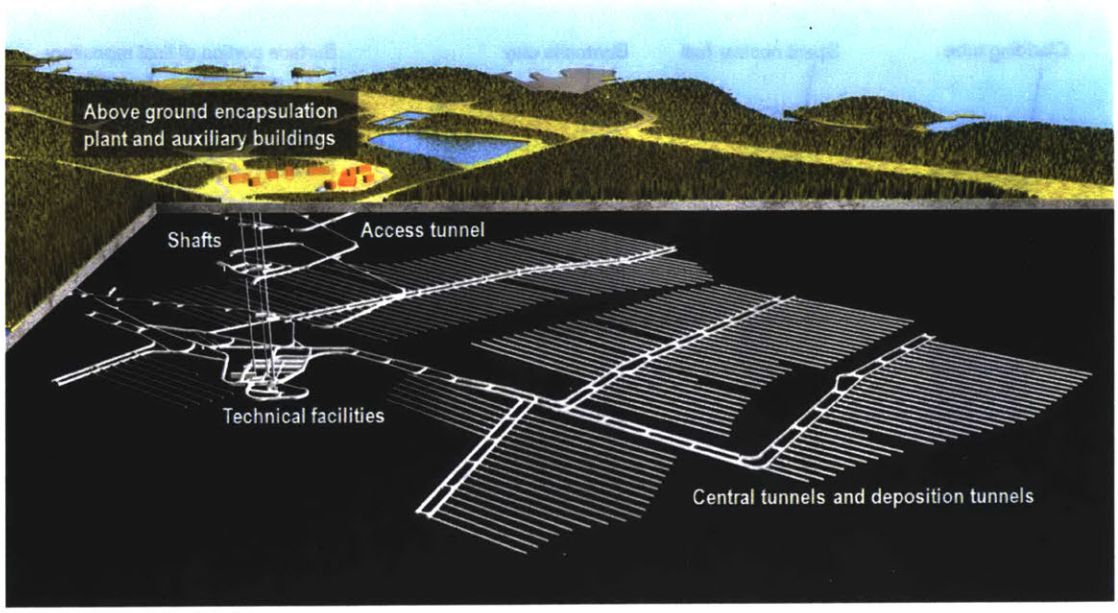

Figure 2-4: ONKALO nuclear waste repository facility design: surface buildings, tunnels to the repository itself, deposition tunnels and deposition holes (Faybishenko et al., 2016a).

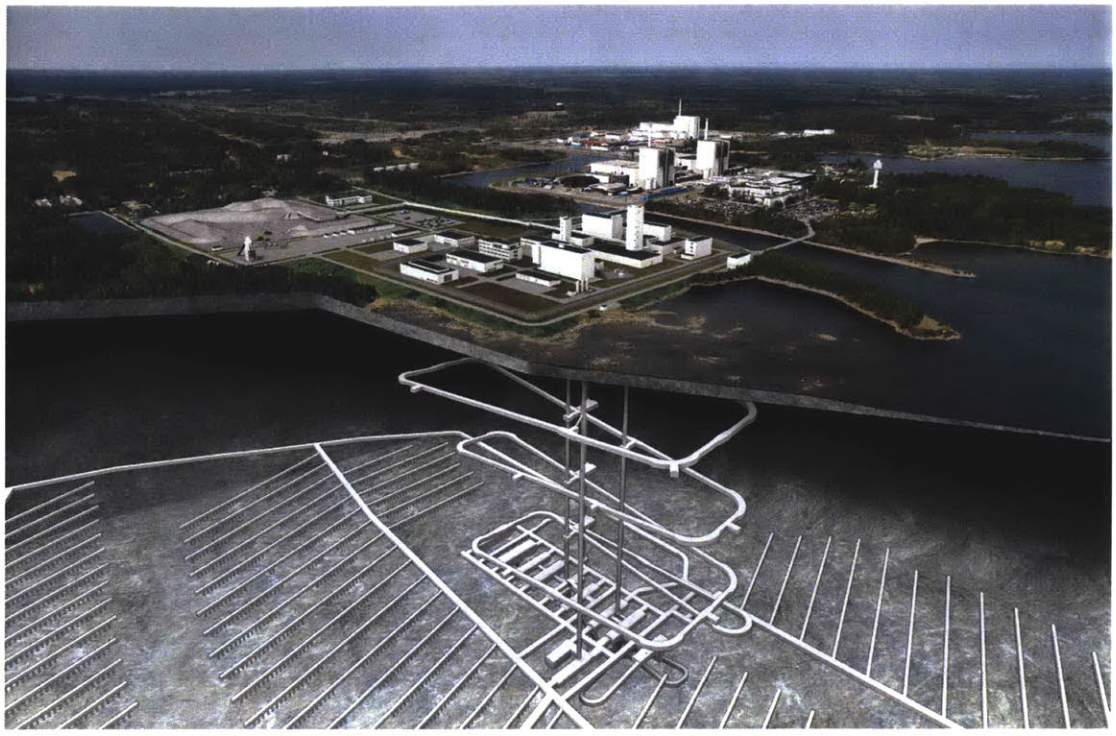

Figure 2-5: Swedish disposal site and projected final repository for spent nuclear fuel in Forsmark and an encapsulation plant in Oskarshamn (SKB, 2019).

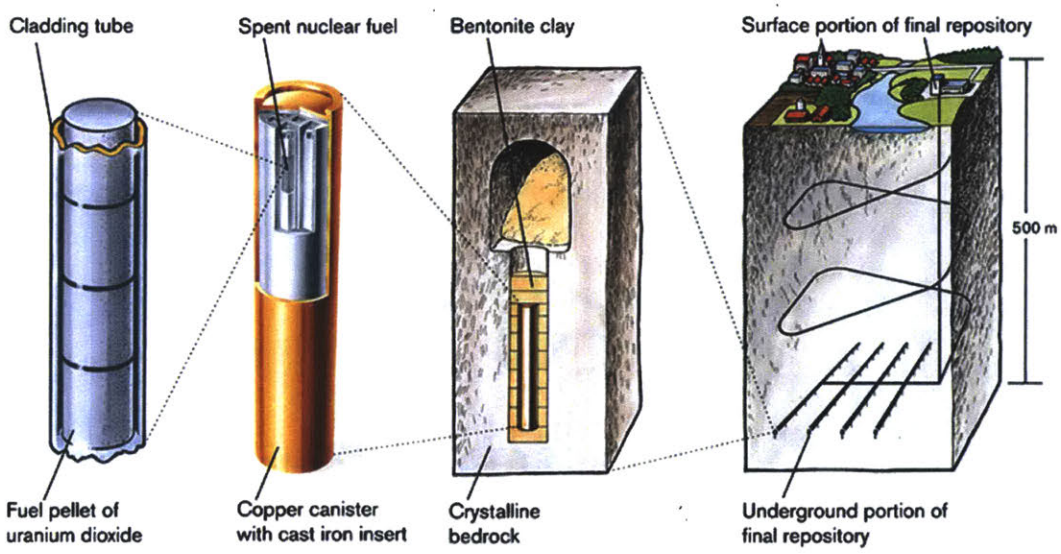

Figure 2-6: SKB disposal method. It is called KBS-3 and is based on three barriers: copper canisters, bentonite clay, and the Swedish bedrock. This system is located in the bedrock in a tunnel at a depth of about 500 meters (SKB, 2019).

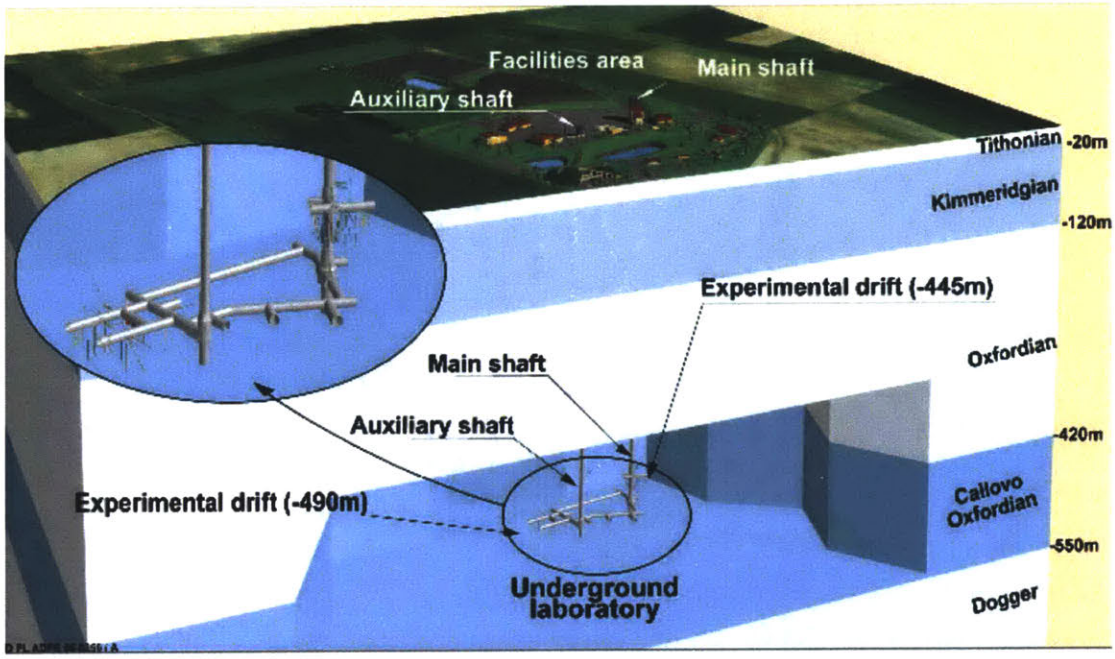

Figure 2-7: Deep geological disposal facility for radioactive waste in France (ANDRA, 2016). The Cigéo project is designed to host all the HLW, ILW and LLW that has been produced and will be produced by existing nuclear facilities (power plants, research centres, etc.). The Cigéo underground facility lies in an argillaceous sedimentary stratum that is 160 million years old: the Callovo-Oxfordian argillite. It is 145 metres thick, lies at a depth of between 400 and 600 metres, and has been stable for more than a hundred million years. Its properties, particularly its stability and very low permeability, make it ideal for a deep disposal facility.

Heat Transport, BRIGHT code. The implemented equations in the code account for all particularities of saline media (salt solubility, hygroscopy of salt, solid matrix deformation of salt being large, phase changes in saturated brines –latent heat, condensation, precipitation of salt, brine inclusions in the solid phase). The porous media considered consists of three phases (solid, liquid and gas) and three main species (salt, water and air). Several other studies had been carried out to analyze the response of clay barriers used as engineered barriers in the disposal of nuclear waste (Gens, do N. Guimarães, Olivella, & Sánchez, 2010; Sánchez, Arroyo, & Olivella, 2004; Seyedi & Gens, 2017).

Extensive research has also been carried out at Lawrence Berkeley National Laboratory University of California (LBLN). The main researchers of this group are J.

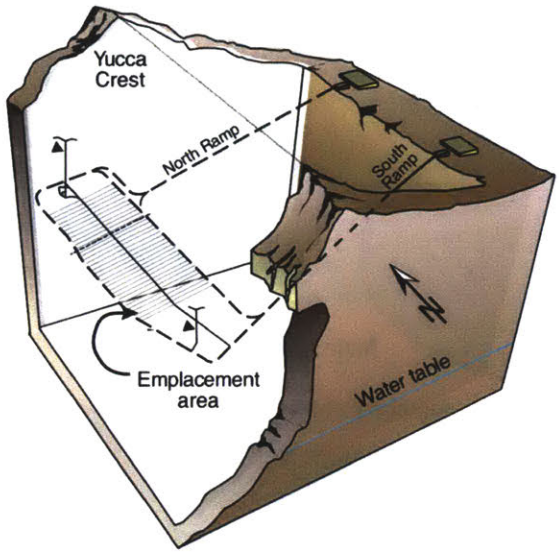

Figure 2-8: Yucca Mountain repository schematic configuration (DOE, 2019).

Rutgvist and J. Birkholzer. Their work is focused on developing a numerical simulator for coupled THM analysis of complex geological media under multiphase flow conditions, with possible coupling to reactive transport modeling. Two existing codes, TOUGH2 and FLAC3D, were joined to develop a numerical simulator for the analysis of coupled THM process for multiphase flow (Rutqvist, Wu, Tsang, & Bodvarsson, 2002). Both codes are well established and widely used in their respective fields. The TOUGH2 code is designed for geohydrological analysis of multiphase, multicomponent fluid flow and heat transport, whereas the FLAC3D code is designed for rock and soil mechanics with thermomechanical and hydromechanical interactions. The two codes are executed on two separate meshes and joined with two coupling modules (Blanco-Martín, Wolters, Rutqvist, Lux, & Birkholzer, 2016).

Applications of TOUGH2-FLAC3D include study of the effect of coupled THM processes on the performance of the proposed nuclear waste repository at Yucca Mountain including drift-scale and mountain-scale THM processes (Bodvarsson et al., 2003; Rutqvist, Freifeld, Min, Elsworth, & Tsang, 2008). TOUGH2-FLAC3D has also been applied in the study of the geomechanics and flow of salt rock mass and granular salt in a nuclear waste repository.

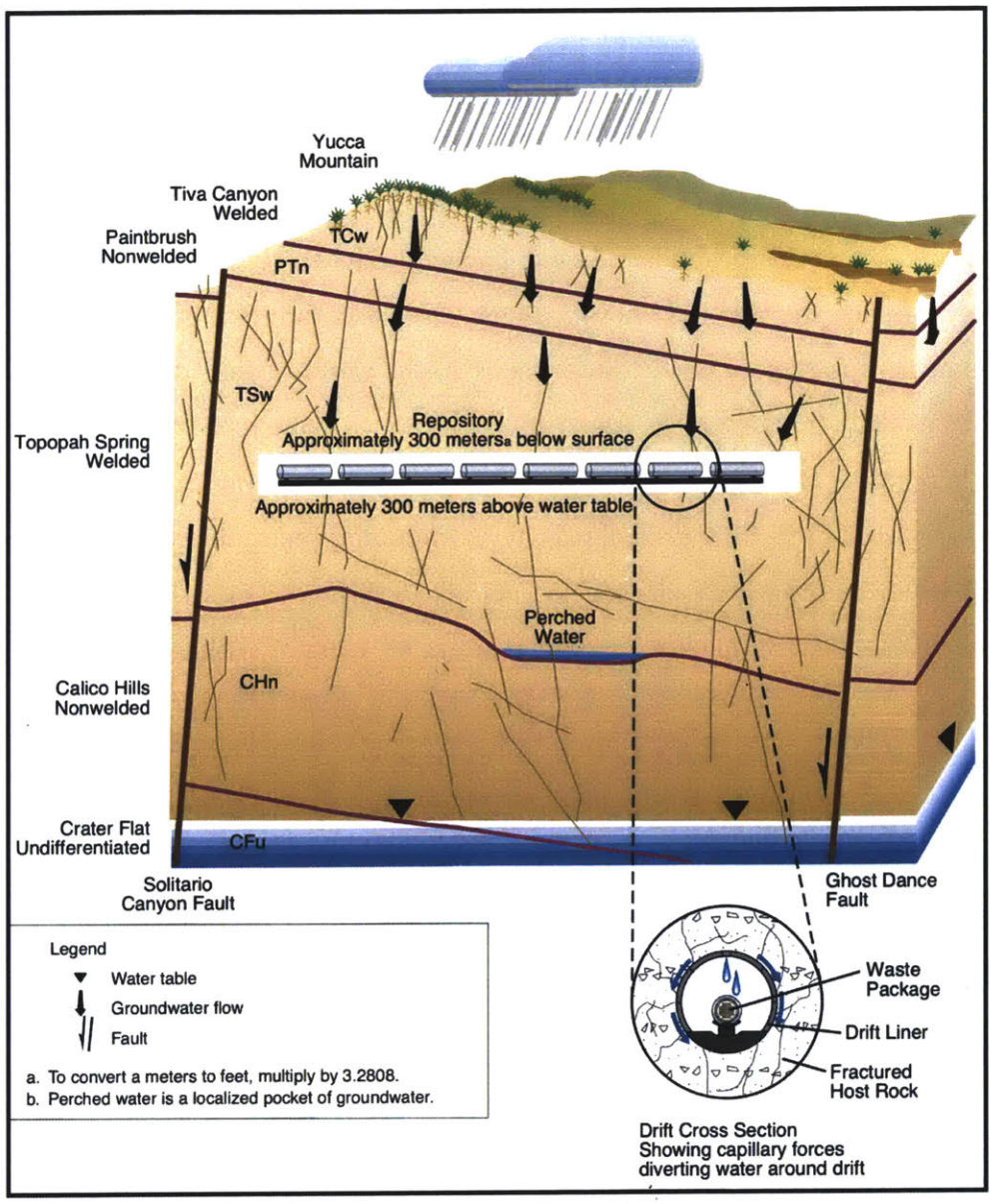

Figure 2-9: Natural features of proposed Yucca Mountain repository site (DOE, 2019).

The French agency for radioactive waste disposal, ANDRA, has also conducted extensive studies including an underground laboratory, shown in Figure 2-7.

SKB carried out various studies on deep boreholes in crystalline basement rocks (Juhlin & Sandstedt, 1989). Early studies, (Claesson, 1992; Claesson, Hellström, & Probert, 1992), were based on analytical formulations to determine the thermally driven groundwater flow around a borehole. In these studies the boreholes were represented by point sources, linear heat sources. The model considered exponentially decreasing heat release and accounted for salt concentration in the water (which counter-balance the thermal buoyancy effects). This study presented an estimation of the upward motion of particles that start in the warm region accounting for water salinity effects. In subsequent years, SKB performed numerical modeling studies of deep boreholes (Marsic, Grundfelt, & Wiborgh, 2006), considering a repository with 45 disposal holes. In their design, canisters containing spent nuclear fuel are stacked in the lower 2 km of 4 km deep holes. In all 45 disposal holes the spent fuel from operating the Swedish nuclear reactors requires 40 years of cooling time.

Later, in 2011, SKB applied for licensing its final repository for spent nuclear fuel at Forsmark (Andersson & Skagius, 2011), pursuing the shallow repository design, called KBS-3 method, abandoning the deep borehole repository type. The Forsmark region forms a part of the sub-Cambrian peneplain in south-eastern Sweden. This peneplain represents a relatively flat surface with a gentle dip towards the east that formed more than 540 million years ago. This repository is designed over crystalline basement.

Final disposal of spent fuel in deep borehole repositories has been studied also by SANDIA National Laboratory, presenting the numerical modeling of deep borehole repositories (B. Arnold & Hagdu, 2013; P. V. Brady et al., 2009). MIT has also studied deep borehole repositories for the final disposal of PWR spent fuel in granite, considering conservative analytical models, in addition to numerical models (Bates, 2015; Lubchenko et al., 2015).

2.5 The deep borehole concept

2.5.1 Definition

Deep-borehole disposal is one of several options for permanent disposal of HLW and spent nuclear fuel. The proposed method consists of entombing the nuclear waste in deep boreholes of 5 km depth in crystalline host rock. The spent fuel will be enclosed in metallic canisters that are placed vertically in deposition boreholes in the bottom 2 km with a back-fill material. The borehole is sealed in the upper 3 km. The disposal zone is significantly deeper than for the typical mined repositories, which implies greater natural isolation from the surface and near-surface environment. Figure 2-10 presents a schematic of the deep-borehole concept. The figure shows the waste disposal zone, called the waste emplacement zone in this thesis, which corresponds to the depths where the nuclear waste is placed. In this thesis we use the term cap rock to refer to the layer of rock above the nuclear waste. For comparison, the Onkalo and WIPP repositories are also shown in the image, as well as the tallest building in the world, the Burj Khalifa.

2.5.2 History of the deep borehole concept

In 1957, the US National Academy of Science (NAS) Committee on Waste Disposal analyzed the disposal of liquid radioactive waste in permeable formations at great depth (1500m). It concluded that with the available technology (at that time) it was not possible to prevent clogging of pores as the solutions are pumped into the rock, or predict or control with certainty the direction and rate of flow in the porous media. NAS also studied the storage of radioactive waste in salt, acknowledging that the disposal could be simplified significantly if the liquid waste was converted to an insoluble solid waste. The disposal of liquid waste was reconsidered irregularly, but only in the late 1970 research focused on the deep disposal of solid waste forms in boreholes because of the advancements in deep drilling technology (Winterle, Pauline, & Ofoegbu, 2011). The early versions of the deep-borehole concept were exclusively

based on information derived from drilling of deep boreholes for hydrocarbons. A feasibility study in 1979 (O'Brien, Cohen, Narastahan, Simkin, & Wollenberg, 1979) provided an in-depth analysis of the deep borehole concept, highlighting uncertainties and technical challenges. This concept was abandoned in the US, in favor of pursuing conventional mined repositories.

Other nations, such as Switzerland, Denmark, Sweden and England, have also researched the deep-borehole concept. SKB carried out various studies during the 1980s and 1990s on the potential for this disposal concept in crystalline basement rocks, as introduced in the previous section. Finally, SKB opted for the disposal method KBS-3.

In the last decade, the deep-borehole concept in the US gained renewed interest. The majority of this work was carried out in the US by SANDIA National Laboratory and MIT. The SANDIA studies included 3D thermal hydraulic analyses of a deep borehole repository in a continuous rock medium, using a finite volume code FEHM (Los Alamos National Laboratory, 2007). Studies considered up to 81 boreholes, and depth varying permeability in the rock. Also, MIT has presented 2D simulations of heat conduction models and 3D thermo-hydraulic analyses for PWR spent fuel disposal in deep boreholes.

All these previous studies of deep borehole repositories were analyzed for conventional spent fuel. So far no studies have been conducted on a disposal system for the innovative reactor design TWR, which produces high linear power spent fuel. Whereas conventional spent fuel, from LWR, produces less heat, uniformly distributed across the rods, TWR produces significantly higher heat in the central region of the rods. Spent fuel requires a well-designed disposal system that will ensure confinement for one million years and that minimize the release of the contained radionuclides into the environment. The lack of studies on borehole disposal systems for TWR spent fuel represents a significant gap of knowledge that is addressed in this thesis.

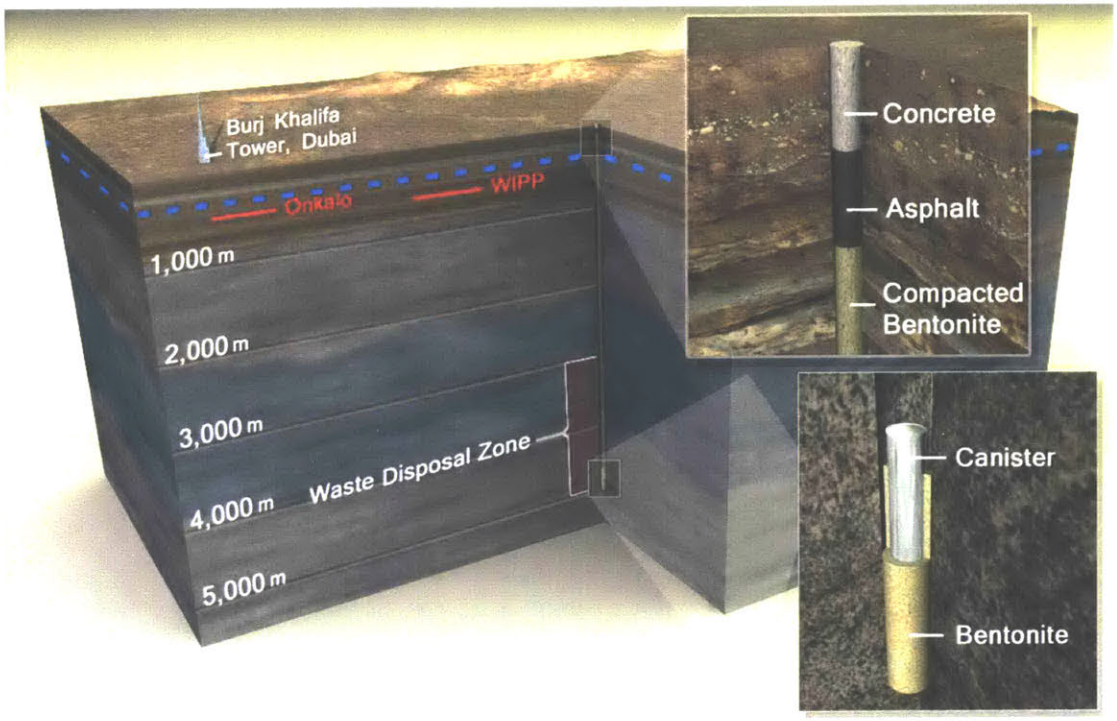

Figure 2-10: Generalized concept for deep borehole disposal. For depth comparison, the image includes the Onkalo repository in Finland at Olkiluoto (500m depth), WIPP (650m depth) in US, and the Burj Khalifa tower the tallest building in the world (P. Brady et al., 2012).

2.5.3 Site characteristics

A geological disposal method performance depends on rock properties, which exhibit large variations in the field. Some specific rock and site conditions are more favorable for a waste repository than others. The reference deep borehole concept adopts crystalline basement rock as the host rock because of its long geological history and tectonic stability within the continental crust. When selecting a site for borehole disposal, the depth to the crystalline basement is critical. A database for the depth to crystalline basement for most of the continental US is presented in Figure 2-11. Regions where the depth of the crystalline basement is less than 2000 m are widely available in the country.

One critical objective of the repository is to produce fluid convection sufficiently small that no radioactive material is transported to the surface within one million years of emplacement. Regions exposed to large geothermal flux from the Earth's

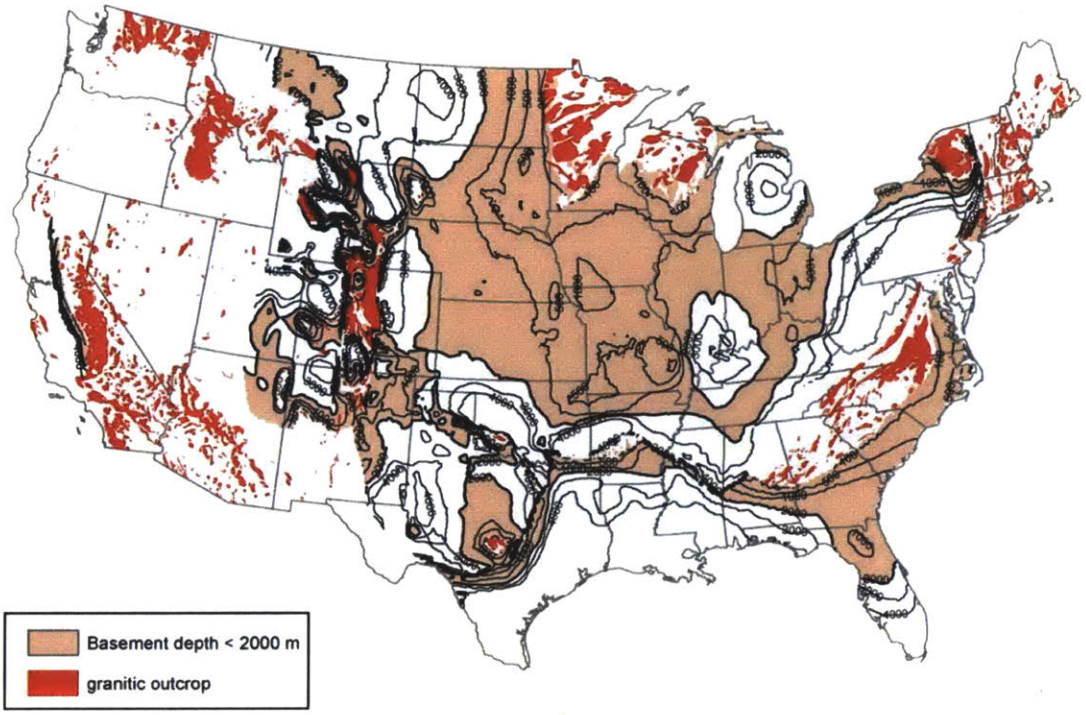

Figure 2-11: Depth to crystalline basement outcrops in the continental US. Depths less than or equal to 2000 m are colored in brown; crystalline basement outcrops are shown in red. (Perry, 2013 as cited in SANDIA, 2013).

crust are likely to enhance fluid convection in the rock repository and therefore are not suitable to host nuclear waste. If a layer of viscous fluid is heated from below, instability can occur which leads to convection cells known as the Rayleigh-Bénard problem. If a saturated porous medium is heated from below, similar instability and convection can occur if heating is large enough, as shown in Figure 2-12. This is of fundamental interest for geothermal convection and is relevant for the disposal of nuclear waste in deep boreholes. Regions exposed to large geothermal flux from the Earth's crust are likely to enhance fluid convection in the rock repository and therefore are not suitable to host nuclear waste. The aim of the repository design is to avoid high geothermal gradients, where fluid convection can be high.

Figures 2-13 shows the geothermal heat flux in US. Figures 2-14 and 2-15 show maps of the estimated geothermal gradient, and estimated temperature at 4 km depth in the US, respectively. Geothermal heat flux is calculated from the temperature gra-

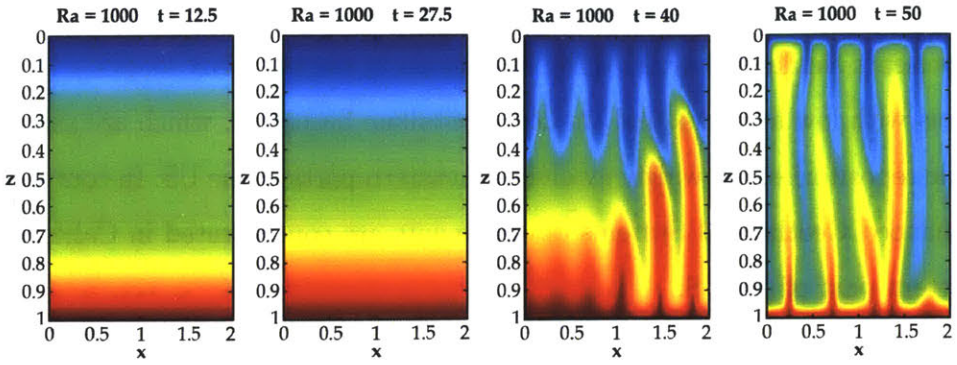

Figure 2-12: Development of fluid instability with time when heating from the bottom of the porous medium for a Rayleigh number of 1000 ($Ra = \frac{\rho_f g k \beta \Delta T h}{\mu K_m}$, where ρ_f refers to the fluid density, g is the gravity, k is the permeability of porous medium, β is the thermal expansion of the fluid, ΔT refers to temperature difference between top and bottom, h refers to the height of the domain, μ represents the dynamic viscosity and K_m represent the thermal conductivity of the medium). Simulations are performed using finite volume method implemented in MATLAB, in the dimensionless space for x, z and time (t). Color scale indicates temperature, with cold at top boundary and hot at bottom boundary.

dient measured in boreholes and estimated values of thermal conductivity for the rock along the borehole. These calculations can be affected by changes in thermal conductivity and vertical groundwater flow. Gradients were measured in a large number of shallow boreholes, but in a limited number in deep boreholes. Consequently, the depth averaged geothermal gradient and the calculated temperature at 4 km depth has significant uncertainty (SANDIA, 2013). Geothermal flux exhibits large variability (see Figure 2-13).

Overall, Western US regions have higher fluxes, while lower values are seen in Eastern US. An exception to this pattern can be seen in Washington, Oregon and Northern California and the Central Valley of California, with extremely small flux. Distinctively, south central South Dakota, Eastern Texas to Western Mississippi and some other isolated scattered regions exhibit higher heat flux. The high heat flux of central South Dakota is next to an anomalous area of low heat flux. This can be interpreted as a regional-scale groundwater flow system in which downward flow suppresses the heat flux in certain zones, and emerges as upward groundwater flow in other zones, increasing the geothermal heat flow in that area (SANDIA, 2013).

The estimated geothermal gradient and temperature at 4 km depth (Figure 2-14 and 2-15) presents similar behavior to the one shown in the heat flux map.

Areas with low heat flux and shallow crystalline basement, which are suitable for borehole repositories, are widely available in eastern parts of the US. In contrast, sites for Enhanced Geothermal Systems developments are concentrated in California and the western part of the US.

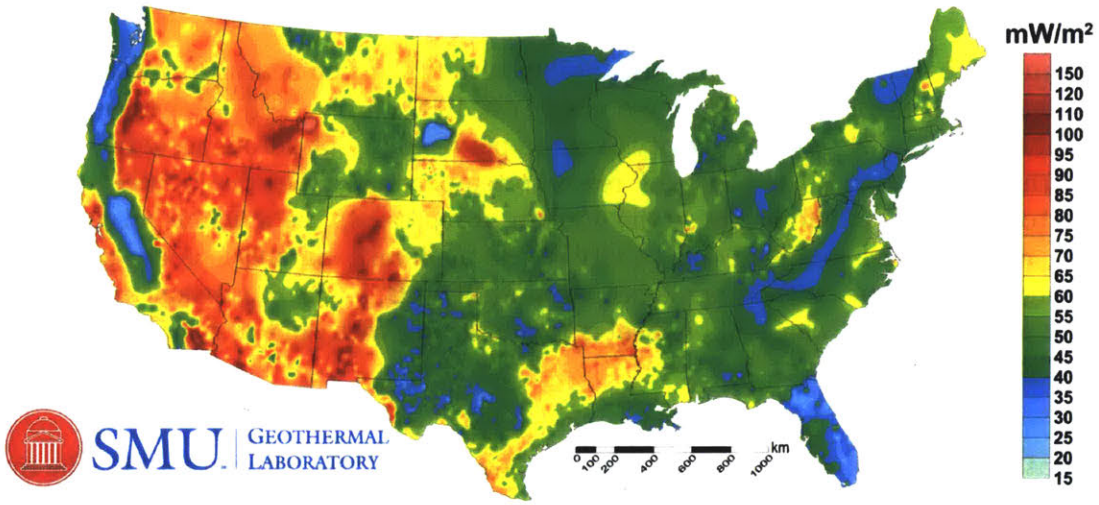

Figure 2-13: Geothermal heat flux in US (SMU Geothermal Laboratory, 2011).

In addition, geothermal heat flux is also relevant during the repository construction, since temperature conditions affect the drilling process, emplacement maneuvers, etc. It also has a significant effect on the kinetics of chemical reactions in the repository, such as corrosion, mineralogical transformations, waste form degradation, radionuclide solubility in water and radionuclide saturation concentrations.

2.6 Deep-borehole field test

In January 2016 the Department of Energy announced the approval of a borehole field test in a crystalline basement rock formation at a site in Rugby, North Dakota of 4880 m depth and 8-inch diameter (DOE, 2016). This field test would allow the collection of deep local geologic data, water chemistry, temperature, geochemistry,

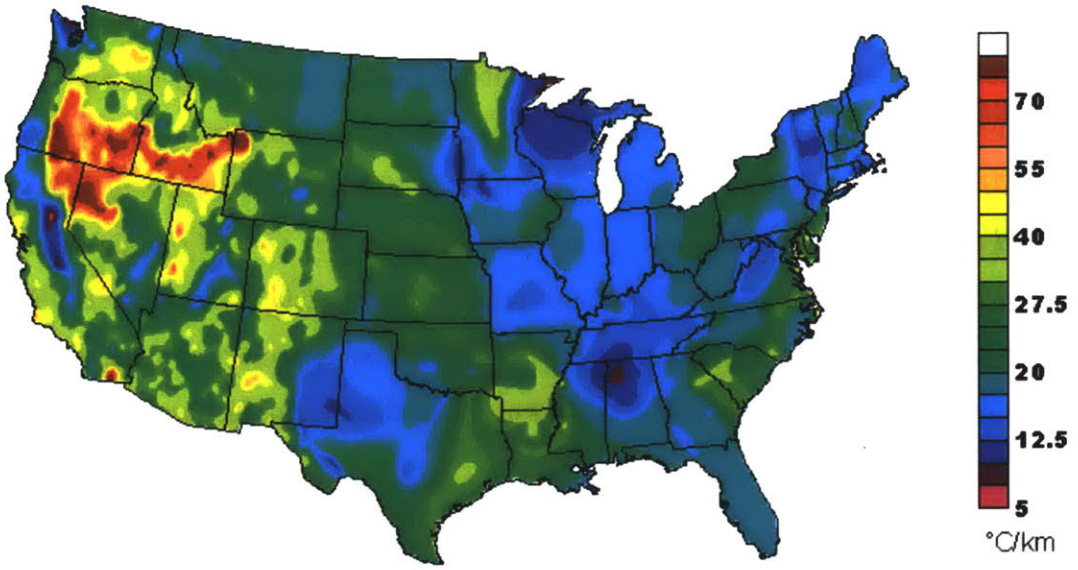

Figure 2-14: Estimated geothermal gradient in US (SMU Geothermal Laboratory 2004, as cited in SANDIA, 2013).

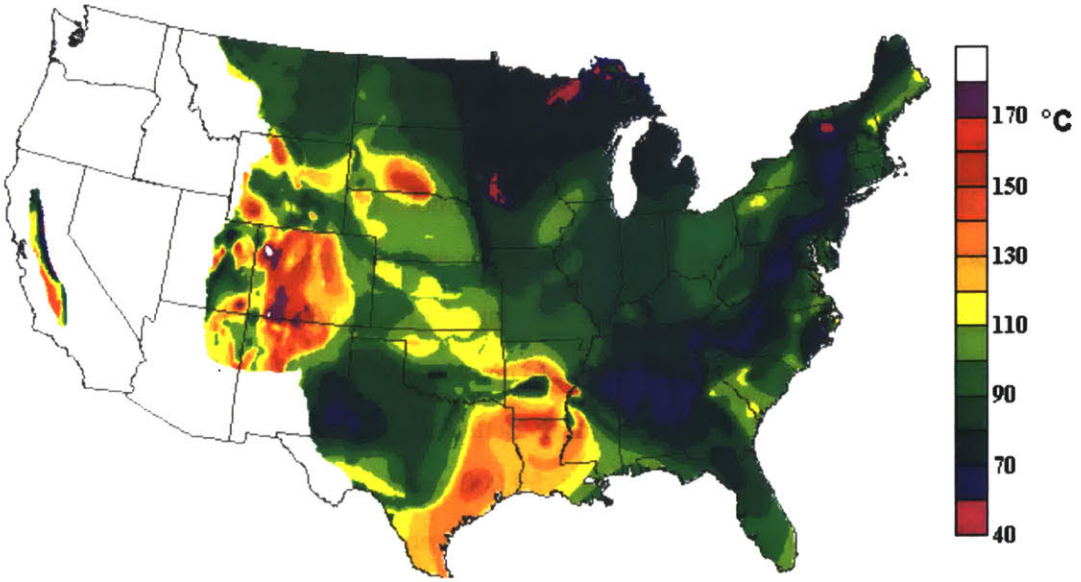

Figure 2-15: Estimated temperature at 4km depth in US. (SMU Geothermal Laboratory, 2004, as cited in SANDIA, 2013).

and groundwater flow. These data would help evaluate whether deep boreholes can provide a safe and practical alternative to mined geologic repositories for nuclear waste. This project specifically prohibits the storage, disposal, or use of nuclear waste at the site of the borehole test, and it requires that the borehole will be permanently

sealed and the land will be restored according to state regulations. This project faced community concerns and rejection that resulted in social opposition of the proposed deep borehole field test. As a result, DOE withdrew the project: "*UPDATE (May 23, 2017): Due to changes in budget priorities, the Department of Energy does not intend to continue supporting the Deep Borehole Field Test (DBFT) project and has initiated a process to effectively end the project immediately*". To date, DOE has no further plans to implement a full-scale demonstration project, leaving the deep borehole with significant practical unknowns for nuclear waste disposal.

2.7 Time scale of the analysis

To date, nuclear regulators require a nuclear waste repository analysis for a one million year time period (EPA, 2008). The original EPA norm established a 10,000 year period of safety analysis of any nuclear waster repository. The Yucca Mountain repository was analyzed for that period of time (American Physical Society Sites, 2019). However, the EPA announced a new compliance period of one million years. This implies that when modeling the response of a nuclear waste repository, the Earth's conditions for such time scale must be known and accounted for in the numerical model used to predict the repository's response to the nuclear waste.

Climate forecasts in the usual sense of the word do not exist on these time scales. Researchers (Ganopolski, Winkelmann, & Schellnhuber, 2016) presented speculative modeling of Earth's condition for next 50,000 years. This is a kind of a climate "forecast" for such a long time scale, but it is a very approximate forecast.

It is known that for the last several million years there have been regular glaciations roughly every 100,000 years and they last for the best part of 100,000 years. The period somewhat is in concordance with various orbital periods related to how the Earth sways slightly and how the Earth-Sun distance oscillates. These are called Milankovitch cycles. The continental configuration and the makeup of greenhouse gases in the atmosphere also affect the glacial inter-glacial cycling. Thus, CO_2 emissions may defer the next glaciation.

However, it is likely that in the next few thousand years CO_2 emissions will decrease, and then after another 20,000-50,000 years the natural CO_2 levels will gradually return. This needs ocean and erosion processes to flush things out in absence of human CO_2 fixing, so it takes time. Overall it is reasonable to anticipate multiple glaciations over the next million years (Hill, 2019).

Nuclear waste repository modeling for such time scales are therefore subjected to significant uncertainty. Climate conditions such as surface temperature of Earth, rain and water saturation of porous media, as well as glaciations have not been predicted for the one million year time scale with current climate models. Concurrently, relevant rock properties such us porosity, permeability, elastic modulus, etc. are somewhat dependent on these climate conditions and are therefore just estimates in any analysis of a nuclear waste repository. Despite this, humankind needs to analyze this uncertain system, to identify any imminent failure mechanism of any proposed disposal system.

Chapter 3

Thermo-Hydraulic Processes Mathematical Formulation

3.1 Introduction

Other than human intrusion, groundwater transport is the only important mechanism affecting the escape of radioactive material from the repository through any leakage of the canisters. Radionuclides can dissolve and be transported in water. The mechanism of radionuclide transport is by fluid convection and diffusion (molecular diffusion and mechanical dispersion). The goal of the disposal system is to ensure with the system design that radionuclide transport process is slow enough and does not cause any escape to the surface. Diffusion is a very slow process, with an effective diffusion coefficient in porous media of the order of $10^{-12}\mathrm{m}^2/\mathrm{s}$ (Szántó, Svingor, Molnár, Palcsu, & I. Futó, 2002), while convection is the most concerning mechanism for radionuclide transport. The aim of the design is to place the nuclear waste in geological formations where the induced convection is minimal, avoiding high geothermal gradients. This section analyzes the thermo-hydraulic response of a nuclear waste repository in granite rock.

3.2 Physical process

The fluid flow and radionuclide migration are driven by the thermal pressurization produced by the decay heat of the nuclear material. The coupled physics are schematized in Figure 3-1. The high-level nuclear waste releases heat to the surrounding host rock, which is saturated with water. The rock and the fluid in the pores are in local thermal equilibrium, given the extremely low fluid velocity and the dimension of the pores (microns to millimeters). Initially, heat is transferred from the nuclear waste across the the rock by conduction. During this period, the fluid is heated, and its density changes. The fluid expands, increasing pore pressure. The resulting pressure field controls fluid advection (also called convection). This fluid advection in turn increases the heat transport within the porous medium. These are the coupled effects. When groundwater flows radioactive containment can be compromised.

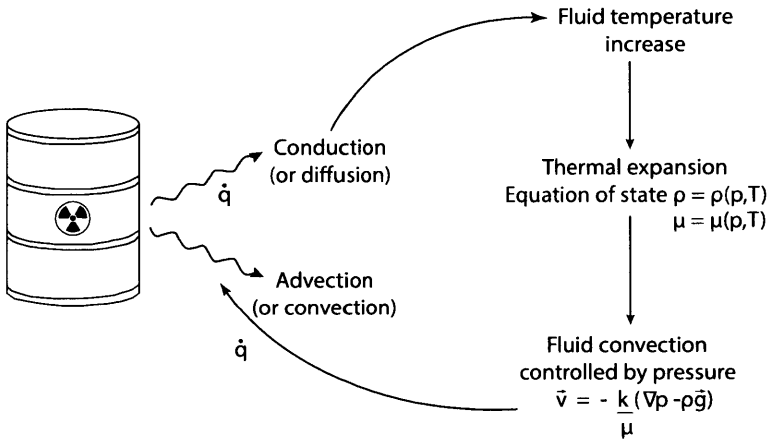

Figure 3-1: Coupled physics that occurs in the host rock.

3.3 Governing equations

A pressure-temperature based formulation is used for single-phase flow in the water-saturated medium. The rock is assumed to be saturated because this would act to promote radionuclide transport, and thus represents the most conservative case.

Restriction to single phase flow is because the pore pressure is always high enough (higher than the saturation pressure) for water to be in the liquid phase. This is verified and explained in Chapter 5. The governing equations using a continuum approach are presented below.

3.3.1 Mass balance

The mass balance of the fluid, assuming no sources or sinks of mass, can be written as:

$$\frac{\partial(\phi\rho_w)}{\partial t} + \nabla.(\rho_w\vec{q}) = 0 \tag{3.1}$$

where

$\vec{q}$ is the Darcy velocity vector

ρ_w is the density of water

ϕ is the porosity of the rock.

It should be mentioned that the fluid pore velocity, $\vec{v}$, is higher than the Darcy velocity as:

$$\vec{v} = \frac{\vec{q}}{\phi} \tag{3.2}$$

3.3.2 Darcy's law

Assuming conditions such that Darcy's law is valid it holds:

$$\vec{q} = -\frac{k}{\mu}(\nabla p - \rho_w\vec{g}) \tag{3.3}$$

where

k is the intrinsic permeability of the medium

μ is the dynamic viscosity of water

$\vec{g}$ is the gravity vector

p is the fluid pressure.

According to Bear (1972), Darcy's law, which assumes a laminar flow, is valid for

Reynolds number less than one, but the upper limit can be extended up to ten. In our problem, fluid velocities are extremely small, of the order of 10^{-10} m/s (presented in Chapter 5), and thus the Reynolds number is significantly smaller than unity.

Combining Equations 3.1 and 3.3, one obtains the following pressure equation for water flow in a deformable compressible medium:

$$\frac{\partial(\phi\rho_w)}{\partial t} - \nabla.\Big(\frac{k\rho_w}{\mu}(\nabla p - \rho_w\vec{g})\Big) = 0 \tag{3.4}$$

Then by the definition of water compressibility,

$$\frac{\partial\rho_w}{\partial t} = \frac{\partial\rho_w}{\partial p}\frac{\partial p}{\partial t} = \beta_{w,p}.\rho_w\frac{\partial p}{\partial t} \tag{3.5}$$

where $\beta_{w,p}$ is the water compressibility coefficient, defined by $\beta_{w,p} = \frac{1}{\rho_w}\frac{\partial\rho_w}{\partial p}$.

Then, assuming constant porosity, and from the definition of water compressibility, Equation 3.4 can be simplified (disregarding for this analysis temperature effects on the fluid density) by:

$$\phi\beta_{w,p}\rho_w\frac{\partial p}{\partial t} - \nabla.\Big(\frac{k\rho_w}{\mu}\nabla p\Big) + \nabla.\Big(\frac{k\rho_w^2}{\mu}\vec{g}\Big) = 0 \tag{3.6}$$

This equation corresponds to a diffusion equation of pressure with diffusivity coefficient defined as:

$$D_p = \frac{k}{\phi\mu\beta_{w,p}} \tag{3.7}$$

Considering typical parameters of the borehole repository (assuming rock intrinsic permeability of typical granite $k = 10^{-16}$ m^2, rock porosity $\phi = 0.01$, water compressibility $\beta_{w,p} = 4 \times 10^{-10}$ Pa^{-1}, and water dynamic viscosity $\mu = 4 \times 10^{-4}$ Pas), the pressure diffusivity is of the order of 10^{-2} m^2/s.

3.3.3 Heat transport

Assuming that thermal equilibrium exists between the fluid and the rock matrix (given the extremely low fluid velocity and the dimension of the pores of microns to millimeters), the energy conservation can be expressed as:

$$\frac{\partial}{\partial t}\left(\left(\phi\rho_w c_w + (1-\phi)\rho_s c_s\right)T\right) - \nabla.(K_m \nabla T) + \rho_w c_w \vec{q}\,\nabla T - q''' = 0 \qquad (3.8)$$

where

c_w is the specific heat of the water

c_s is the specific heat of the solid matrix

K_m is the average thermal conductivity of the rock-fluid system which is a function of the thermal conductivity of the rock K_s, and the water K_w, $K_m = \phi K_w + (1-\phi)K_s$

q''' is the heat production per unit volume

T is the rock and fluid temperature.

Furthermore, assuming ϕ, k and K_m to be constant Equation 3.8 is expressed as:

$$C_m \frac{\partial T}{\partial t} - K_m \nabla.(\nabla T) + \vec{q_E}\nabla T - q''' = 0 \qquad (3.9)$$

where

$\phi\rho_w c_w + (1-\phi)\rho_s c_s$ is replaced by C_m, the average heat capacity of the medium

$\rho_w c_w \vec{q}$ is replaced by $\vec{q_E}$.

Equation 3.9 is an advection-diffusion equation with thermal diffusivity defined by:

$$D_T = \frac{K_m}{C_m} \qquad (3.10)$$

For typical values of the borehole repository (assuming water density $\rho_w = 1000$ kg/m^3, water specific heat $c_w = 4186$ J/kg°K, water thermal conductivity $K_w = 0.628$ W/m°K, rock density $\rho_s = 2700$ kg/m^3, rock matrix specific heat $c_s = 790$ J/kg°K,

and rock matrix thermal conductivity $K_s = 3$ W/m°K, the thermal diffusivity is of the order of 10^{-6} m^2/s. The characteristic length of isotropic heat diffusion is:

$$L_T \approx \sqrt{D_T.t} \tag{3.11}$$

where

D_T represents the thermal diffusivity

t represents the time.

For one million years, this characteristic length scale is about 5 km. The estimation of this length scale guides us in the definition of the boundary of the modeled domain, so as not to affect the solution around the borehole.

The difference in magnitude of the thermal and pressure diffusivity coefficients, 10^{-6} and 10^{-2} m^2/s respectively, governs the heat and pressure propagation, which has direct implications on the physical response in time of the nuclear waste repository. At a given location the increase in pore fluid pressure is reached significantly earlier than the temperature increase. This increase in the pore pressure can lead to tensile or shear failure, if the increase is large enough.

Equations 3.4 and 3.9 are the pressure-temperature based governing equations of the repository.

3.4 Fluid thermodynamic properties

Based on the IAPWS-97 formulation[1], the water-steam equation of state (WSEOS) approach can be applied in the water, steam, and supercritical regions. The WSEOS is used to calculate the phase thermodynamic properties (i.e. density, internal energy, viscosity) of water and steam. The IAPWS-97 formulation uses pressure ($\leqslant$100 MPa) and temperature ($\leqslant$ 800 °C) as input parameters and returns density and internal

[1]IAPWS is an international non-profit association of national organizations concerned with the properties of water and steam, particularly thermophysical properties, cycle chemistry guidelines, and other aspects of high-temperature steam, water and aqueous mixtures relevant to thermal power cycles and other industrial and scientific applications.

energy. This formulation can be applied to water, steam and supercritical domain. Based on the density and temperature as input variables, the viscosity formula in IAPWS-97 is then used to calculate the viscosity of either water or steam, depending on the input density value.

For the repository analysis it is required to study and simulate buoyancy-driven groundwater flow caused by the heat decay of the spent fuel released to the surrounding host rock, in combination with the natural geothermal flux, and this throughout the lifetime of the nuclear waste. Water salinity increases fluid density, which can suppress thermal fluid convection (Claesson, 1992; Lubchenko et al., 2015). In this work, water is assumed to be fresh devoid of salinity, representing the most conservative case for radionuclide migration. In addition, there are not enough experimental data supporting the existence of salty water in granitic formations at large depths (of the order of 10 km), as a general feature, to form a design safety basis for deep borehole repositories. Very limited experimental data for just a few locations (mainly at the Lake Superior region of Canada) and relative shallow depth (up to 2 km) have been found in the literature (Frape, Blyth, Blomqvist, McNutt, & Gascoyne, 2003).

An important consideration in TWR spent fuel disposal is the thermodynamic state of the fluid in the pores of the rock when large amounts of heat are released. Due to the very large depth of the proposed boreholes, fluid pressure is high (about 50 MPa), above the critical pressure for water (22.06 MPa). TWR spent fuel releases significantly more heat than conventional spent fuel, and therefore the fluid potentially reaches values higher than the critical temperature (373.9 °C), see Figure 3-2. At these high pressures, even though there is no phase transition such as boiling, there is still a significant decrease of density at a certain temperature (shown in right plot of Figure 3-2). In addition to all the potential risks of structural problems due to the potential melting of the canister and fuel, and the thermal effects in the host rock, one of the concerns is that the spent fuel releases so much heat that the water would reach the critical temperature. Reaching these high temperatures increases buoyancy significantly due to the non-linear dependence of density with respect to temperature, which in turn could enhance fluid convection and therefore

pose a problem for radionuclide migration. In order to determine the likelihood of this problem, our numerical simulations calculated the exact temperatures reached in the host rock and in the fluid.

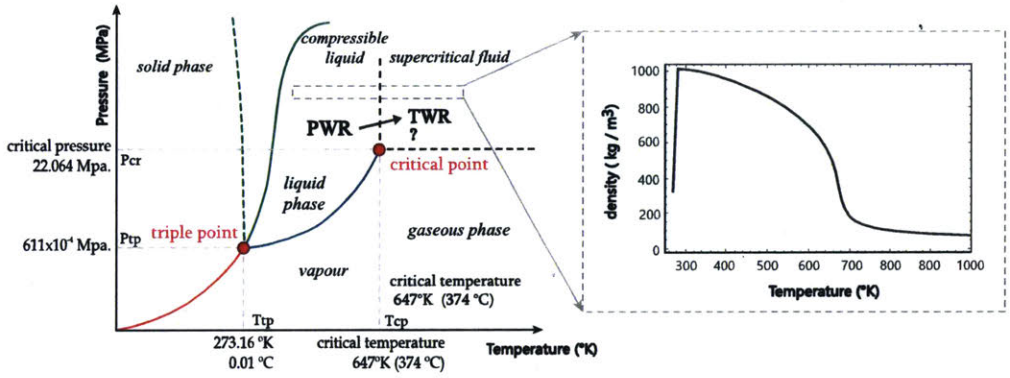

Figure 3-2: Water phase diagram, for PWR spent fuel and TWR spent fuel (left), and steep variation of water density with temperature at a high pressure (30MPa) (right).

3.5 Numerical implementation

3.5.1 Numerical requirements

Nuclear regulations require the analysis of the performance of the repository for a million years. Because of the complex processes to be analyzed, and the time and length scales involved in the problem, it is crucial to have an adequate modeling tool. This application should be capable of accurately modeling the coupled thermal field and induced fluid flow around the deep borehole repository at different time and length scales. This requires a robust numerical code with strong coupling of all physical phenomena.

The numerical simulations of the coupled thermo-hydraulic behavior of a nuclear waste repository, for a million years, are computationally very expensive. To perform repository simulations, we use an open-source, finite element-based code, called FALCON (Fracturing And Liquid CONservation). The set of equations of fluid flow and heat transport are implemented in MOOSE under the name of FALCON application.

3.5.2 MOOSE framework

MOOSE (Multiphysics Object Oriented Simulation Environment) is an open source, object-oriented, C++, finite element framework developed at Idaho National Laboratory (Gaston et al., 2009). MOOSE was designed for the development of tightly coupled multi-physics solvers. The MOOSE framework provides all the different tools for performing the simulation. The user provides the physics and MOOSE supplies the numerical solution implementation. The user can optimize parameters for pre-conditioning, time stepping, linear iterations, non-linear iterations, among others, as well as using a Newton solver or a Pre-conditioned Jacobian-Free Newton-Krylov (PJFNK) solver.

Users can develop their own application based on the physics to model. MOOSE allows the development of applications to solve the partial differential equations (PDEs) of interest. Each PDE term is implemented in a "kernel" which returns a residual and the Jacobian contributions (if applicable and chosen for inclusion).

The used application FALCON and all other applications created in MOOSE have the layered structure shown in Figure 3-3. MOOSE uses the PETSc non-linear solver package and libMesh to provide the finite element discretization. MOOSE and application codes developed upon it provide considerable flexibility to exchange solver libraries and to make use of diverse large-scale parallel computing resources. The top layer of MOOSE is the kernels which is the interphase with the physics. Then MOOSE provides the residual and Jacobian evaluations defined in the kernels implemented in each application.

The MOOSE framework incorporates multi-parallel capabilities which allow the application codes developed over MOOSE to run efficiently on multi-core workstations, laptops, and super computers. The code parallelization is hidden from the users and code developers. All applications developed in MOOSE inherit many advanced computing capabilities such as dimension-independence, massive parallelism, high order finite elements and adaptive mesh refinement with both structured and unstructured meshes (see Figure 3-4).

Although MOOSE was originally developed for nuclear fuel performance analysis, the modular capability of the code allows one to study other kind of physics outside nuclear applications.

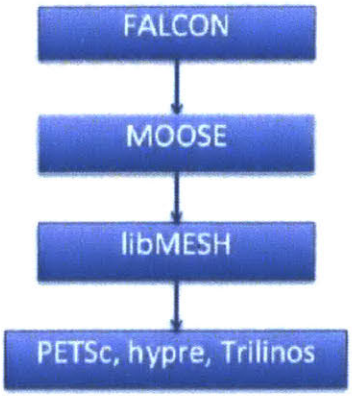

Figure 3-3: Hierarchical framework used to build FALCON application, based on the MOOSE framework (Podgorney et al., 2011).

3.5.3 Weak form of the governing equations

The governing partial differential equations are Equations 3.4 and 3.8. In addition, FALCON solves Equation 3.4 as[2]:

$$\phi \frac{\partial \rho_w}{\partial p} \frac{\partial p}{\partial t} - \nabla . \Big(\frac{k \rho_w}{\mu} (\nabla p - \rho_w \vec{g}) \Big) = 0 \tag{3.12}$$

Equations 3.8 and 3.12 are implemented in MOOSE in the weak form. Let φ be a test function defined in each element of the mesh, then the weak form of the governing equations for pressure and temperature over the domain Ω are obtained by integration by parts. The final equations are:

$$\int_\Omega \phi \frac{\partial \rho_w}{\partial p} \frac{\partial p}{\partial t} \varphi \, d\Omega - \int_\Omega \vec{q_m} \nabla \varphi \, d\Omega - \int_\Omega \varphi q''' \, d\Omega + \int_{\partial\Omega} \vec{q_m} \vec{n} \varphi \partial\Omega = 0 \tag{3.13}$$

[2]This equation was modified in the code as it is explained in Chapter 4.

$$\int_\Omega \frac{\partial T}{\partial t} C_m \varphi \, d\Omega + \int_\Omega \nabla\varphi (K_m \nabla T) \, d\Omega - \int_\Omega \nabla\varphi (T\vec{q_E}) \, d\Omega - \int_\Omega \varphi q''' \, d\Omega + \int_{\partial\Omega} (-K_m \nabla T + T\vec{q_E})\vec{n}\varphi \partial\Omega = 0 \tag{3.14}$$

where

$\vec{q_m}$ represents the term $\vec{q}\rho_w$

$\vec{q_E}$ represents the term $\rho_w c_w \vec{q}$

$\vec{q}$ is the Darcy flux, defined in Equation 3.3

$\partial\Omega$ is the boundary of the domain Ω

$\vec{n}$ is the normal vector to the boundary.

Using the following inner product notation to represent integrals since it is more compact, the heat transfer equation can be written as:

$$\underbrace{(\frac{\partial T}{\partial t} C_m, \varphi)}_{kernel} + \underbrace{(\nabla\varphi, K_m \nabla T)}_{kernel} - \underbrace{(\varphi, q''')}_{kernel} - \underbrace{(\nabla\varphi, T\vec{q_E})}_{kernel} + \underbrace{\langle \varphi, (-K_m \nabla T + T\vec{q_E})\vec{n} \rangle}_{boundary\ term} = 0 \tag{3.15}$$

where

$\langle , \rangle$ represents the integral terms over the boundary of the domain

$\vec{n}$ is the normal vector to the boundary

$(,)$ represents the integral terms over the domain.

The C++ code is based on the inner product notation. Each portion of the equation will be inherited from an existing MOOSE type and the unique aspects of our equations defined.

3.5.4 Time integration

MOOSE and all the applications used in this thesis use a finite difference discretization for time integration using the implicit Euler method. Implicit schemes allow for larger

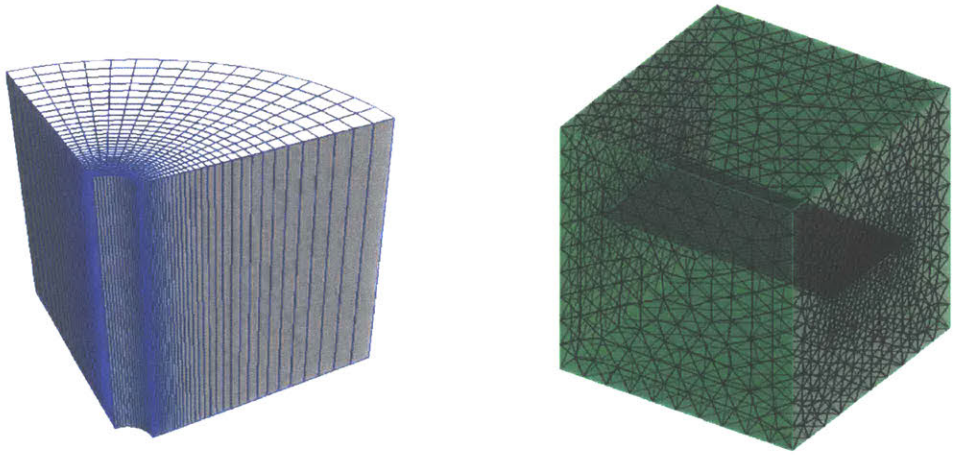

(a) Structured mesh with hexahedral elements representing a porous media with a cavity.

(b) Unstructured mesh with tetrahedral elements representing a porous medium with a planar fracture.

Figure 3-4: Unstructured and structured mesh examples.

time steps, reducing the total computational cost of solving Equations 3.13 and 3.14 in each time step.

3.5.5 Spatial discretization

The spatial discretization in finite element is described by a mesh. A mesh is a connectivity graph consisting of nodes, edges and elements. This topology defines the physical domain of the problem. MOOSE can read and write several mesh formats. MOOSE has two different methods for dealing with the mesh. It has a built-in capability for generation of simple geometries using a structured mesh, and also can read a mesh generated by meshing software, such as Trelis or Cubit (for older versions from SANDIA National Laboratory). For relatively complicated geometries unstructured meshes are used. This thesis used meshing capabilities of Trelis, Cubit 15 and Cubit 14 to generate a mesh file that is referenced in the FALCON input file. The EXODUS II format was used in this work.

3.5.6 Numerical integration in MOOSE

MOOSE uses numerical integration to evaluate the integral terms in the weak form of the governing equations. The integrals over a domain Ω in the weak form are approximated with Gaussian Quadrature, see Equation 3.16. The quadrature rule is an approximation of a definite integral of a function, usually by the weighted sum of function values at specified points within the domain of integration, the quadrature points q_p. Under certain common situations, the quadrature approximation is exact. An n-point Gaussian quadrature rule is a quadrature rule constructed to yield an exact result for polynomials of degree $2n$-1 or less by a suitable choice of the nodes $\vec{x}_i$ and weights w_i for $i = 1, ..., n$. To compute the integrals, the functions are evaluated at set points $\vec{x}_{q_p}$ and consider an associated weight w_{q_p}. The integrand is evaluated at the quadrature points in order to compute the integrals:

$$\int_{\Omega} f(\vec{x})\, d\Omega \approx \sum_{q_p} f(\vec{x}_{q_p}) w_{q_p} \tag{3.16}$$

where

$\vec{x}_{q_p}$ is the spatial location of the q_pth quadrature point

w_{q_p} is its associated associated weight.

Considering the integral over the domain Ω as the sum of the integrals over the elements Ω_e:

$$\int_{\Omega} f(\vec{x})\, d\Omega \approx \sum_{e} \int_{\Omega_e} f(\vec{x})\, d\Omega_e \tag{3.17}$$

where

Ω_e is an element in the domain Ω.

The integrals over the elements are mapped to integrals over the reference elements by a change of variables:

$$\sum_{e} \int_{\Omega_e} f(\vec{x})\, d\Omega_e = \sum_{e} \int_{\hat{\Omega}_e} f(\vec{\xi})\, |J_e|\, d\hat{\Omega}_e \tag{3.18}$$

where

J_e is the Jacobian of the mapping (change of coordinates) from the physical element to the reference element.

The reference element integrals are computed numerically using the quadrature (typically Gaussian Quadrature):

$$\sum_e \int_{\hat{\Omega}_e} f(\vec{\xi}) \, |J_e| \, d\hat{\Omega}_e = \sum_e \sum_{q_p} f(\vec{x}_{q_p}) w_{q_p} J_e(\vec{x}_{q_p}) \tag{3.19}$$

MOOSE handles the multiplication by the Jacobian and the weight automatically, in Equation 3.19. The kernel implemented in MOOSE is only responsible for computing the $f(\vec{x}_{q_p})$ part of the integrand.

3.5.7 Matrix form of the problem

The weak form of the governing equations is verified by the unknown pressure and temperature. Let u be the approximate finite element numerical solution of the PDEs for each variable pressure and temperature:

$$u(\vec{x}) = \sum_{i=1}^{N} \psi_i(\vec{x}) u_i \tag{3.20}$$

where

$\vec{x}$ is the coordinate vector

ψ_i is the shape function i

u_i is the solution of the PDEs at node i

N is the number of nodes.

For math simplification the shape functions ψ_i are taken to be equal to the test functions φ_i of the weak form. Then by substituting the numerical solution, u, into the weak form of the governing equations and after computing all the integral terms, evaluating the function of interest at the quadrature points as explained above, a

system of equations of N unknowns is obtained for each variable. By solving this system of equations the unknowns u_i, the numerical solution at node i, is found.

3.5.8 Non-linear system solution

By computing all the integral terms of the weak form of the equations, the we get a system of nonlinear equations, which can be expressed as:

$$\vec{R}(\vec{u}) = 0 \tag{3.21}$$

where
$\vec{u}$ is the vector of unknowns, u_i the solution at node i
$\vec{R}(\vec{u})$ is known as the residual vector.

Now the problem is to find the values of the nodal degrees of freedom (pressure and temperature) such that the above equation is satisfied. In general, this equation does not have a closed form solution (or some algorithm to find the closed form solution). Hence, we employ numerical root finding methods to find an approximate solution. It is necessary to iterate in the solution of Equation 3.21. The main point of concern is the utilization of an iterative scheme that has good convergence characteristic and that can be used effectively.

MOOSE has two solvers for non-linear systems: Newton and Pre-Conditioned Jacobian-Free Newton Krylov (PJFNK). The basic principles of the first iterative method are presented below. Because it demonstrated better convergence for our problem, it was the method chosen for our simulations.

3.5.8.1 Newton Method

We obtained a non-linear system of equations to solve:

$$R_i(\vec{u}) = 0, i = 1, ..., N \tag{3.22}$$

where

$\vec{u}$ contains the variable at the nodes of the finite element discretization, $\vec{u} = u_j, j = 1, ..., N$.

Assuming that in the iterative solution we have evaluated $\vec{u}^{\,i}$, at iteration $(i+1)$, then the Taylor expansion gives:

$$\vec{R}(\vec{u}^{\,i+1}) = \vec{R}(\vec{u}^{\,i}) + J(\vec{u}^{\,i})\delta\vec{u}^{\,i+1} + \text{ higher order terms} \tag{3.23}$$

where the Jacobian matrix, of size (N,N) is defined by:

$$J_{ij}(\vec{u}) = \frac{\partial R_i(\vec{u})}{\partial u_j} \tag{3.24}$$

We want to find the increment vector that turns the residual to zero. Neglecting the higher order terms in Equation 3.23, we can calculate the increment in the solution vector by solving:

$$J(\vec{u}^{\,i})\delta\vec{u}^{\,i+1} = -R_i(\vec{u}^{\,i}) \tag{3.25}$$

And the improved unknown solution is:

$$\vec{u}^{\,i+1} = \vec{u}^{\,i} + \delta\vec{u}^{\,i+1} \tag{3.26}$$

Newton's method, given an initial guess that is within the sphere of convergence of the method, has quadratic convergence when reducing the residual vector to zero. This procedure is repeated until the solution satisfies the original non-linear equations within a certain margin defined. In our simulation we used as the non-linear relative tolerance of the residual a value of 10^{-8} and 10^{-4} when the first one could not be reached. The Jacobian entries are nontrivial; they depend on the partial derivatives of the kernels which may be difficult or time-consuming to compute analytically. In a multi-physics setting with many coupled equations and complicated material properties, the Jacobian might be extremely difficult to determine.

3.5.9 FALCON code structure

The code used to perform the thermo-hydraulic analysis is the open-source geothermal reservoir simulation code FALCON (Xia et al., 2016). Some of the core computational capabilities include fully coupled and fully implicit solver, dimension independent physics, automatically parallel, and modular development of code. Below is a description of the main classes of FALCON referenced in the input file. MOOSE uses a hierarchical, block-structured input file. The syntax is completely customizable. MOOSE expects the following basic blocks in an input file for the simulations of a simple problem:

- `[Mesh]`
- `[Variables]`
- `[Kernels]`
- `[BCs]`
- `[Outputs]`

3.5.9.1 Variables

The *Variables* block declares the nonlinear variables that will be solved for in the simulation. FALCON solves for pressure and temperature at each node in a finite element mesh. In this block, the type of interpolation function used is defined. In addition, this block of the input file defines the scaling factor of each variable in the overall residual (read Section 3.5.10 for scaling's definitions). Variables can be defined separately in each part of the mesh, allowing the user to solve for different physics in different parts of the domain.

An example of a variable block in the input file is:

```
[Variables]
    [./nonlinear_variable1]
        order = <FIRST | SECOND | ...>
        family = <LAGRANGE | HERMITE | ...>
    [../]
```

```
    [./nonlinear_variable2]
        ...
    [../]
[]
```

3.5.9.2 Kernels

FALCON uses kernels to describe each part of the governing physics represented by each term of the PDE. Three kernels are used to define each of the governing equations. The mass conservation equation is composed by two physics kernels and one Dirak kernel. The two physics kernels consist of the time derivative term *PTMassTimeDerivative*, and the mass flux term *PTMassResidual* that accounts for gradient of pressure and gravity. The Dirak kernel represents a point mass source or sink, *PTMassPointSource*. The energy conservation equation is described by two physics kernels and one Dirak kernel. The two physics term are the time derivative term *PTEnergyTimeDerivative*, and the energy flux term *PTEnergyResidual* that consists of conductive flux and convective flux (and stabilization terms if needed). The Dirak kernel represents the point energy source/sink *PTEnergyPointSource*. Table 3.1 summarizes the kernels implemented in FALCON.

Table 3.1: Physics and Dirak Kernels for mass and energy conservation in FALCON.

Kernel	**Physical meaning**	**Term**
PTMassTimeDerivative	Time derivative term of mass conservation	$\phi \frac{\partial \rho_w}{\partial p} \frac{\partial p}{\partial t} \varphi$ on q_p
PTMassResidual	Mass flux term of mass conservation	$-\rho_w \vec{q} \nabla \varphi$ on q_p
PTMassPointSource	Point mass source/sink term of mass conservation	$-q''' \varphi$ on q_p
PTEnergyTimeDerivative	Time derivative term of energy conservation	$C_m \frac{\partial T}{\partial t} \varphi$ on q_p
PTEnergyResidual	Flux term of energy conservation equation	$(K_m \nabla T - \vec{q_E} T) \nabla \varphi$ on q_p
PTEnergyPointSource	Point energy source/sink term of energy conservation	$-q''' \varphi$ on q_p

3.5.9.3 Materials

FALCON has a class called *PTGeothermal* where all the material properties of the porous medium and thermodynamic properties of the liquid-phase water are calculated from user input parameters. Materials can be accessed by kernels and other parts of the code. Each material property is defined in each quadrature point of the mesh. User input material properties include: intrinsic permeability, porosity, density of the rock, density of the fluid, viscosity of the fluid, gravity vector, specific heat capacity of the rock, specific heat capacity of the fluid, medium average thermal conductivity, and reference temperature. Default values are used if they are not specified in the input file.

Numerical non-physical oscillations of the temperature will develop in space in convection-dominated (large Peclet number) problems, as has been theoretically proven (Tezduyar, Park, & Deans, 1987; Augustin et al., 2011). This is a significant problem of the standard Galerkin finite element. The spatial oscillations are reduced by a family of discretization schemes such as the upwind scheme. FALCON has the option of numerical stabilization with the Streamline Upwind Petrov-Galerkin method, SUPG (Hughes, Franca, & Mallet, 1986). In this work, no stability issues were found in the heat transport given the small fluid velocities.

3.5.9.4 Boundary conditions

In the MOOSE and FALCON code there is a class called Boundary Conditions, and it represents the surface integrals in the weak forms, Equations 3.13 and 3.14. To apply these boundary conditions the boundary topology, the variable, and either a scalar or normal gradient to the boundary has to be specified. Two types of boundary conditions are used in the repository modeling: Dirichlet and Neumann. Dirichlet boundary conditions were used for fixed values for temperature and pressure at the surface of the repository. Symmetry boundaries imply no-flux conditions, which were implemented as Neumann boundary condition for the corresponding variable, pressure and temperature. In this work a total of four boundary conditions are used, as shown

in Table 3.2 and explained below. One of them is inherited from MOOSE, DirichletBC, two others, from FALCON called PTEnergyInflowBC and PTMassFluxBC. These last two were used to impose a fixed geothermal flux for temperature and no mass flux respectively at the bottom of the domain.

Table 3.2: FALCON Boundary Condition Kernels used.

Kernel	**Physical meaning**
DirichletBC	Establishes an user-input variable value on a specific boundary surface. This BC class is supplied by MOOSE. It is used to define temperature and pressure at certain surfaces of the modeled domain.
PTEnergyInflowBC	Establishes an energy influx normal to specific boundary surface,$(-K_m \nabla T + T\vec{q_E})\vec{n}$.
PTMassFluxBC	Establishes a mass flux value, $\vec{q_M}.\vec{n}$ normal to a specific boundary surface. A positive value means injection, while a negative value means production.

The Neumann boundary conditions for our problem ($\nabla T.\vec{n} = 0$ and $\nabla p.\vec{n} = 0$ at the vertical surfaces of the domain which correspond to symmetry planes) are satisfied implicitly and are not necessary to be defined in the input file. However, for non-zero Neumann or other boundary conditions many built-in objects are provided by MOOSE (e.g., NeumannBC). Custom boundary conditions derived from the existing objects within MOOSE can be created if necessary.

3.5.9.5 Functions

Function objects allow the user to evaluate analytic expressions defined by spatial coordinates (x, y, z) and time, t. This object was used for the heat generation of the nuclear waste and for the initial conditions of temperature in the steady solver, which was ultimately used to determine the initial conditions for pressure and temperature in the transient solver.

3.5.9.6 Initial conditions

Initial conditions for calculating the numerical solution must be specified. They can be defined by using *Functions* or by reading them from another EXODUS file. In this work both methods were used as will be explained in Chapter 5.

3.5.9.7 User Objects

The UserObject system provides data and calculation results to other MOOSE objects. In our simulations one UserObject is used to calculate all fluid properties from the IAPWS-97 table.

3.5.9.8 Executioner

There are two main types of Executioners: Steady and Transient.

1. Steady Executioner

   Steady-state executioners generally solve the non-linear system just once. Executioner options are defined in the Executioner block in the input file and control the solver. They are shown in Table 3.3.

Table 3.3: Common executioner options.

Option	Definition
l_tol	Linear Tolerance (default: 10^{-5})
l_max_its	Max Linear Iterations (default: 10000)
nl_rel_tol	Nonlinear Relative Tolerance (default: 10^{-8})
nl_abs_tol	Nonlinear Absolute Tolerance (default: 10^{-50})
nl_max_its	Max Nonlinear Iterations (default: 50)

2. Transient Executioners

   Transient executioners solve the nonlinear system at least once per time step. Executioner options are defined in the Executioner block in the input file and control the solver. They are shown in Table 3.4.

Table 3.4: Common transient executioner options.

Option	Definition
dt	Starting time step size
num_steps	Number of time steps
start_time	The start time of the simulation
end_time	The end time of the simulation
scheme	Time integration scheme (discussed next)

The MOOSE framework has implemented several time integration methods, both explicit and implicit methods, of different stability and order of truncation error. Some of the TimeIntegrators provided by MOOSE are:

- Implicit
  - Backward Euler (default)
  - BDF2
  - Crank-Nicolson
  - Implicit-Euler
  - Implicit Midpoint (implemented as two-stage RK method)
  - Diagonally-Implicit Runge-Kutta (DIRK) methods of order 2 and 3.
- Explicit
  - Explicit-Euler
  - Various two-stage explicit Runge-Kutta methods (Midpoint, Heun, Ralston, TVD)

MOOSE supports adaptive time stepping. If the solver does not converge, then that time step is aborted and the solver decreases the time step size (depending on parameters of the Executioner and the TimeStepper) and continues until convergence of the solver is reached.

3.5.9.9 Output

MOOSE supports several formats of the file to save the numerical solution: n, among others. Also, MOOSE post-processors can save the values of the numerical solution

at discrete locations in the domain in comma-separated values (csv) files.

3.5.10 Convergence criteria and scaling

In an iterative numerical solution, the residual never reaches the exact value of zero. However, the smaller the value of the residual, the more accuracy in the numerical solution. The goal of the solver is to reduce the residual sufficiently up to a threshold to consider that the solver has converged to the right solution of the non-linear equations. For convergence analysis MOOSE calculates one residual norm for the two governing equations. The residual vector norm accounts for the individual norm of the temperature and pressure residuals. Each contribution to the overall residual has different dimensions. Because of this, individual residuals must be non-dimensionalized or scaled. MOOSE requires scaling the variables in order to weight their contributions to the overall non-linear residual appropriately. The individual residuals are multiplied by some scaling factors to produce initial residuals of the same order at each time step. The overall residual norm is:

$$||R|| = \sqrt{(C_T||R_T||)^2 + (C_p||R_p||)^2} \tag{3.27}$$

where

$||R_p||$ is the norm of the Equation 3.13

C_p is the scaling of pressure

$||R_T||$ is the norm of the Equation 3.14

C_T is the scaling of temperature.

The scaling factors for each variable are defined in the input file, for instance:

```
[Variables]
    [./porepressure]
    [../]
    [./temperature]
        initial_condition = 293
```

```
        scaling = 1E-8
    [../]
[]
```

The convergence criterion is controlled by the parameter nl_rel_tol which defines the relative decrease of the residual to stop the iterations at each time step, or at each steady simulation (depending on the type of problem). The default value of this parameter is 10^{-8}. If this parameter is set too small, then MOOSE seems not to converge and needs very small time steps to proceed with the calculations. If this parameter is set too large, then MOOSE converges to an inaccurate result. The value of this parameter has been adjusted depending on the problem studied in each simulation.

Chapter 4

Source Code Verification and Cross-Code Validation

4.1 Introduction

The FALCON source code (Xia, Plummer, Podgorney, & Ghassemi, 2016) was downloaded from GitHub in 2016. By that time, the code was a recent code developed by INL and we got access to it just when the code was open-source for first time. Therefore this code has not been widely used when we tested it for first time. We performed several rigorous validation cases of the source code FALCON. Some of the tests are summarized below.

4.2 Validation cases

4.2.1 Heat conduction in a square

A 2D conduction case was analyzed in a square domain for an isothermal initial condition of T_o. At time=0 a fixed temperature of T_s is imposed at the boundary of the domain, see Figure 4-1. The square has length 2a. Thermal properties of the material were taken to be typical rock values.

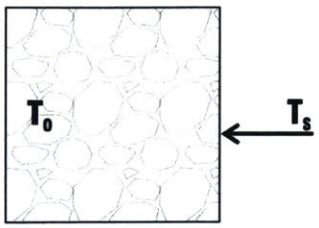

Figure 4-1: Model setup.

The heat transport equation is:

$$\rho_r c_r \frac{\partial T}{\partial t} - k_r \nabla.(\nabla T) = 0 \tag{4.1}$$

where

ρ_r is the density of the material

c_r is the specific heat of the material

k_r is the thermal conductivity of the material

T is temperature of the material.

4.2.1.1 Analytical solution

Using Fourier series, the analytical solution of the above equation is found to be (Carslaw & Jaeger, 1959):

$$\begin{aligned} T(x,y,z) =& T_s + \frac{16(T_o - T_s)}{\pi^2} \sum_{m=0}^{\infty}\sum_{n=0}^{\infty} \frac{(-1)^{m+n}}{(2m+1)(2n+1)} \cos\left(\frac{(2m+1)\pi x}{2a}\right) \\ & \cos\left(\frac{(2n+1)\pi y}{2b}\right) e^{-\alpha_{m,n} t} \end{aligned} \tag{4.2}$$

where

$\alpha_{m,n} = \frac{\kappa\pi^2}{4}\left[\frac{(2m+1)^2}{a^2} + \frac{(2n+1)^2}{b^2}\right]$

$\kappa = \frac{k_r}{\rho_r c_r}$

$x \in (-a, a)$

$y \in (-b, b)$.

4.2.1.2 Numerical solution

We used linear interpolation functions. The parameters used for this problem are:

$T_s = 100$ °C

$T_o = 200$ °C

$a = b = 0.5$ m

k_r=2.7 W/m°C

ρ_r= 2700 W/m°C

c_r= 1000 J/kg°C.

4.2.1.3 Comparison between numerical and analytical solution

1. Spatial discretization

   Using a fixed time step, 1×10^4 s, we computed the numerical solution using different grid sizes (considering an increasing number of elements in x, $n_x = 50, n_x = 100, n_x = 500$), shown in Figure 4-2. No significant variations in the numerical solution can be seen for the three different grid sizes considered. Grid convergence is reached. The FALCON solution matches the analytical solution relatively well, however some small differences can be seen.

2. Time discretization

   Using a fixed number of elements ($n_x = 50$) we computed the numerical solution using smaller time steps (dt=1×10^4s, dt=1×10^3 s, dt=1×10^2 s, dt=1×10^1 s), shown in Figure 4-3. The time discretization error explains the differences between the analytical solution and the numerical solutions. By using a small time step, the agreement between the analytical and the numerical solution is excellent.

3. Analytical solution truncation error

The coefficients of the Fourier series decay very fast with the number of terms in the analytical solution. This can be seen when comparing the solutions considering the first 100 terms with the first 1000 terms, see Figure 4-4. Therefore, it is acceptably accurate to consider the first 100 terms in the analytical solution in the previous comparison. There are no significant differences in the analytical solution used for validation when considering more than 100 terms.

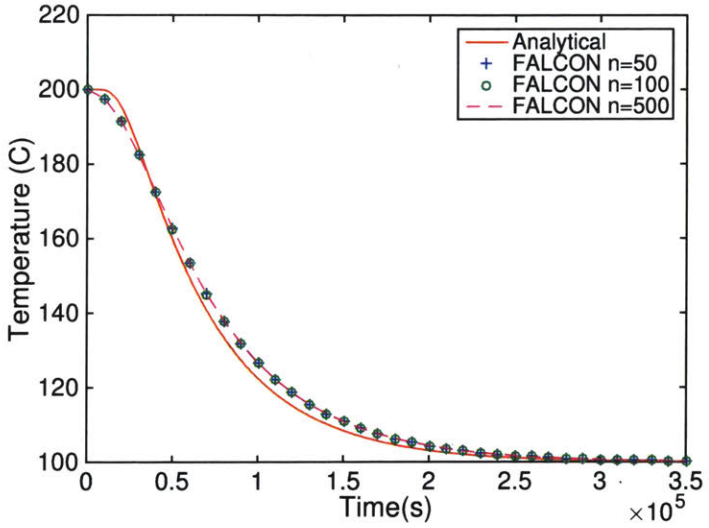

Figure 4-2: Temperature at (0,0), comparison of FALCON and analytical solution for different grid resolutions (n indicates the number of elements in x direction in the mesh).

4.2.2 Coupled thermal-hydraulic model: hydrostatic equilibrium with heat flux at bottom boundary

A saturated porous medium of prismatic shape was considered, with the boundary conditions schematized in Figure 4-5. This case study aims to test the steady solver convergence and the geothermal heat flux boundary. A porous medium of constant properties of 10 km depth was studied. The porous medium is saturated with fresh water. The boundary conditions, shown in Figure 4-5, are:

- Fixed temperature and pressure at the top surface

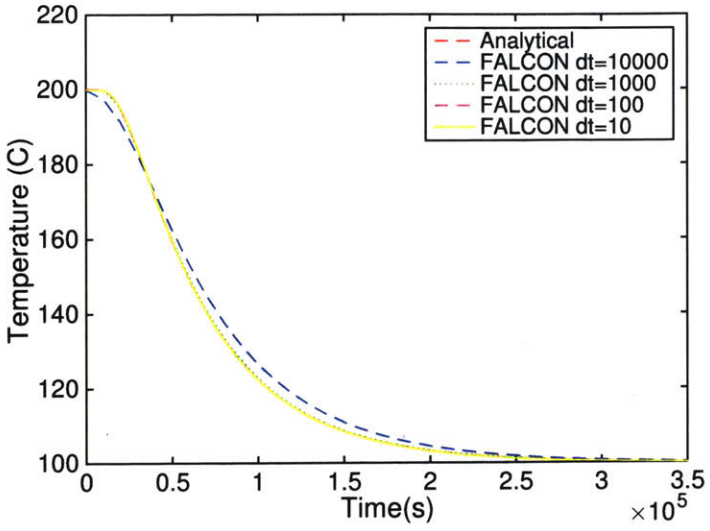

Figure 4-3: Temperature at (0,0), comparison of FALCON and analytical solution for different time steps, dt.

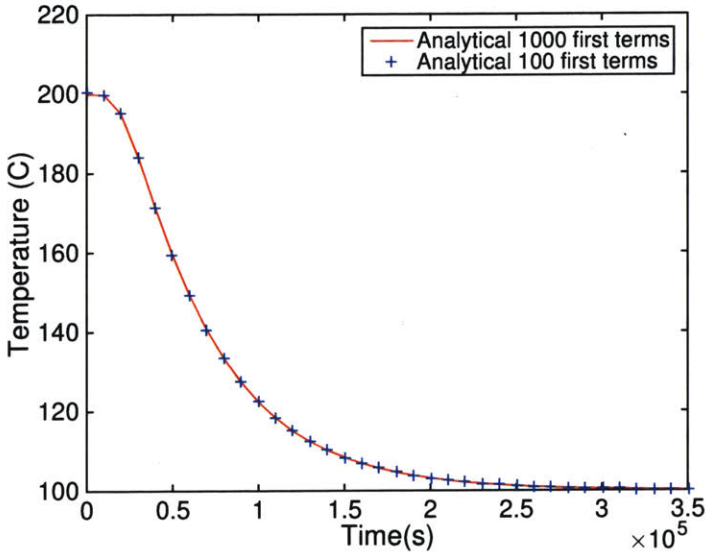

Figure 4-4: Comparison of analytical solution for different number of terms in the Fourier series.

- Constant heat flux at the bottom of the domain
- No water flux at the bottom boundary
- No flux (mass and heat) boundary at the vertical faces.

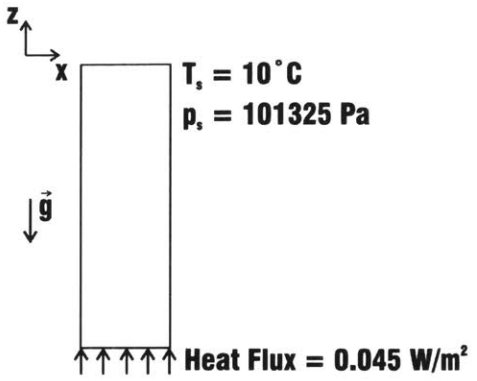

Figure 4-5: Model setup.

The goal of this validation case is to find numerically the density as a function of depth, $\rho(z)$, the pressure as a function of depth, $p(z)$, and the temperature, $T(z)$ as a function of depth, to then verify analytically the equilibrium for the numerically computed pressure and density, and to compare the computed temperature with an analytical expression.

4.2.2.1 Analytical solution

A very large natural geothermal flux from the Earth's crust can produce fluid instabilities that are undesirable for borehole repositories. Assuming this heat flux is not large enough to produce fluid instabilities, the system can reach an equilibrium steady state defined by:

$$\frac{\partial}{\partial z}(k_{eff}\nabla T) = 0 \tag{4.3}$$

where

k_{eff} is the effective conductivity of the porous medium

z is the vertical coordinate defined positive upward and $z = 0$ at the top surface

T is the temperature.

Considering constant thermal conductivity of the medium (k_{eff}) and considering

a heat flux boundary at the bottom of the modeled region, with heat flux $q'' > 0$, the equilibrium solution is:

$$T(z) = T_0 - \frac{q''}{k_{eff}} z = 0 \tag{4.4}$$

where

T_0 is the temperature at the surface.

And we also know that in equilibrium the fluid pressure is defined by:

$$p(z) = p_0 + \int_z^0 \rho_f(T, p) g \, dz = 0 \tag{4.5}$$

where

p_0 is the pressure at the top boundary defined at $z = 0$

ρ_f is the fluid density, which is a function of fluid pressure and temperature

g is the gravity constant.

4.2.2.2 Numerical Solution

We used linear interpolation functions in FALCON and uniform mesh resolution of 100 m in the vertical direction for the entire domain. In the following figures we present the numerical solution, and when possible, the analytical solution is included in the graph for comparison.

4.2.2.3 Comparison between numerical and analytical solution

Perfect correspondence between the analytical and the numerical temperature profile can be seen in Figure 4-6a. In addition, the directly computed pressure in FALCON matches the pressure determined analytically from the integral of the numerically computed density, as seen in Figure 4-6b. Water density increases with pressure and decreases with temperature. Temperature and pressure effects produce the net effect shown in Figure 4-6c. It is interesting to note that for the case studied, the

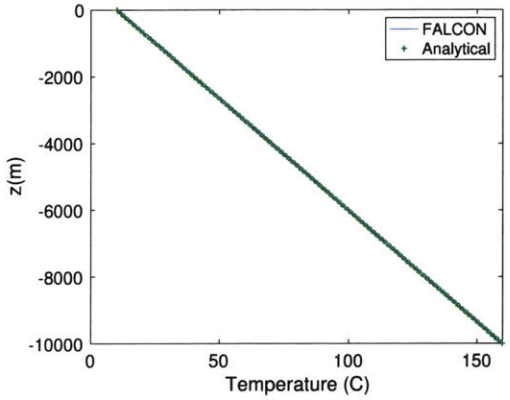

(a) Comparison of temperature profile between FALCON and analytical solution.

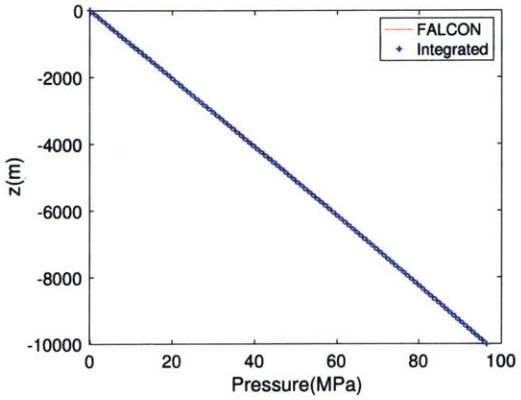

(b) Comparison of pressure between FALCON and analytically computed values from fluid density computed by FALCON.

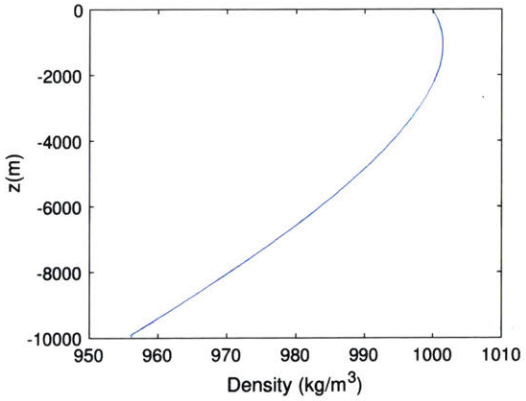

(c) Fluid density as function of depth computed numerically by FALCON.

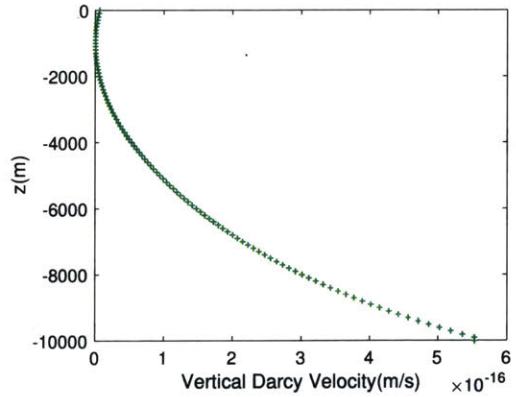

(d) FALCON Darcy velocities as function of depth.

Figure 4-6: Numerical solution for temperature and pressure and its comparison with analytical expressions; numerically computed fluid density and fluid velocities.

largest density is found at around 1 km depth. In order to verify that the steady solver has effectively converged, we computed the Darcy velocity, shown in Figure 4-6d. The numerically computed Darcy velocity with FALCON lies within the range of 2.9583×10^{-19} m/s to 5.5372×10^{-16}m/s. Machine Epsilon[1] in double precision, IEEE format is 2.2204×10^{-16}. Therefore, the calculated Darcy velocity can be considered zero in practical terms (order of magnitude), which indicates the steady solver has converged to the right solution. Moreover, at steady state (zero fluid velocities), the numerical solution should match the analytical steady state solution, which we do indeed see in Figure 4-6a.

4.2.3 Cross-code validation: FALCON 2011 vs FALCON 2016

The goal is to reproduce with FALCON 2016 the results obtained with the FALCON 2011 code. FALCON (Xia et al., 2016) was developed in 2016 and despite having the same name as the previous version, FALCON 2011, it has a different formulation. From now on, we shall refer to the code officially named FALCON as FALCON 2016 to better differentiate it from its predecessor. Numerical results were obtained using FALCON 2011 for the case of PWR spent fuel in an infinite array of boreholes (Lubchenko et al., 2015). These results are used for validation of the new open source FALCON 2016.

4.2.3.1 FALCON 2011 source code

FALCON 2011 is an open source code developed by INL in 2011 (Podgorney et al., 2011). The FALCON code has been developed to support simulation of both conventional hydrothermal and enhanced geothermal system (EGS) reservoirs, with a primary design focus on EGS resources. While this code uses the IAPWS-97 formulation for water, which has quite an effective operating range of pressure ($\leq$ 100MPa) and temperature($\leq$ 800 °C), code development focused on subcritical conditions (Huang,

[1]Machine Epsilon is the smallest number of ϵ such that $(1+\epsilon) \neq 1$. Machine Epsilon, ϵ_{Mach}, is a machine-dependent floating point value that provides an upper limit on the relative error due to the rounding in floating point arithmetic.

2019). This source code has been extensively tested and widely used by the scientific community related to geothermal resources therefore it provides good results to compare the newest open source FALCON 2016.

4.2.3.2 Benchmark

The validation benchmark consists of analyzing one single borehole in an infinite array of identical boreholes. We tested first the steady state solver for a non-uniform mesh which includes the borehole, in contrast to the previous case which has uniform resolution and did not include the discretization of the borehole. We solve the steady state imposing the same boundary conditions as used previously in Section 4.2.2. The mesh contains three material blocks: rock, waste, and seal. The model considered corresponds to an infinite array of boreholes, considering a square lattice of separation between boreholes of 200 m. Because of the symmetries of the problem, to reduce the computational cost, only one quarter of the complete domain is modeled, shown in Figure 4-7.

The mesh was generated with Cubit15.0 developed by SANDIA. The mesh consists of hexahedral elements. The radioactive material extends from -3 km to -5 km, being $z = 0$ at the top boundary of the modeled domain. The mesh is refined at the extremes of the heat source (nuclear waste) for numerical stability since it is the region with the largest gradients of temperature, shown in Figure 4-8. The total depth of the domain is 10 km, which is considered deep enough so as not to affect the solution. The boundary conditions (shown in Figure 4-5) are:

- Fixed surface temperature, 10 °C
- Fixed surface pressure, 1 atm (101325 Pa)
- Constant heat flux at the bottom of the domain, 45 mW/m^2
- No mass flux at the bottom boundary
- Symmetry boundary at the four vertical faces of the numerical domain.

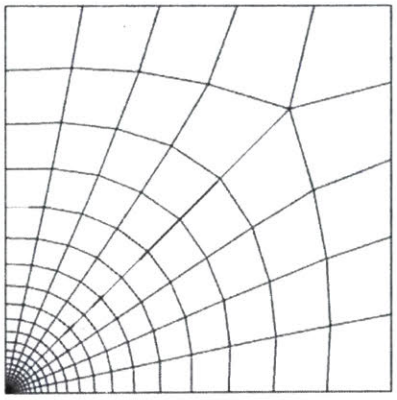

Figure 4-7: Top view of the mesh, of dimensions 100 m by 100 m and depth of 10 km. The borehole axis is located at the bottom left corner of the square section and it has a radius of 17 cm (because of its dimensions it is not visible in the mesh).

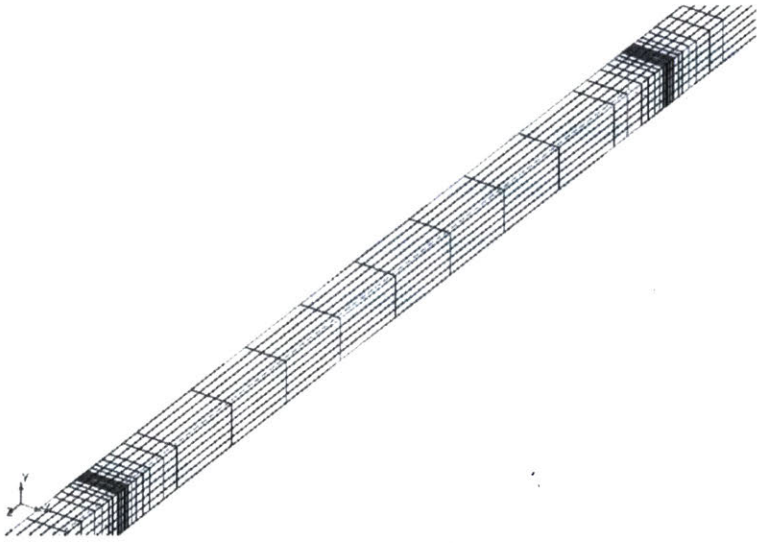

Figure 4-8: Isometric view of the mesh representing the nuclear waste emplacement zone. The mesh is refined at the extremes of the emplacement zone. Image to scale.

Table 4.1 presents the rock and repository properties considered for the numerical results.

Table 4.1: Summary of rock and repository properties.

Property	**Value**
Rock density	2750 kg/m^3
Rock thermal conductivity	3 W/m°C
Rock specific heat	790 J/kg°C
Geothermal flux	45 mW/m^2
Surface temperature	10 °C
Surface pressure	101325 Pa
Rock permeability	10^{-16} m^2
Rock porosity	0.01
Emplacement depth	3 km to 5 km
Borehole diameter	0.34 m
Borehole spacing (square lattice)	200 m
Canister thermal conductivity (average)	0.628 W/m°C
Canister specific heat (average)	499 J/kg°C
Canister density (average)	4405 kg/m^3
Canister porosity	0.01
Canister permeability	10^{-15} m^2

4.2.3.3 Steady state

We first solve for the steady state and we conclude that the steady solver has effectively converged to the right numerical solution for this non-uniform mesh. Values of temperature matching the analytical calculations, pore pressure matching the previous validation case, and Darcy fluid velocity of the order of Machine Epsilon.

4.2.3.4 Transient simulation

This simulation corresponds to the response of the system after the spent fuel has been placed into the borehole. The initial condition for the transient simulation corresponds to the steady state found previously, where the temperature is determined by the geothermal flux at the bottom and the surface temperature, and the pore pressures are determined by the corresponding density at each point. The volumetric heat source corresponds to the PWR spent fuel heat production.

Decay Heat

The volumetric decay heat of PWR spent fuel as function of time, $q'''(t)$ expressed in W/m^3, considering 25 years of cooling time, corresponds to (Malbrain et al., 1982):

$$q'''(t) = 2176\left(\frac{25}{25+t}\right)^{0.75} \tag{4.6}$$

where

t represents the time in years elapsed since the end of the cooling time period, and is therefore considered to be zero at emplacement.

4.2.3.5 Analytical approximation for fluid velocity

We can obtain an analytical expression for the Darcy velocity in the cap rock by considering a simplified model in which the water flow in the cap rock is the response to the thermal expansion of the fluid in the porous medium. Given the very large aspect ratio of the volume considered, 10 km depth and 200 m width, fluid velocity can be considered uniform in each horizontal plane. An analytical expression for the Darcy velocity in the cap rock zone can be found making several approximations (Bates, 2015):

1. All thermal energy released by the spent fuel is transferred to a homogeneous insulated volume of the surrounding host rock saturated with water, with heat capacity $(\rho c)_{eff}$. In reality, the net energy absorbed by the rock is smaller than this.

2. All lateral boundaries are impermeable.

3. The flow in the rock above the waste zone (cap rock) is upward and uniform for all times.

4. The pressure gradient is uniform across any horizontal plane in the cap rock.

5. Compressibility of the rock, and thermal effects on the rock are neglected. Coupled thermo-hydro-mechanical effects in the rock are neglected, and therefore no

changes in porosity due to thermal expansion and compression are considered.

6. Convection within the cap rock is negligible.

The total heat produced by the spent fuel is (see Figure 4-9):

$$q(t) = q'''(t) L_e \pi r_b^2 \tag{4.7}$$

where

L_e is the emplacement length

r_b the radius of the borehole.

The considered volume of porous rock surrounding the borehole absorbs the heat released by the spent fuel. Thus, the average temperature, called T, of the volume V_r considered increases by:

$$\frac{dT}{dt} = \frac{q'''(t) L_e \pi r_b^2}{(\rho c)_{eff} V_r} \tag{4.8}$$

where

$(\rho c)_{eff}$ is the effective heat capacity of the porous medium (weighted average of the product of density and specific heat for each components: solid grains and water).

The fluid in the pores and the rock are at the same temperature. The volume of fluid contained in a volume V_r, is ϕV_r, assuming the rock is saturated. Then, by definition of thermal expansion, the increment of volume of water is given by:

$$\frac{dV}{dT} = \beta_w \phi V_r \tag{4.9}$$

where

β_w is the thermal expansion coefficient of water

ϕ is the porosity.

The water leaves the considered control volume through the top surface of area A with a superficial velocity (Darcy velocity), $u(t)$, as schematized in Figure 4-9. The

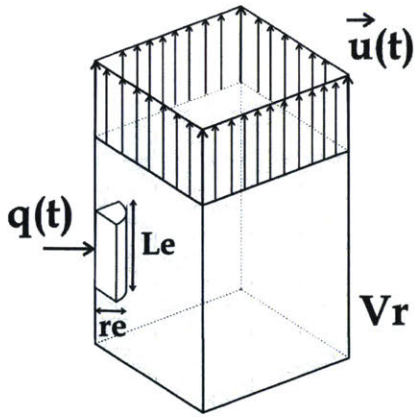

Figure 4-9: Schematic of the fluid velocity governed by thermal expansion, which is produced by decay heat.

volume change is related to the superficial velocity by:

$$\frac{dV}{dt} = u(t)A \tag{4.10}$$

Combining Equations 4.9 and 4.10 we get:

$$u(t) = \frac{dV}{Adt} = \frac{\beta_w \phi V_r dT}{Adt} = \frac{\beta_w \phi V_r q'''(t) L_e \pi r_b^2}{A(\rho c)_{eff} V_r} \tag{4.11}$$

Therefore the velocity in the cap rock is:

$$u(t) = \frac{\beta_w \phi V_r L_e \pi r_b^2 q'''(t)}{A(\rho c)_{eff} V_r} \tag{4.12}$$

This expression for $u(t)$ corresponds to flow purely due to thermal expansion of the pore fluid, for a constant thermal expansion coefficient (independent of pressure), not accounting for any compressibility effects in the rock and variations of porosity due to thermal expansion of the rock matrix.

The expression for $u(t)$ represents an over-prediction of the velocity magnitude for initial times since it takes some time for the pressure wave to propagate from the

heat source to the location considered in the cap rock. The analytical derivation does not account for this propagation time of the pressure and it assumes the fluid moves instantly governed by the heat source. Therefore, Equation 4.12 provides an upper limit of the fluid velocity for comparison with the numerical solution.

4.2.3.6 Comparison of numerical results

When comparing numerical results between the old closed source code, FALCON 2011, with the new open source version of FALCON 2016 several significant differences are observed. Figures 4-11, 4-12 and 4-13 show the comparison of temperature, pore pressure and fluid velocity at a particular location in the rock. In summary:

1. Temperature

   Predictions are in good agreement between the two codes. The temperature results match well the validated predictions by the old source FALCON 2011 code which were validated against the FEHM[2] code. See Figure 4-11.

2. Fluid pressure

   The new code, FALCON 2016, produces incorrect initial pressures, significantly higher than the correct results. In addition, FALCON 2016 original source code significantly over-predicts the maximum transient of pressure. See Figure 4-12.

3. Pore velocity

   Since the pressure field is incorrect, velocities are incorrect as well. Velocities are computed as auxiliary variables in FALCON 2016 from the pressure field. FALCON 2016 predicts initial fluid velocities. The prediction that the initial velocities are not zero is wrong because the initial conditions of the simulation corresponds to a hydrostatic state. Later in time, the Darcy velocities are two orders of magnitude smaller than the validated results. However, the slope of velocity with time matched perfectly the validated results, imposed by the

[2]FEHM, Finite Element Heat and Mass Transfer Code, is an open source code developed by Los Alamos National Laboratory (Los Alamos National Laboratory, 2007).

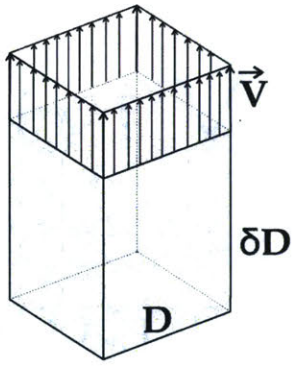

Figure 4-10: Control volume considered in Equation 4.13.

volumetric heat source as the flow is mainly due to water expansion. See Figure 4-13.

4. Mass conservation

We considered the mass balance of a control volume D within the total domain, as schematized in Figure 4-10. This volume extends from 2 km below the top boundary to the bottom boundary of the numerical domain. The following relation must be verified:

$$\frac{\partial}{\partial t} M(D,t) = -\int_{\partial D} \rho \vec{v} \vec{n} \, dA \tag{4.13}$$

$$\frac{\partial}{\partial t} \int_D \rho \phi \, dV = -\int_{\partial D} \rho \vec{v} \vec{n} dA \tag{4.14}$$

where

$M(D,t)$ represents the mass of the control volume D

ϕ is the porosity

ρ is the fluid density

∂D represent the boundaries of the control volume D

$\vec{n}$ is the vector normal to the boundary ∂D

$\vec{v}$ is the fluid velocity.

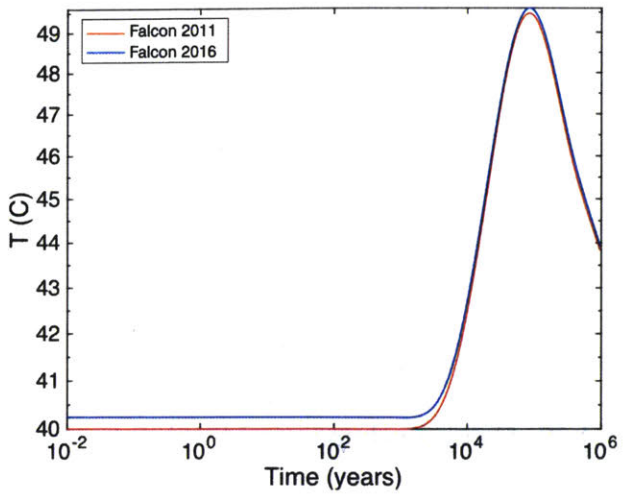

Figure 4-11: Temperature comparison at the cap rock (2km depth).

The integral terms of Equation 4.14 were computed in ParaView. The time derivative was approximated by the difference between two consecutive time steps of the volumetric integral. It was found that the vertical mass flux through the top surface is two orders of magnitude different than the local variation of mass, as expected, since the Darcy velocities obtained are two orders smaller than the correct values. Mass is not conserved for a control volume within the domain.

We found that two errors were causing the above wrong calculations:

1. A bug in the newest MOOSE source code.

   While performing all the simulations a bug was found in the MOOSE 2016 source code. This bug was causing the wrong initial pressure field and initial velocities. For the transient simulation the code was taking for its computations a wrong initial pressure field even though the right initial values were clearly defined in the input file. This error in the MOOSE source code was verified by contacting the main developers of MOOSE at INL. It is remarkable how even small deviations from the right initial condition for pressure led to very different transient results in pressure, and even generated an extremely large non-realistic

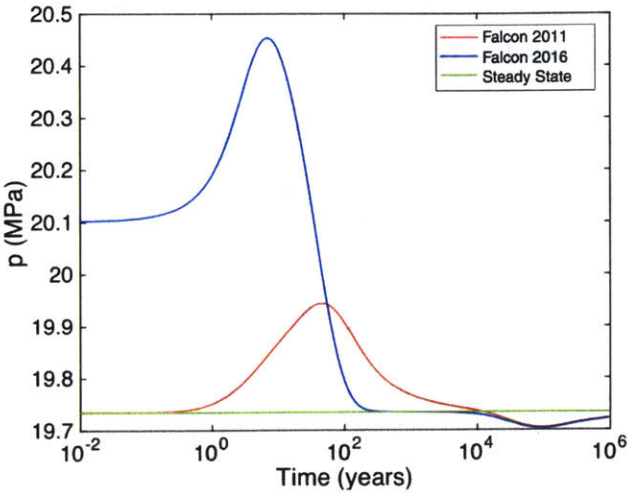

Figure 4-12: Pressure comparison at the cap-rock (2km depth).

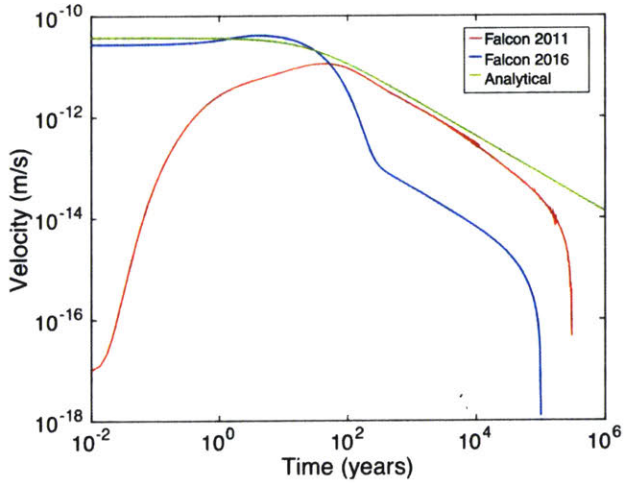

Figure 4-13: Vertical Darcy velocity comparison at the cap-rock (at 2km depth).

maximum of pressure. Even more, it took an extremely long simulation time for the code to reach the steady correct value when the heat input was set to zero. This bug in MOOSE 2016 has been fixed by the MOOSE developers and the code was updated in GitHub.

2. An error on how the code FALCON 2016 resolves the local time derivative of the term in the mass balance equation:

$$\frac{\partial}{\partial t}(\phi\rho_w) \tag{4.15}$$

The old version of FALCON 2011 solved this term correctly by finite differences, evaluating the difference with respect to the term in one previous time step. However, the newest version of FALCON 2016, solves this term approximately, neglecting the local time derivative of temperature, as:

$$\frac{\partial}{\partial t}(\phi\rho_w) = \phi\frac{\partial\rho_w}{\partial p}\frac{\partial p}{\partial t} + \phi\frac{\partial\rho_w}{\partial T}\frac{\partial T}{\partial t} + \rho_w\frac{\partial\phi}{\partial t} \approx \phi\frac{\partial\rho_w}{\partial p}\frac{\partial p}{\partial t} \tag{4.16}$$

The third term in Equation 4.16 is omitted, since FALCON 2016 does not account for variations in porosity. This approximation also neglects the term of the local derivative of temperature $\phi\frac{\partial\rho_w}{\partial T}\frac{\partial T}{\partial t}$. In our problem, a significant heat source is included in the domain, therefore that term cannot be neglected. We found only one paper (Xia et al., 2016) in the literature using the newest source code FALCON 2016, for an analysis of a geothermal system. For the particular case studied in that paper, the neglected term is probably insignificant, so the missing term has no big impact in the solution and therefore results are correct. Neglecting that term is what is causing wrong results in pressure and therefore velocity. After all, we conclude that the source code has to be modified to correctly compute the term $\theta\frac{\partial\rho_w}{\partial T}\frac{\partial T}{\partial t}$, see below.

4.2.4 Code modifications and validation

The time derivative term was modified in the weak form of the mass balance equation. This was done by two methods: a finite difference in time (called Falcon FD in the

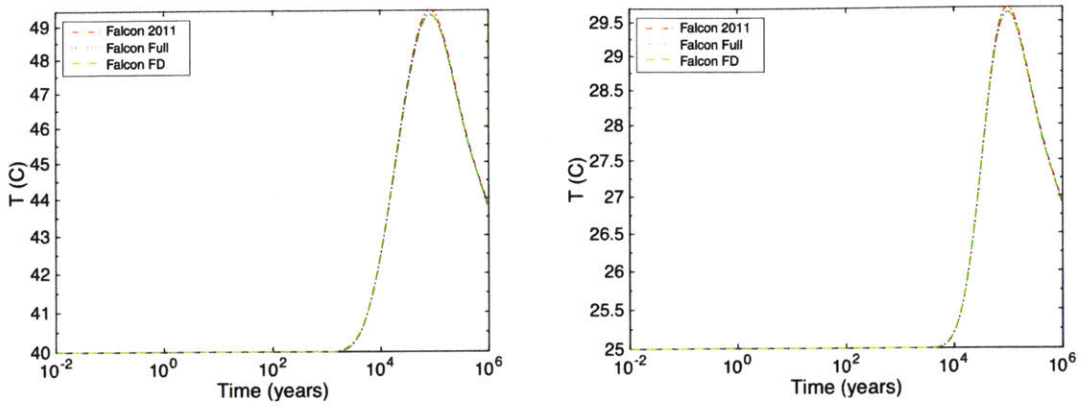

Figure 4-14: Left: temperature in the cap-rock (2km depth). Right: temperature in the seal (1km depth). Nomenclature in the caption of the plot: FALCON 2011 code, Falcon FD refers to finite difference method of computation of the term $\frac{\partial}{\partial t}(\theta\rho_w)$, Falcon Full refers to the method of including the term $\phi\frac{\partial\rho_w}{\partial T}\frac{\partial T}{\partial t}$.

plots below), and by the inclusion of the missing term in the analytical expression (called Falcon Full in the plots below) (see Appendix D). The comparison of the results of the original and the modified code are shown in Figures 4-14, 4-15 and 4-16. They present the evolution with time of temperature, pressure and velocity at two locations in the domain. Virtually perfect matching between FALCON 2011 and our two modified versions of FALCON 2016 has now been reached.

4.2.5 Code improvement summary

We identified errors in the source code that led to wrong results. The original source code FALCON 2016 downloaded from GitHub was not able to replicate validated results obtained with FALCON 2011. This was due to two issues:

1. a bug in the MOOSE framework

2. an error in how FALCON 2016 code solves the mass balance equation. We addressed these errors by modifying the source code. Results of the newly modified code were in excellent agreement with previously validated results of FALCON 2011. We reported these errors to the authors of the code, and made the corrected code publicly available in GitHub.

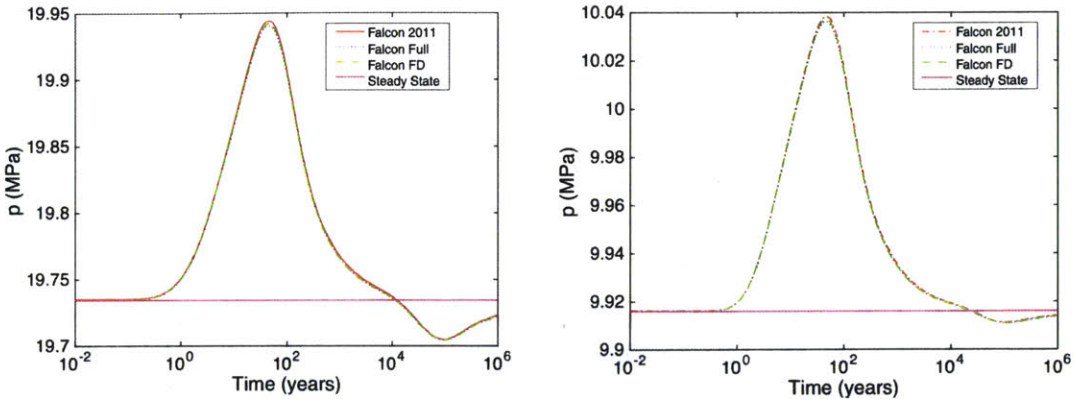

Figure 4-15: Left: pressure in the cap rock (2km depth). Right: pressure in the seal (1km depth). Nomenclature in the caption of the plot: Steady state refers to the initial pressure value, which corresponds to steady state at that location in the domain.

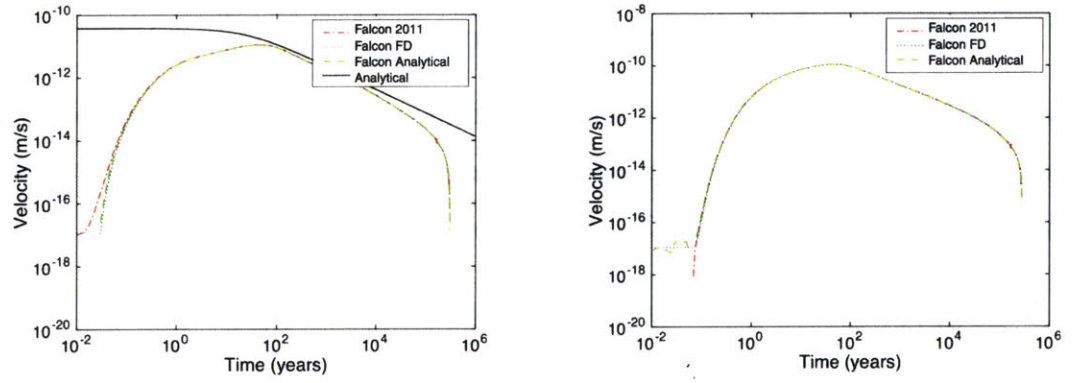

Figure 4-16: Left: vertical Darcy velocity in the cap-rock (2km depth). Right: vertical Darcy velocity in the seal (1km depth). Nomenclature in the caption of the plot: Analytical refers to the analytical expression of velocity defined by Equation 4.12.

Chapter 5

Application

5.1 Introduction

This chapter includes analysis of repository options for disposal of TerraPower TWR spent fuel, utilizing a corrected and validated version of FALCON 2016. The repository analyzed is the deep borehole type (5 km deep), which makes use of a large rock volume to isolate the radionuclides from the human environment. As discussed in Chapter 2, this concept is different from another design in which the waste is deposited in tunnels just several hundred meters below the surface. See Figure 5-1.

5.2 Computational resources

5.2.1 HPC cluster for simulations

The simulations were performed on two computer clusters at MIT: Engaging cluster and Acqua cluster. The queue used in the Engaging cluster has 50 computational nodes with 128GB of RAM and Intel(R) Xeon(R) CPU E5-2683 v4 @ 2.10GHz24-core processors. Acqua cluster has different types of nodes depending on the queue: 10 nodes with 24GB of RAM and 2x Intel(R) Xeon(R) CPU X5650 @2.67GHz core processors, 10 nodes with 32GB of RAM 2x Intel(R) Xeon(R) CPU E5-2630 v2 @ 2.60GHz, and 10 nodes with 64GB of RAM 2x Intel(R) Xeon(R) CPU E5-2620 v4 @

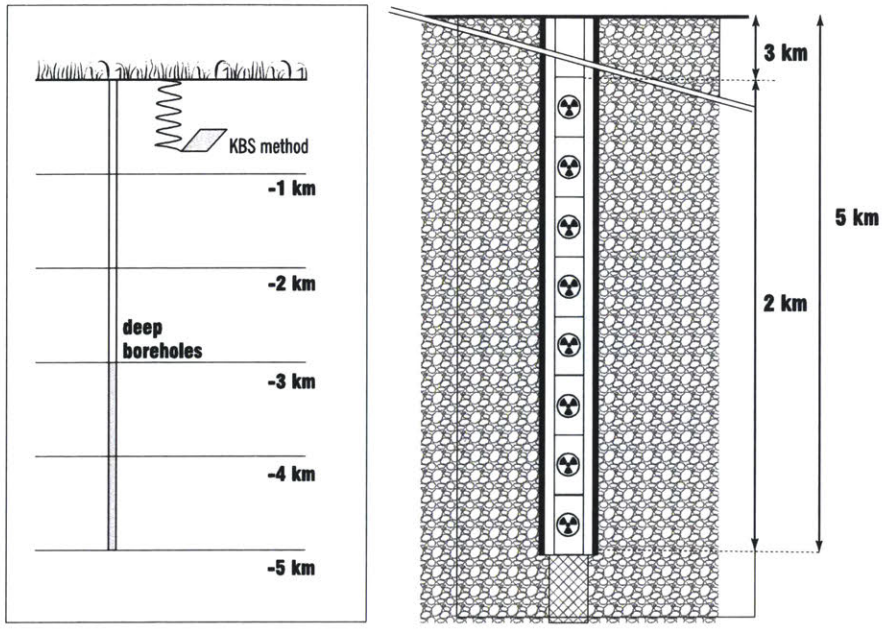

Figure 5-1: Deep borehole concept comparison with mined repositories. KBS method from SKB in Sweden is shown for comparison.

2.10GHz processor.

The number of nodes used in each simulation varied depending on the memory required by the solver and the number of degrees of freedom in each simulation.

5.2.2 Post processing

Post-processing the files generated by MOOSE required a high RAM computer (128GB). Post-processing tasks included, among others: C++ code execution, generation of text files containing data saved in the binary files of MOOSE, and ParaView visualizations.

5.3 Conceptual model

5.3.1 Host rock

For the purpose of this research, we assume a hypothetical repository in a continuous medium of granite with uniform and constant properties. A definitive location for a TWR repository site has not yet been defined. The performance of a deep geological disposal method depends on rock properties, which exhibit large variations in the field. Particular rock and site characteristics may be more or less favorable for waste repository performance. High rock permeability allows significant fluid convection within the rock, whereas low permeability produces a high transient pore pressure maxima, which can result in rock failure if the increase of pressure is large enough.

In this study, which is not site specific, rock permeability is assumed to be isotropic, and the water table is assumed to be at the surface of the rock mass because this represents the most conservative case for radionuclide migration to the surface. Reference host rock properties used in this work are presented in Table 5.1. Typical granite intrinsic permeability varies within the range 10^{-17} to $10^{-14}\,\mathrm{m}^2$ (Manning & Ingebritsen, 1999). In this work $10^{-16}\,\mathrm{m}^2$ is assumed as a reference permeability for granite, and 1 % for rock porosity (unless stated otherwise).

In addition, the geothermal heat flux is a critical thermal boundary condition that influences the flow in the rock. Regions exposed to large geothermal flux from the Earth's crust are likely to enhance fluid convection in the repository and therefore are not suitable to host nuclear waste. A geothermal heat flux from the Earth's crust of 45 $\mathrm{mW/m}^2$ is imposed at the bottom boundary of the modeled rock, as a reference geothermal flux for the East region of the US, see Figure 2-13.

The thermal conductivity of the rock is a critical parameter that affects how heat is being transferred through the rock mass. Rock thermal conductivity has to be high enough to avoid reaching melting conditions in the rock, fuel assembly and canister. Similarly, it must be high enough to avoid reaching super-critical conditions in the fluid in the pores of the rock. The thermal conductivity of granite depends on porosity and water content. An experimental study (Cho, Kwon, & Choi, 2009) analyzed

the variations of thermal conductivity of granite samples due to different porosities, under dry and water-saturated conditions. This study determined that for dry granite samples, thermal conductivities range from 2.12 W/m°K for rocks with high porosity to 3.12 W/m°K for ones with low porosity. In addition, they found that water-sorbed samples have greater thermal conductivities than dry samples of the same granite. Under saturated conditions, the study found that the thermal conductivities ' range from 2.99 W/m°K for granites with high porosity to 3.62 W/m°K for ones with low porosity. In this study, we assume a thermal conductivity of 3 W/m°K, considering the low porosity of 1%. For the considered heat flux value, this thermal conductivity produces a constant gradient of 15 °C/km in the rock.

Table 5.1: Reference site properties, used in the simulations unless stated otherwise.

Parameter	**Value**
Rock density	2750 kg/m^3
Thermal conductivity of rock	3 W/(m°K)
Specific heat of rock	790 J/(kg°K)
Geothermal flux	45 mW/m^2
Surface temperature	10 °C
Porosity	0.01
Rock permeability	1×10^{-16} m^2
Thermal diffusivity	1.38×10^{-6} m^2/s

5.3.2 Borehole and nuclear waste

Modeling a nuclear waste repository with dimensions of several kilometers at a resolution of a spent fuel pin diameter (of the order of mm, see Figure 1-11) for one million years is unfeasible due to the computation cost. The waste filled borehole material is modeled as a time-dependent volumetric heat source, consistent with the heat production of TWR spent fuel assemblies that have been cooled for 25 years, and subsequently stacked one on top of the other 2000 m deep, between 3000 m and 5000 m below the repository surface. The heat generation is distributed uniformly in a volume representing a canister of 34 cm diameter, assumed equal to the diameter of the borehole. We did not consider any gap filler material in this study since we are

interested in analyzing the repository behaviour at a relatively large scale, not near field.

Nuclear waste package properties are therefore homogenized across the canister volume. This implies that the borehole is represented in the numerical model as a uniform block of constant and uniform physical properties: specific heat, thermal conductivity, density, porosity and permeability. The numerical model assumes that the canisters are permeable, with permeability one order higher than the host rock reference value. Table 5.2 presents repository and canister properties used in this work, in agreement with values used in previous studies, performed by SANDIA National Laboratory (B. Arnold & Hagdu, 2013) and MIT (Lubchenko et al., 2015).

5.3.2.1 Heat source

A TWR spent fuel assembly has a total height of 5.577 m. Nuclear fuel is placed only within a 2.5 m length of the rods, as detailed in Section 1.3.4. The decay heat function of the fuel length of 2.5 m of the TerraPower TWR, expressed in W/m, corresponds to (Hejzlar, 2016):

$$\overline{q'(t)} = 458\left(\frac{10}{t_c + t}\right)^{0.575} \tag{5.1}$$

where
the overline indicates that it is the averaged value in the fuel length
the prime indicates that it is the heat generation per unit length
t_c represents the post irradiation cooling time of the spent fuel
t is the time elapsed since entombment in years.

From Equation 5.1, which holds in the central 2.5 m part of the total height of the rods, we then computed the heat generation per assembly. Converting the heat generation per assembly into unit volume of waste package (of 17 cm of radius which corresponds to the borehole radius) we obtain the volumetric heat source, $q'''(t)$, expressed in W/m^3:

$$q'''(t) = 2101.9\left(\frac{10}{t_c + t}\right)^{0.575} \tag{5.2}$$

where

t_c is the cooling time in years

t is the time elapsed since entombment in years.

Considering a cooling time of 25 years, Equation 5.2 can be expressed as (see Appendix B for derivation):

$$q'''(t) = 1241.06\left(\frac{788400000}{788400000 + t}\right)^{0.575} \tag{5.3}$$

where

t is the time elapsed since entombment in seconds.

The simulations start time, $t = 0$, coincides with the time at which the spent fuel is placed in the boreholes, after it has been cooled for t_c years.

5.3.2.2 Near Field representation

A three dimensional near field thermal analysis, performed with ABAQUS, has shown that with an adequate selection of the assembly void filler material inside the metallic canister, such as high-conductivity aluminum zinc alloy (commercially known as Zamak-3), axial heat conduction is strong enough to produce an almost uniform axial temperature profile reaching the host rock (Rodríguez-Buño, Driscoll, Baglietto, & Park, 2016). This thesis examines the far field host rock response, and therefore does not aim to predict temperatures inside or immediately near the borehole. This allowed us to use the TWR spent fuel heat decay averaged over the entire length of the assembly for the far field host rock modeling.

Table 5.2: Reference repository and canister properties, used in the simulations unless stated otherwise.

Parameter	Value
Space between boreholes	200 m
Borehole diameter	0.34 m
Emplacement region depth	3 to 5 km
Fuel burn-up	180 MWd/kg
Interim storage time before emplacement	25 years
Average canister thermal conductivity	0.628 W/(m°K)
Average canister specific heat	499 J/(kg°K)
Porosity of the rock and the canister	0.01
Canister permeability	10^{-15} m^2
Average canister density	4405 kg/m^3

5.3.3 Repository geometry

Analyzing an entire repository comprising hundreds of boreholes has an extremely high computational cost. For this reason, two simplified conceptual geometries were analyzed: infinite and semi-infinite. The first simplification assumes a square grid of boreholes, repeated infinitely in both directions. See Figure 5-2. Under this assumption, the symmetries of this problem reduce the model domain to only one quarter of a borehole, producing the least computational cost. For reasons that will be discussed in Section 5.5, this model imposes unrealistic conditions on fluid flow and is therefore inadequate for performance assessment. The second simplification is a semi-infinite array of boreholes within the natural host rock, still arranged on a square grid but with boreholes extending infinitely in one direction and finitely in the perpendicular direction. Unlike the first model, this one includes the surrounding host rock. See Figure 5-3. This configuration can model realistic flow patterns, such as convective cells, and therefore provides a meaningful evaluation of a nuclear waste repository.

5.4 Infinite array of boreholes

This model represents the limit case of a repository that comprises an extremely large number of boreholes. The reference parameters presented in Tables 5.1 and 5.2 are

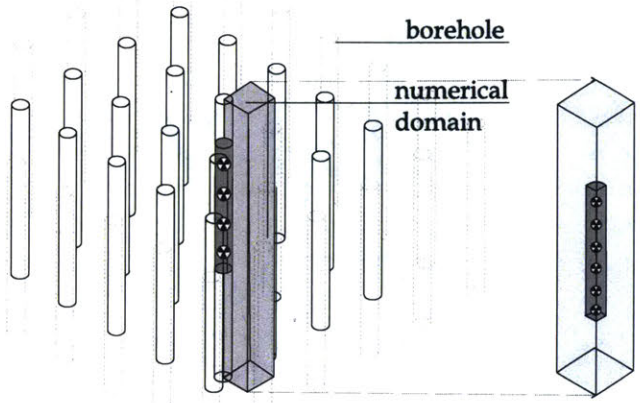

Figure 5-2: At the left: 3D schematic of the infinite array geometry. At the right: 3D schematic of the numerical domain.

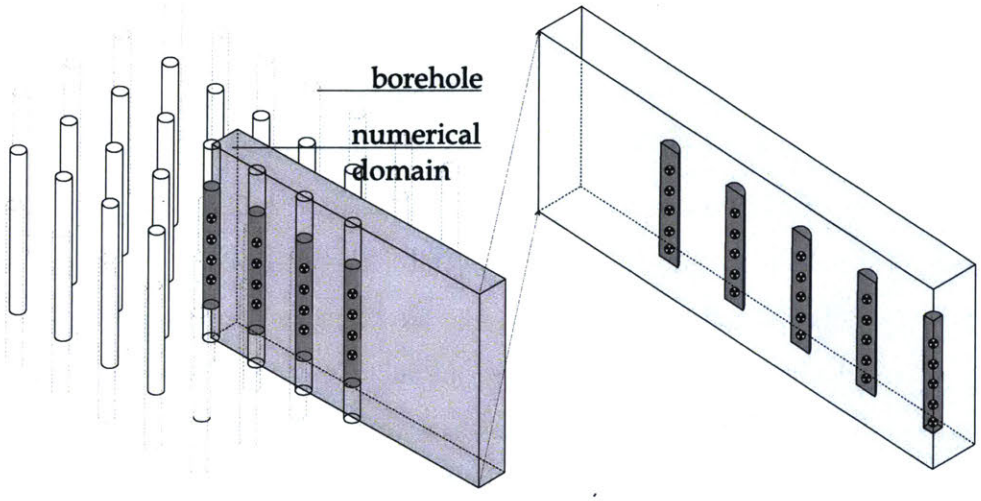

Figure 5-3: At the left: 3D schematic of the semi-infinite array geometry. At the right: 3D schematic of the numerical domain. For simplicity the figure shows only 4 boreholes. The numerical model consists of 10 half boreholes and one quarter borehole, which with the symmetry boundaries represent 21 boreholes in the physical model.

used for the analysis.

5.4.1 Spatial discretization

The finite element mesh was generated using the CUBIT 15.1 software. For this case, the 3D reference domains considered have dimensions 100m x 100m x 10km. See Figure 5-4. The mesh consists of quadrilaterally-faced hexahedral elements. For numerical stability, as well as to produce reasonably accurate temperatures and capture the thermally driven flow near the borehole, the mesh is refined at the extremes of the heat source volume in the horizontal and vertical direction (at 3 km and 5 km depth), which is where temperature gradients are highest (shown in Figure 5-4). The mesh was defined such that the separation between horizontal faces of elements didn't surpass 100 m. The bottom boundary of the model domain is defined 10 km below the model surface, considered deep enough so as not to affect the solution. The vertical boundaries of the model domain are defined by the symmetry planes of the array. The results presented in this section were obtained for a mesh with 25,886 elements and 60,378 degrees of freedom (for pressure and temperature). This model consists of three material blocks: the rock, the waste and the seal (the cylindrical volume above the waste). In this model the seal has permeability one order higher than the host rock, and the same value of porosity.

5.4.2 Boundary conditions

The boundary conditions used in the model have constant values over the entire simulation time. Earth's conditions for a one-million-year timespan have significant uncertainties. For this reason we opted for constant boundary conditions. The ones used in the model, shown in Figure 5-5, are:

1. Top boundary:
    - Temperature = 10°C
    - Pore pressure = 101,325 Pa (1atm)

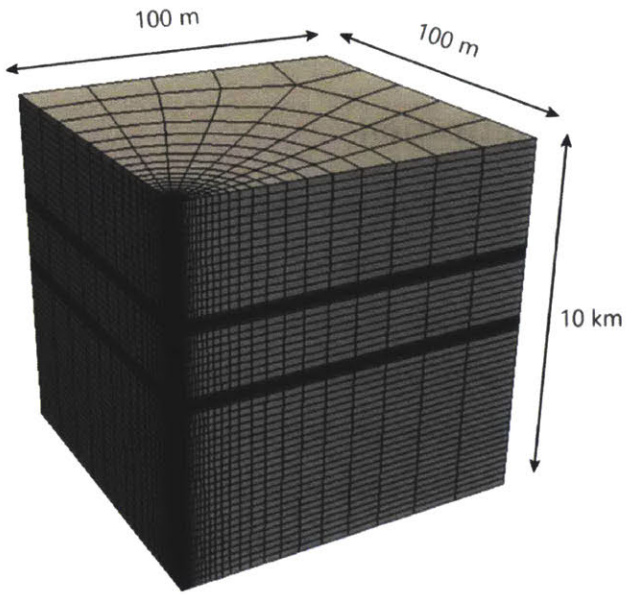

Figure 5-4: Isometric view of the mesh of the infinite array. Image not to scale, horizontal axis was stretched by a factor of 100 for visualization.

2. Bottom boundary:

   - Inward heat flux = $0.045\,\mathrm{W/m^2}$
   - No mass flux

3. Lateral vertical boundaries:

   - Symmetry boundaries

     This imposes "no mass flux" and "no heat flux" boundaries on the vertical faces of the numerical domain.

5.4.3 Initial conditions

As explained in Section 4.2.2, there is no analytical expression for the pore pressure for this problem due to the highly non-linear dependence of fluid density on pressure and temperature for the range of this problem (high pressures and high temperatures). Therefore, the only way to determine the initial conditions for pressure in the repository is with numerical methods. As such, the general scheme is to perform two

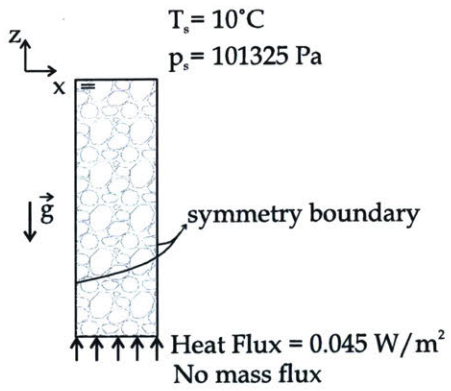

Figure 5-5: Schematic of boundary conditions.

subsequent simulations: the first to find steady state and thus determine the initial values to use in the second simulation, which will represent the actual repository after waste emplacement.

We used the FALCON steady solver to determine initial pore pressure and temperature, resulting only from the natural geothermal flux. Boundary conditions for the determination of the initial pressure and temperature field are defined in Section 5.4.2. IAPWS-97 water properties are used in all the simulations carried out. Results are shown in Figure 5-6. Temperature increases linearly with depth, reaching 160 °C at 10 km depth. See Figure 5-6a. Pressure increases with depth reaching 96 MPa at 10 km depth. See Figure 5-6b. Temperature and pressure have competing effects on fluid density. Water density increases with pressure while it decreases with temperature. Temperature and pressure produce the net effect shown in Figure 5-6c. It is interesting to note that for the studied case, the largest density is found at around 1 km depth.

To verify numerical convergence of the solver it was checked that the Darcy velocities computed from the resolved final pressure distribution are negligible (always smaller than Machine Epsilon, $\epsilon_{Mach} \approx 1.11^{-16}$ for binary64 floating point format), which means the code has converged to steady state. The steady state results correspond to hydrostatic equilibrium, therefore the values of pressure do not depend on rock permeability nor porosity because it is assumed that all the pores are in-

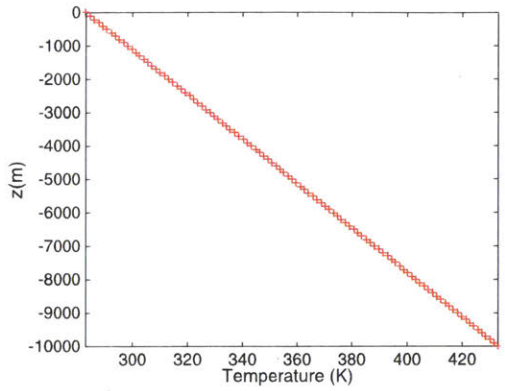

(a) Temperature as function of depth.

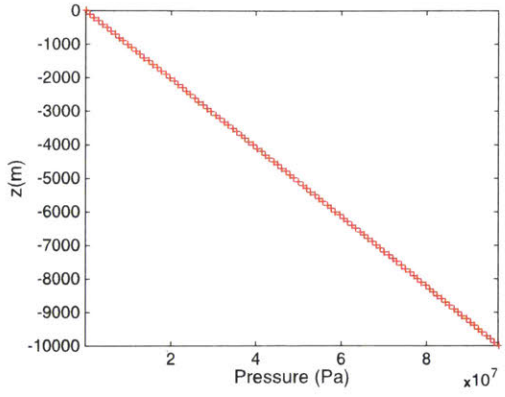

(b) Pore pressure as function of depth.

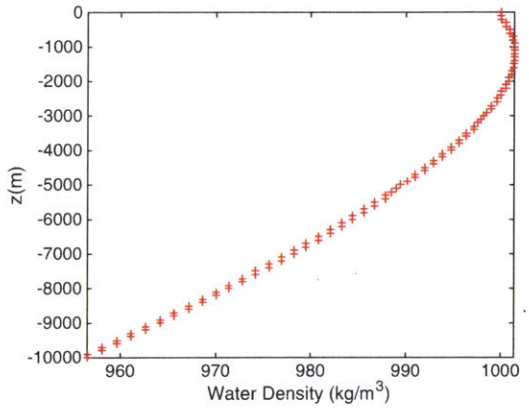

(c) Fluid density as function of depth.

Figure 5-6: Initial conditions.

terconnected. In contrast, thermal conductivity of the porous medium affects the initial state, determining the rock temperature and therefore fluid density and pore pressure, ultimately.

5.4.4 Transient simulation

5.4.4.1 Temperature field

We solved the evolution of temperature in the domain due to the decay heat of the TWR spent fuel for the 1 million year simulation time. Model parameters of the

repository used in the simulation are shown in Tables 5.1 and 5.2.

The temperature increase with respect to the initial temperature at each point in the domain at different times after fuel emplacement are shown in Figure 5-7. In this way, we study the changes due to the decay heat. Initial temperature in the rock varies with the depth considered, which is determined by the geothermal heat flux, as explained before.

The numerical domain has dimensions 100m by 100m by 10km. It is important to note that for the following visualizations, the horizontal dimension has been stretched by a factor of 100. See Figure 5-7a and 5-7b. The plots show how the heat front propagates from the borehole. Due to large aspect ratio of the domain, which is 0.01 (10 km depth and 100 m width), and the large length of the waste emplacement (2 km), initially heat appears only to diffuse horizontally. Only upon the heat wave reaching the symmetry boundary does the vertical diffusion of heat become apparent in the visualization, producing horizontal isothermal planes, as in Figures 5-7c, 5-7d and 5-7e.

Eventually, the temperature in the rock decreases. This is explained by the reduction of the heat at the source. The heat source is a monotonic function of time because of the decay of radionuclides with relatively short half-lives. Later in time, other radionuclides decay, contributing to the overall behaviour of the spent fuel. In addition to this, at a certain time (beyond 320,000 years), heat is transferred to the atmosphere through the surface of the repository, which contributes to the cooling of the rock. The simulations show a long-term thermal effect for the time span of one million years, as shown in Figure 5-7f.

The bottom boundary was considered a no mass and constant heat flux boundary. At a certain time, around 130,000 years, the heat front reaches the bottom boundary. In reality, the heat front would simply continue, but in this model it reflects because of the boundary condition. After this time, computed temperatures therefore provide an upper limit of the temperatures in the rock, and the simulation represents a conservative calculation of rock temperature. The accepted way to represent mass flux and heat flux at such boundary in a numerical model is by using infinite elements.

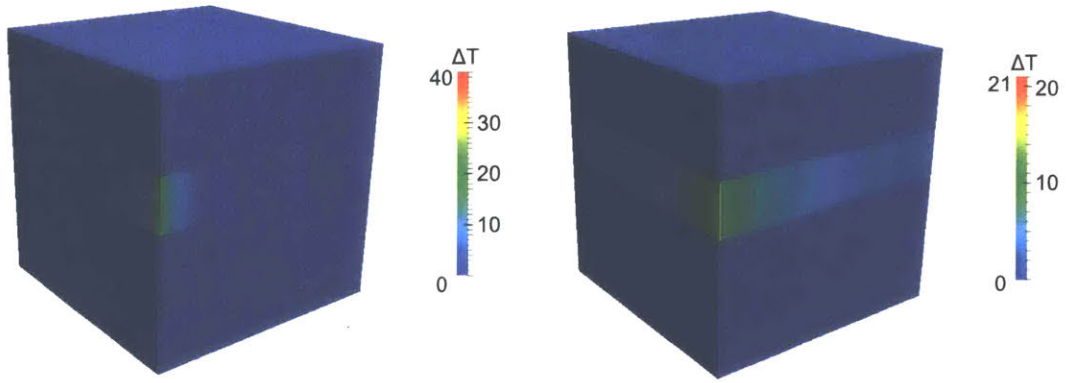

(a) 5 years

(b) 100 years

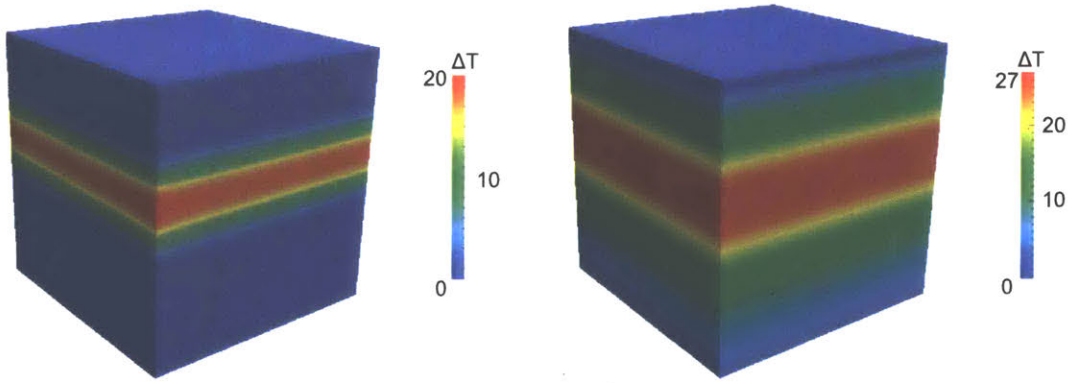

(c) 5,000 years

(d) 104,800 years

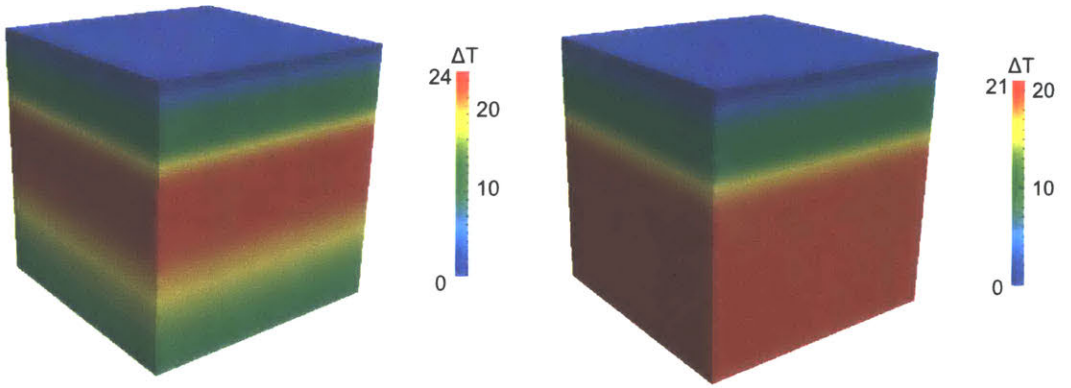

(e) 312,647 years

(f) 951,294 years

Figure 5-7: Temperature increase ΔT(°C) due to decay heat for different times.

Infinite elements are used in boundary value problems defined in unbounded continua. However, to date, MOOSE cannot handle infinite elements. For this reason, it was considered a constant heat flux boundary knowing that for times larger than 150,000 years, the simulation provides a conservative calculation.

Figure 5-8 presents the temperature as a function of time at different radial distances from the borehole axis at a fixed depth of 4 km below the repository surface (corresponding to the middle plane of the waste emplacement zone). Temperature as a function of time in the rock is not monotonic. It increases with time, reaching a first local maximum and then decreasing. Later in time a second maximum of temperature can be seen for the problem analyzed. The magnitude of the first local maximum diminishes strongly with the radial distance from the borehole axis, while the magnitude of second maximum does not change. The first maximum depends on the magnitude of the heat source, the specific heat of the waste package and the rock between the source and location studied, and the thermal conductivity of the waste package and the rock between the source and the location studied. The absolute maximum temperature is reached in the center of the waste package, as expected. This maximum is 109°C, and it is reached at 4 years after waste emplacement. This value is below the melting point of the canister material and assembly, and hence considered safe. The maximum temperature at the canister surface is 96.1°C and it is reached at 5.96 years after waste emplacement. The temperature of the rock, measured at 10 meters from the borehole axis reaches a first local maximum at 33 years of waste emplacement. After this local maximum, temperature decreases slightly because of the reduction of the magnitude of the heat source. Later in time, rock temperature increases again due to interference of heat fronts from adjacent boreholes (which in the model domain is represented by the heat wave reaching and being reflected by the symmetry boundaries).

Figure 5-9 presents a comparison of rock temperature at the middle of emplacement depth (at 4 km below the repository surface and 10 meters from the borehole axis) for PWR and TWR spent fuel disposal, for the same infinite repository. For TWR spent fuel results, the second peak, about 100°C, is significantly higher than the

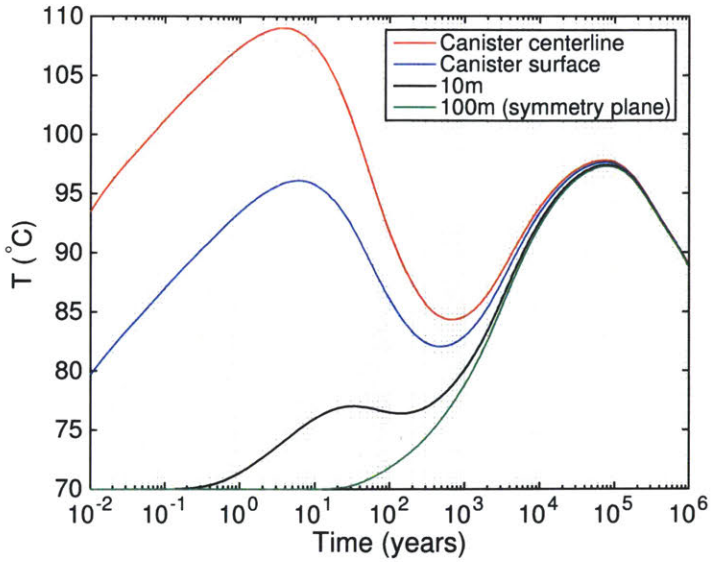

Figure 5-8: Temperature as a function of time for different radial distances from borehole axis at 4 km depth below repository surface.

first local maximum, around 75°C, and higher than the maximum of 90°C produced for PWR spent fuel. Rock temperatures for TWR spent fuel are smaller than PWR spent fuel for the first 3,500 years. Afterwards, the TWR rock temperature surpasses the PWR value due to a gentler decline of heat from radioactive decay in TWR spent fuel compared to PWR spent fuel.

5.4.4.2 Thermally driven fluid flow

The heat released by the nuclear waste increases fluid temperature, causing the fluid to expand, which in turn increases the pore pressure near the borehole. Because of this high pressure in the porous medium, the fluid is driven away.

Figure 5-10 presents the Darcy velocity as a function of time for different locations in the rock. Velocity in the cap-rock is always positive (see lines corresponding to 1 and 2 km depth). The maximum velocity in the waste, which corresponds to the centerline, is reached at 5 years. At the same time, velocity is directed downward at the symmetry plane (100 m from the borehole), which corresponds to the discontinuous line in the logarithmic scale for velocities. This indicates the existence of some initial convection in the waste emplacement zone. Maximum velocity in the cap-rock

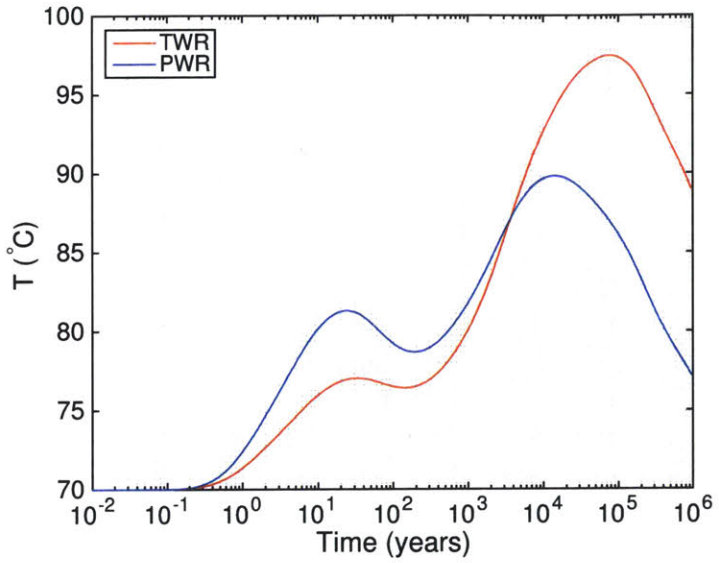

Figure 5-9: Temperature as function of time at 4 km depth (mid depth of nuclear waste emplacement) at 10 m from borehole axis, and a comparison of TWR and PWR results.

is reached at a later time (about 100 years) due to the time required for propagation of the pressure wave through the rock. Afterward, Darcy velocity decreases in all regions in the same way, with the slope given by the decay heat function. This shows a clear fluid expansion regime.

Figure 5-11 presents a vertical view of the temperature increase in the domain and the streamlines at 390,000 years after waste emplacement (only the part of the streamlines above 4 km depth are plotted). Streamlines are vertical, in agreement with the uniform temperature distribution in horizontal planes.

Figure 5-12 displays the vertical Darcy velocity as a function of time, at 2 km depth (1 km above the waste) and 10 m from borehole axis. Results are presented for different rock permeabilities: 10^{-14}, 10^{-16}, 10^{-17} and 10^{-18}m^2. Darcy velocities follow the same behavior after 400 years for the permeabilities 10^{-16} and 10^{-17}m^2 (curves overlapping). For rock permeability of 10^{-18} m^2 this matching occurs at a later time, and for 10^{-14} m^2 at a significantly earlier time. It is interesting to note that the numerical Darcy velocity curves have a slope in the log-log scale graph that matches the exponent of the heat generation function, see Figure 1-18. This shows

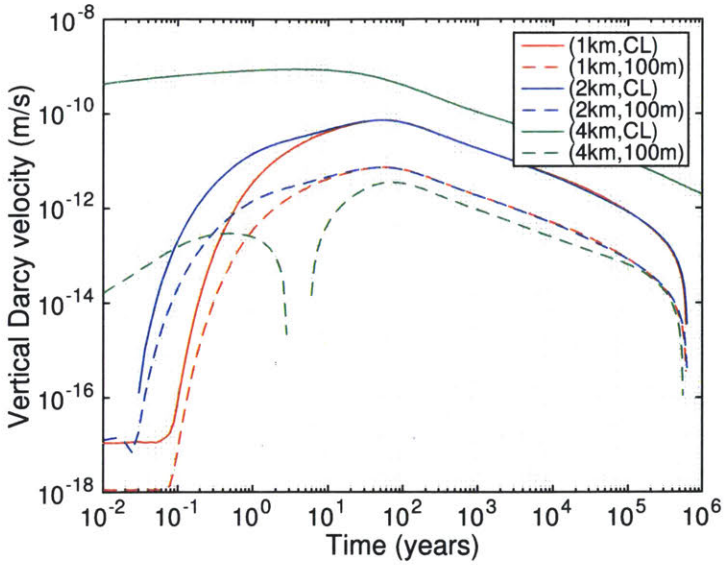

Figure 5-10: Vertical Darcy velocity as a function of time at the borehole centerline and at the symmetry plane, at 1, 2, and 4 km depth.

that the fluid flow corresponds to a pure water expansion regime driven by the heat source. The analytical relation for expansion flow, Equation 4.12, is also included in the plot. This analytical expression for Darcy velocity corresponds to flow due purely to thermal expansion of the fluid in the pores. As seen in Figure 5-12, there is excellent agreement between the numerical Darcy velocities and the analytical relation.

Figure 5-12 also shows that the numerically computed Darcy velocity is smaller than the analytical expression for the first 400 years (on average). The exact time for when both values match depends on the rock permeability. This time period corresponds to the propagation time of the pressure wave from the heat source to the location studied, in this case 2 km below the repository surface. This response time depends inversely on permeability since pressure diffusivity increases with permeability, see Equation 3.7. The analytical model does not consider this phenomenon, and it assumes pressure is transmitted instantly from the heat source to the rock above the waste. Therefore, the analytically derived expression for Darcy velocity in the cap-rock provides an upper limit for comparison with the numerical solution at early times.

In addition, Figure 5-12 shows that the numerically computed vertical Darcy

velocities become negative at around 600,000 years after waste emplacement. In the numerical domain, once the heat wave reaches the upper boundary, heat is lost through flux at this surface. This effect causes the average temperature of the domain to decrease, and the water flow direction to reverse. This process was not considered in the analytical model, therefore from this time, the analytical expression is no longer valid, but still provides an upper limit for the numerical results. We conclude that the flow regime in the cap-rock in this infinite array corresponds to a pure water expansion regime proportional to the heat source.

Regarding the effect of the fluid flow on the heat transport in the repository, it is necessary to introduce the Péclet number, Pe. This dimensionless number quantifies the ratio of advective transport of heat to heat diffusion, and it is defined by:

$$\mathrm{Pe} = \frac{\rho_f c_f |\vec{v}| \nabla T}{k_{eff} \Delta T} \approx \frac{\rho_f c_f |\vec{v}| L}{k_{eff}} \tag{5.4}$$

where

c_f is the specific heat of the fluid at constant pressure

$|\vec{v}|$ is the magnitude of the fluid velocity

L is the characteristic length scale

k_{eff} is an effective thermal conductivity (average value for the porous medium composed of fluid in the pores and rock skeleton).

The Péclet number in the model can be estimated to be of the order of 10^{-2}, significantly smaller than unity. This indicates that advective heat transport in the thermal-hydrologic model is negligible for the configuration considered. Heat transfer is conduction dominated.

5.4.4.3 3D trajectories and breakthrough time

We developed a C++ code to track particles through time in the simulations, for all the configurations considered (presented in Appendix A). To date, MOOSE does not have particle trackers. Our code reads the Exodus file where the simulation results are saved as a binary file. Once the initial position of the particle to follow is defined the

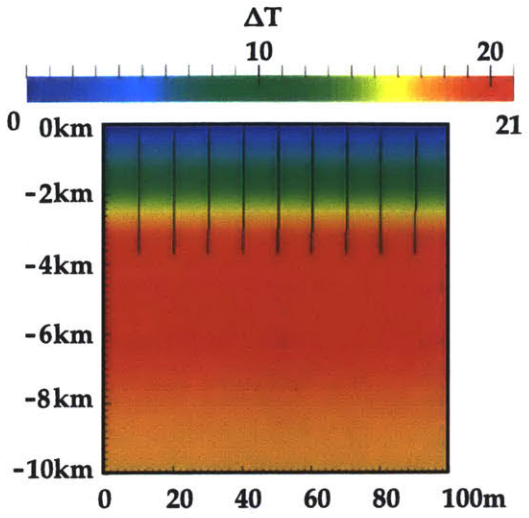

Figure 5-11: Temperature increase $\Delta T(°C)$ due to decay heat and streamlines starting at a depth of 4000 m, at 390,000 years. The Horizontal axis was stretched by a factor of 100 for visualization.

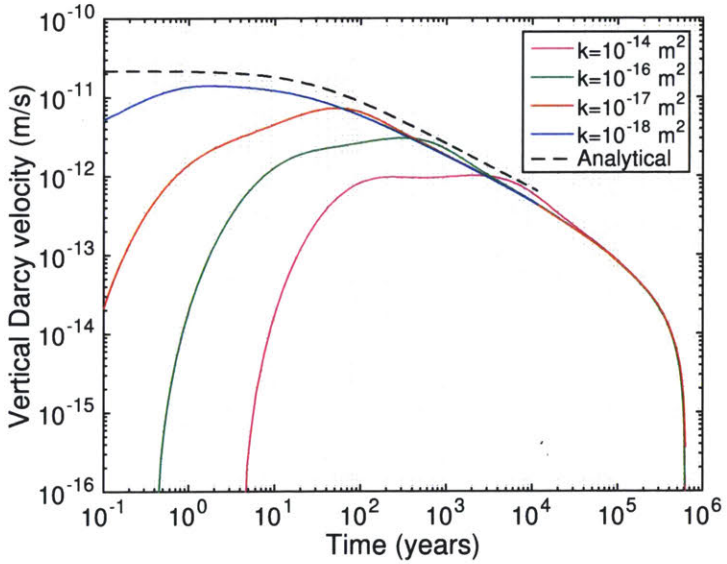

Figure 5-12: Vertical Darcy velocity at 2 km depth and 10 m from the borehole axis for different rock permeabilities.

trajectory of the particle is computed numerically by integration in time of Equation 5.5. Four different interpolation methods for velocity (related to Darcy velocity by Equation 3.2) throughout the trajectory were implemented in the code to compare the results. We created a Python script that interpolates all the element properties to properties on the nodes of the mesh, using the interpolation method implemented in ParaView in the CellDataPointData filter for each time step in the simulation. Then our C++ code performs all the calculations. The velocity interpolation methods used are called:

1. None

   It considers the closest node velocity and considers constant velocity of the particle during each time step dt. See Figure 5-13.

2. Velocity in time

   It considers the closest node velocity and it averages it at two consecutive time steps $(t, t + dt)$. See Figure 5-14.

3. Predictor-corrector

   It considers the average velocity of two nodes: initial closest node, and then the predicted closest node at one time step later, assuming the particle moves with the former velocity first. See Figure 5-15.

4. By elements

   It considers the particle has the velocity of elements in the mesh in which is located. See Figure 5-16.

For performance assessment of the repository it is critical to evaluate if the resulting fluid flow allows the transport of the radioactive material to the human environment. The velocity fields determine the mechanisms of radionuclide migration to the repository surface. The fluid particle trajectories were computed numerically from the numerical velocity field, by:

$$\frac{d\vec{x}}{dt} = \vec{v_f}(\vec{x}, t) \tag{5.5}$$

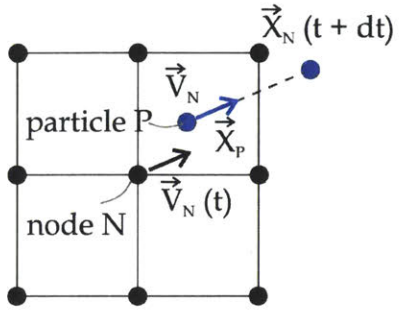

Figure 5-13: Interpolation method 1, called None.

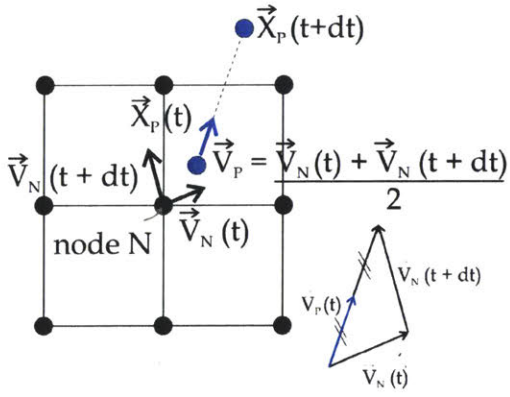

Figure 5-14: Interpolation method 2, called Velocity in time.

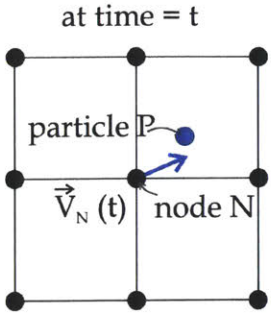

(a) At time t the particles takes the velocity of the closest node.

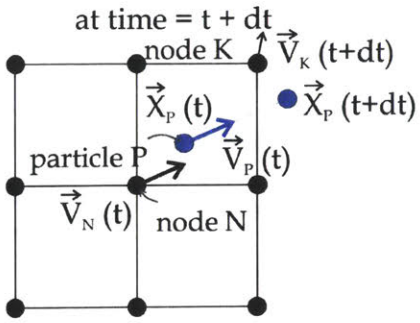

(b) The particle finds its position at time $t+dt$ with the velocity read in a), and reads the velocity of the new closest node.

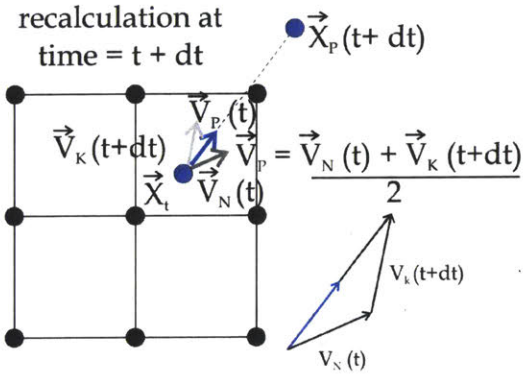

(c) Using the velocity found in b), the code averages it with the velocity found in a) and computes the new particle position at time $t+dt$.

Figure 5-15: Interpolation method 3, called Predictor-Corrector.

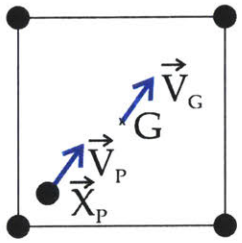

Figure 5-16: Interpolation method 4, called By elements.

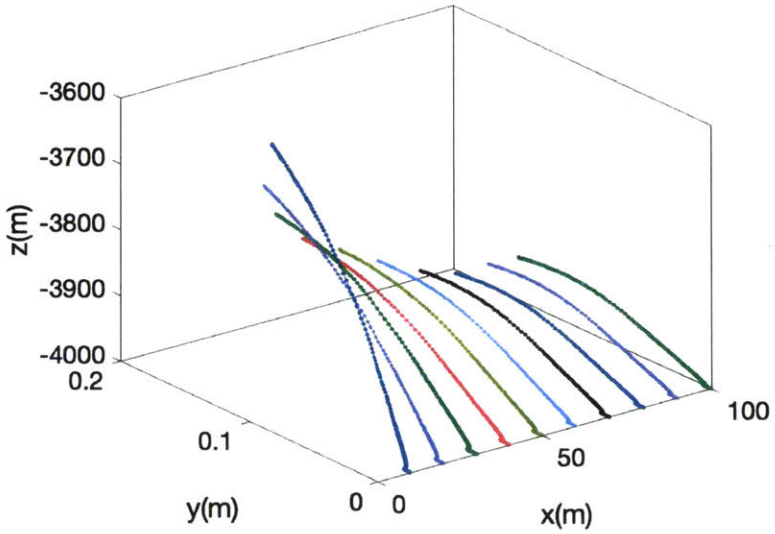

Figure 5-17: Trajectories for particles that start at the mid depth of the boreholes at different distance from central borehole: (10,0,-4000), (20,0,-4000), (30,0,-4000), (40,0,-4000), (50,0,-4000), (60,0,-4000), (70,0,-4000), (80,0,-4000), (90,0,-4000) and (100,0,-4000). Reference parameters are used for this simulation.

where

$\vec{x}$ defines the Eulerian position of the particle

t represents time

$\vec{v_f}$ corresponds to the pore fluid velocity.

Figure 5-17 presents the 3D trajectories of 10 particles whose initial position are aligned at the mid emplacement depth in the rock, with initial coordinates: (10,0,-4000), (20,0,-4000), (30,0,-4000), (40,0,-4000), (50,0,-4000), (60,0,-4000), (70,0,-4000), (80,0,-4000), (90,0,-4000) and (100,0,-4000). For the infinite lattice of boreholes studied, it was observed that fluid particles do not break through at the surface. We can see that particles are displaced mainly in the vertical direction, as the horizontal displacement is extremely small. The maximum upward displacement corresponds to particles closest to the heat source. For the particles studied, the maximum upward displacement is 397 m. This means that at 1 million years the particle remains at 3602 m below the repository surface.

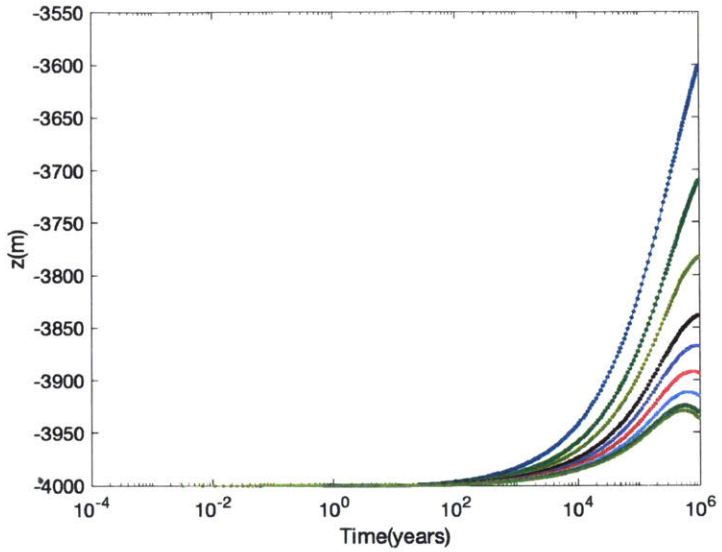

Figure 5-18: Location as function of time for particles that start at the mid depth of boreholes at different distance from borehole: (10,0,-4000), (20,0,-4000), (30,0,-4000), (40,0,-4000), (50,0,-4000), (60,0,-4000), (70,0,-4000), (80,0,-4000), (90,0,-4000) and (100,0,-4000). Reference parameters presented in Tables 5.1 and 5.2 are used for this simulation.

Figure 5-18 presents the location as a function of time for the 10 particles considered. All of them remain below the repository surface at the end of the simulation. The plot shows that the location as a function of time is not monotonic for some particles. Some particles reach a maximum displacement before 1 million years, after which the vertical coordinate decreases (negative sign). The farther away from the heat source, the earlier in time the maximum occurs, which can be explained by a relative cooling of the rock. For particles closer to the heat source the depth is a monotonic function of time. Particle trajectories can be approximated by vertical lines. Figure 5-19 shows trajectories for 27 particles that start at the borehole mid depth at different distances from the borehole.

5.5 Semi-infinite array of boreholes

This model represents a more realistic case of a nuclear waste repository that comprises an infinite number of boreholes in one direction and a finite number in the

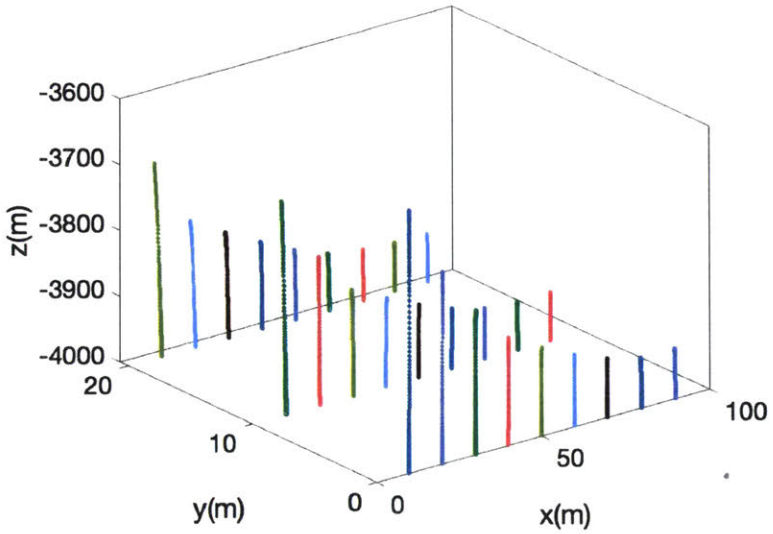

Figure 5-19: Trajectories for 27 particles that start at the borehole mid-depth at different distances from borehole axis.

other direction, thus including the natural host rock of the repository site. The ultimate goal would be to model a repository that has a finite number of boreholes in both directions. However, such a case presents a computational burden. Therefore we use this semi-infinite model as a good and conservative case study. The reference parameters presented in Tables 5.2 and 5.1 are used for the analysis.

For the analysis we considered 21 boreholes in width, in a square lattice with a side length of 200 m that extends infinitely in the orthogonal direction, as shown in Figure 5-3. This model includes the surrounding natural host rock. The model domain has a horizontal extension of 40 km, large enough to minimize the effect of the lateral boundaries on the simulation results in the warmest region of the boreholes. The other dimensions are 100 m in horizontal width and 10 km in depth, as seen in Figures 5-20 and 5-21. Boreholes are identical: all with the same diameter (34 cm), depth (5 km), emplacement length (2 km), and heat load (heat decay in the borehole volume defined by Equation 5.3).

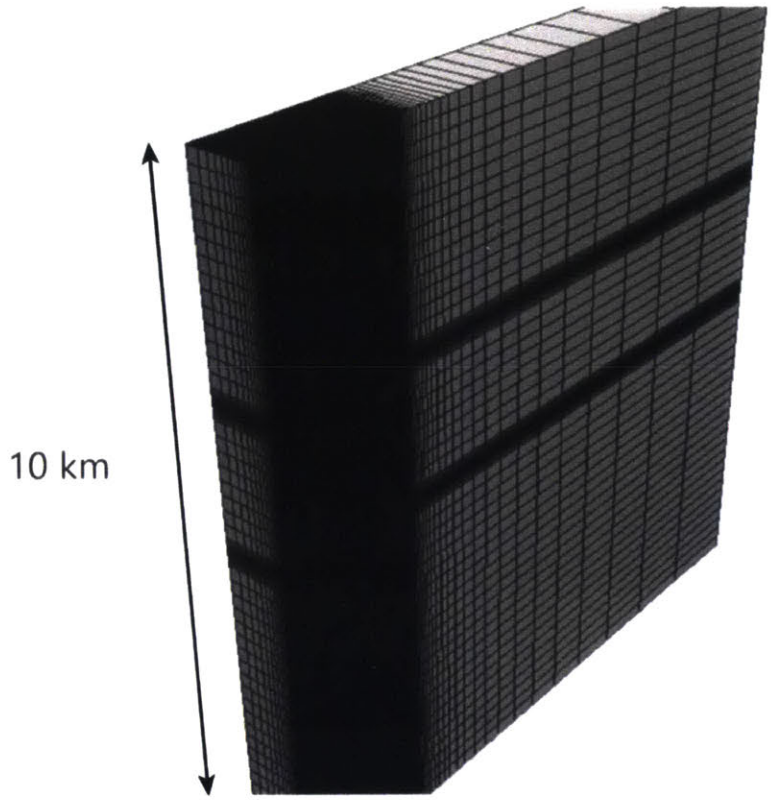

Figure 5-20: Isometric view of the mesh indicating depth of the numerical domain (images to scale).

5.5.1 Spatial discretization

Because of the large number of elements of the numerical domain, this configuration has significantly higher computational cost than the previous one, but provides realistic insight for a performance assessment. The mesh was generated with Cubit 15 and is defined by hexahedral elements. The mesh of the model is refined at the vertical extremes of the nuclear waste and becomes coarser further away from the cluster of boreholes. The results presented in this section were obtained for a mesh with 773,410 elements and 1,682,760 degree of freedom (for pressure and temperature). This model consists of two material blocks: the rock and the waste. This model considers the cylindrical volume above the waste to have the same properties as the host rock.

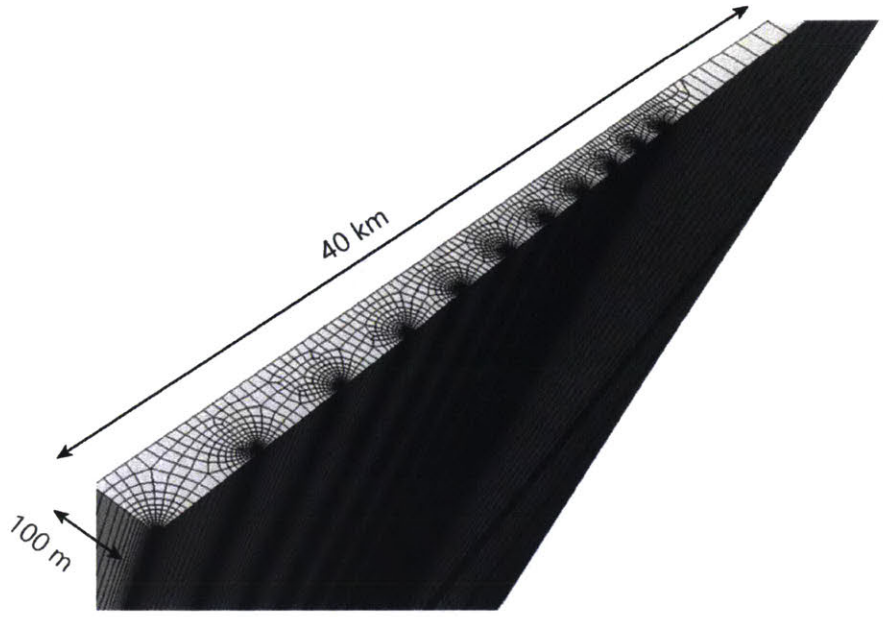

Figure 5-21: Isometric view of the mesh indicating horizontal extent of numerical domain and discretization around boreholes (images to scale).

5.5.2 Boundary conditions

Boundary conditions are the same as the ones defined for the infinity array, described in Section 5.4.2. In this semi-infinite array model the "right "boundary (which corresponds to the boundary of the natural host rock) is defined 40 km apart from the central borehole, far enough so it does not affect the numerical solution.

5.5.3 Initial conditions

The initial pore pressure and temperature resulting from the geothermal flux at the bottom of the domain are found with the FALCON steady solver, as explained in Section 5.4.3. IAPWS-97 water properties are used in all the simulations.

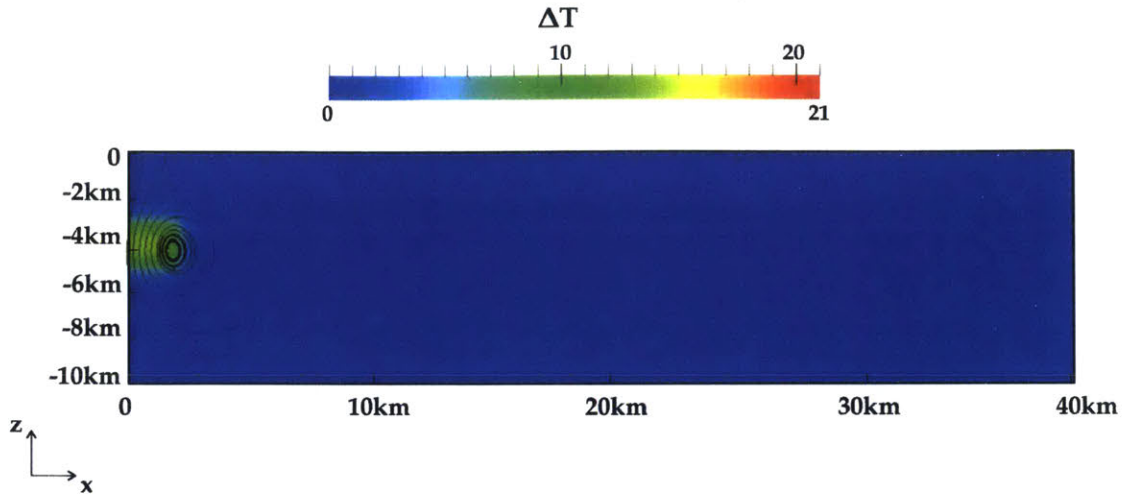

Figure 5-22: Temperature increase $\Delta T(^{\circ}C)$ due to decay heat and streamlines in the semi-infinite array at 2,700 years.

5.5.4 Transient simulation

5.5.4.1 Temperature field

The temperature increase fields at different times after fuel emplacement are presented in Figures 5-22 to 5-25, for the repository reference parameters (Tables 5.1 and 5.2). The simulations show that initially the warmest region of the domain is at the boreholes. As time progresses, the emplacement region (volume of rock that includes the boreholes) reaches an almost uniform temperature, higher than the adjacent natural host rock, see Figure 5-22. Heat diffuses with time from the central heated region to the rest of the domain, radially like a point source behavior (circular isotherms), see Figures 5-23 and 5-24. The zone of highest temperature is at the central borehole. Figure 5-25 shows a long-term thermal effect for the time span of one million years in the volume of rock surrounding the boreholes. The simulation shows the onset of a large-scale convective cell throughout the entire repository at around 1000 years after waste emplacement. This convection cell remains stationary until the end of the simulation.

Figures 5-26 and 5-27 present pressure increases due to the decay heat, with respect to the natural initial pore pressure at each location in the rock at two different

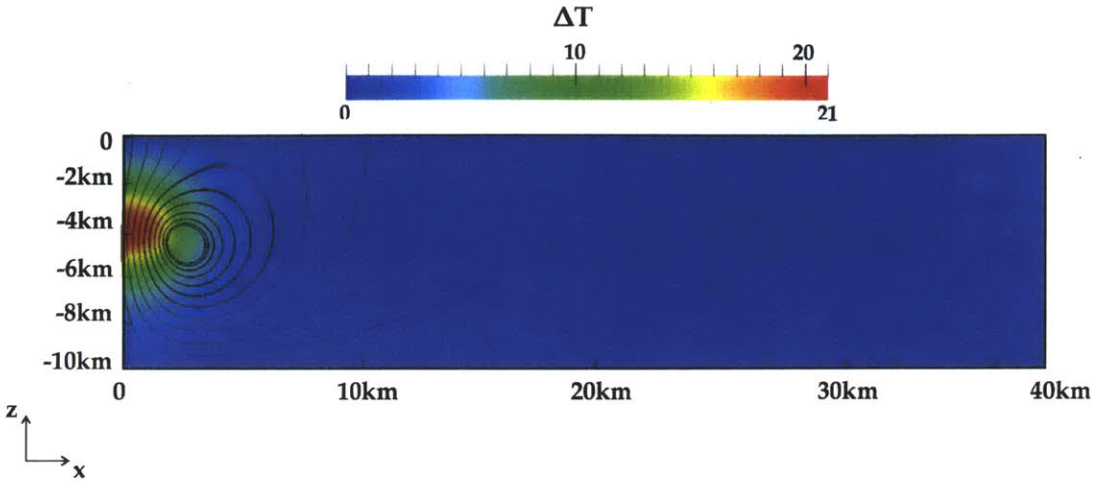

Figure 5-23: Temperature increase $\Delta T(^{\circ}C)$ due to decay and streamlines in the semi-infinite array at 63,000 years.

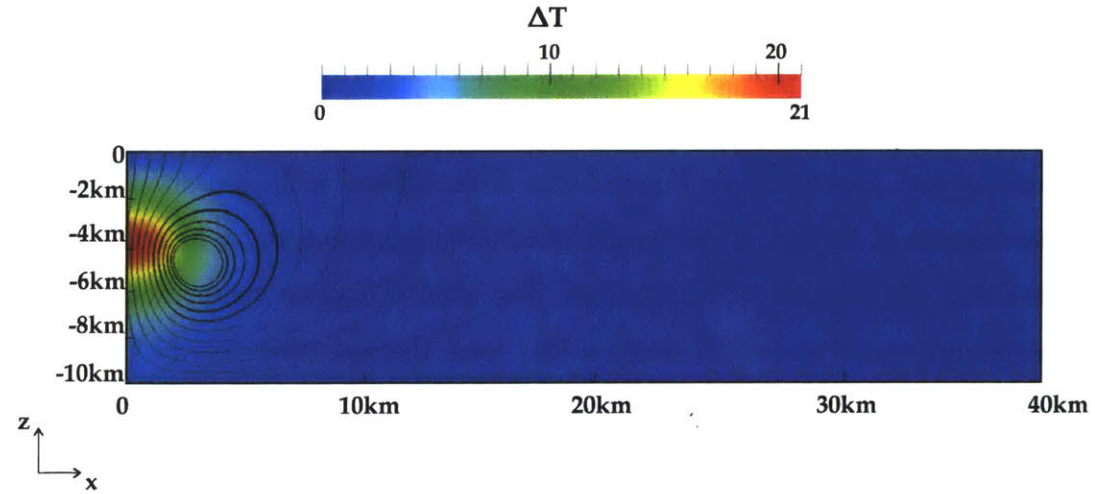

Figure 5-24: Temperature increase $\Delta T(^{\circ}C)$ due to decay heat and streamlines in the semi-infinite array at 87,000 years.

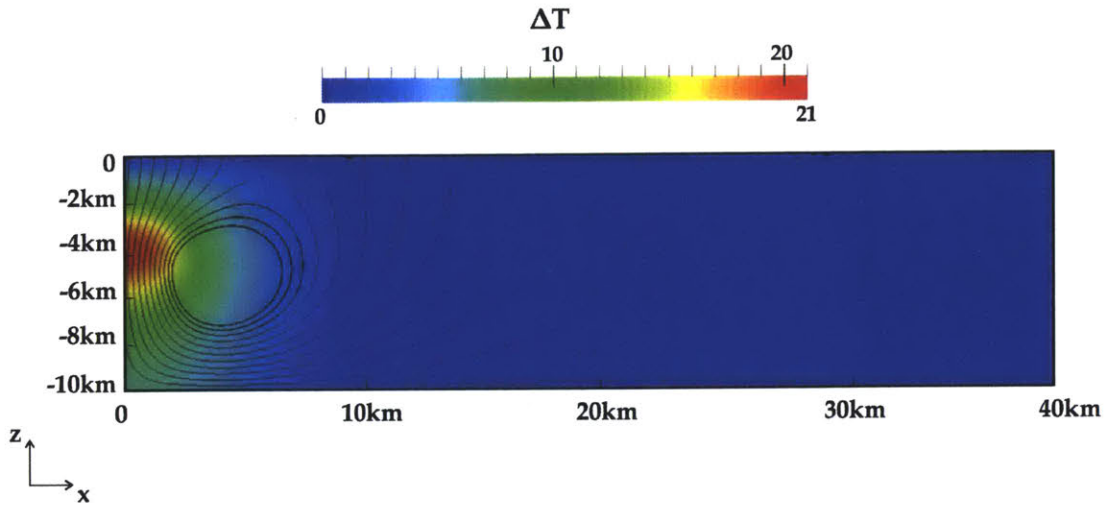

Figure 5-25: Temperature increase ΔT(°C) due to decay heat and streamlines in the semi-infinite array at 222,000 years.

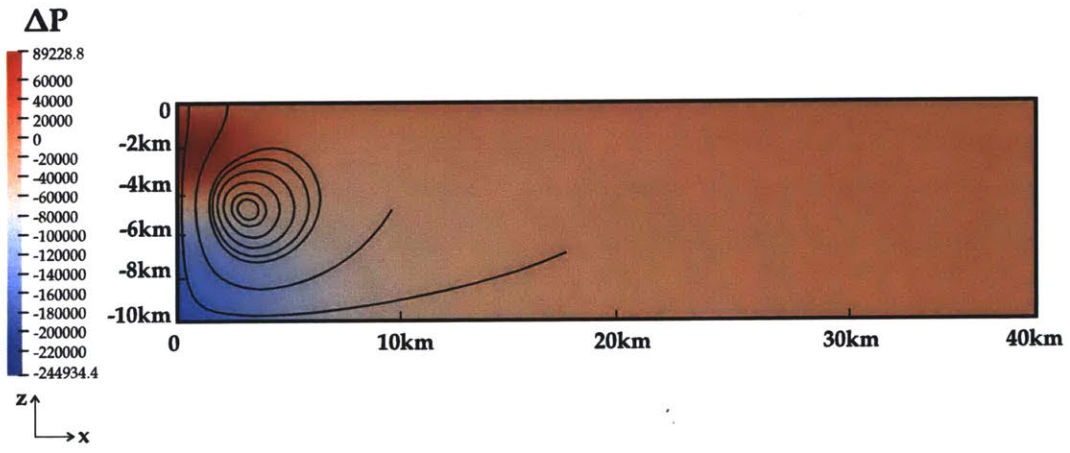

Figure 5-26: Pressure increase Δp(Pa), and streamlines in the semi-infinite array at 182,000 years. At this time the maximum pressure increase in the domain is Δp_{max}=69,316 Pa.

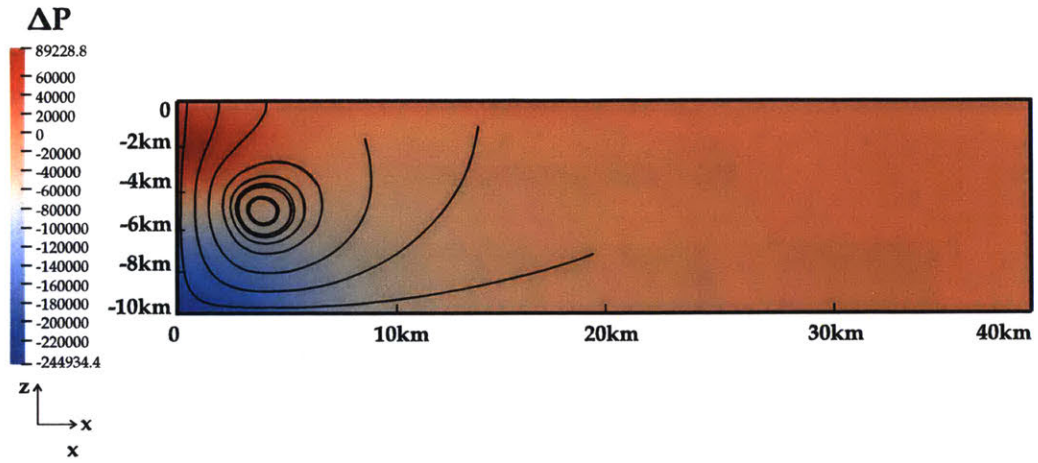

Figure 5-27: Pressure increase Δp(Pa), and streamlines in the semi-infinite array at 472,000 years. At this time the maximum pressure increase in the domain is Δp_{max}=52,354 Pa.

time steps. Simulations show that at early times there is a high pressure zone surrounding the nuclear waste. This is caused by the water expansion of the fluid that is being heated up. Later in time fluid instabilities are triggered by the existence of a colder fluid in the adjacent rock volume. A zone of relative depression with respect to initial values is established at the bottom of the waste. At 182,000 years the maximum pore pressure increase is 69,316 Pa. At 472,000 years this maximum over pressure is 52,354 Pa.

Figure 5-28 presents eight different locations in the rock where temperature and vertical fluid velocity are considered. Figure 5-29 presents a comparison of temperature as a function of time at eight different locations in the rock, considering 2 km and 4 km below the repository surface, and different horizontal distances from central borehole axis: 0, 1000, 2000, 2200 m. The last x coordinate considered (2200 m) corresponds to a location that, in contrast to the other points considered, is not within the nuclear waste emplacement area. Points at greater depth are exposed to higher temperature. For the points located within the emplacement depth (between 3 and 5 km below the surface), there is a first maximum of temperature and a higher absolute maximum later in time as a consequence of all the incident heat waves from the adjacent boreholes, as was also seen for the infinite array configuration. For points

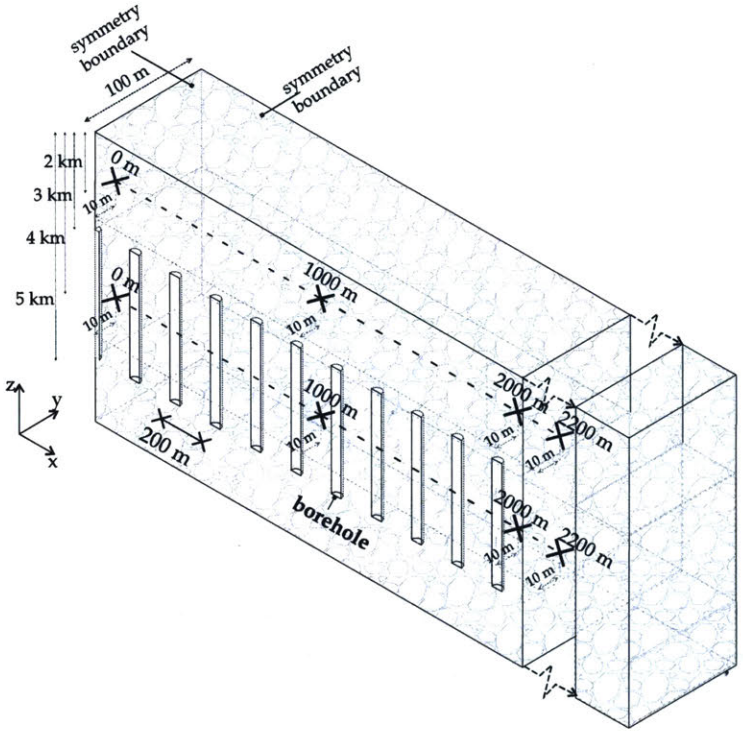

Figure 5-28: 3D schematic of the numerical domain indicating with crosses the locations of the rock referenced in Figures 5-29 and 5-30. Figure not to scale for visualization purposes.

above the waste, there is only one maximum of temperature at a significant later time, which corresponds to the required time for the heat wave to reach the location considered.

5.5.4.2 Thermally driven fluid flow

In all simulations, water never reaches supercritical conditions, which avoids enhanced convection due to high gradients of densities. This will be detailed in the following section.

Figure 5-30 presents the vertical component of Darcy velocity as a function of time at the eight different locations in the rock considered, as shown in Figure 5-28. Selected points include 2 km and 4 km below the repository surface and different

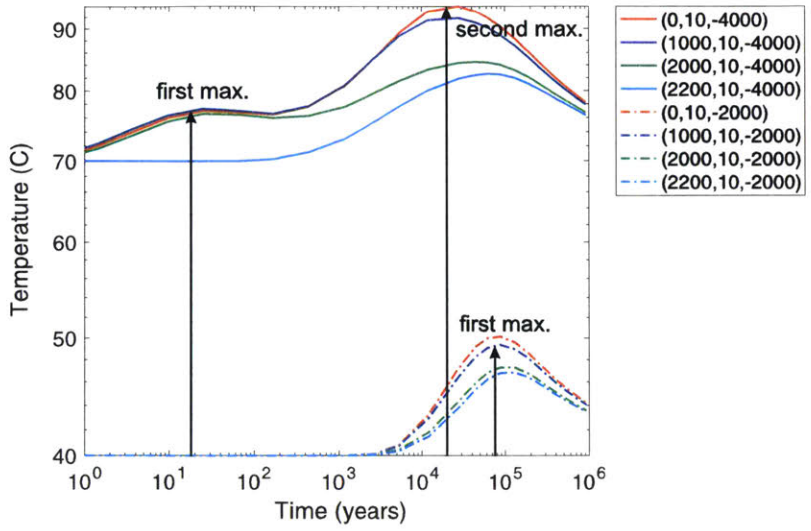

Figure 5-29: Comparison of temperature as a function of time at eight different locations in the rock, shown in Figure 5-28, considering 2 km and 4 km below the repository surface, and different horizontal distances from central borehole axis: 0, 1000, 2000, 2200 m. The last x coordinate considered (2200 m) corresponds to a location that, in contrast to the other points considered, is not above the nuclear waste emplacement area.

horizontal distances from central borehole axis: 0, 1000, 2000, 2200 m. The last x coordinate considered (2200m) corresponds to a location that, in contrast to the other points considered, is not above the nuclear waste emplacement area. As a general trend, velocity increases with time, to a first local maximum to then decrease. Later in time the fluid velocity reaches a second maximum significant higher than the first one. This behaviour is verified by all the points analyzed with the exception of the point outside the projected area of the waste, which observes fluid velocity later in time. This maximum corresponds to the convective cell that remains until one million years. The fluid velocity is higher closer to the mid point of the central borehole. Outside the waste emplacement zone the magnitude of the velocity decreases. The upward vertical fluid velocity above the edge of the borehole array is smaller than the vertical fluid velocity above the central borehole of the arrangement.

Figure 5-31 presents temperature, pressure and Darcy vertical velocity for two different points in the rock at different depths: 4 km and 2 km depth. The first

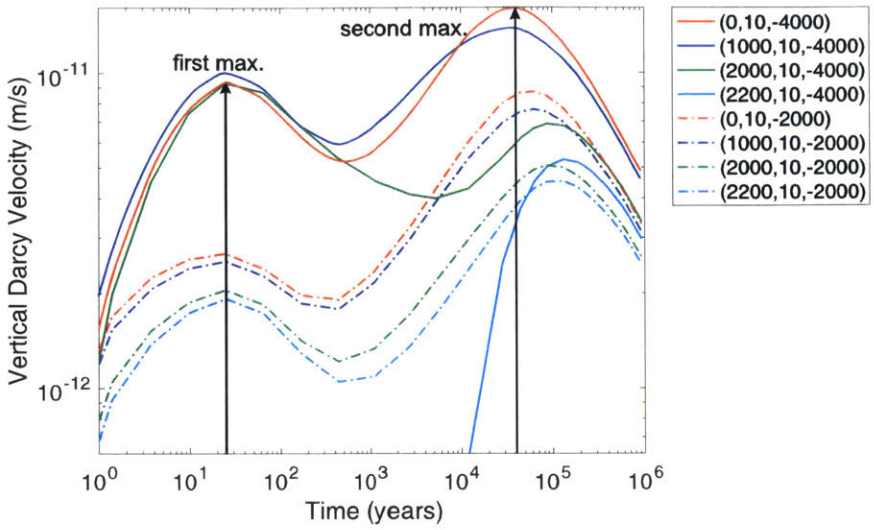

Figure 5-30: Comparison of vertical Darcy velocity as a function of time at eight different locations in the rock, considering 2 km and 4 km below the repository surface, and different horizontal distances from central borehole axis: 0, 1000, 2000, 2200 m. The last x coordinate considered (220 0m) corresponds to a location that, in contrast to the other points considered, is not above the nuclear waste emplacement area.

point corresponds to the point located within the emplacement zone. The second one is located in the cap rock (above the waste). Figure 5-32a shows the temperature evolution at a point between boreholes. This graph shows the same behaviour as the one shown for the infinite array for a point close to the waste. The second maximum occurs at 20,000 years after waste emplacement. Temperature in the cap rock increases reaching its maximum at 80,000 years, as seen Figure 5-32b. Pressure increases significantly earlier than temperature, as seen in Figures 5-32c and 5-32d. Vertical Darcy velocity exhibit the same behavior of having an absolute maximum later in time when convection has been established a the two locations considered. Velocities in the waste emplacement zone are larger than in the cap rock, about one order of magnitude difference, as seen in Figures 5-32e and 5-32f.

Figure 5-33 presents the vertical Darcy velocity as a function of time in the cap-rock above the central borehole of the repository (at 2 km depth) for two rock permeabilities: 10^{-16} and 10^{-17}m^2. As a comparison, the vertical Darcy velocity above the borehole for the infinite array is also included in the graph. For the semi-infinite

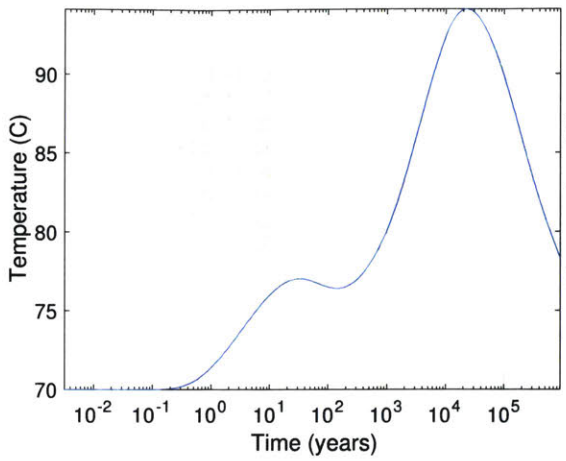

(a) Temperature at 4 km below repository surface and 10 m from borehole axis.

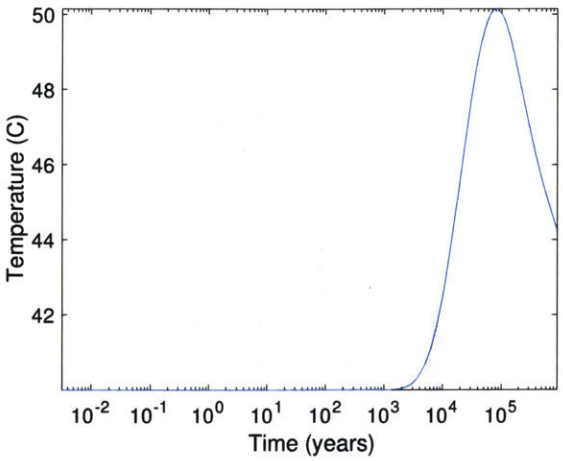

(b) Temperature at 2 km below repository surface and at borehole axis.

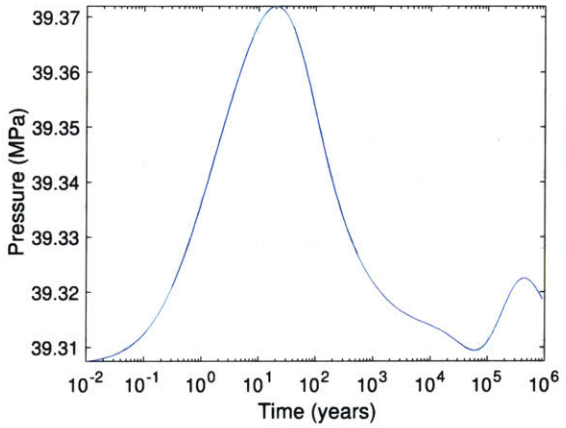

(c) Pressure at 4 km below repository surface and 10 m from borehole axis.

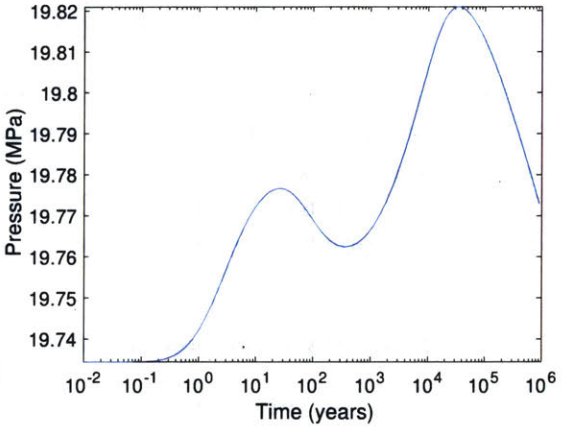

(d) Pressure at 2 km below repository surface and at borehole axis.

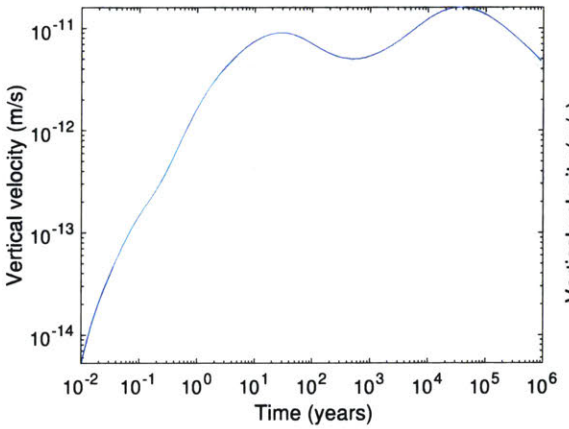

(e) Vertical Darcy velocity at 4 km below repository surface and 10 m from borehole axis.

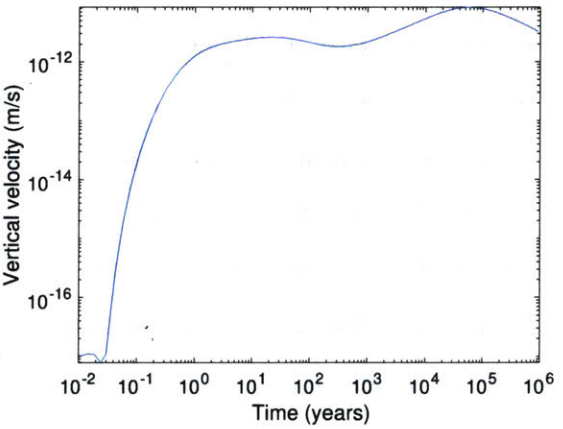

(f) Vertical Darcy velocity at 2 km below repository surface and at borehole axis.

Figure 5-31: Temperature, pressure and Darcy vertical velocity for two different points in the rock.

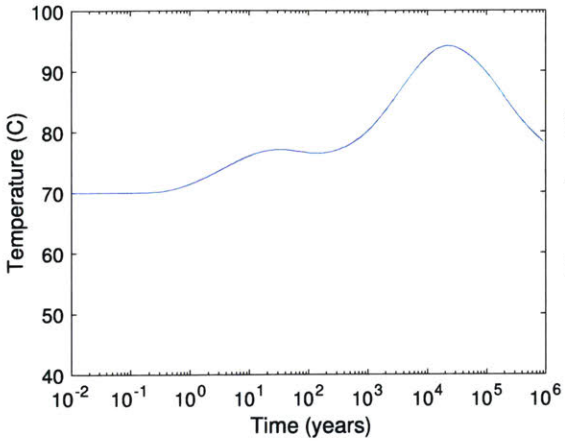

(a) Temperature at 4 km below repository surface and 10 m from borehole axis.

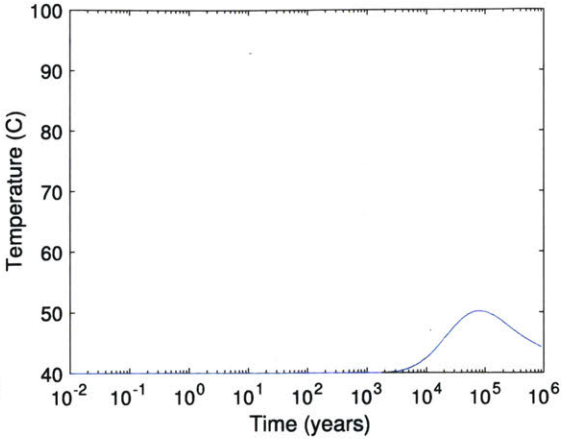

(b) Temperature at 2 km below repository surface and at borehole axis.

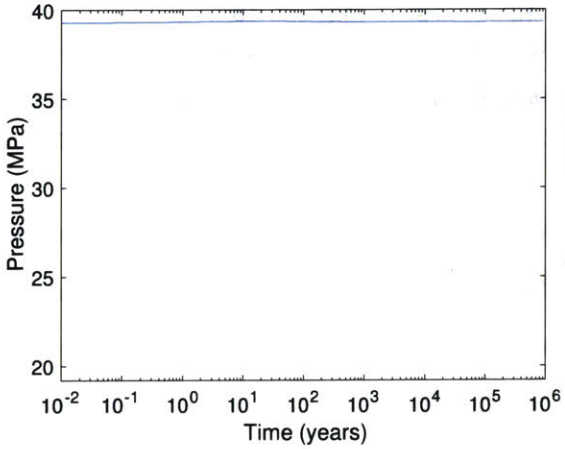

(c) Pressure at 4 km below repository surface and 10 m from borehole axis.

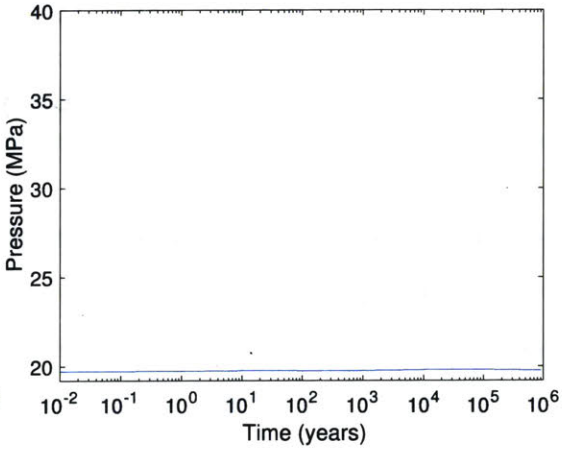

(d) Pressure at 2 km below repository surface and at borehole axis.

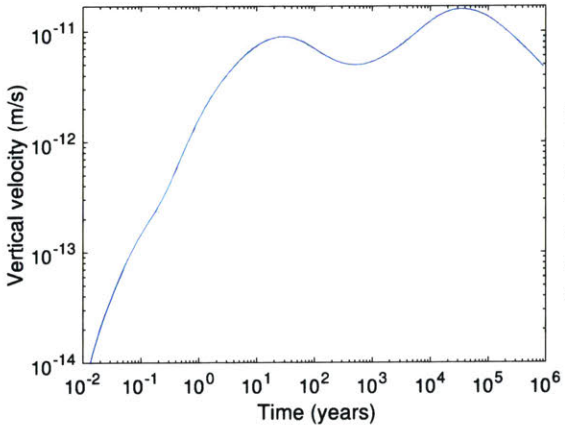

(e) Vertical Darcy velocity at 4 km below repository surface and 10 m from borehole axis.

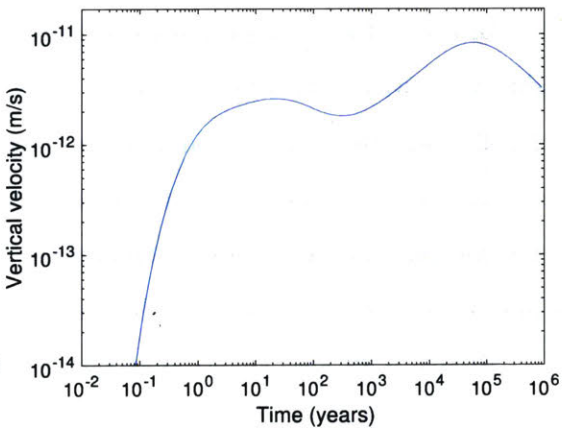

(f) Vertical Darcy velocity at 2 km below repository surface and at borehole axis.

Figure 5-32: Same as Figure 5-31 but plots are at same scale, not all curves are visible.

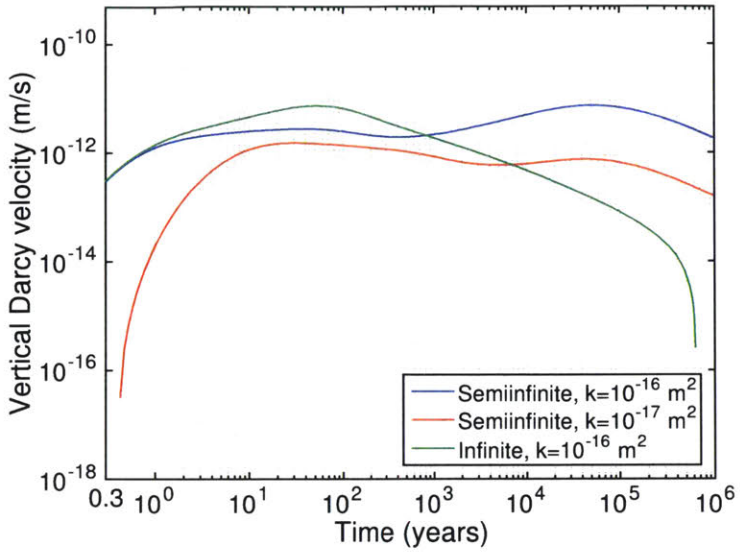

Figure 5-33: Comparison of vertical Darcy velocity above the center borehole at 2 km depth for two permeabilities, and comparison with infinite array of boreholes velocity.

configuration of boreholes, heat induced vertical groundwater flux above the waste disposal is significant for the duration of the simulation. The fluid flow is primarily characterized by convection, and becomes sensitive to rock permeability. This stands in contrast to the infinite configuration, where the flow corresponds to the water expansion (dependent on rock porosity and the thermodynamic properties of water only) and the decrease of velocity tracks the decay of the heat source.

In the initial time period (less than 900 years after fuel emplacement) the flow is directed away from the repository, caused by water expansion. However, by about 1,000 years the borehole area is uniformly heated and a large-scale convective cell through the repository is established, as seen in Figure 5-23. This large-scale convection pattern, with closed streamlines from the heated borehole area to the colder host rock, is stationary until the end of the simulation (Figures 5-24 and 5-25).

Figure 5-33 also shows that for the first 800 years the vertical Darcy velocities are smaller than the velocities in the infinite configuration. This can be explained by the fact that there are more paths for displacement of fluid particles than in the infinite configuration. After 800 years of fuel entombment, velocity does not decrease proportionally to the heat decay as it does for pure water expansion. Furthermore,

significantly larger vertical Darcy velocities than in the infinite configuration can be seen after 10,000 years, indicating the onset of the convection cell. For the reference permeability of $10^{-16}m^2$, Darcy velocity reaches a second maximum at 51,000 years. Higher maxima correspond to higher rock permeabilities.

Fluid convection in the domain is fully established at around 10,000 years after fuel emplacement. This time scale corresponds to the time of the second maximum of temperature in the heated region, as seen in Figure 5-32a. The temperature difference between the waste zone and the surrounding natural and relatively colder rock governs the convection in the repository. Therefore, fluid convection can be limited by reducing this maximum of temperature, as will be discussed in Section 5.5.5.

5.5.4.3 3D trajectories and breakthrough time

As introduced in Section 5.5, we developed a C++ code to track particles through time in the simulation. To date, MOOSE does not have particle trackers. Our code reads the Exodus file where the simulation results are saved as a binary file. Once the initial position of the particle to follow is defined the trajectory of the particle is computed numerically by integration in time of Equation 5.5. Four different interpolation methods for fluid velocity throughout the trajectory were implemented in the code to compare the results. The velocity interpolation methods used are called:

1. None (Int.1)

   It considers the closest node velocity and considers constant velocity of the particle during each time step dt.

2. Velocity in time (Int.2)

   It considers closest node velocity and averages it at two consecutive time steps $(t, t + dt)$.

3. Predictor-corrector (Int.3)

   It considers the average velocity of two nodes: initial closest node, and then the

predicted closest node at one time step later, assuming the particle moves with the former velocity first.

4. By elements (Int.4)

   It considers the particle has the velocity of elements in the mesh in which it is located.

Numerical results obtained with our code found that for the array of boreholes studied for the reference permeability of 10^{-16}m^2 fluid particles near the nuclear waste break through at the surface. This is in agreement with results obtained with ParaView. Breakthrough was verified by using the ParticleTracker filter from ParaView. This was performed for validation purposes of our code. However, this filter does not provide quantitative data, while our code does.

We studied the breakthrough time for different particles using different interpolation methods. Table 5.3 presents the breakthrough time computed for three particles that have the initial position $\vec{x}(0)$ indicated in the Table. The same particles are studied with other repository characteristics for comparison. A particle that starts at 10 m from the central borehole at the mid emplacement plane depth (4 km below repository surface) breaks through the repository surface at a time scale of 145,000 years after waste emplacement. Figure 5-34 presents the Lagrangian vertical coordinate as a function of time for the three particles presented in Table 5.3.

Table 5.3: Breakthrough times in years for three particles using four different interpolation methods defined as Int.1, Int.2, Int.3 and Int.4 in the list of methods presented above.

$\vec{\mathbf{x}}(0)$	**Int.1**	**Int.2**	**Int.3**	**Int.4**
(10,10,-4000)	146,363	145,101	156,947	143,815
(20,10,-3756)	140,777	142,302	152,279	139,844
(87,45,-2156)	108,486	107,012	109,875	105,757

As another example of fluid breakthrough to the surface, we follow Lagrangian particles generated randomly. Their initial positions are chosen such that $x(0) \in (10, 800), y(0) \in (0, 100)$ and $z(0) \in (-6000, -2000)$, with uniform probability over

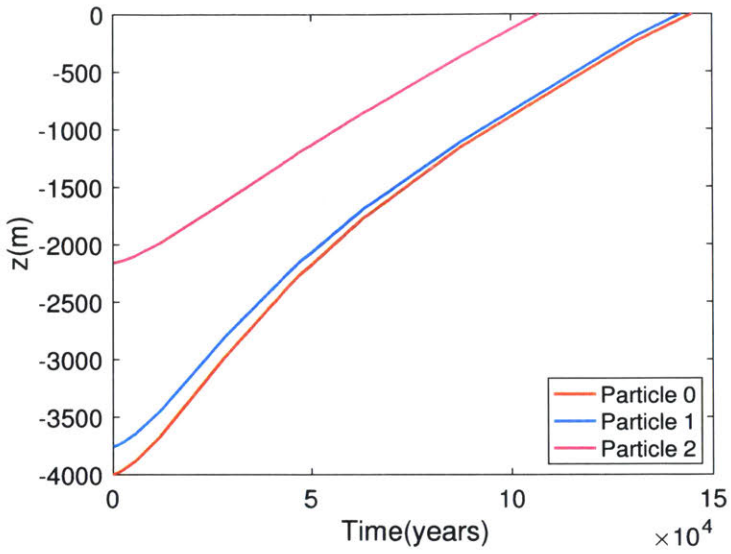

Figure 5-34: Lagrangian vertical coordinate as a function of time for the three particles presented in Table 5.3.

the given intervals. Particles reach the surface within one million years, and most interestingly, this result applies to particles that start below the nuclear waste, as shown in Figure 5-35. Those trajectories are governed by the large-scale convective cell throughout the entire repository, shown in Figure 5-36. Figure 5-37 shows the trajectory of particles that start at the mid depth of the waste disposal zone and 10 meters from the borehole axis line.

Trajectories of particles that start near the boreholes at 4 km depth are shown in Figure 5-38.

5.5.4.4 Water phase diagram

One of the major concerns in nuclear waste disposal is the risk of reaching extremely high temperatures if heat dissipation in the rock is not large enough. Extremes high temperature can produce melting of the granite, of the canister and of the spent fuel assembly. It is a primary goal of the present thesis to investigate if there is any high-temperature phase change in the disposal system. The melting temperature of dry granite is 1215–1260°C at ambient pressure (Larsen, 1929). The melting point decreases strongly with the presence of water, to 650 °C at a few kBar pressure

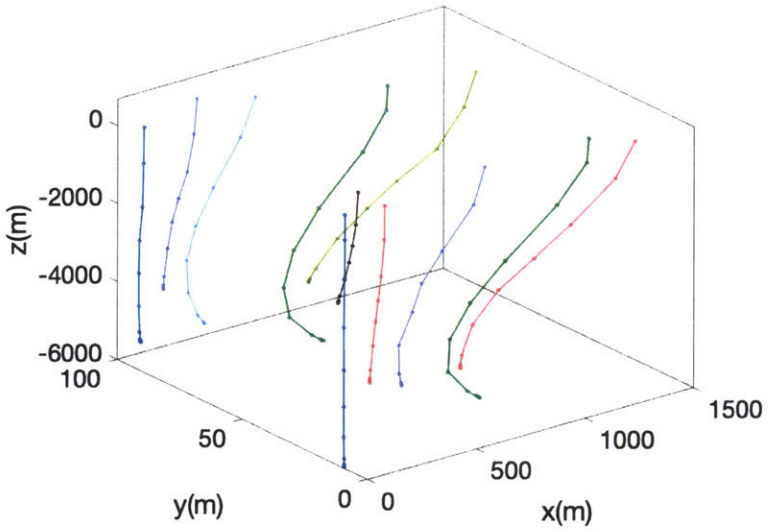

Figure 5-35: Trajectories of 11 randomly generated particles. Their initial positions have a uniform distribution such that $x(0) \in (10, 800), y(0) \in (0, 100)$ and $z(0) \in (-6000, -2000)$.

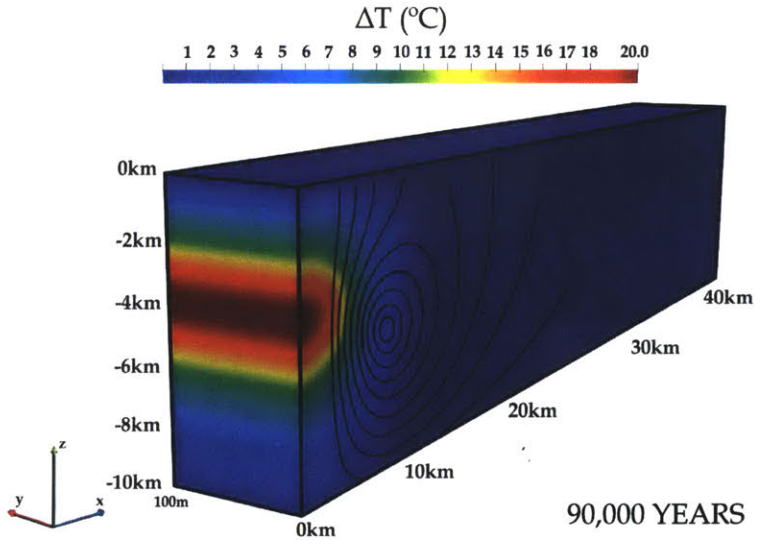

Figure 5-36: Temperature increase ΔT(°C) due to decay heat and streamlines in the repository at 90,000 years after waste emplacement.

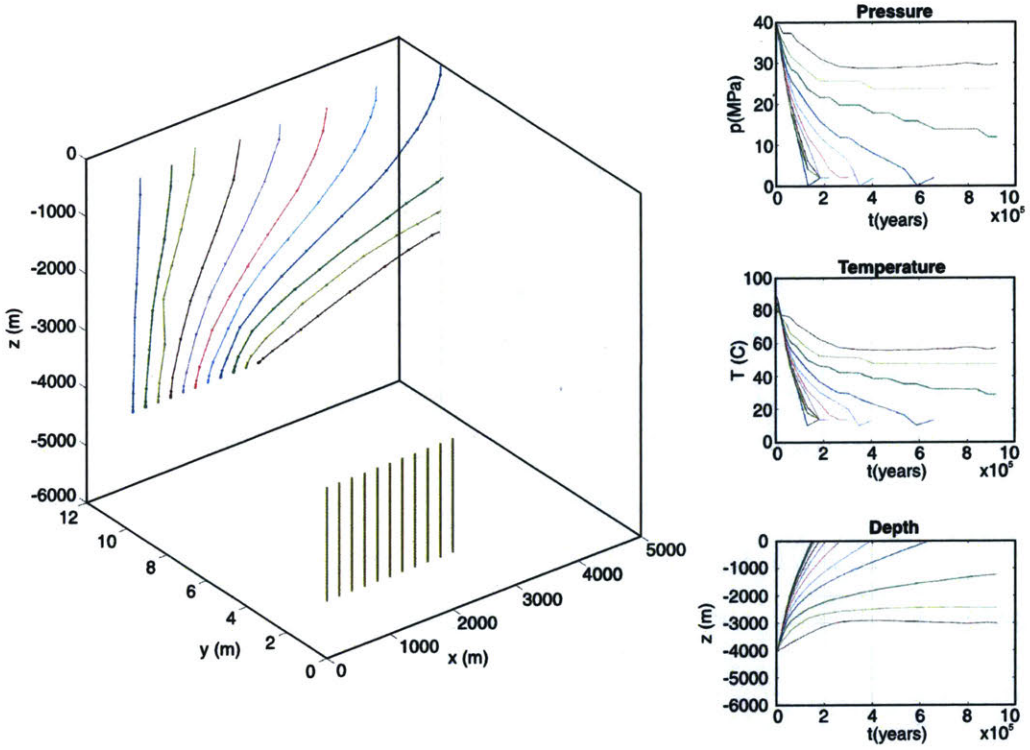

Figure 5-37: Trajectories of 11 particles whose initial position belongs to a line at the middle depth of the disposal zone, equally spaced between boreholes. Vertical lines in green represent the nuclear waste in the numerical domain. Plots at the right present pore pressure, temperature and depth as a function of time for each particle, from top to bottom.

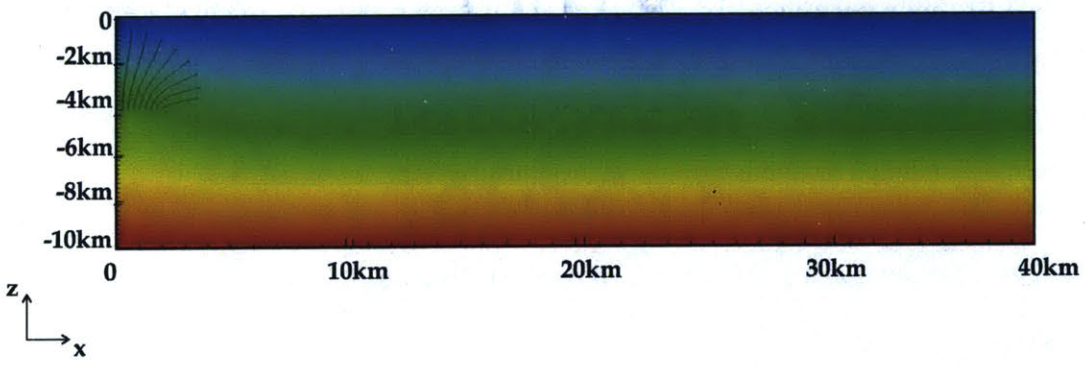

Figure 5-38: Trajectories for fluid particles that start at 4 km below repository surface up to 131,000 years from emplacement (permeability of 10^{-16}m^2).

(Holland & Powell, 2011).

In addition to structural problems due to melting, it is critical to determine whether water changes to gas phase or becomes super critical. As explained in Section 3.4, TWR spent fuel releases significantly more heat than conventional spent fuel, and therefore the fluid can potentially reach values higher than the critical temperature (373.9 °C), see Figure 3-2. At these high pressures, even though there is no phase transition such as boiling, there is still a significant decrease of density at a certain temperature (shown in right plot of Figure 3-2). Reaching these high temperatures increases buoyancy significantly due to the non linear dependence of density with respect to temperature, which in turn could enhance fluid convection and therefore pose a problem for radionuclide migration. Another potential problem in the nuclear waste repository is the boiling of the fluid while it rises. While a particle raises, temperature decreases, and pressure decreases as well. If pressure reduction is high enough, the fluid can reach boiling conditions.

We verified that single-phase conditions exist throughout the model domain during the simulations. Pore pressures are high enough at the depths of the waste disposal zone that boiling does not occur from the waste heat. Water does not reach super critical conditions. In addition, when particles rise, pressure and temperature conditions are such that liquid water does not change to the gas phase. Even though pressure decreases while ascending, temperature decreases in such a way that water remains liquid. For instance, Figure 5-39 presents the paths described by the three particles defined in Table 5.3 while they rise to the repository surface. Particle paths in the P-T diagram never cross the boiling point curve. All particle paths are controlled and converge to the same point (101325Pa,10°C) which corresponds to the repository surface. This helps to avoid boiling while fluid rises.

5.5.4.5 Investigation of different particle paths

So far a radionuclide particle in the water in the emplacement zone and 10 m from the borehole axis was considered. This leads to particles breaking at the surface at 145,000 years. This neglects the time it takes for the particles to diffuse from

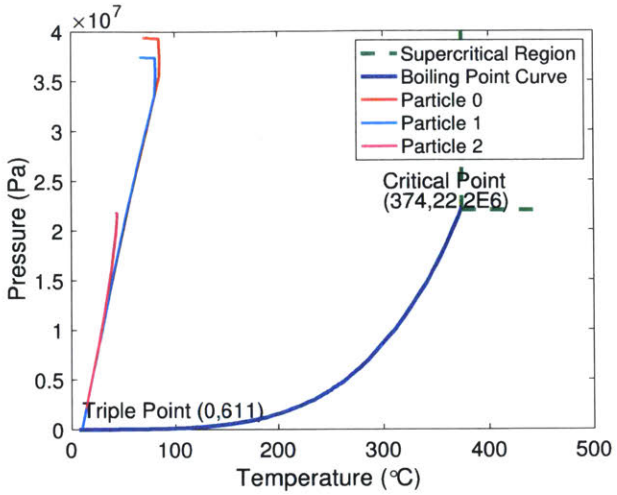

Figure 5-39: Water phase diagram including paths described by the three particles with initial position $\vec{x}(0)$ defined in Table 5.3.

the waste to a location 10 m away. In the following, this is considered for different diffusion coefficient assumptions.

The diffusion time scale can be estimated by:

$$t_D = \frac{L^2}{2D_p} \tag{5.6}$$

where L represents the distance (m)

D_p represents the pore diffusion coefficient (m^2/yr)

The key parameter to determine this time scale is the effective diffusion coefficient for the readionuclides. The diffusion coefficient depends on each radionculide and on porous media properties. Spent fuel contains a large inventory of radionuclides that decay with time. Table 5.4 presents some diffusion coefficients for some readionuclides found in the literature (Li & Chiou, 1993; Bucur, Popa, Arsene, & Olteanu, 2000; Szántó et al., 2002).

For the case of ^{237}Np, the required time for diffusion is t=5,000d years. This time represents only 3.4% of the advective transport time from the waste emplacement zone (10 meters radially from the borehole axis) to the surface, which was determined to be 145,000 years. Therefore, the total breakthrough time for the reference case is 150,000

Table 5.4: Diffusion coefficient in porous medium (D_p) for different radionuclides and their respective diffusion time (t_D) in years to diffuse 10 m.

Radionuclide	$\mathbf{D_p(m^2/yr)}$	$\mathbf{t_D(yr)}$
^{237}Np	0.01[a]	5,000
^{137}Cs	2.0498×10^{-4} [b]	243,920
^{60}Co	1.5579×10^{-4} [b]	320,950
^{3}H	4.73×10^{-4} [c]	105,700
^{99}Tc	1.45×10^{-4} [c]	344,670
^{125}I	1.89×10^{-4} [c]	264,250
^{36}Cl	7.25×10^{-5} [c]	689,340
^{85}Sr	3.15×10^{-6} [c]	15,855,000

[a] In crystalline rock (Li & Chiou, 1993).
[b] In clay (montmorillonite 14.5%, illit 9% and kaolin 1.9%) (Bucur et al., 2000).
[c] In granite (Szántó et al., 2002).

years, significantly smaller than the million years required as period of analysis by the nuclear regulators.

For ^{137}Cs and ^{60}Co, diffusion time is larger (243,920 and 320,950 years) and comparable with the advective time scale to travel from the waste emplacement zone to the repository surface (145,000 years). The time required for ^{3}H to diffuse 10 m is about 0.7 of the advective transport time to reach the surface. For ^{99}Tc, ^{125}I and ^{36}Cl the diffusion time becomes comparable to or even larger than the advective transport time. Lastly, ^{85}Sr diffusion time is extremely long and does not pose a problem for the one-million-year limit.

Another more extreme particle path is the movement vertically from the waste rather than 10 m from it. This is investigated for 13 particles starting directly from the waste in the borehole. Three particles are chosen to start at the center of the borehole at different of depths. Ten particles are randomly generated within the borehole volume. Their initial positions have a uniform distribution such that $x(0) \in (0, 0.17\text{m})$, $y(0) \in (0, 0.17\text{m})$ and $z(0) \in (-5000\text{m}, -3500\text{m})$, shown in Figure 5-40. The radius of the borehole is 0.17 m and it extends from 3 km to 5 km below the surface. Figures 5-41 and 5-42 present top and front view of the trajectories,

respectively. Using our code to track particles we found that the breakthrough time of the 13 particles analyzed is 120,000 years, 30,000 years earlier than the breakthrough time of the particles at the rock previously shown, see Table 5.5. In the model domain, the borehole volume has a permeability and porosity one order higher than the host rock since we can assume canister disintegration within one million years. The borehole volume above the canister was assumed to have the same properties as the host rock. In the field, seal material properties might be different from the rock properties, and radioactive material would escape earlier or later than these 120,000 years, depending on the properties of the produced seal.

All this shows that the borehole is the critical path for radionuclides to migrate to the surface. It represents the shortest path and the highest velocity zone (warmest region and more permeable than the unaltered host rock if we assume canister disintegration). Particles from the waste are able to migrate to the surface about 30,000 years earlier than particles at 10 meters from the borehole.

The reference repository configuration exhibits particle breakthrough to the surface at 120,000 years, significantly earlier than the required one-million-year limit. This shows that we cannot guarantee radionuclides containment for one million years, and that coupled chemical models must be included in the analysis. Chemical models that account for radioactive decay are critical to determine if, given the time scale, the inventory of radionuclides reaching the surface is harmless for humans or not. In addition, diffusion into the rock matrix and retardation due to sorption and desoption in the host rock can contribute to the reduction of radionuclides reaching the surface. Once all these effects are modeled, a more realistic evaluation can be obtained for spent fuel disposal.

5.5.5 Sensitivity studies

5.5.5.1 Advective heat transport

Sensitivity studies are performed to assess the relative contributions of advective versus conductive heat transport in the thermal-hydraulic model. Comparison of a

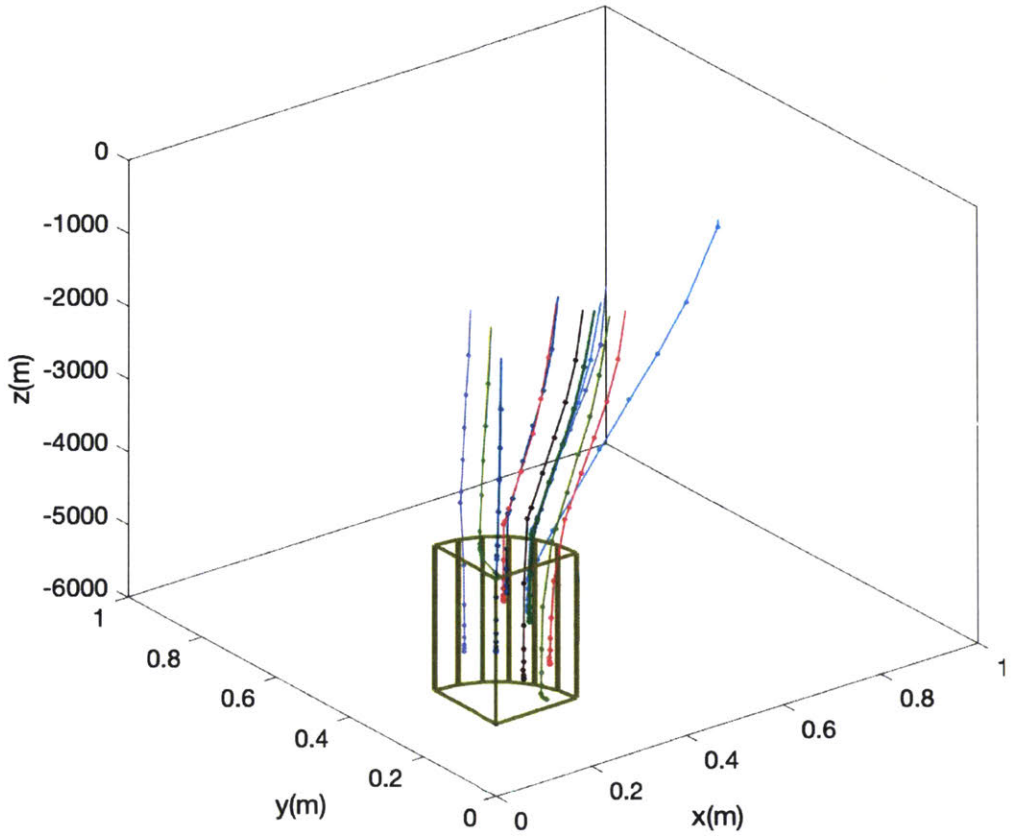

Figure 5-40: 3D trajectories of 13 particles that start inside the borehole volume. Three of them are at the center of the borehole at different depths. Ten particles are randomly generated within the borehole volume. Horizontal and vertical scale are different in the plot for visualization purposes. The one-quarter cylinder in the plot represents the central borehole volume that contains nuclear waste.

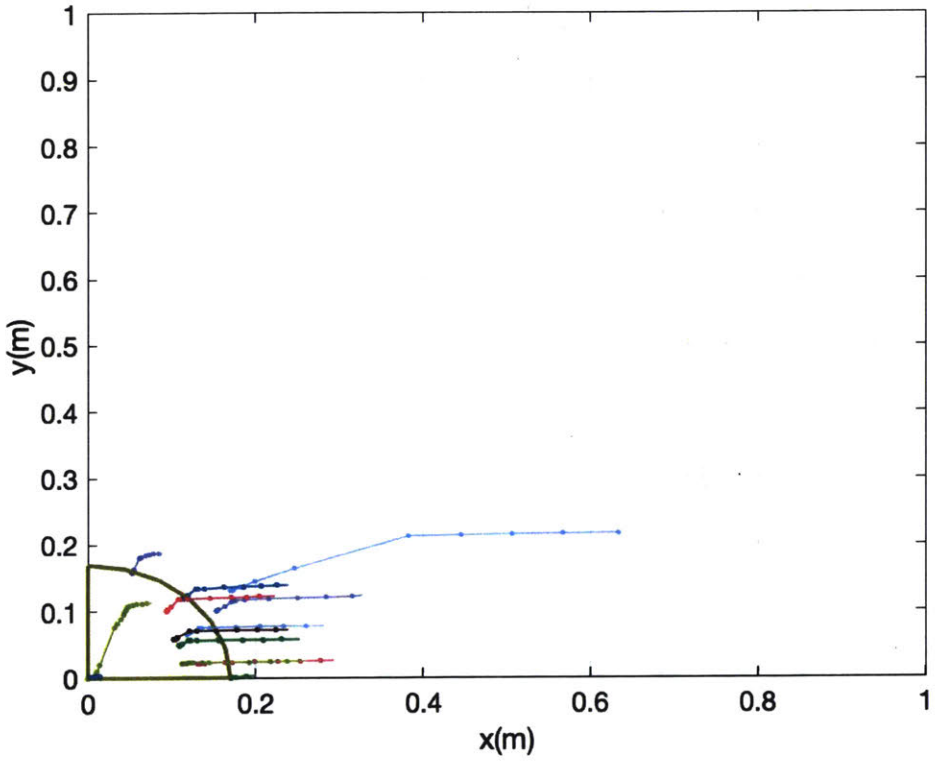

Figure 5-41: Top view of the trajectories of particles randomly and deterministically generated inside the borehole volume. The one-quarter cylinder in the plot represents the borehole volume that contains nuclear waste.

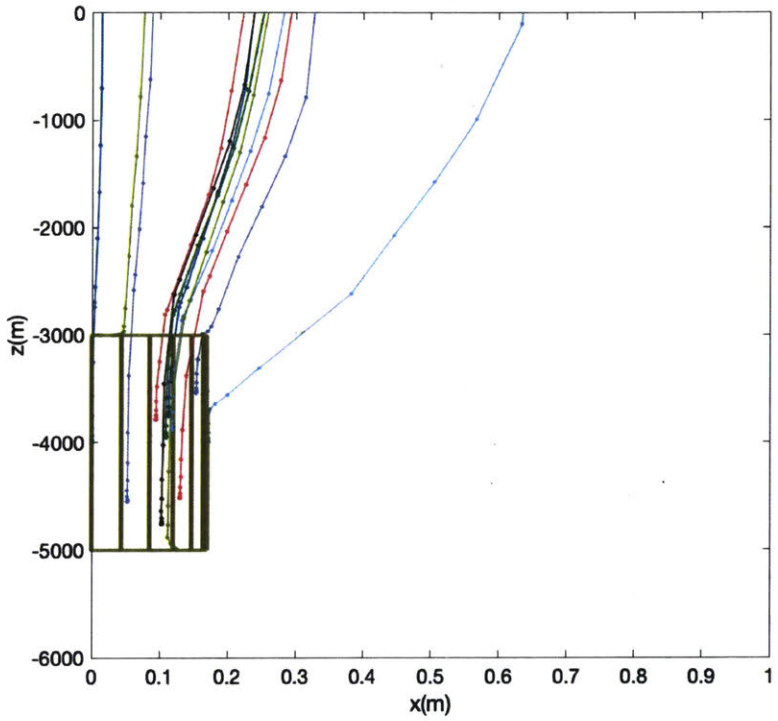

Figure 5-42: Vertical view of the trajectories of particles randomly and deterministically generated inside the borehole volume. Horizontal and vertical scale are different in the plot for visualization purposes. The one-quarter cylinder in the plot represents the borehole volume that contains nuclear waste.

Table 5.5: Breakthrough times in years for 13 particles using the second method of interpolation, defined as Int.2 previously. The first three particles' initial position was determined to be at the center of the borehole at 3, 4 and 5km depth, which coincides with the top surface of the nuclear waste, the center and the bottom boundary of the waste. The remaining 10 particles were generated randomly.

$\vec{x}(0)$	**Breakthrough time**
(0,0,-4000)	123,817
(0,0,-3000)	127,023
(0,0,-5000)	121,585
(0.0522696,0.157628,-4549.73)	119,508
(0.093779,0.100572,-3785.17)	124,258
(0.169483,0.130675,-3740.9)	137,142
(0.112887,0.118967,-3757.35)	123,714
(0.108664,0.048429,-3956.99)	124,468
(0.124973,0.0230422,-4985.46)	126,276
(0.102924,0.0578153,-4758.99)	122,042
(0.152973,0.100617,-3535.17)	127,148
(0.130062,0.0223285,-4516.02)	120,247
(0.117881,0.0655236,-3885.99)	125,549

heat conduction-only model to the thermal-hydraulic model shows extremely small differences in temperatures, indicating that heat transport in the thermal-hydraulic model is conduction dominated, see Figures 5-43 and 5-44. This result is expected, given the extremely small convective groundwater flow rates (Darcy velocity), smaller than 0.03 mm/year. The Péclet number is smaller than unity and can be estimated to be of the order $10^{-2}(Pe = \frac{\rho_f c_f \vec{v} L}{k_{eff}} \approx 0.007)$.

5.5.5.2 Sensitivity to rock permeability

We compared the thermo-hydraulic response of the nuclear waste repository with one order permeability smaller, $10^{-17}\mathrm{m}^2$, see Figure 5-45. Temperature is the same as the reference case, as heat transport is conduction dominated. Convective heat transport is negligible, Pe << 1, the same as results for the infinite array. For the smaller permeability case, pore pressure increases significantly. This pore pressure increase can lead to rock failure if the pressure increase is large enough. Flow is dominated by convection imposed by a large-scale convective cell within the repository

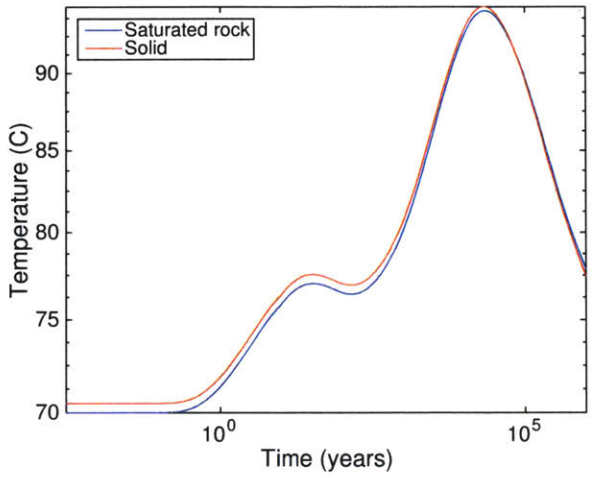

Figure 5-43: Comparison of temperature at 4 km below repository surface and 10 m from the borehole axis for the saturated porous medium and for a solid.

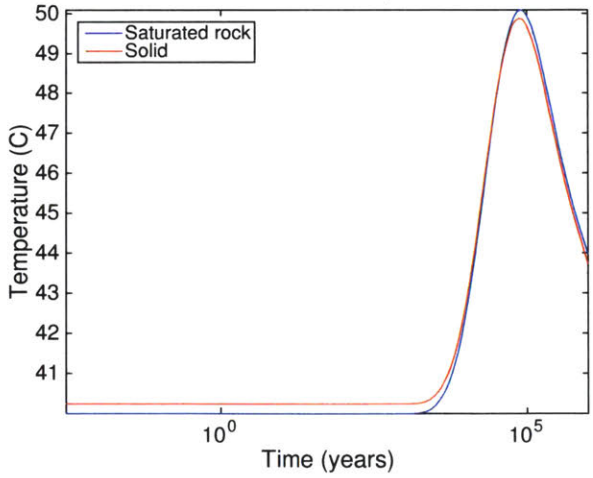

Figure 5-44: Comparison of temperature at 2 km below repository surface and at the centerline of borehole axis for a saturated porous medium and for a solid.

and fluid velocity becomes sensitive to permeability, in contrast to the results for the infinite array. Fluid velocity decreases about one order of magnitude for the smaller permeability case.

We found that fluid particles that start near the nuclear waste do not breakthrough to the surface within the one-million-year time span, see Table 5.6 and Figures 5-47 and 5-48. Water remains liquid while particles ascend, as shown in Figure 5-49. This denotes that for extremely small permeability deep borehole repository can be considered as an option.

Table 5.6: Particles' positions at the end of simulation (t_f=709,579.52 years), for a rock permeability of 10^{-17}m^2. Particles do not reach the surface within one-million-year time span (verified for the four interpolation methods implemented in our code).

$\vec{x}(0)$	$\vec{x}(t_f)$
(10,10,-4000)	(14.0506, 10.1002, -2334.52)
(20,10,-3756)	(28.2684, 10.0419, -2167.52)
(87,45,-2156)	(1127.919, 44.9864, -1034.39)

5.5.5.3 Sensitivity to thermal conductivity

We considered two different thermal conductivities to quantify the effect of heat transport in the repository. It should be highlighted that because of tectonic stability the deep borehole repository is designed to be in granite host rock. We first considered a case of a lower thermal conductivity of 2 W/m°K (which corresponds to shale) and a case of higher thermal conductivity of 5 W/m°K (which corresponds to salt). We first determined the initial conditions in the rock for both cases resulting from the same constant geothermal flux, presented in Figure 5-50. Smaller thermal conductivity significantly increases the temperature. As a consequence, pore pressure, fluid density and viscosity decrease.

Small thermal conductivity produces a large increase in the temperature in the rock, see Figures 5-51a and 5-51b, and an appreciable increase in pore pressure, see Figure 5-51d. The low conductivity medium produces a higher pressurization of the saturated rock which causes higher fluid flow, see Figure 5-51f. This in turn

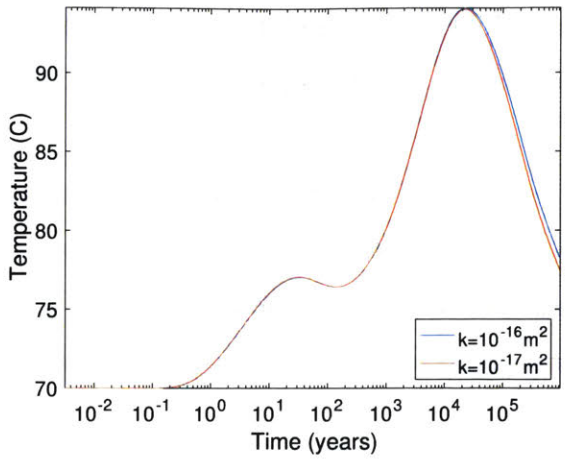

(a) Temperature at 4 km below repository surface and 10 m from borehole axis.

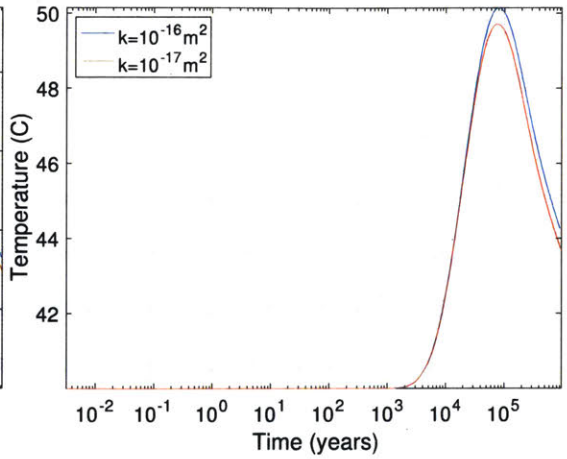

(b) Temperature at 2 km below repository surface and at borehole axis.

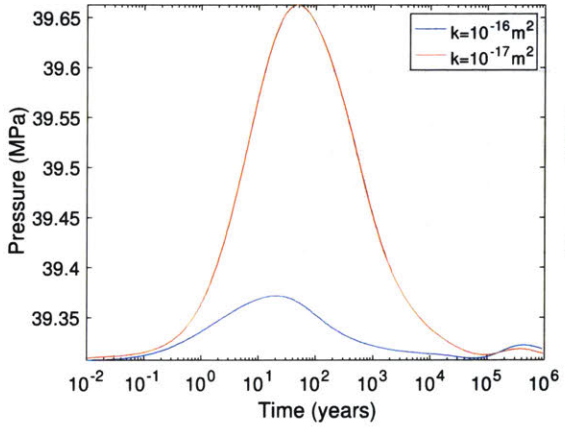

(c) Pressure at 4 km below repository surface and 10 m from borehole axis.

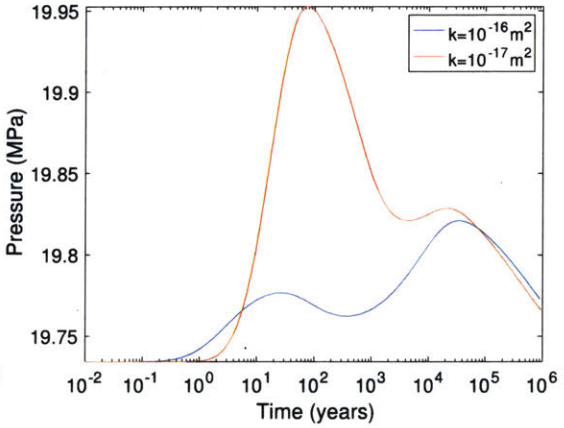

(d) Pressure at 2 km below repository surface and at borehole axis.

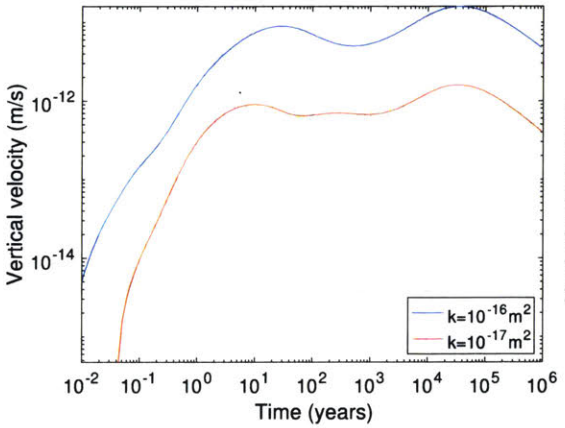

(e) Vertical Darcy velocity at 4 km below repository surface and 10 m from borehole axis.

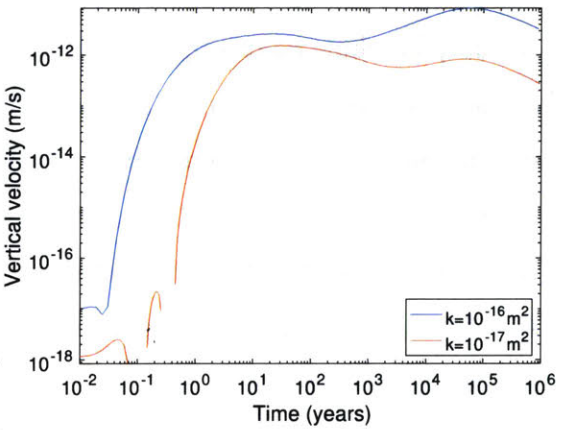

(f) Vertical Darcy velocity at 2 km below repository surface and at borehole axis.

Figure 5-45: Temperature, pressure and Darcy vertical velocity comparison at two different points in the rock, for intrinsic permeability 10^{-16}m^2 and 10^{-17}m^2.

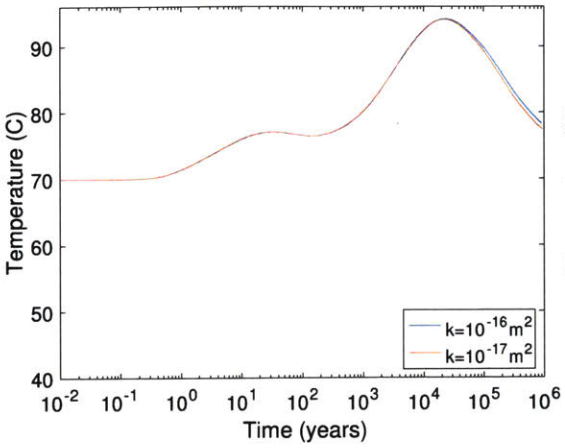

(a) Temperature at 4 km below repository surface and 10 m from borehole axis.

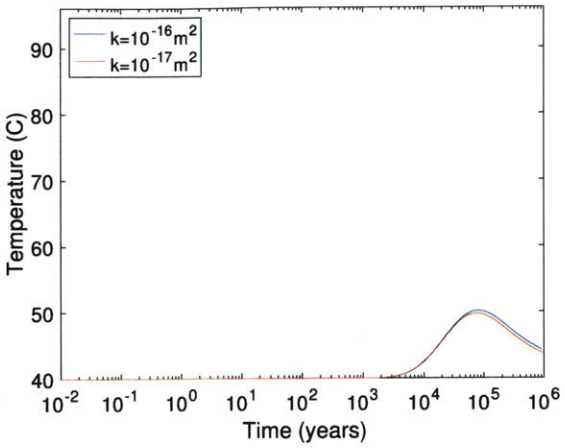

(b) Temperature at 2 km below repository surface and at borehole axis.

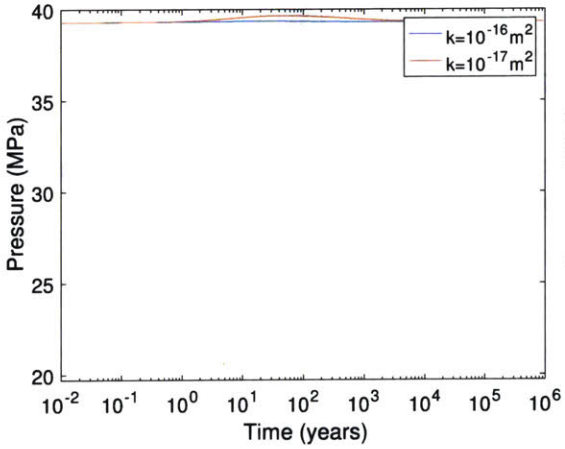

(c) Pressure at 4 km below repository surface and 10 m from borehole axis.

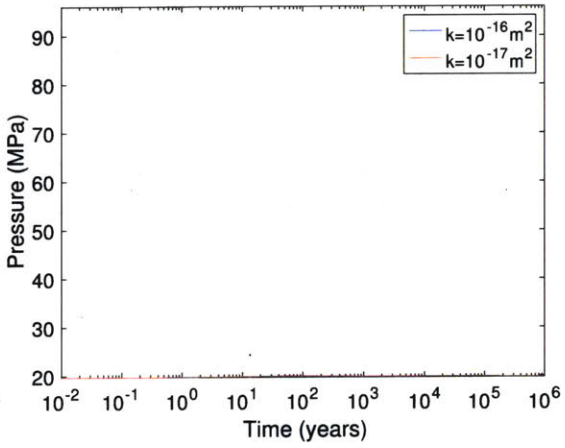

(d) Pressure at 2 km below repository surface and at borehole axis.

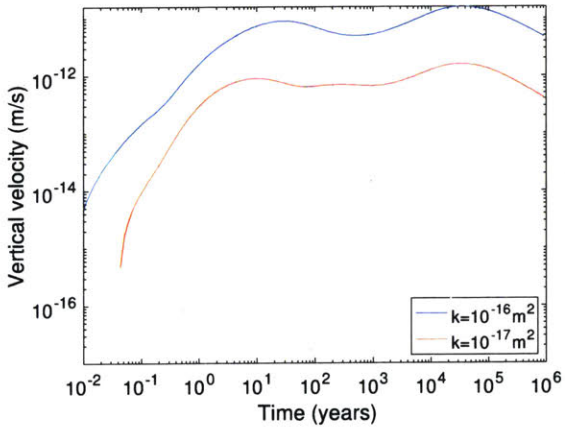

(e) Vertical Darcy velocity at 4 km below repository surface and 10 m from borehole axis.

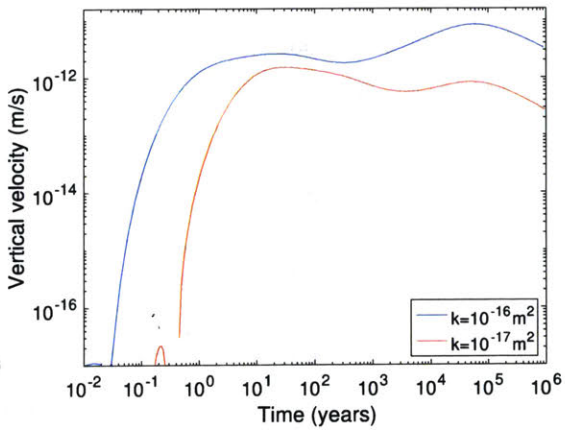

(f) Vertical Darcy velocity at 2 km below repository surface and at borehole axis.

Figure 5-46: Same as Figure 5-45 but plots are at same scale, not all curves visible.

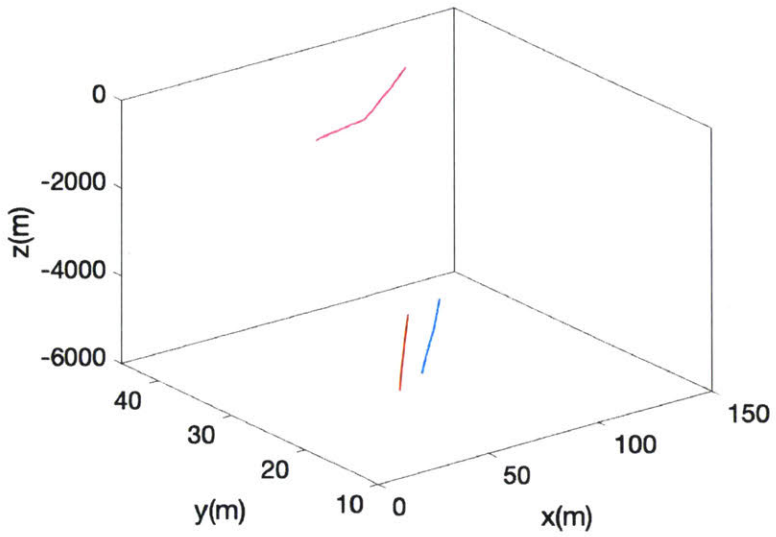

Figure 5-47: Trajectories for fluid particles that start at 4 km below repository surface up to 1 million years from emplacement (permeability of $10^{-17}\mathrm{m}^2$).

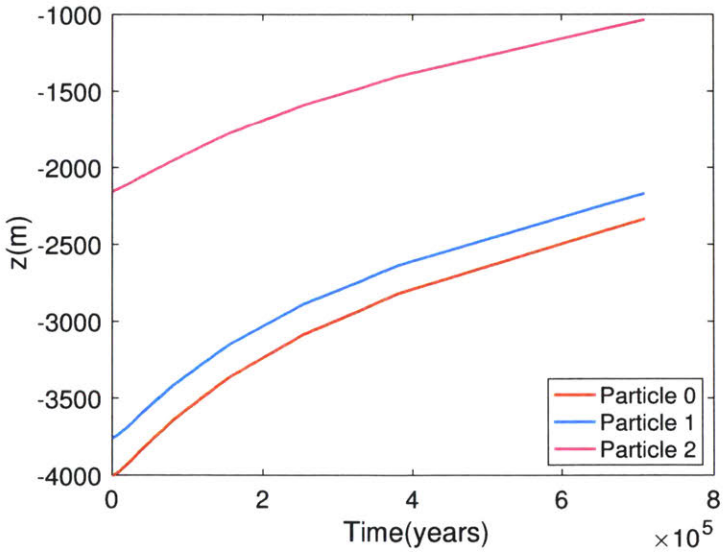

Figure 5-48: Lagrangian vertical coordinate as a function of time for the three particles presented in Table 5.6.

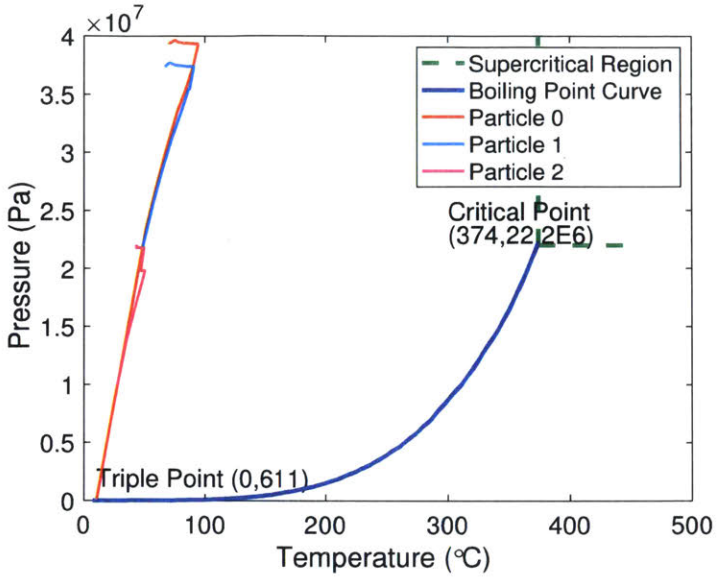

Figure 5-49: Water phase diagram including paths described by the three particles with initial position $\vec{x}(0)$ defined in Table 5.6.

causes fluid particle near the nuclear waste to escape to the repository surface at a significantly earlier time, 90,000 years time scale as shown in Table 5.7, compared with a high conductivity medium, where breakthrough time is of the order of 370,000 years, as shown in Table 5.8. Figures 5-53 presents the 3D trajectories of the three particles referenced in Tables 5.7 and 5.8, and Figure 5-54 presents the Lagrangian vertical coordinate as a function of time for the same three particles for both thermal conductivities.

Table 5.7: Breakthrough times in years for a thermal conductivity of 2 W/m°K for the four different interpolation methods implemented.

$\vec{x}$ (0)	Int.1	Int.2	Int.3	Int.4
(10,10,-4000)	90,731	98,005.8	87,816.1	81,620.2
(20,10,-3756)	94,979.8	79,043	91,322.7	82,934.1
(87,45,-2156)	58,019.6	67,178.4	65,845.25	70,269

5.5.5.4 Sensitivity to borehole spacing

We considered the case of increasing the borehole spacing. Because the second maximum is a consequence of borehole interference, it can therefore be reduced by increas-

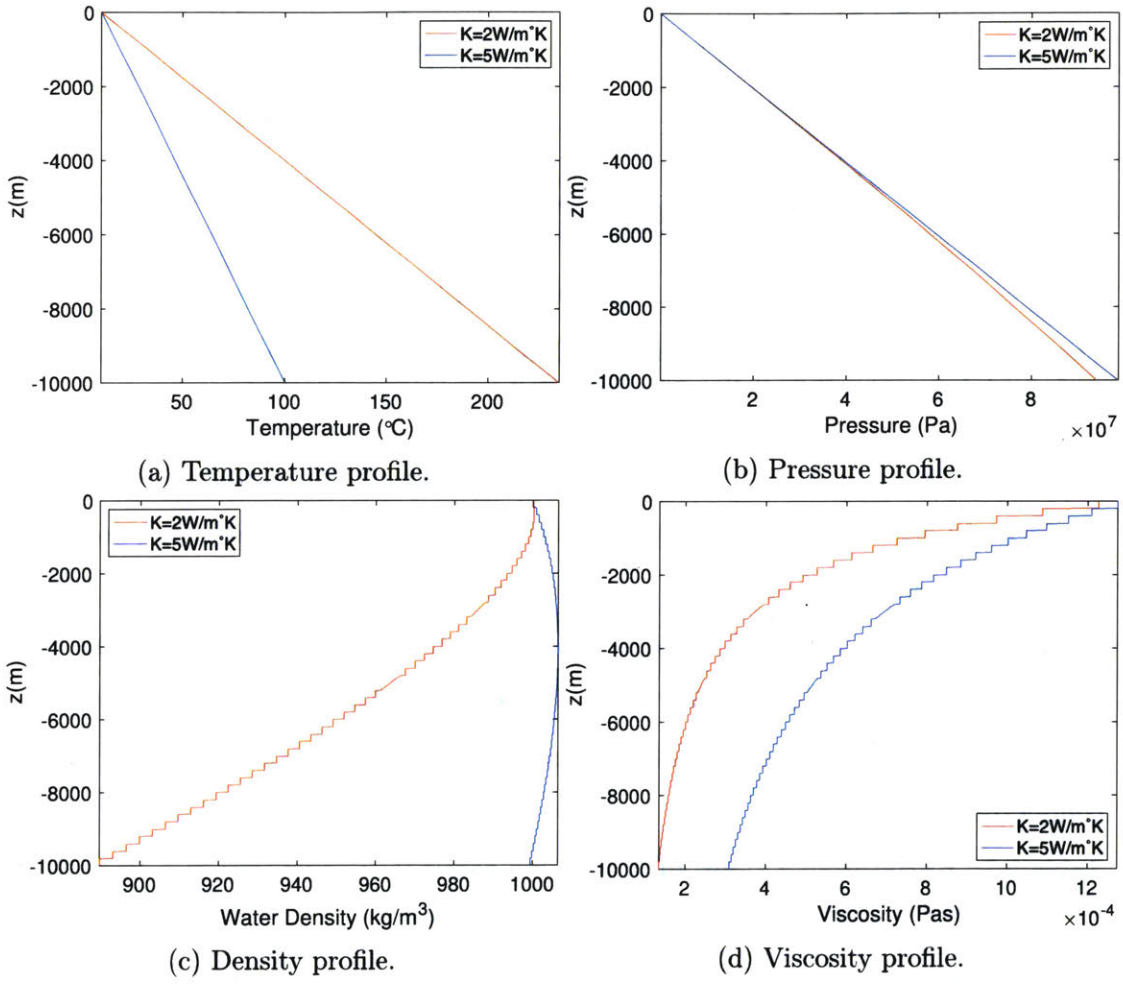

(a) Temperature profile.

(b) Pressure profile.

(c) Density profile.

(d) Viscosity profile.

Figure 5-50: Temperature, pressure, fluid density and viscosity in the rock before waste emplacement, comparison for two rock thermal conductivities of 2 and 5 W/m°K.

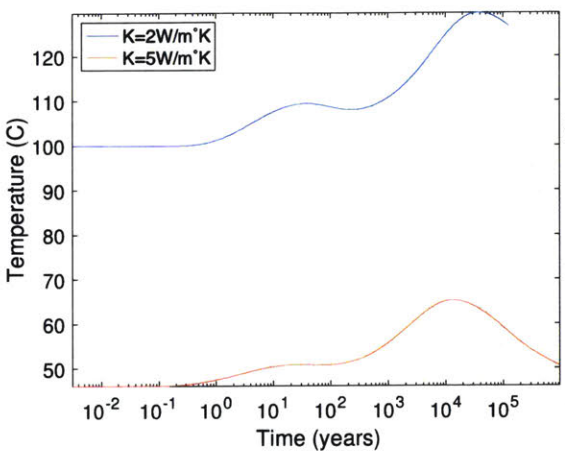

(a) Temperature at 4 km below repository surface and 10 m from borehole axis.

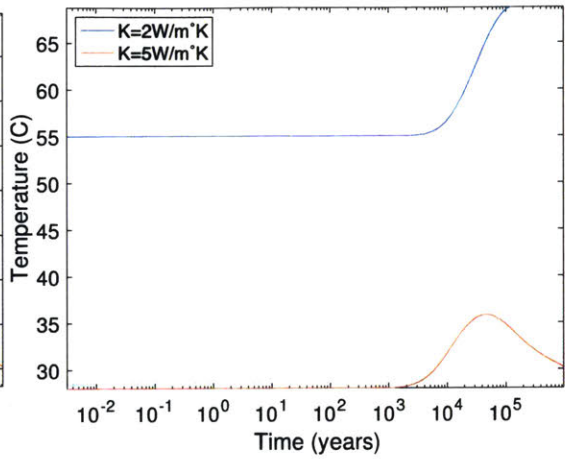

(b) Temperature at 2km below repository surface and at borehole axis.

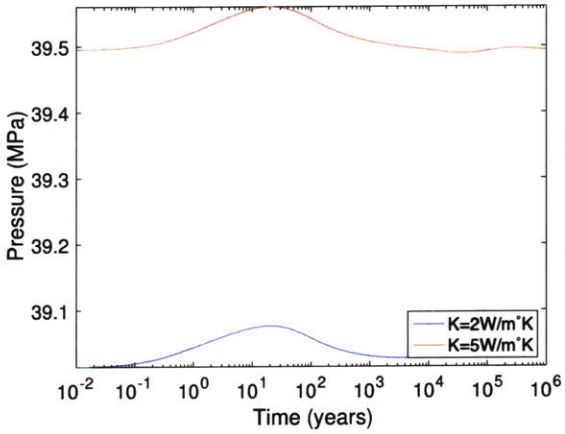

(c) Pressure at 4 km below repository surface and 10 m from borehole axis.

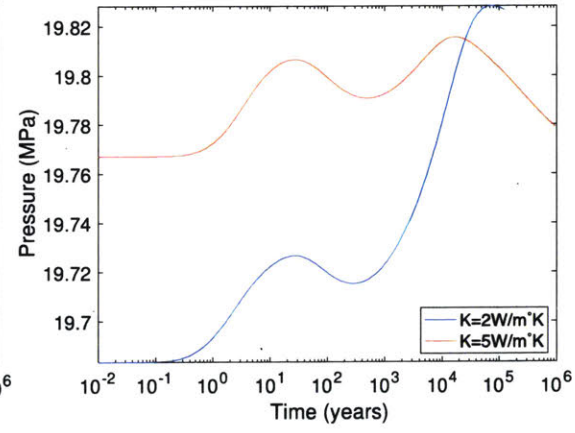

(d) Pressure at 2 km below repository surface and at borehole axis.

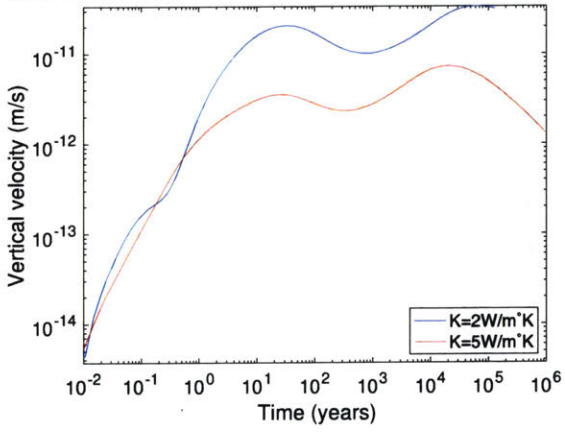

(e) Vertical Darcy velocity at 4 km below repository surface and 10 m from borehole axis.

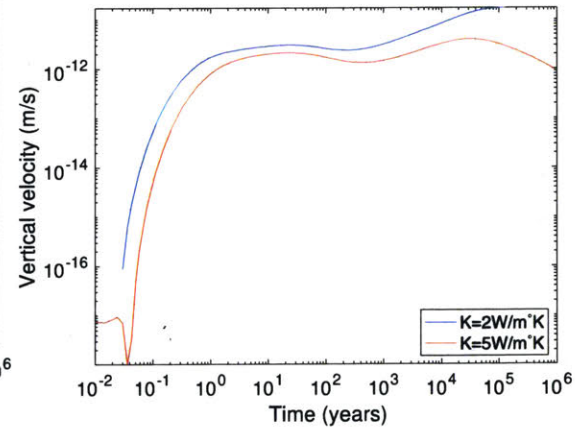

(f) Vertical Darcy velocity at 2 km below repository surface and at borehole axis.

Figure 5-51: Temperature, pressure and Darcy vertical velocity comparison at two different points in the rock, for rock thermal concavities of 2 and 5 W/m°K.

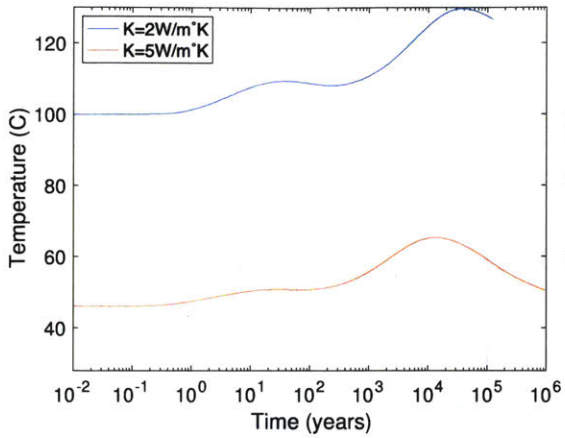

(a) Temperature at 4 km below repository surface and 10 m from borehole axis.

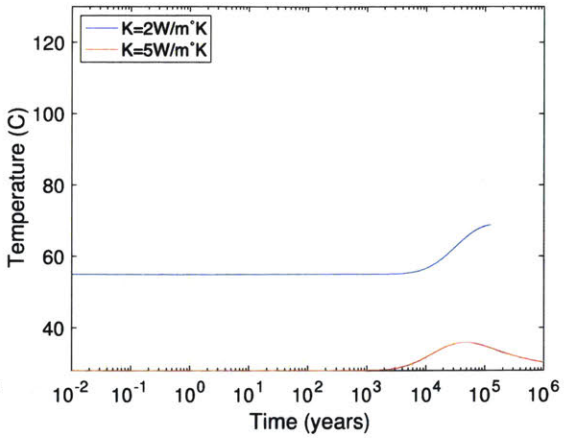

(b) Temperature at 2 km below repository surface and at borehole axis.

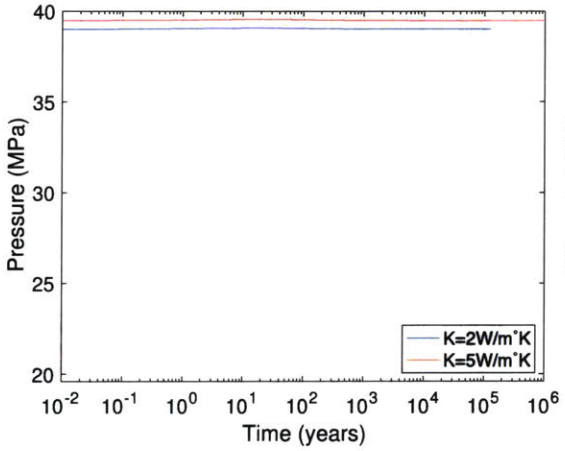

(c) Pressure at 4 km below repository surface and 10 m from borehole axis.

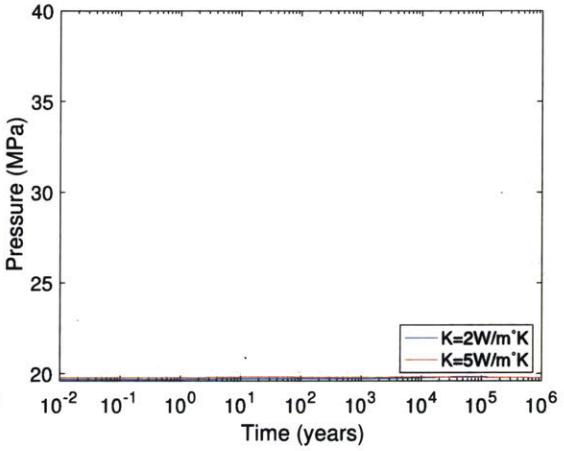

(d) Pressure at 2 km below repository surface and at borehole axis.

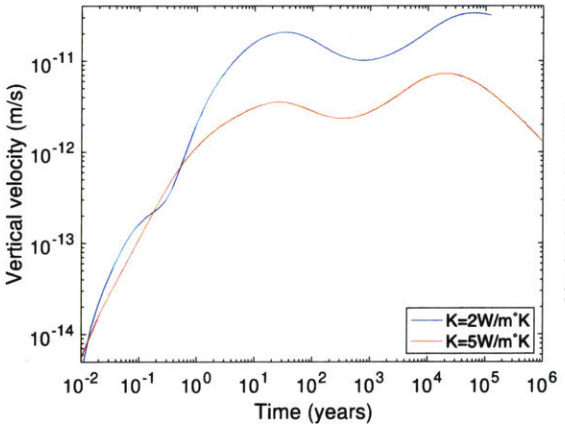

(e) Vertical Darcy velocity at 4 km below repository surface and 10 m from borehole axis.

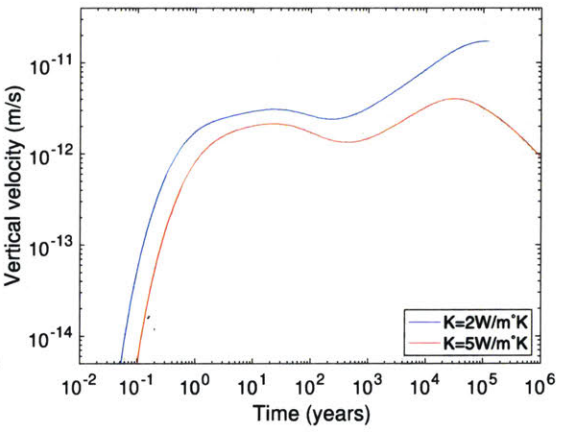

(f) Vertical Darcy velocity at 2 km below repository surface and at borehole axis.

Figure 5-52: Same as Figure 5-51 but plots are at same scale, not all curves visible.

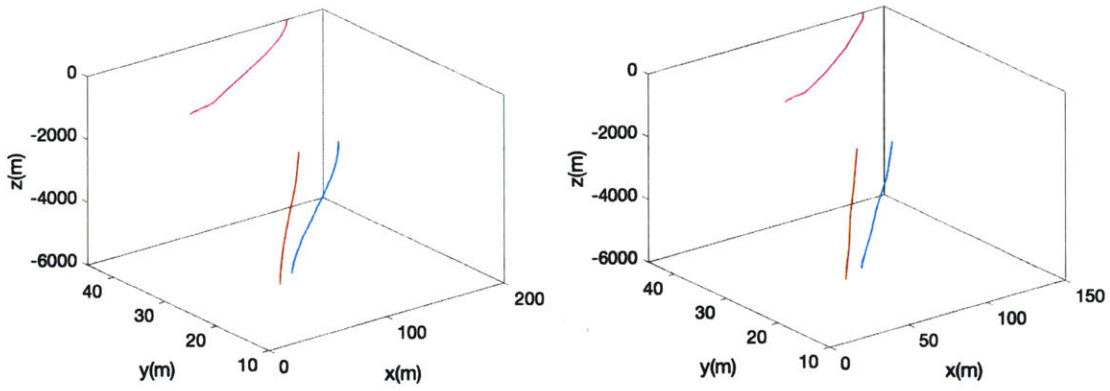

(a) Thermal conductivity of 2 W/m°K. (b) Thermal conductivity of 5 W/m°K.

Figure 5-53: Trajectories for fluid particles that start at 4 km below repository surface up to 1 million years from emplacement for two rock thermal conductivity 2 and 5 W/m°K.

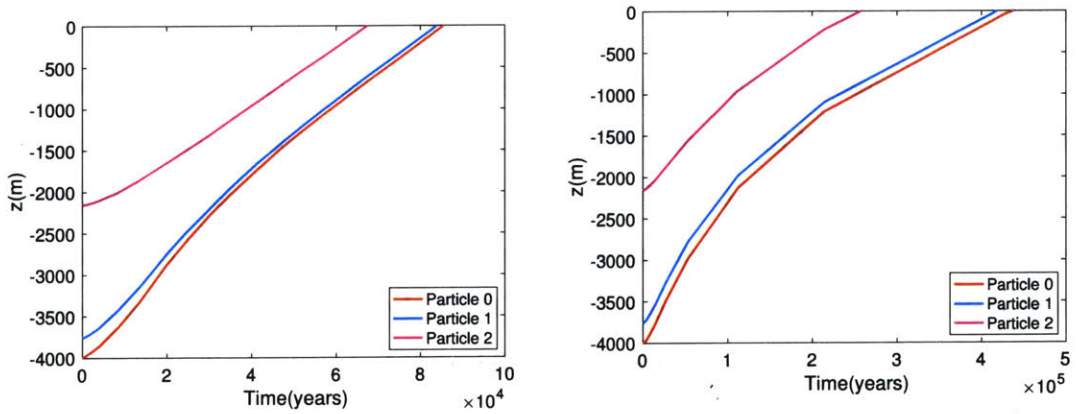

(a) Thermal conductivity of 2 W/m°K. (b) Thermal conductivity of 5 W/m°K.

Figure 5-54: Lagrangian vertical coordinate as a function of time for the three particles presented in Tables 5.7 and 5.8.

Table 5.8: Breakthrough times in years for a thermal conductivity of 5 W/m°K for the four different interpolation methods implemented.

$\vec{x}(0)$	Int.1	Int.2	Int.3	Int.4
(10,10,-4000)	370,089	438,632	486,284	486,284
(20,10,-3756)	360,279	419,199	456,691	456,691
(87,45,-2156)	225,179	256,990	280,208	280,208

ing the borehole spacing. Figure 5-55 shows a comparison of temperature evolution near the central borehole for two different borehole separations, 200m and 400m. The temperature maximum for the 400m configuration is significantly smaller than in the 200m configuration, and occurs at a later time, as expected, for both the cap rock and the emplacement zone. In addition to heat radial diffusion, for a widely spaced borehole configuration, the effect of heat loss through the surface can become non negligible, also causing a significant reduction of the temperature maximum seen in the rock. Pressure and vertical fluid velocity decrease significantly by increasing the borehole separation, as shown in Figure 5-55 as well. In addition, by looking at the three selected particles for comparison, shown in Table 5.9, we see that particles that start near the nuclear waste in the waste emplacement zone do not break through the surface.

From an engineering point of view, increasing borehole spacing has the drawback of increasing the cost of the repository because of the larger area of rock needed. Area of land suitable to host spent fuel for permanent disposal will increase, increasing the cost of the repository and potential social rejection. As a reference, each borehole has an overall cost estimate of about $40M\$$[1] (P. Brady et al., 2012). These economic aspects are beyond the scope of this thesis. However, from a scientific point of view, increasing borehole spacing is a viable option. This thesis considered the reference value of 200 m borehole spacing proposed by SANDIA in the early development of the borehole concept.

[1] All costs considered are in 2011 US$ and approximately for 2011 expenses.

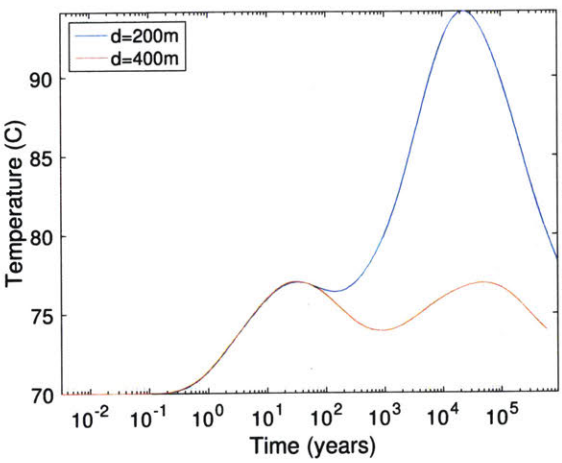

(a) Temperature at 4 km depth and at 10 m from central borehole axis.

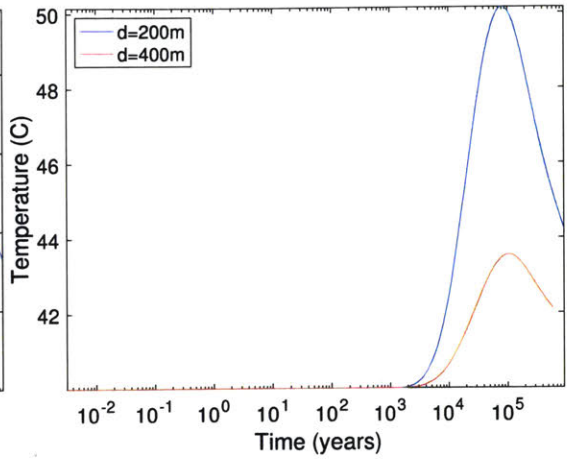

(b) Temperature at 2 km depth and at 10 m from central borehole axis.

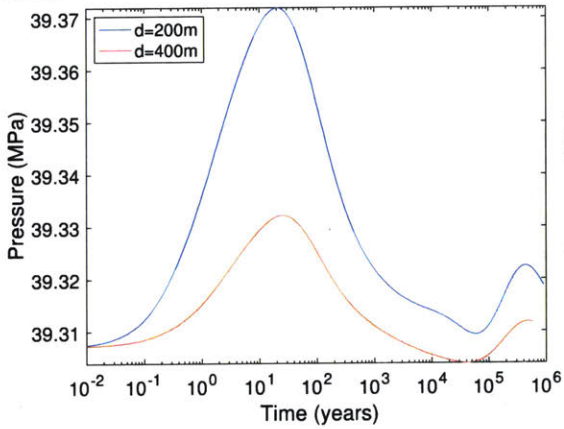

(c) Pressure at 4 km depth and at 10 m from central borehole axis.

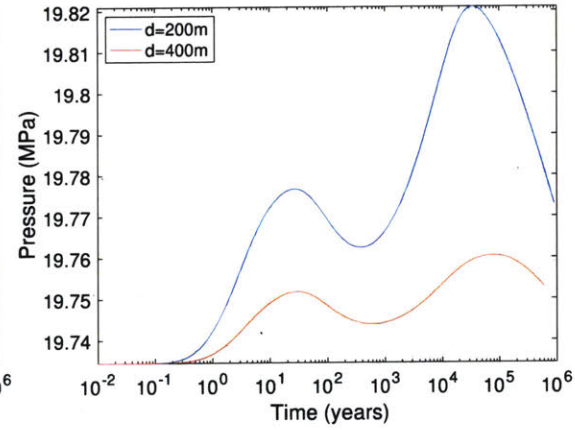

(d) Pressure at 2 km depth and at 10 m from central borehole axis.

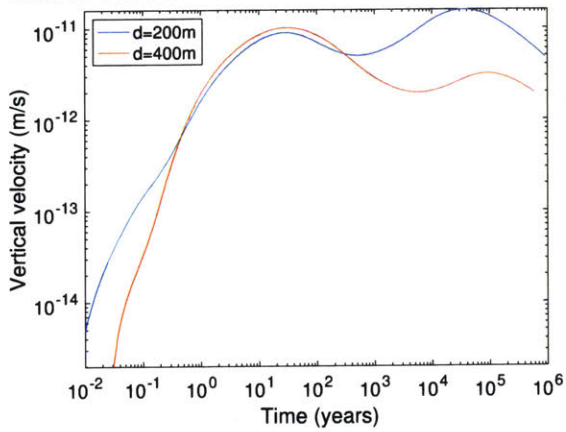

(e) Vertical velocity at 4 km depth and at 10 m from central borehole axis.

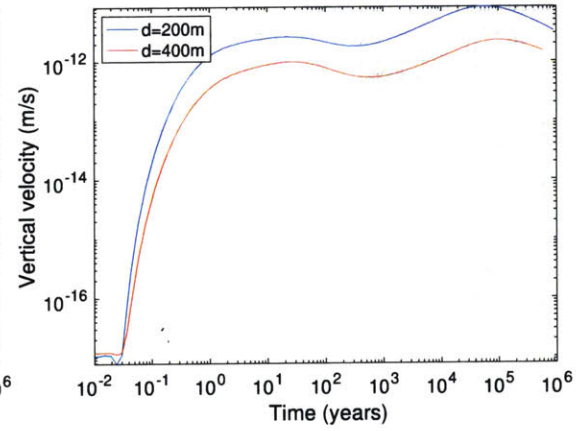

(f) Vertical velocity at 2 km depth and at borehole axis.

Figure 5-55: Temperature, pressure, fluid density and viscosity in the rock before waste emplacement, comparison for two borehole spacing.

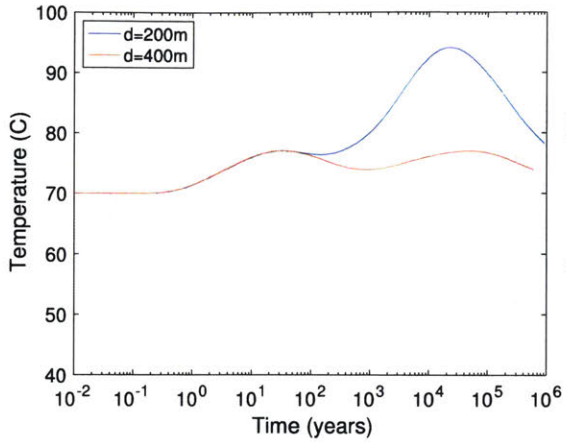

(a) Temperature at 4 km depth and at 10 m from central borehole axis.

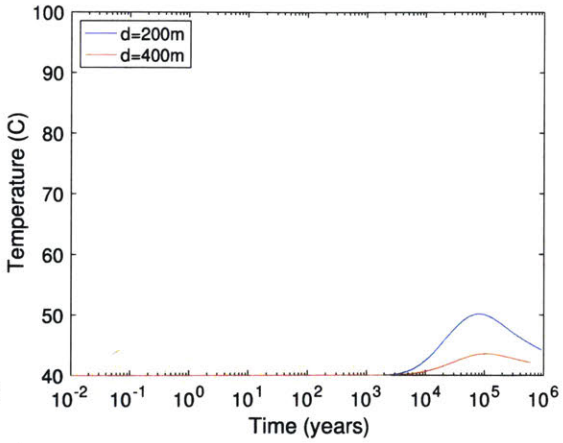

(b) Temperature at 2 km depth and at 10 m from central borehole axis.

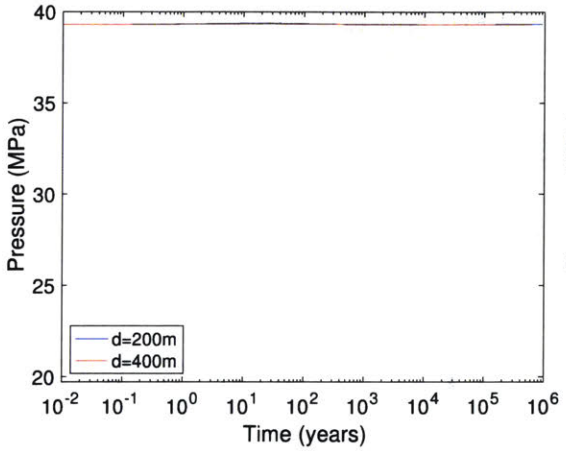

(c) Pressure at 4 km depth and at 10 m from central borehole axis.

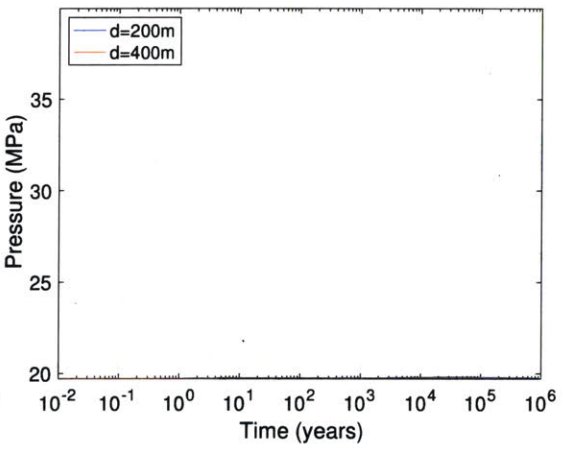

(d) Pressure at 2 km depth and at 10 m from central borehole axis.

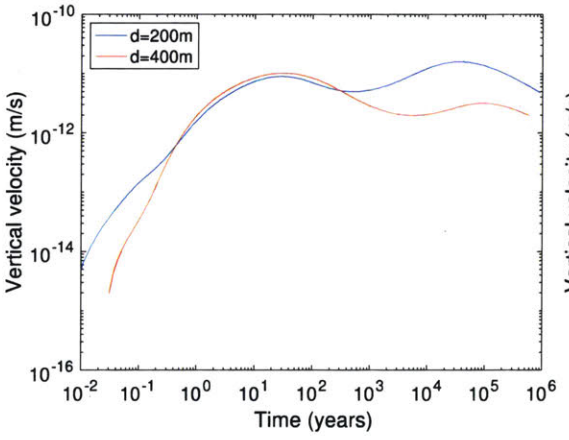

(e) Vertical velocity at 4 km depth and at 10 m from central borehole axis.

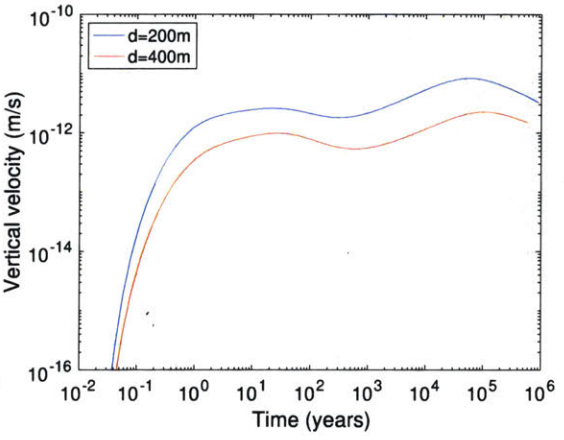

(f) Vertical velocity at 2 km depth and at borehole axis.

Figure 5-56: Same as Figure 5-55 but plots are at same scale, not all curves visible.

Table 5.9: Breakthrough times in years for a repository of 400 m of borehole spacing for the three reference particles, using the first interpolation method Int1.

$\vec{x}(0)$	$\vec{x}(t_f)$
(10,10,-4000)	Does not reach the surface
(20,10,-3756)	Does not reach the surface
(87,45,-2156)	Reach the surface at 431,044 years

5.5.6 Comparison between PWR and TWR

One of the major goals of this research is to investigate the effects of TWR spent fuel on the host rock when compared to PWR spent fuel disposal in a deep borehole repository.

Figure 5-57 presents a comparison of the rock temperature at 4 km below the repository surface, which corresponds to the middle plane of the waste emplacement zone, and at 10 meters radially from the central borehole vertical axis, for TWR and PWR spent fuel generated temperatures for both the semi-infinite and infinite array respectively. The TWR results show that there is a local maximum of temperature at around 33 years of waste emplacement. This maximum is 7°C greater than the local natural temperature before waste emplacement, at the depth considered. For the next hundred years the temperature decreases as a consequence of diminished heat source and radial diffusion of heat. Following this local minimum, temperature increases again due to borehole interference, which refers to the superposition of the heat waves from different boreholes. This trend culminates in an absolute maximum of temperature of 94.6°C at 80,000 years after emplacement.

From the comparison of the temperatures produced by the spent fuel of PWR, we observe that temperatures for TWR are smaller than temperatures for PWR spent fuel for the first 3,200 years. After this time, TWR temperatures surpass PWR results, reaching an absolute maximum higher than PWR, 94.6°C and 89°C respectively. This corresponds to larger total heat released, due to lower decline in the log-log scale of heat production as a function of time. For comparison Figure 5-57 includes the temperature at the same location for the infinite array. The Figure shows

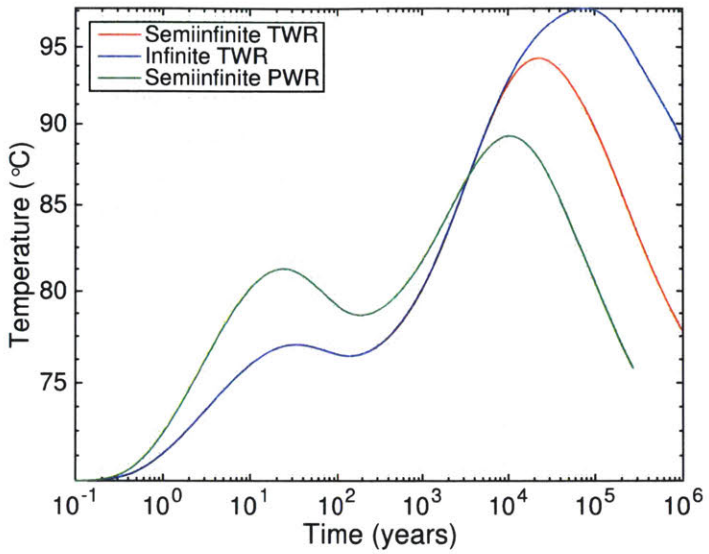

Figure 5-57: Temperature evolution in the host rock at 4 km depth 10 m from the central borehole axis.

that, for the initial time period after emplacement, there is no difference between the temperature evolution near the borehole for the infinite and semi-infinite configuration. This behavior is expected because the initial physical conditions are the same for both models. The infinite array configuration predicts a slightly higher absolute maximum of temperature, 97.6°C, at a later time, 75,000 years. Intuitively, this can be attributed to the interference of a larger number of boreholes (infinite). Therefore, the infinite model serves as a conservative reference case for a thermal analysis, with a low computational cost.

Figure 5-58 presents a comparison of the vertical Darcy velocity above the central borehole (at 2 km depth) for both TWR and PWR spent fuel for two rock permeabilities, 10^{-16} and 10^{-17}m^2. From the comparison we can see that initially (before about 300 years) the groundwater flow for the TWR spent fuel exhibits smaller Darcy velocities than for the PWR spent fuel due to the smaller heat induced expansion. As shown previously, initial rock temperature is smaller for TWR than PWR repository. After 3,200 years, TWR induced groundwater fluid velocities are higher than PWR ones, but the difference in magnitude is not large. The groundwater velocities for TWR and PWR, are similar in the order of 10^{-12} m/s (0.0315 mm/yr).

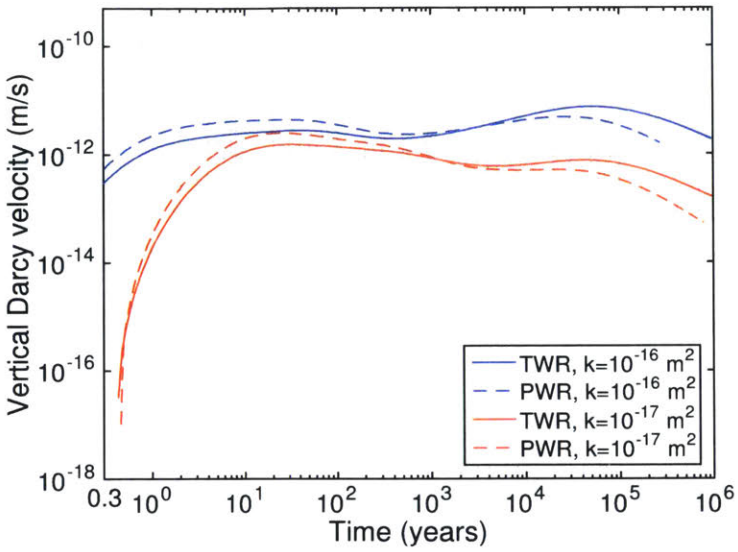

Figure 5-58: Comparison of Darcy vertical velocity above the center borehole at 2 km depth for TWR and PWR spent fuel, for two rock permeabilities.

5.5.7 Implications of particles from the waste zone reaching the repository surface

Spent fuel contains long-lived radionuclides, such as:

1. ^{129}I: with 15.7 million years half-life
2. ^{238}U: with 4.5 billion years half-life
3. ^{232}Th: with 14.05 billion years half-life.

Once radionuclides reach the surface they can be transported by water bodies or dispersed by wind. Among all the radionuclides, ^{129}I is the one that poses significant concern because of its high mobility in the environment (Scott, Hu, Yao, Xin, & Lian, 2015). Iodine has 37 known isotopes, all of them radioactive with the only exception of ^{127}I. ^{129}I is highly soluble in water. Additionally, iodine easily combines with other elements once released into the environment, including organic matter in soil (EPA, 2017a). Once released from the spent fuel, ^{129}I will remain in the environment for millions of years given its extremely long half-life. In contrast, the isotope ^{131}I with

a short half-life of 8 days, decays away completely in a time scale of the order of months.

Another reason of concern is the biological affinity of iodine (Scott et al., 2015). External exposure to large amounts of iodine can cause burns to the eyes and skin. Internal exposure can affect the thyroid gland. The thyroid gland uses iodine to produce thyroid hormones and cannot distinguish between radioactive iodine and stable nonradioactive iodine (American Thyroid Association, 2019). Moreover, once iodine is released into the biosphere, humans can ingest it in water, food, or even breath it in. In addition, animals consuming grass contaminated with iodine incorporate iodine to the milk . Humans eating milk products will be internally exposed to iodine (Schöne, Spörl, & Leiterer, 2017) . The iodine that is absorbed by the thyroid gland, can potentially result in thyroid cancer if the exposure levels are considerably high.

Chapter 6

Conclusions and Future Work

The final disposal of high-level nuclear waste remains a major unresolved issue worldwide (Faybishenko et al., 2016a). To date, 62 years after the first commercial nuclear reactor became operational in the US, the country has not finalized a plan to permanently dispose of the spent fuel (Blue Ribbon Commission, 2012). The high-level waste is stored at nuclear facilities waiting for the government to find a solution. In this sense, everything remains to be done.

Spent nuclear fuel contains many isotopes, some of them with extremely long half-lives (such as 4.468 billion years for ^{238}U) and high activity (such as ^{99}Tc[1]). For this reason, spent nuclear fuel must be deposited in a system that guarantees safety for such a time scale. To date, geological disposal remains the only long-term solution available for final disposal (Birkholzer, Houseworth, & Tsang, 2019). In the geological disposal the main barrier of the radioactive material is the natural host rock. Disposal systems use additionally a metallic canister, a filler material in the canisters, and a back-fill material.

The conclusions of this thesis are divided into research conclusions, conclusions regarding current codes, and future work.

[1] ^{99}Tc has low specific activity but it is produced in such quantities that its overall contribution to decay heat is large.

6.1 Research problem addressed

Well designed nuclear waste disposal systems must ensure the confinement of radionuclides over one million years (EPA, 2008; NRC Proposed Rule 10 CFR, 2019). Other than human intrusion, groundwater transport is the only important mechanism for escape of radioactive material from the repository after any leakage from the canisters. Radionuclides can dissolve and be transported in water by fluid convection and diffusion (molecular diffusion and mechanical dispersion). Diffusion is a very slow process (the effective diffusion coefficient in porous media is of the order of $10^{-12}m^2/s$ (Szántó et al., 2002)), while convection is the most significant mechanism for radionuclide transport.

The Traveling Wave Reactor (TWR) is an innovative reactor design whose spent fuel disposal is studied in this thesis. The majority of the nuclear reactors operating in the world and in the US are Pressurized Water Reactors (PWR) or Boiling Water Reactors (BWR), which are cooled with light water. This stands in contrast to the TWR, which is cooled with liquid sodium. The TWR produces significantly more energy per unit of fuel than a conventional PWR: 180 MWd/kgHM versus 60 MWd/kgHM (Gilleland et al., 2016a), which makes this reactor extremely appealing. This type of reactor is also capable of sustaining fission when fueled primarily with natural or depleted uranium. Little enrichment is needed to start fission, and no chemical reprocessing of the spent fuel is required. The TWR requires about one-fiftieth the uranium needed by a LWR to produce the same amount of electricity. In the long term, using depleted uranium reduces the amount of waste in the overall nuclear life cycle (Ellis et al, 2010). As a consequence of this higher fuel efficiency, the TWR spent fuel is more radioactive and produces significantly larger amounts of heat when compared to conventional nuclear waste (see Chapter 1 for quantitative data of the differences between PWR and TWR spent fuel).

The goal of this research is to determine if it is safe to dispose of TWR spent fuel in deep borehole repositories. Assuming canister failure, this work studies if the groundwater flow generated by the spent fuel decay heat, in addition to the natural

geothermal flux from the Earth, would result in radionuclide breakthrough to the surface. In addition, this research compares TWR spent fuel disposal to that of a conventional PWR.

The work presented in this thesis consists of coupled thermal-hydraulic simulations of a deep borehole repository with the aim of determining if TWR spent fuel can be disposed of using this method. The numerical simulations were carried out with our modified version of the newest open source code, FALCON, which is based on the MOOSE framework. This work represents the first investigation of a disposal method for TWR spent fuel and as such, the work may be useful in the future for repository design revision, preparation of licensing documents, or evaluation of license applications.

6.2 Conclusions regarding the codes

The numerical modeling used the MOOSE framework in a high-performance computing environment. Use of such capabilities made large scale simulations possible using multiple processors in parallel.

However, due to errors in the source code, validated PWR results could not be replicated. In particular, there was a bug in the MOOSE framework and an error in how FALCON solves the mass balance equation. We addressed these errors by modifying the source code. Results of the newly modified code were in excellent agreement with previously validated results of FALCON 2011. We reported these errors to the authors of the code, and made the corrected code available on GitHub.

This thesis is much more than just an output of findings about nuclear waste disposal systems by using computational fluid dynamics and computational mechanics. Because we used open source code, such as MOOSE, we have been exposed to all the phases of code development in the past few years. MOOSE is a relatively new computational framework that was introduced for the first time in 2009 with very limited capabilities. From the early stages of this research up to date, MOOSE has undergone significant changes. These ranged from different versions of MOOSE, newer numeri-

cal implementations of the physical equations to be solved, and new classes; to new versions of the C++ language, which introduced new features, enlarged standard libraries, new modules, and more. Development of MOOSE documentation only began in the last year. MOOSE is under continuous development, and has a lot of potential to model many types of physics and coupling between them, but in order to leverage its capabilities, more documentation is essential. These past years of research have been primarily a tremendous learning experience in code development for modeling multi-physics.

6.3 Research conclusions

6.3.1 General conclusions

We examined vertical deep boreholes in granite as a final disposal method for the TWR and for PWR spent fuel. The numerical simulations focused on two simplified conceptual geometries: infinite and semi-infinite. The infinite model of the nuclear waste repository assumes that the array of boreholes extends infinitely in x and y directions. Under this assumption, the symmetries of this problem reduce the model domain to only one-quarter of a borehole. It was found that this model:

1. Provides an accurate estimation of the thermal field at low computational cost.

2. Predicts no radionuclide migration to the surface.

This geometry does not allow convection between the heated rock around the boreholes and the relatively colder adjacent natural rock. As a consequence, upward fluid particle displacement in the cap rock is less than 390 m, significantly smaller than the waste depth of 3 km. Particle trajectories can be approximated by vertical lines. Some particles reach a maximum displacement before one million years have elapsed, after which the vertical coordinates decreases. This can be explained by a relative cooling of the rock. The further away from the heat source, the earlier in time the maximum occurs. For particles closer to the heat source the depth is a

monotonically increasing function of time. This geometry provides a good thermal analysis with a very low computational cost. However, the infinite arrangement of identical boreholes is not appropriate for performance assessment of a nuclear waste repository since it imposes unrealistic restrictions on the flow. Therefore a finite cluster of boreholes needed to be studied.

The second conceptual model of the nuclear waste repository considered in this work is the semi-infinite array of boreholes within the natural host rock, infinite in one direction and finite in the perpendicular direction. Unlike the first model, this one includes the undisturbed host rock surrounding the entire repository. It was found that this model:

1. Can model flow patterns that predict radionuclide migration to the surface of the repository.

2. Has a high computational cost that requires the use of high performance computing capabilities.

The more realistic semi-infinite array of boreholes with relatively colder host rock was investigated over one million years, as required by nuclear regulatory agencies. We found that (considering the reference parameters detailed in Chapter 5):

1. For the first 25 years after waste emplacement the warmest region of the domain is at the boreholes. As time progresses, the emplacement region (volume of rock that includes the boreholes) reaches an almost uniform temperature, higher than the adjacent natural host rock. Heat diffuses with time from the central heated region to the rest of the domain, radially like the behavior of a point source (circular isotherms). The zone of highest temperature is at the central borehole (in the dimension of the repository in which the number of boreholes is finite.).

2. The rock near the central borehole and within the disposal depth (4km below repository surface) reaches a first local maximum temperature of 76°C at 33 years after nuclear waste emplacement. After that, the rock cools down. An extended period of elevated temperatures with a significantly larger absolute second maximum of 96°C begins after 5,000 years.

3. The spent fuel produced a long-term thermal disturbance in the volume of rock surrounding the boreholes for the duration of the simulation, i.e. at no point in the one million year time span did the rock return to its pre-waste-emplacement temperature.

4. No melting conditions for the granite, the canister, or the assembly were found.

5. A convective cell several kilometers in diameter sets in on both sides of the borehole array at around 1000 years after waste emplacement. This convection cell remains stationary until the end of the simulation.

6. At early times there is a high-pressure (pore pressure larger than initial) zone surrounding the nuclear waste. This is caused by the expansion of the pore water that is being heated. Later in time, fluid instabilities are triggered by the presence of a colder fluid in the adjacent rock volume. A zone of relative depression (with respect to initial conditions) is established at the bottom of the nuclear waste. At 182,000 years the maximum pore pressure increase is 69,316 Pa. At 472,000 years this maximum over pressure is 52,354 Pa.

7. Thermally induced fluid flow driven by heat from the radioactive material has significant potential for the upward transport of dissolved radionuclides. Single-phase conditions exist throughout the model domain during the simulations, which prevents rapid leakages to the surface that would have been driven by the highly buoyant gas phase.

8. Supercritical conditions are not reached in the fluid, which avoids enhanced convection due to high gradients of densities.

9. Points closer to the mid-emplacement depth (between 3 and 5 km below the surface), are exposed to higher temperature than the cap-rock. There is a first maximum of temperature and a higher absolute maximum later in time as a consequence of all the incident heat waves from the adjacent boreholes, as was seen for the infinite array configuration. For points in the cap rock (above the

waste), there is only one maximum of temperature at a significantly later time, which corresponds to the required time for the heat wave to reach the location considered.

10. Vertical fluid velocity increases with time to a first local maximum, then decreases. Later in time, the fluid velocity reaches a second maximum significantly higher than the first one. This second maximum corresponds to the convective cell that remains through the end of the simulation. This behaviour is verified by all the points analyzed (waste zone and cap-rock) with the exception of the point outside the projected area of the waste, which observes fluid velocity later in time. The fluid velocity is higher closer to the midpoint of the central borehole. Velocities in the waste emplacement zone are larger than in the cap-rock, with a difference of about one order of magnitude. The upward vertical fluid velocity above the edge of the borehole array is smaller than the vertical fluid velocity above the central borehole of the arrangement. Points located outside the projected area of the borehole array ($x > 2000$m) exhibit smaller velocity.

11. Above the waste, thermally driven vertical upward fluid flow persists for an extended period of time, which leads to fluid particle breakthrough to the repository surface at a time scale of 145,000 years. Once initiated, vertical fluid flow persists in the waste disposal zone for the duration of the one million year simulation.

12. Fluid pore velocity above the central borehole, induced by the large-scale convective cell through the repository, is of the order of 3 mm/yr.

13. Heat transport in the repository is conduction dominated, since the advective heat transport term is negligible.

Based on modeling the thermo-hydraulic process (excluding any coupled thermal or mechanical deformation of the porous medium) for the duration of one million years, with a rock permeability of 10^{-16}m^2 and the reference borehole spacing of 200 meters, this research concludes that the deep borehole disposal concept cannot

guarantee radionuclide containment for spent fuel from a TWR. It was found that particles that start at the emplacement depth (z dimension) at 10m from the borehole axis (radial dimension), break through to the surface at 145,000 years. The diffusion time for a radionuclide to propagate from the nuclear waste to the point considered, 10 m away, varies with each radionuclide. Different isotopes diffuse at different rates, which is consistent with intuition. This ranges from 5,000 years to 260,000 years or more. As a consequence, we found that radionuclides from the spent fuel can break though the surface at a time scale of about 145,000 years. This changes for different assumptions as will be shown in the sensitivity analysis presented in Section 6.3.3. In those cases conclusions 11) and 12) change. In addition, for the reference repository considered, it was found that radionuclides rising directly from the waste break through the surface at 120,000 years.

6.3.2 Comparison between PWR and TWR

Simulations have shown that TWR spent fuel produces lower temperature than PWR spent fuel for the first 3,200 years. After this time, TWR temperatures surpass PWR results, reaching an absolute maximum higher than that for PWR: 95°C and 89°C respectively. In addition, groundwater flow magnitudes similar to those of PWR spent fuel were obtained. Preliminary calculations show that fluid particles for PWR spent fuel disposal also reach the surface of the repository, for the reference borehole spacing and permeability. Based on these simulations, we conclude that TWR spent fuel produces effects on the host rock comparable to conventional spent fuel (PWR).

6.3.3 Repository performance sensitivity

We also investigated how the nuclear waste repository responds to different repository parameters, such as rock permeability, rock thermal conductivity, and borehole spacing.

6.3.3.1 Rock permeability

We found that repository isolation performance is highly dependent on rock permeability. We identified breakthrough to the surface of particles from the waste emplacement zone for rock permeability of $10^{-16}m^2$ or larger. For this reference permeability, particles that start at the waste emplacement zone at 10 m from the central borehole axis reach the surface at a time scale of 145,000 years. Smaller permeabilities, such as $10^{-17}m^2$, did not permit particles from the waste zone to break through to the surface. For the reference case, the breakthrough time accounts also for the diffusion time from the nuclear waste to the location considered. This diffusion time varies with the species of radionuclide. Some, such as (^{237}Np), diffuse in a relatively short time, while others, such as (^{125}I), require a length of time that is comparable to the advective transport time of 145,000 years. Even longer diffusion times are exhibited by (^{36}Cl, ^{85}Sr), and others. In summary, the overall breakthrough time of some radionuclides, but not all, is less than the one million year limit. Moreover, effective rock permeabilities in the field are usually larger than this value; therefore a deep borehole disposal system for TWR with spacing of 200 meters cannot guarantee complete radionuclide isolation from Earth's surface for one million years, as required by the particular interpretation of current regulation predicated in this work.

6.3.3.2 Rock thermal conductivity

Repository performance is highly affected by rock thermal conductivity. This property of the rock highly depends on the chemical and mineral composition of the rock. Thermal conductivity depends also on fluid content: type of fluid and degree of saturation of the pore space. The presence of water in the pores increases the thermal conductivity (enhances the heat transport in the porous medium). Water thermal conductivity is small (compared to granite, and still higher than air), but it has no significant effect given the small amount of volume in granite, 1%.

Rocks with low thermal conductivity (similar to shale) lead to high temperatures, higher pore pressures and larger fluid velocity after waste emplacement. This can

produce rock failure conditions if the pore pressure increase is large enough. In addition, particles that start at the waste emplacement zone break through the surface at significantly earlier times, around 90,000 years.

On the other hand, highly conductive rocks (similar to salt) produce the inverse effect. Particles that start at the waste emplacement zone break through the surface at significantly larger times on the order of 380,000 years. This clearly shows that rock thermal conductivity has a significant effect on repository performance.

6.3.3.3 Borehole spacing

In addition, our study shows that the rock temperature maximum is significantly reduced by increasing borehole spacing. Boreholes with a larger spacing of 400 meters (instead of the reference value of 200 m) exhibit a second maximum of temperature of the rock in the waste emplacement zone significantly smaller than the one seen in the reference case of 200 m, and even smaller than the first one reached at 33 years. This configuration did not show particles that start at the waste emplacement zone breaking through to the surface. This shows that the distance between boreholes is an important factor for the escape of radioactive material into the biosphere.

We found that for the reference repository, particles directly from the waste are capable of migrating to the surface about 30,000 years earlier than particles at 10 meters from the central borehole. This shows that the borehole itself is the critical path of radionuclide migration to the surface. It represents the shortest path and the highest velocity zone (warmest region and more permeable than the unaltered host rock). The reference repository configuration exhibits particle breakthrough to the surface at 120,000 years, significantly earlier than the required one million year minimum. This shows that we cannot guarantee radioactive material containment for one million years, and that coupled chemical models must be included in the analysis. Chemical models that account for radioactive decay are critical to determine if, given the time scale, the inventory of radionuclides reaching the surface is harmless to humans. In addition, diffusion into the rock matrix and retardation due to sorption and desorption in the host rock could contribute to the reduction of radionuclides

migration. Once all these effects are modeled for one million years, a more realistic evaluation can be obtained for spent fuel disposal.

6.4 Future Work

6.4.1 Experimental work

The US needs an underground research laboratory to provide the researchers with the experimental data and in-situ behavior of rock at great depths: high pressure, high temperature, and chemically reducing conditions. This information is essential to include in the numerical models that will be used to predict the behavior of the rock for one million years.

In addition, limited experimental studies on the chemistry of different radionuclides in the porous media represents a significant knowledge gap identified in the literature. Studies to determine the water solubility kinetics, constants of equilibrium, and sorption and desorption coefficients are essential. These need to be addressed for the radionuclide inventory of both TWR and PWR spent fuel.

These data will help to understand the physical processes occurring very deep underground and the transport of radionuclides in the porous medium. In turn this will allow scientists and policymakers to make more informed decisions about whether deep borehole repositories are a viable method for disposal of high-level nuclear waste.

6.4.2 Numerical modeling

6.4.2.1 Coupled physics

Future numerical modeling needs to include more coupled physics:

1. Rock deformation due to thermal effects on the rock skeleton and mechanical effects due to pore pressure and external loads must be analyzed. These two effects produce changes in porous media permeability and porosity, which in turn affect the fluid flow. In addition, the rock volumetric deformation affects the pressure in the pores, which in turn governs the resulting fluid flow.

2. Chemical processes that include radioactive decay, radionuclide dispersion into the porous rock, and retardation effects (sorption and desorption processes) must be analyzed as well. Further coupled chemical transport models must be analyzed to accurately evaluate if particles brought to the surface at a time scale of 145,000 years represent a significant risk for human life.

To date, previous studies on deep borehole repositories have considered only continuous media. For a more realistic representation of the sites, it is essential to include fractures in the modeled domain, which have a significant effect on the fluid flow and breakthrough times.

In addition, water salinity can result in slower convection (Claesson, 1992; Claesson et al., 1992; B. Arnold, Hadgu, Clayton, & Herrick, 2011; Lubchenko et al., 2015), and therefore should be analyzed. The ultimate goal of the numerical modeling efforts must address the problem of predicting the thermo-hydraulic-mechanical-chemical response of a repository that includes fractures in the porous medium.

6.4.2.2 Geometries

Recommendations for future work include the modeling of a finite cluster of boreholes and the use of a deeper numerical domain to avoid possible boundary effects. This modeling has to rely on high performance computing capabilities, since the computational cost of these simulations is high. These future investigations will strengthen the reliability of the performance assessment conducted here.

6.4.3 Engineering aspects

A parallel area of research that needs to be addressed is the study and design of borehole seals. The seals must be made from a medium of extremely low permeability to prevent radionuclide escape. This requires extensive research on how these characteristics can be achieved in the lab and in the field.

This thesis considers a deep-borehole design where the boreholes are vertical with a waste emplacement length of 2 km, but we want to highlight that canister failure

conditions may exist due to vertical loads on the canisters in combination with mud pressure normal to the canister surface. Analytical mechanical calculations on the cylindrical canister (excluding any thermal effect) indicate failure conditions in the material of the canister. These calculations were confirmed with ADINA Structures Structures Finite Element model (Rodríguez-Buño et al., 2016), a mechanical model that assumes linear elasticity.

Another significant failure mechanism is that the rock surrounding the borehole is at failure due to stress concentration around the hole. This creates a high permeability rock volume around the borehole that hosts nuclear material, providing a path for radionuclides escape to the surface. These issues need to be addressed in detail in any future study.

6.5 Impact of the current results

This research contributes greatly to the understanding of deep borehole repositories in granite host rock as an option for final disposal of both Light Water Reactor and Traveling Wave Reactor spent fuel. This thesis provides a valuable resource for TWR licensing efforts in the United States.

This research identified failure in the containment of the radioactive material in the deep borehole repositories depending on different properties considered. These findings, which are detailed in Chapter 5, are summarized in Table 6.1. All the previous studies carried out on the borehole type repository (for PWR spent fuel) did not report waste particles breaking through to the surface (B. Arnold et al., 2011; Hadgu & Arnold, 2010). This is the first work reporting this and presenting breakthrough times. As detailed in Chapter 5, our results show that the reference spacing of boreholes of 200 meters does not guarantee radionuclide containment, but a larger spacing should remediate this problem.

Previous studies supporting the feasibility of deep borehole repositories rely on water salinity at great depths (Claesson, 1992; Lubchenko et al., 2015) to avoid the transport of radioactive material to the repository surface. However, there are

Table 6.1: Breakthrough times for different deep borehole repositories considered. k, K and d represent the intrinsic permeability (m^2), the thermal conductivity (W/m°K) and the borehole spacing (m) respectively.

$k(m^2)$	K(W/m°K)	d(m)	Breakthrough time
10^{-16}	3	200	145,000 years
10^{-17}	3	200	None
10^{-16}	2	200	90,000 years
10^{-16}	5	200	380,000 years
10^{-16}	3	400	None

not enough experimental data supporting the existence of salty water in granitic formations at large depths (of the order of 10 km), as a general feature, to form a design safety basis for deep borehole repositories. Very limited experimental data for just a few locations (mainly at the Lake Superior region of Canada) and relative shallow depth (up to 2 km) have been found in the literature (Frape et al., 2003).

This study found cases in which material from the emplacement zone reaches the surface, and also cases in which this does not happen. Specifically for the proposed reference spacing of 200 m, this work demonstrates that deep borehole disposal is unacceptable by current regulatory standards in the United States. However, with modifications, the deep borehole disposal is viable. Further study of these modifications is warranted by the results of this work.

Appendix A

Codes for particle tracking

Main.cpp

```
#include <iostream>
#include <random>
#include <chrono>
#include <ctime>
#include <iomanip>

#include "filemanager.h"
#include "particlemanager.h"


using namespace std;

void generateData(InitData &d)
{
    d.file_sufix = "csv_data/data_";
    d.file_elems = "csv_data/elements.txt";
    d.dir_out = "csv_data_out/";
    d.file_cant = 182;
```

```
    d.user_vars = {"V_:0", "V_:1", "V_:2", "porepressure", "
       temperature", "density_water", "viscosity_water"};
    d.times = {....};
    d.node_cant = 852003;

    // interpoaltion types:
//  d.interp = InitData::none;
    d.interp = InitData::vel_time;
//    d.interp = InitData::pred_corrector;
//    d.interp = InitData::by_element;
}

vector<Coord> createPoints()
{
    // an array of points:
    vector<Coord> pts = {{10, 10, -4000}, {20, 10, -3756},
       {87, 45, -2156}};

    // random points:
    int cant = 3;
    random_device rd;
    mt19937 gen(rd());
    uniform_real_distribution<> dis_x(10, 800);
    uniform_real_distribution<> dis_y(0, 100);
    uniform_real_distribution<> dis_z(-6000, -2000);

    for (int i = 0; i < cant; i++) {
        pts.push_back({static_cast<double>(dis_x(gen)),
                       static_cast<double>(dis_y(gen)),
                       static_cast<double>(dis_z(gen))});
```

```
    }
    return pts;
}

int main()
{
    cout << "___particle_path_2019_" << endl << endl;

    InitData miData;
    generateData(miData);

    FileManager fm(miData);
    vector<ResultInfo> res;

    vector<Coord> points = createPoints();
    for(auto p : points) {
        ResultInfo r;

        chrono::steady_clock::time_point start = std::chrono
            ::steady_clock::now();

        ParticleManager pm(miData, p);
        fm.firstFile();
        while (fm.haveFiles()) {
            fm.openFile();
            if(fm.isFileOpen()) {
                pm.partTime(fm.getIndex());
                pm.partCoord(fm.getFile());
                pm.partNodePos();
                pm.partVarsData(fm.getFile());
```

```
                pm.partDeltaCoords();
                pm.dataPrint();
                pm.partRegister();
            }
            fm.closeFile();
            fm.nextFile();
            if(pm.endCondition()) {
                r.zero_zeta = pm.timeWhenReachSurface();
                r.part_surface = true;
                cout << endl << "***␣This␣particle␣reached␣
                    surface␣in␣time:␣";
                cout << r.zero_zeta << "␣years" << endl;
                break;
            }
        }
        chrono::steady_clock::time_point end = std::chrono::
            steady_clock::now();
        auto total = chrono::duration_cast<std::chrono::
            seconds>(end - start).count();
        r.interp = miData.getInterpType();
        r.part_ini = pm.getTrayectory()[0];
        r.duaration = total;
        cout << "simulation␣last:␣"<< total << "seconds" <<
            endl;

        fm.recordToFile(pm.getTrayectory());
        res.push_back(r);
    }
    fm.recordToInfoResulta(res);
    return 0;
```

```
}
```

filemanager.h

```
#ifndef FILEMANAGER_H
#define FILEMANAGER_H

#include <fstream>
#include <iostream>
#include <sstream>
#include <vector>
#include "type_defs.h"


class FileManager
{
public:
    FileManager(InitData &d);

    void firstFile();
    bool haveFiles();
    void openFile();
    bool isFileOpen();
    void nextFile();
    void closeFile();

    void recordToFile(vector<Particle> particles);
    void recordToInfoResulta(vector<ResultInfo> rs);

    int getIndex();
```

```
    ifstream &getFile();
    int getCol(ifstream &file, string name);

    static void moveToLine(ifstream &file, int lines); //
       move lines in file

private:
    string getFileName(int index);
    void getNodesCoords();                    // all simulation
       coords
    void getVariablesNames();

    ifstream in;                    // the file
    InitData &data;                 // info so we can start the
       simulation
    int file_index;                 // the actual index file that
        I'm working now
};

#endif // FILEMANAGER_H
```

filemanager.cpp

```
#include "filemanager.h"

FileManager::FileManager(InitData &d) : data(d)
{
    file_index = 1;
    cout << "___total nodes: " << data.node_cant << endl;
    cout << "___obtaining node coordinates ..." << endl;
```

```
    getNodesCoords();
    cout << "   getting variables names ..." << endl;
    getVariablesNames();
    cout << "   starting simulation ... " << endl;
    cout << "initial state: " << endl;
}

void FileManager::firstFile()
{
    file_index = 1;
}

bool FileManager::haveFiles()
{
    return file_index < data.file_cant;

}

void FileManager::openFile()
{
    in.open(getFileName(file_index));
}

bool FileManager::isFileOpen()
{
    if(in.fail()) {
        cout << "file cannot open ... continue" << endl;
        return false;
    } else {
        cout << file_index << ": working with " <<
```

```
            getFileName(file_index) << "..." << endl;
        return true;
    }
}

void FileManager::nextFile()
{
    file_index++;
}

void FileManager::closeFile()
{
    if(in.is_open())
        in.close();
}

void FileManager::recordToFile(vector<Particle> particles)
{
    static int record_index = 0;

    ofstream out(data.dir_out + "particle_0" + to_string(
       record_index) + ".csv");
    out << "time,node_id,x,y,z,dx,dy,dz";
    for(auto v : particles[0].vars) {
        out << "," << v.first;
    }
    out.precision(12);
    out << endl;
    for(auto p : particles) {
        out << p.time << "," << p.coords.id << ",";
```

```
            out << p.coords.x << "," << p.coords.y << "," << p.
                coords.z << ",";
            out << p.dcoords.x << "," << p.dcoords.y << "," << p.
                dcoords.z;
            for(auto v : p.vars) {
                out << "," << v.second;
            }
            out << endl;
        }
        out.close();
        record_index++;
}

void FileManager::recordToInfoResulta(vector<ResultInfo> rs)
{
        ofstream res(data.dir_out + "_result.txt");
        res << "particle track 2019 " << endl;
        res << "interp type: ";
        res << data.getInterpType() << endl;
        res << "-------------------------------" << endl << endl;
        int index = 1;
        for(auto r : rs) {
            res << "particle " << index << "->" << endl;
            res << "  initial coord: [" << r.part_ini.coords.x <<
                ", " << r.part_ini.coords.y << ", " << r.part_ini
                .coords.z << "]" << endl;
            if(r.part_surface)
                res << "  reach surface in: " << r.zero_zeta << "
                    years." << endl;
            else
```

```
            res << "  never reach surface" << endl;
        res << "total duration: " << r.duaration << endl;
        res << "**********   " << endl;
        index++;
    }
    res.close();
}

int FileManager::getIndex()
{
    return file_index;
}

ifstream &FileManager::getFile()
{
    return in;
}

int FileManager::getCol(ifstream &file, string name)
{
    int file_col = -1;
    string line;
    getline(file, line);
    stringstream reg(line);
    string subreg;
    for (int c = 0; getline(reg, subreg, ','); ++c) {
        if(subreg == name) {
            file_col = c;
            break;
        }
```

```
    }
    return file_col;
}

string FileManager::getFileName(int index)
{
    string NUM;
    if(index < 10)
        NUM = "000" + to_string(index);
    else if (index < 100)
        NUM = "00" + to_string(index);
    else if (index < 1000)
        NUM = "0" + to_string(index);
    else
        NUM = to_string(index);
    string out = data.file_sufix + NUM + ".csv";  // file
       path
    return out;
}

void FileManager::getNodesCoords()
{
    ifstream file(data.file_sufix + "0000.csv");
    int col_id = getCol(file, "PedigreeNodeId");
    file.seekg(0);
    int col_x = getCol(file, "Points:0");
    moveToLine(file, 2);
    Coord c;
    string line;
    string substr;
```

```
    for (int i = 0; i < data.node_cant; ++i) {
        getline(file, line);
        stringstream reg(line);
        c.n_pos = i + 1;
        int j = 0;
        while (getline(reg, substr, ',')) {
            if(j == col_id) {
                c.id = stoi(substr);
            } else if(j == col_x) {
                c.x = stod(substr);
                getline(reg, substr, ',');
                c.y = stod(substr);
                getline(reg, substr, ',');
                c.z = stod(substr);
                break;
            }
            j++;
        }
        data.node_coords.push_back(c);
    }
    file.close();
    cout << endl << "\t... finishing getting coords..." <<
       endl;
}

void FileManager::getVariablesNames()
{
    ifstream file(data.file_sufix + "0000.csv");

    string line;
```

```
    getline(file, line);
    stringstream reg(line);

    string subreg;
    while (getline(reg, subreg, ','))
        data.vars_names.push_back(subreg);
    file.close();
}

void FileManager::moveToLine(ifstream &file, int lines)
{
    file.seekg(0);
    for (int i = 1; i < lines; ++i)
        file.ignore(numeric_limits<streamsize>::max(), '\n');
}
```

particlemanager.h

```
#ifndef PARTICLEMANAGER_H
#define PARTICLEMANAGER_H

#include <limits>
#include <cmath>
#include <iostream>
#include <iomanip>
#include <vector>
#include <string>
#include <fstream>
#include <sstream>
#include <map>
```

```
#include "type_defs.h"
#include "filemanager.h"

using namespace std;


class ParticleManager
{
public:
    ParticleManager(InitData &d, const Coord pnt_initial);

    void partTime(int file_index);        // time step of the
       corresponding file
    void partCoord(ifstream &in);         // particle coords
    void partNodePos();                   // node position of
       the present particle
    void partVarsData(ifstream &in);      // data for this
       particle
    void partDeltaCoords();
    void partRegister();                  // write particles
       to collection
    bool endCondition();                  // when particle
       reaches surface
    void dataPrint();                     // to terminal

    double timeWhenReachSurface();        // time particle
       reaches zero
    vector<Particle> getTrayectory();

private:
```

```
    Coord interpVelInTime(ifstream &in);          // velocity
       at one node, at two different times
    Coord interpPredCorrector(ifstream &in);      // predictor
        corrector
    Coord interpByElement(ifstream &in);          // elements

    InitData &data;              // info to start application
    Particle part_actual;        // present particle
    vector<Particle> parts;      // trajectory
};

#endif // PARTICLEMANAGER_H
```

particlemanager.cpp

```
#include "particlemanager.h"

ParticleManager::ParticleManager(InitData &d, const Coord
   pnt_initial) : data(d)
{
    // first particle initialization from file 0 where mostly
        of data is 0
    part_actual.time = 0.0;
    part_actual.dtime = 0.0;
    part_actual.coords = pnt_initial;
    partNodePos();
    part_actual.dcoords = {0.0, 0.0, 0.0};
    for(auto vn : data.user_vars)
        part_actual.vars[vn] = 0.0;
    ifstream in(data.file_sufix + "0000.csv");
    partVarsData(in);
```

```
    in.close();
    partRegister();
    dataPrint();
    cout << "<---Tratectory--->" << endl;
}

void ParticleManager::partTime(int file_index)
{
    part_actual.time = data.times[static_cast<size_t>(
        file_index)];
    part_actual.dtime = part_actual.time - parts[parts.size()
        -1].time;
}

void ParticleManager::partCoord(ifstream &in)
{
    Particle pOld = parts[parts.size()-1];
    Coord c;

    switch (data.interp) {
    case InitData::vel_time:
        c = interpVelInTime(in);
        break;
    case InitData::pred_corrector:
        c = interpPredCorrector(in);
        break;
    case InitData::by_element:
        c = interpByElement(in);
        break;
    default:
```

```
        c.x = pOld.vars["V_:0"];
        c.y = pOld.vars["V_:1"];
        c.z = pOld.vars["V_:2"];
    }

    part_actual.coords.x = pOld.coords.x + c.x * part_actual.
       dtime * 100.0;
    part_actual.coords.y = pOld.coords.y + c.y * part_actual.
       dtime * 100.0;
    part_actual.coords.z = pOld.coords.z + c.z * part_actual.
       dtime * 100.0;
}

void ParticleManager::partNodePos()
{
    Coord c = part_actual.coords;
    int64_t pos = -1; int id = -1;
    double final, act;
    final = data.node_coords[0].distance(c);
    if(final < numeric_limits<double>::epsilon()) {
        pos = data.node_coords[0].n_pos;
        id = data.node_coords[0].id;
    } else {
        for(size_t i = 1; i < data.node_coords.size(); ++i) {
            act = data.node_coords[i].distance(c);
            if(act < numeric_limits<double>::epsilon()) {
                pos = data.node_coords[i].n_pos;
                id = data.node_coords[i].id;
                break;
            } else if(act < final) {
```

```
                final = act;
                pos = data.node_coords[i].n_pos;
                id = data.node_coords[i].id;
            }
        }
    }
    part_actual.coords.n_pos = pos;
    part_actual.coords.id = id;
}

void ParticleManager::partVarsData(ifstream &in)
{
    string line;
    FileManager::moveToLine(in, static_cast<int>(part_actual.
       coords.n_pos + 2));
    getline(in, line);
    stringstream reg(line);
    string subre;
    for (size_t c = 0; getline(reg, subre, ','); ++c) {
        string vn = data.vars_names[c];
        for(auto &v : part_actual.vars) {
            if(vn == v.first) {
                v.second = stod(subre);
                break;
            }
        }
    }
}

void ParticleManager::partDeltaCoords()
```

```
{
    part_actual.dcoords.x = (part_actual.coords.x - parts[
        parts.size()-1].coords.x) * 1000;
    part_actual.dcoords.y = (part_actual.coords.y - parts[
        parts.size()-1].coords.y) * 1000;
    part_actual.dcoords.z = (part_actual.coords.z - parts[
        parts.size()-1].coords.z) * 1000;
}

void ParticleManager::partRegister()
{
    parts.push_back(part_actual);
}

bool ParticleManager::endCondition()
{
    return (part_actual.coords.z >= 0.0);
}

void ParticleManager::dataPrint()
{
    cout << "Particle: " << endl;
    cout << "time: " << part_actual.time << " --- dt: " <<
        part_actual.dtime << endl;
    cout << "dcoords (x1000): <" << part_actual.dcoords.x <<
        ", " << part_actual.dcoords.y << ", " << part_actual.
        dcoords.z << ">";
    cout << endl;
    cout << "coords: [" << part_actual.coords.x << ", " <<
        part_actual.coords.y << ", "
```

```
            << part_actual.coords.z << "];  n_pos: " <<
               part_actual.coords.n_pos << ", n_id: " <<
               part_actual.coords.id << endl;

    for(auto vn : part_actual.vars)
        cout << vn.first << " = " << vn.second << endl;
    cout << endl;
}

double ParticleManager::timeWhenReachSurface()
{
    double t0 = parts[parts.size() - 2].time;
    double t1 = parts[parts.size() - 1].time;
    double z0 = parts[parts.size() - 2].coords.z;
    double z1 = parts[parts.size() - 1].coords.z;
    double t = 0.0;
    t = (t0 - t1) / (z0 - z1) * (0 - z0) + t0;
    cout << "pre_last: " << "t: " << parts[parts.size() - 2].
       time * 3.17098e-8 << ", z: " <<  parts[parts.size() -
       2].coords.z << endl;
    cout << "last: " << "t: " << parts[parts.size() - 1].time
        * 3.17098e-8 << ", z: " <<  parts[parts.size() - 1].
       coords.z << endl;
    return t * 3.17098e-8;
}

vector<Particle> ParticleManager::getTrayectory()
{
    return parts;
}
```

```
Coord ParticleManager::interpVelInTime(ifstream &in)
{
    Coord c;
    Particle pOld = parts[parts.size()-1];
    int vel_pos = 0;

    in.seekg(0);
    string line;
    getline(in, line);
    stringstream reg(line);
    string subreg;
    for (int c = 0; getline(reg, subreg, ','); ++c) {
        if(subreg == "V_:0") {
            vel_pos = c;
            break;
        }
    }
    FileManager::moveToLine(in, static_cast<int>(pOld.coords.
       n_pos + 2));
    string line2;
    getline(in, line2);
    stringstream reg2(line2);
    string subreg2;
    for (int vp = 0; getline(reg2, subreg2, ','); ++vp) {
        if(vp == vel_pos) {
            c.x = stod(subreg2);
            getline(reg2, subreg2, ',');
            c.y = stod(subreg2);
            getline(reg2, subreg2, ',');
```

```
            c.z = stod(subreg2);
            break;
        }
    }
    c.x = (c.x + pOld.vars["V_:0"]) * 0.5;
    c.y = (c.y + pOld.vars["V_:1"]) * 0.5;
    c.z = (c.z + pOld.vars["V_:2"]) * 0.5;

    return c;
}

Coord ParticleManager::interpPredCorrector(ifstream &in)
{
    Coord c;
    Particle pOld = parts[parts.size()-1];
    int vel_pos = 0;

    part_actual.coords.x = pOld.coords.x + pOld.vars["V_:0"]
       * part_actual.dtime * 100.0;
    part_actual.coords.y = pOld.coords.y + pOld.vars["V_:1"]
       * part_actual.dtime * 100.0;
    part_actual.coords.z = pOld.coords.z + pOld.vars["V_:2"]
       * part_actual.dtime * 100.0;

    partNodePos();

    in.seekg(0);
    string line;
    getline(in, line);
    stringstream reg(line);
```

```
    string subreg;
    for (int c = 0; getline(reg, subreg, ','); ++c) {
        if(subreg == "V_:0") {
            vel_pos = c;
            break;
        }
    }
    FileManager::moveToLine(in, static_cast<int>(part_actual.
       coords.n_pos + 2));
    string line2;
    getline(in, line2);
    stringstream reg2(line2);
    string subreg2;
    for (int vp = 0; getline(reg2, subreg2, ','); ++vp) {
        if(vp == vel_pos) {
            c.x = stod(subreg2);
            getline(reg2, subreg2, ',');
            c.y = stod(subreg2);
            getline(reg2, subreg2, ',');
            c.z = stod(subreg2);
            break;
        }
    }

    c.x = (c.x + pOld.vars["V_:0"]) * 0.5;
    c.y = (c.y + pOld.vars["V_:1"]) * 0.5;
    c.z = (c.z + pOld.vars["V_:2"]) * 0.5;

    return c;
}
```

```
Coord ParticleManager::interpByElement(ifstream &in)
{
    Coord c;
    Particle pOld = parts[parts.size()-1];
    int nid = pOld.coords.id;
    vector<vector<int>> els;    // nodes_id with its elements


    // 1. get all elements that contain node 'nid'
    ifstream fel(data.file_elems);
    string line, subreg;
    int cant = 0;
    while (getline(fel, line)) {    // each line has 8 numbers
        that all are the ids
        istringstream reg(line);
        while (getline(reg, subreg, '␣')) {  // iterate each
            node in one line
            if(nid == stoi(subreg)) {
                reg.seekg(0);
                vector<int> ns;
                while (getline(reg, subreg, '␣')) {
                    ns.push_back(stoi(subreg));
                }
                els.push_back(ns);
                cant++;
                break;
            }
        }
        if(cant == 8) {    // to reduce computational cost. We
```

```
            know that each element has 8 nodes at least
            break;
        }
    }

    // 2. get the nodes coords
    vector<array<Coord, 8>> cs;            // all coords -- 4 u
        8
    for(auto e : els) {
        unsigned i = 0;
        array<Coord, 8> temp;
        for(auto n : e) {
            for(auto nc : data.node_coords) {
                if(n == nc.id) {
                    temp[i] = nc;
                    break;
                }
            }
            i++;
        }
        cs.push_back(temp);
    }

    // 3. get the element who contain the particle
    array<Coord, 8> ns;
    for(auto e : cs) {
        ns = e;
        // 3.1.1. get > x
        double max_x = ns[0].x;
        for(unsigned i = 1; i < ns.size(); ++i) {
```

```
        if(max_x < ns[i].x) {
            max_x = ns[i].x;
        }
    }
    // 3.1.2. get the < x
    double min_x = ns[0].x;
    for(unsigned i = 1; i < ns.size(); ++i) {
        if(min_x > ns[i].x) {
            min_x = ns[i].x;
        }
    }
    // si estoy entre las x
    if(pOld.coords.x >= min_x && pOld.coords.x <= max_x)
       {
        // 3.2.1. get the > y
        double max_y = ns[0].y;
        for(unsigned i = 1; i < ns.size(); ++i) {
            if(max_y < ns[i].y) {
                max_y = ns[i].y;
            }
        }
        // 3.2.2. get the < y
        double min_y = ns[0].y;
        for(unsigned i = 1; i < ns.size(); ++i) {
            if(min_y > ns[i].y) {
                min_y = ns[i].y;
            }
        }
        if(pOld.coords.y >= min_y && pOld.coords.y <=
           max_y) {
```

```
                // 3.2.1. get the > z
                double max_z = ns[0].z;
                for(unsigned i = 1; i < ns.size(); ++i) {
                    if(max_z < ns[i].z) {
                        max_z = ns[i].z;
                    }
                }
                // 3.2.2. get the < z
                double min_z = ns[0].z;
                for(unsigned i = 1; i < ns.size(); ++i) {
                    if(min_z > ns[i].z) {
                        min_z = ns[i].z;
                    }
                }
                if(pOld.coords.z >= min_z && pOld.coords.z <=
                    max_z) {
                    break;
                }
            }
        }
    }

// 4. speed of the element
int vel_pos = 0;
in.seekg(0);
string line3;
getline(in, line3);
stringstream reg(line3);
string subreg3;
for (int c = 0; getline(reg, subreg3, ','); ++c) {
```

```
        if(subreg3 == "V_:0") {
            vel_pos = c;
            break;
        }
    }
    Coord sum;
    for(auto n : ns) {
        FileManager::moveToLine(in, static_cast<int>(n.n_pos
            + 2));
        string line2;
        getline(in, line2);
        stringstream reg2(line2);
        string subreg2;
        double nvx = 0.0, nvy = 0.0, nvz = 0.0;
        for (int vp = 0; getline(reg2, subreg2, ','); ++vp) {
            if(vp == vel_pos) {
                nvx = stod(subreg2);
                getline(reg2, subreg2, ',');
                nvy = stod(subreg2);
                getline(reg2, subreg2, ',');
                nvz = stod(subreg2);
                break;
            }
        }
        sum.x += nvx;
        sum.y += nvy;
        sum.z += nvz;
    }
    if(ns.size() > 0) {
        c.x = sum.x / ns.size();
```

```
            c.y = sum.y / ns.size();
            c.z = sum.z / ns.size();
        }
        fel.close();
        return c;
}
```

type defs.h

```
#ifndef TYPE_DEFS_H
#define TYPE_DEFS_H

#include <limits>
#include <cmath>
#include <vector>
#include <string>
#include <map>

using namespace std;


struct Coord
{
    Coord() {
        x = 0;
        y = 0;
        z = 0;
        n_pos = -1;
        id = -1;
    }
```

```
Coord(double _x, double _y, double _z) {
    x = _x;
    y = _y;
    z = _z;
    n_pos = -1;
    id = -1;
}
double x, y, z;
int64_t n_pos;
int id;

double distance(const Coord &c) {
    return sqrt(pow(x - c.x, 2) + pow(y - c.y, 2) + pow(z
        - c.z, 2));
}

bool operator==(const Coord &o) {
    double e = numeric_limits<double>::epsilon();
    if(fabs(x - o.x) < e && fabs(y - o.y) < e && fabs(z -
        o.z) < e)
        return true;
    return false;
}

string to_string() const {
    string cad = "[";
    cad += std::to_string(x) + ", " + std::to_string(y) +
        ", " + std::to_string(z) + "]";
    return cad;
}
```

```
};

struct Particle
{
    double time;
    double dtime;
    Coord coords;
    map<string, double> vars;        // variables data
    Coord dcoords;                   // the deltas
};

struct InitData
{
    string file_sufix;               // path and prefix of the
       file
    string file_elems;               // file with all the
       elements
    string dir_out;
    int file_cant;
    vector<string> user_vars;
    vector<double> times;
    int node_cant;
    vector<Coord> node_coords;  // all coords and pos of
       nodes
    vector<string> vars_names;  // all variables name in file

    enum interp_type {none, vel_time, pred_corrector,
       by_element} interp;

    string getInterpType() {
```

```
        switch (interp) {
        case InitData::none: return "none";
        case InitData::vel_time: return "vel_time";
        case InitData::pred_corrector: return "predictor-
            corrector";
        case InitData::by_element: return "by_element";
        }
        return "";
    }
};

struct ResultInfo
{
    bool part_surface = false;
    double zero_zeta = 0.0;
    string interp = "none";
    Particle part_ini;
    long long duaration;
};


#endif // TYPE_DEFS_H
```

Appendix B

Decay heat of TWR waste package

Nomenclature used in the formulas:

l: length of active fuel $[m]$, $l = 2.5m$

L: total waste canister length $[m]$, $L = 6m$

A_{hex}: area of hexagonal cross section of fuel assembly, i.e. area of a hexagon $[m^2]$, $A_{hex} = \frac{\sqrt{3}}{2}h^2$

h: twice the apothem of a hexagon $[m]$, $h = 16cm$

A_{can}: area of circular cross section of waste canister $[m^2]$, $A_{can} = \pi R_b^2$

R_b: radius of canister, i.e. radius of borehole $[m]$, $R_b = 17cm$

V_1: volume of active fuel length $[m^3]$, $V_1 = l \cdot A_{hex}$

V_2: volume of cylindrical waste canister $[m^3]$, $V_2 = L \cdot A_{can}$

$\bar{q}$: average linear power output for active fuel length $[W/m]$, provided by TerraPower, $\bar{q} = 458 \left(\frac{10}{t_c+t}\right)^{0.575}$

t: time elapsed since spent fuel emplacement in repository $[y]$

t_c: cooling time in pools: after removal from reactor, before emplacement $[y]$

q_1''': volumetric heat production of active fuel length $[W/m^3]$

q_2''': volumetric heat production of waste canister $[W/m^3]$

$$q_1''' = \frac{\bar{q}}{A_{hex}} \tag{B.1}$$

$$q_1'''V_1 = q_2'''V_2 \tag{B.2}$$

$$q_2''' = \frac{q_1'''V_1}{V_2} \tag{B.3}$$

$$q_2''' = \frac{\bar{q}}{A_{hex}}\frac{V_1}{V_2} \tag{B.4}$$

$$q_2''' = \frac{\bar{q}}{A_{hex}}\frac{l \cdot A_{hex}}{L \cdot A_{can}} \tag{B.5}$$

$$q_2''' = \frac{\bar{q}l}{A_{can}L} \tag{B.6}$$

$$q_2''' = \frac{\bar{q}l}{L\pi R_b^2} \tag{B.7}$$

$$q_2''' = 458\left(\frac{10}{t_c + t}\right)^{0.575}\left(\frac{2.5}{6\pi \cdot 0.17^2}\right) \tag{B.8}$$

$$q_2''' = 2101.9\left(\frac{10}{t_c + t}\right)^{0.575} \tag{B.9}$$

In analogy to PWR spent fuel decay heat, considering a cooling time of 25 years:

$$q_2''' = 2101.9\left(\frac{25}{25 + t}\right)^{0.575}\left(\frac{10}{25}\right)^{0.575} \tag{B.10}$$

Which can be expressed as:

$$q_2''' = 1241.1\left(\frac{25}{25 + t}\right)^{0.575} \tag{B.11}$$

Appendix C

Shape functions and Time stepper

Shape functions

MOOSE supports several shape function families: Lagrange, Hermite, Hierarchic, Monomial, and Clough-Toucher. Lagrange family and first order shape functions are the most common and default. Other families of interpolation function (Lagrange second order, third order Hermite) were tested, presenting a significant increase in the computational cost of the simulations and not affecting the solution. First order Lagrange polynomial were used in all the simulations.

Time stepper

In all the simulations we used an adaptive time stepper, SolutionTimeAdaptiveDT, from MOOSE. This time stepper increase or decrease the time step by a percentage, default value is 10%. The direction (increase or decrease) is chosen by the algorithm based on the processor time to compute the previous time steps. If the solver fails to converge the time step is decreased by a factor of 0.5. The initial time step for the time stepper was defined tobe 1×10^5 seconds (1.15 days) in all the simulations. Figure C-1 shows that as a general trend time step increases. However, Figure C-2 shows that there are occasions in which time stepper changed direction of time step change and reduced the time step. There are three times in which the solver did not converge and the time step was reduced by a factor of 0.5.

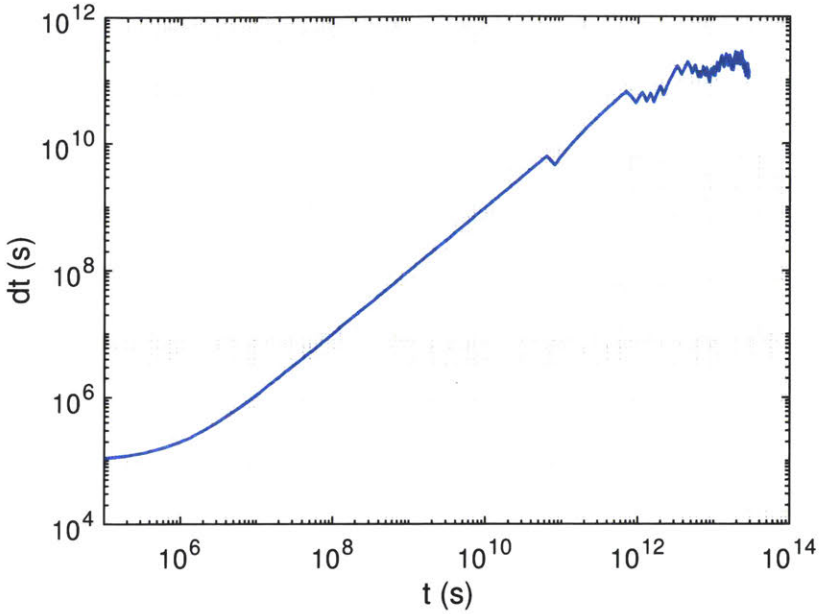

Figure C-1: Time step as a function of time, for the simulation of the semiinfinite array of boreholes considering a permeability of $10^{-16}\mathrm{m}^2$ and 773,410 elements in the mesh.

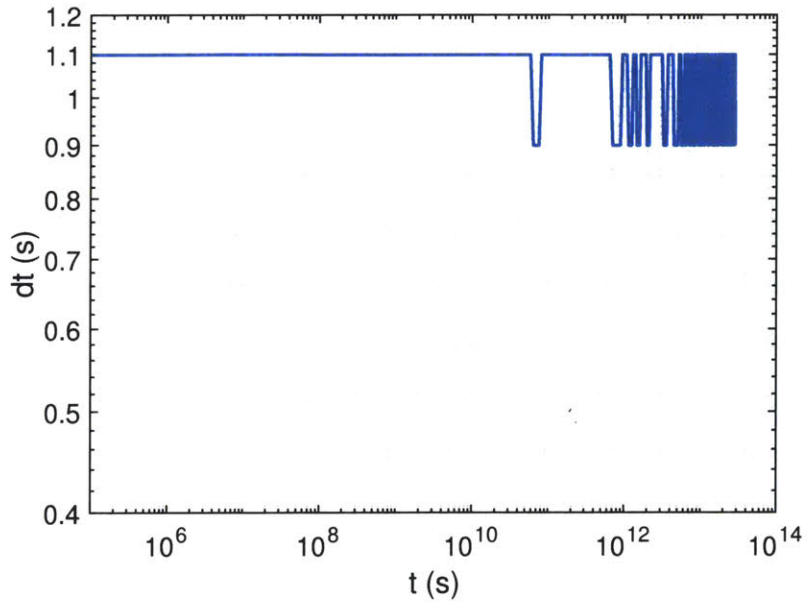

Figure C-2: Ratio of two consecutive time steps.

Appendix D

FALCON main kernel modifications

PTMassTimeDerivative.cpp

```
...
Real
PTMassTimeDerivative::
computeQpResidual()
{
  return _poro[_qp]*_drop[_qp]*TimeDerivative::
      computeQpResidual();
}
...
```

PTMassTimeDerivativeFD.cpp

```
...
Real
PTMassTimeDerivative_FD::
computeQpResidual()
{
  if(_t_step == 1)
    return _poro[_qp]*_drop[_qp]*TimeDerivative::
        computeQpResidual();
```

```
  else
    return _test[_i][_qp] * _poro[_qp] * (_wrho[_qp] -
        _wrho_old[_qp]) / _dt;
}
...
```

PTMassTimeDerivativeFull.cpp

```
...
Real
PTMassTimeDerivative_Full::
computeQpResidual()
Real
PTMassTimeDerivative_Full::
computeQpResidual()
{
  return _poro[_qp]*_drop[_qp]*TimeDerivative::
      computeQpResidual() + _test[_i][_qp]*_poro[_qp]*_drot[
      _qp]*_dTdt[_qp];
}
...
```

FALCON code is available at https://github.com/idaholab/falcon.

References

Ahrens, J., Geveci, B., & Law, C. (2005). *Paraview: An end-user tool for large data visualization, visualization handbook.* CRC Press.

American Physical Society Sites. (2019). *The revised radiation protection standards for the yucca mountain nuclear waste repository.* Retrieved from `https://www.aps.org/units/fps/newsletters/200901/vandenbosch.cfm#_edn4`

American Thyroid Association. (2019). *Nuclear radiation and the thyroid.* Retrieved from `https://www.thyroid.org/nuclear-radiation-thyroid/`

Andersson, J., & Skagius, K. (2011). *Long-term safety for the final repository for spent nuclear fuel at forsmark. main report of the sr-site project. volume i, ii and iii.* (Tech. Rep.). SKB.

Armand, G., Souley, M., Su, K., Renaud, V., & Wileveau, Y. (2006, 10). Hydromechanical response to a mine by test experiment in a deep claystone.

Arnold, B., Hadgu, T., Clayton, D., & Herrick, C. (2011). Thermal-hydrologic-chemical-mechanical modeling of deep borehole disposal. In *Ihlrwmc 2011, albuquerque, nm, april 10-14, 2011* (p. 527-533). Albuquerque, New Mexico.

Arnold, B., & Hagdu, T. (2013). Thermal-hydrologic modeling of a deepborehole disposal system. In *14th international high-level radioactive waste management conference.* Albuquerque, New Mexico.

Arnold, B. W., Brady, P. V., Bauer, S. J., Herrick, C., Pye, S., & Finger, J. (2011). *Reference design and operations for deep borehole disposal of high-level radioactive waste.* (Tech. Rep.). SANDIA.

Augustin, M., Caiazzo, A., Fiebach, A., Fuhrmann, J., John, V., Linke, A., & Umla, R. (2011, 11). An assessment of discretizations for convection-dominated convection-diffusion equations. *Comp. Meth. Appl. Mech. Engrg., 200*, 3395-3409. doi: 10.1016/j.cma.2011.08.012

Bates, E. (2015). *Optimization of deep boreholes for disposal of high-level nuclear waste.*

Bathe, K.-J. (2014). *Finite element procedures.* Prentice Hall, Pearson Education, Inc.s.

Bear, J. (1972). *Dynamics of fluids in porous media.* American Elsevier Publishing Company.

Belgian Nuclear Research Centre. (2019). *Hades underground laboratory.* Retrieved from `http://science.sckcen.be/en/Facilities/HADES` (Last accessed 31 May 2019)

Birkholzer, J., Houseworth, J., & Tsang, C.-F. (2019). *Geologic disposal of high-level radioactive waste—status, key issues, and trends.* Retrieved from `https://www.osti.gov/servlets/purl/1210901`

Blanco-Martín, L., Wolters, R., Rutqvist, J., Lux, K.-H., & Birkholzer, J. T. (2016). Thermal–hydraulic–mechanical modeling of a large-scale heater test to investigate rock salt and crushed salt behavior under repository conditions for heat-generating nuclear waste. *Computers and Geotechnics*, *77*, 120–133.

Blue Ribbon Commission. (2012). *Blue ribbon commission on america's nuclear future.* Retrieved from `https://www.energy.gov/sites/prod/files/2013/04/f0/brc_finalreport_jan2012.pdf` (Last accessed 14 September 2019)

Blum, R., & Bresnahan, C. (2015). *Linux command line and shell scripting bible, 3rd edition.* Wiley.

Bodvarsson, G. S., Birkholzer, J., Finsterle, S., Liu, H., Rutqvist, J., & Wu, Y. (2003). The use of Tough2/iTough2 in support of the Yucca Mountain Project: success and limitations . In *Proceedings, TOUGH Symposium 2003* (pp. 1–14). Berkeley, California.

Brady, P., Arnold, B., Altman, S., & Vaughn, P. (2012). *Deep borehole disposal of nuclear waste: Final report.* Retrieved from `https://pdfs.semanticscholar.org/8dd8/9e2bb1c3a122aed918b6595813ad5135ac45.pdf`

Brady, P. V., Arnold, B. W., Freeze, G. A., Swift, P. N., Bauer, S. J., Kanney, J. L., ... Stein, J. S. (2009). *Deep borehole disposal of high-level radioactive waste.* (Tech. Rep.). SANDIA.

Bucur, C., Popa, A., Arsene, C., & Olteanu, M. (2000, 01). Diffusion coefficients of critical radionuclides from radioactive waste in geological medium.

Carslaw, H., & Jaeger, J. (1959). *Conduction of heat in solids.* Oxford at the Clarendon Press.

Center for Nuclear Waste Regulatory Analyses San Antonio, T. (2011). *Regulatory perspectives on deep borehole disposal concepts.* Retrieved from https://www.nrc.gov/docs/ML1114/ML111470719.pdf (Last accessed 31 May 2019)

Cho, W., Kwon, S., & Choi, J. (2009). The thermal conductivity for granite with various water contents. *Engineering Geology, 107*(3), 167 - 171. Retrieved from http://www.sciencedirect.com/science/article/pii/S0013795209001434 doi: https://doi.org/10.1016/j.enggeo.2009.05.012

Chun-LiangZhang. (2018). Thermo-hydro-mechanical behavior of clay rock for deep geological disposal of high-level radioactive waste. *Journal of Rock Mechanics and Geotechnical Engineering, 10*(5), 992-1008.

Claesson, J. (1992). *Buoyancy flow in fractured rock with a salt gradient in the groundwater - an initial study.* (Tech. Rep.). SKB.

Claesson, J., Hellström, G., & Probert, T. (1992). *Buoyancy flow in fractured rock with a salt gradient in the groundwater. a second study of coupled salt and thermal buoyancy.* (Tech. Rep.). SKB.

Cohen, B. (1987). *Radon, a homeowner's guide to detection and control.* Consumer's Union, New York.

C++ reference. (n.d.). Available at https://en.cppreference.com/w/ (last accessed 2019/07/08).

DOE. (2016). *Energy department selects battelle team for a deep borehole field test in north dakota.* Retrieved from https://www.energy.gov/articles/energy-department-selects-battelle-team-deep-borehole-field-test-north-dakota

Earth & Environmental Sciences Area – Berkeley Lab. (2019a). *Stripa reports.* Retrieved from https://eesa.lbl.gov/publication-lists/stripa-reports/ (Last accessed 31 May 2019)

Earth & Environmental Sciences Area – Berkeley Lab. (2019b). *Stripa reports.* Retrieved from https://eesa.lbl.gov/publication-lists/stripa-reports/ (Last accessed 31 May 2019)

EPA. (2008). *Response to comments: Amendments to the public health and environmental radiation and indoor air.* (Tech. Rep.). Author. Retrieved from https://www.epa.gov/sites/production/files/2015-05/documents/rtc-document-final.pdf

EPA. (2017a). *Deep borehole disposal of nuclear waste: Final report.* Retrieved from https://www.epa.gov/radiation/radionuclide-basics-iodine

EPA. (2017b). *Deep borehole disposal of nuclear waste: Final report.* Retrieved from http://www.wise-uranium.org/

Faybishenko, B., & Birkholzer, J. (2015, 8). Challenging issues for nuclear waste disposal in deep geological formations: Status report on fifth worldwide review.

Faybishenko, B., Birkholzer, J., Sassani, D., & Swift, P. (2016a). *International approaches for deep geological disposal of nuclear waste: Geological challenges in radioactive waste isolation. fifth worldwide review.* Lawerence Berkley National Laboratory and Sandia National Laboratory.

Faybishenko, B., Birkholzer, J., Sassani, D., & Swift, P. (2016b, 12). International approaches for nuclear waste disposal in geological formations: Geological challenges in radioactive waste isolation—fifth worldwide review. *Lawrence Berkeley National Laboratory. LBNL Report Number 1006984.* (https://escholarship.org/uc/item/3xn5j2sf)

Frape, S. K., Blyth, A., Blomqvist, R., McNutt, R. H., & Gascoyne, M. (2003). Deep Fluids in the Continents: II. Crystalline Rocks. *Treatise on Geochemistry*, *5*, 605. doi: 10.1016/B0-08-043751-6/05086-6

Freiesleben, H. (2013). Final disposal of radioactive waste. *EPJ Web of Conferences*, *54*. Retrieved from https://www.epj-conferences.org/articles/epjconf/pdf/2013/15/epjconf_lnes2012_01006.pdf

French National Radioactive Waste Management Agency. (2016). *Cigéo project: Deep geological disposal facility for radioactive waste in meuse/haute-marne departments.* Retrieved from http://science.sckcen.be/en/Facilities/HADES

Ganopolski, A., Winkelmann, R., & Schellnhuber, H. J. (2016). Critical insolation–CO2 relation for diagnosing past and future glacial inception. *Nature*, *529*(200), 731–744. doi: https://doi.org/10.1038/nature16494

Gaston, D., Newman, C., Hansen, G., & Lebrun-Grandié, D. (2009). MOOSE: A parallel computational framework for coupled systems of nonlinear equations. *Nuclear Engineering and Design*, *239*(10), 1768–1778. doi: https://www.sciencedirect.com/science/article/pii/S0029549309002635

Gens, A., do N. Guimaraes, L., Olivella, S., & Sánchez, M. (2010). Calculation of phase relations involving haplogranitic melts using an internally consistent thermodynamic dataset. *Journal of Rock Mechanics and Geotechnical Engineering*, *2*(2), 97–102. Retrieved from https://academic.oup.com/petrology/article/42/4/673/1495774

Gens, A., do N. Guimarães, L., Olivella, S., & Sánchez, M. (2010). Modelling thermo-

hydro-mechano-chemical interactions for nuclear waste disposal. *Journal of Rock Mechanics and Geotechnical Engineering*, *2*(2), 97–102.

Gilleland, J., Petroski, R., & Weaver, K. (2016a). The traveling wave reactor: Design and development. *Engineering*, *2*, 88–96. Retrieved from `https://sudonull.com/posts/739-Bill-Gates-and-the-fast-sodium-reactor`

Gilleland, J., Petroski, R., & Weaver, K. (2016b). The traveling wave reactor: Design and development. *Engineering*(2).

Hadgu, T., & Arnold, B. (2010, 12). Thermal hydrology modeling of deep borehole disposal of high-level radioactive waste. *AGU Fall Meeting Abstracts*.

Hadgu, T., Martinez, M., Bean, J., Arguello, J. G., Jové-Colón, C. F., & Hansen, F. (2009). *Deep borehole disposal of high-level radioactive waste.* (Tech. Rep.). SANDIA.

Hadgu, T., Martinez, M., Bean, J., Arguello, J. G., Jové-Colón, C. F., & Hansen, F. (2013). Thermal-hydrologic-chemical-mechanical modeling of deep borehole disposal. In *2013 international radioactive waste management conference.* Albuquerque, New Mexico.

Hejzlar, P. (2016). personal communication.

Hejzlar, P., Petroski, R., Cheatham, J., Touran, N., Cohen, M., Troung, B., ... Gilleland, J. (2013). TerraPower, LLC Traveling Waver Reactor Development Program Overview. *Nuclear Engineering and Technology*, *45*(6), 731–744. doi: http://dx.doi.org/10.5516/NET.02.2013.520

Hill, C. (2019). Personal communication.

Holland, T., & Powell, R. (2011). Calculation of phase relations involving haplogranitic melts using an internally consistent thermodynamic dataset. *Journal of Petrology*, *42*(4), 673–683. Retrieved from `https://academic.oup.com/petrology/article/42/4/673/1495774`

Huang, H. (2019). Personal communication.

Hudson, J. A., Backstrom, A., Rutqvist, J., Jing, L., Backers, T., Chijimatsu, M., ... Shen, B.-T. (2009). Characterising and modelling the excavation damaged zone in crystalline rock in the context of radioactive waste disposal. *Environmental Geology*, *57*, 1275–1297.

Hughes, T., Franca, L., & Mallet, M. (1986, 1 1). A new finite element formulation for computational fluid dynamics: I. symmetric forms of the compressible euler and navier-stokes equations and the second law of thermodynamics. *Computer*

Methods in Applied Mechanics and Engineering, *54*(2), 223–234. doi: 10.1016/0045-7825(86)90127-1

Idaho National Laboratory. (2019). *Moose, multiphysics object oriented simulation environment.* https://mooseframework.inl.gov. (Accessed: 2019-07-11)

International Association for the Properties of Water and Steam. (2007). *Revised release on the iapws industrial formulation 1997 for the thermodynamic properties of water and steam.* Retrieved from http://www.iapws.org/relguide/IF97-Rev.html

Juhlin, C., & Sandstedt, H. (1989). *Storage of nuclear waste in very deep boreholes: Feasibility study and assessment of economic potential.* (Tech. Rep.). SKB.

Kazimi, M., & Todreas, N. (2011). *Nuclear systems volume i: Thermal hydraulic fundamentals, second edition.* CRC Press.

Klein, C., & Carmichael, R. S. (2019). *Rock.* Retrieved from https://www.britannica.com/science/rock-geology

Knief, R. A. (2008). *Nuclear engineering theory and technology of commercial nuclear power.* American Nuclear Society.

Langer, M., Schneider, H., & Kühn, K. (1991). *The salt dome of gorleben—target site for the german radioactive waste repository* (Tech. Rep.). Lawrence Berkeley Laboratory.

Larsen, E. (1929). The temperatures of magmas. *American Mineralogist*, *14*, 81–94. Retrieved from https://pubs-geoscienceworld-org.libproxy.mit.edu/ammin/issue/14/3

Li, S.-H., & Chiou, S.-L. (1993). Radionuclide migration in fractured porous rock: Analytical solution for a kinetic solubility-limited dissolution model. *Nuclear Technology*, *104*(2), 258-271. Retrieved from https://doi.org/10.13182/NT93-A34889 doi: 10.13182/NT93-A34889

Litt, S. A. (n.d.). *Recent developments in disposal of high-level radioactive waste and spent nuclear fuel.* Retrieved from https://ourwastematters.com/2015/08/29/disposing-nuclear-waste/

Los Alamos National Laboratory. (2007). *Fehm: A control volume finite element code for simulating subsurface multi-phase multi-fluid heat and mass transfer.* Retrieved from https://www.lanl.gov/orgs/ees/fehm/pdfs/FEHM_LAUR-07-3359.pdf

Lu, H. (2009). *Evaluation of transmutation performances of tru and llfps with a*

super fast reactor. Retrieved from http://goneri.nuc.berkeley.edu/tokyo/2009-03-12_Lu.pdf

Lubchenko, N. (2015). *Transient modeling of host rock for a deep borehole nuclear waste repository.*

Lubchenko, N., Rodríguez-Buño, M., Bates, E., Baglietto, E., Driscoll, M., & Podgorney, R. (2015). Modeling of the groundwater transport around a deep borehole nuclear waste repository. In *16th international topical meeting on nuclear reactor thermal hydraulics (nureth-16)* (pp. 1–5). Chicago, Illinois.

Malbrain, C., Lester, R., & Deutch, J. (1982). Analytical Approximations for the Long Term Decay Behaviour of Spent Fuel and High Level Waste. *Nuclear Technology*, *57*, 292–921.

Manning, C., & Ingebritsen, S. (1999). Permeability of the continental crust: Implications of geothermal data and metamorphic systems. *Reviews of Geophysics*, *37*(1), 127–150.

Marsic, N., & Grundfelt, B. (2013). *Modelling of thermally driven groundwater flow in a facility for disposal of spent nuclear fuel in deep boreholes.* (Tech. Rep.). SKB.

Marsic, N., Grundfelt, B., & Wiborgh, M. (2006). *Very deep hole concept thermal effects on groundwater flow.* (Tech. Rep.). SKB.

Marsic, N., Hartley, L., Jackson, P., & Poole, M. (2001). *Development of hydrogeological modelling tools based on nammu.* (Tech. Rep.). SKB.

Martín, L. B., Wolters, R., Rutqvist, J., Lux, K.-H., & Birkholz, J. T. (2015). Comparison of two simulators to investigate thermal–hydraulic– mechanical processes related to nuclear waste isolation in saliferous formations. *Computers and Geotechnics*, *66*, 219–229.

McCombie, C., & Thury, M. (1996). *Swiss hlw programme: Status and key issues.* (Tech. Rep.). Lawrence Berkeley Laboratory.

National Conference of State Legislature. (2017). *State restrictions on new nuclear power facility construction.* Retrieved from http://www.ncsl.org/research/environment-and-natural-resources/states-restrictions-on-new-nuclear-power-facility.aspx (Last accessed 14 September 2019)

NRC. (2008). *Dissolution .kinetics of commercial spent nuclear fuels in the potential yucca mountain repository environment.* Retrieved from https://www.nrc.gov/docs/ML0831/ML083120074.pdf

NRC. (2019). *Backgrounder on radioactive waste.* Retrieved from https://www.nrc.gov/reading-rm/doc-collections/fact-sheets/radwaste.html (Last accessed 14 September 2019)

NRC Proposed Rule 10 CFR. (2019). *Disposal of high-level radioactive wastes in a geologic repository at yucca mountain, nevada.* Retrieved from https://www.nrc.gov/reading-rm/doc-collections/cfr/part063/full-text.html#part063-0113

Nuclear Energy Agency. (2006). *Physics and safety of transmutation systems.* Retrieved from https://www.oecd-nea.org/science/docs/pubs/nea6090-transmutation.pdf

Nuclear Energy Agency. (2009). *Spent fuel composition as a function of burn-up and cooling times.* Retrieved from https://www.oecd-nea.org/pt/docs/1999/neastatus99/AnnexE.pdf

O'Brien, M. T., Cohen, L. H., Narastahan, T. N., Simkin, T. L., & Wollenberg, H. A. (1979). *The very deep hole concept: Evaluation of an alternative for nuclear waste disposal* (Tech. Rep.). EARTH SCIENCES DIVISION LAWRENCE BERKELEY LABORATORY.

Olivella, S., Gens, A., Carrera, J., & Alonso, E. (1995). Numerical formulation for a simulator code bright for the coupled analysis of saline media. *Engineering Computations*, *13*(7), 87–112.

Pintado, X. (2016, 05). Verification of the het flow dissipation calculation in nuclear spent fuel repository..

Podgorney, R., Huang, H., Lu, C., Gaston, D., Permann, C., Guo, L., & Andrs, D. (2011). *Falcon: A physics-based, massively parallel, fully-coupled, finite element model for simultaneously solving multiphase fluid flow, heat transport, and rock deformation for geothermal reservoir simulation.* (Tech. Rep.). Idaho National Laboratory.

Poinssot, C., & Geckeis, H. (2012). *Radionuclide behaviour in the natural environment.* Woodhead Publishing.

Posiva. (2019). *Posiva.* Retrieved from http://www.posiva.fi/frontpage

Quammen, C. (2015). Scientific data analysis and visualization with python, vtk, and paraview. *PROC. OF THE 14th PYTHON IN SCIENCE CONF. (SCIPY 2015)*, 31–38. Retrieved from https://conference.scipy.org/proceedings/scipy2015/pdfs/cory_quammen.pdf

Radioactive waste management, GOV.UK. (2017). *The multi-barrier approach,*

the science file. Available at https://assets.publishing.service.gov.uk/government/uploads/system/uploads/attachment_data/file/654537/3._The_multi-barrier_approach_Proof_6__1_.pdf (2019/08/08).

Ritchie, H., & Roser, M. (2019). Co_2 and greenhouse gas emissions. *Our World in Data.* (https://ourworldindata.org/co2-and-other-greenhouse-gas-emissions)

Rodríguez-Buño, M., Driscoll, M., Baglietto, E., & Park, Y. (2016). *Terrapower project intermediate report.* (Tech. Rep.). Massachusetts Institute of Technology.

Rutqvist, J. (2015). Fractured rock stress-permeability relationships from in situ data and effects of temperature and chemical-mechanical couplings. *Geofluids*, *15*, 48–66.

Rutqvist, J., Borgesson, L., Chijimatsu, M., Kobayashi, A., Jing, L., Nguyen, T., ... Tsang, C.-F. (2001). Thermohydromechanics of partially saturated geological media: governing equations and formulation of four finite element models. *International Journal of Rock Mechanics and Mining Sciences*, *38*, 105–127.

Rutqvist, J., Freifeld, B., Min, K.-B., Elsworth, D., & Tsang, Y. (2008). Analysis of thermally induced changes in fractured rock permeability during 8 years of heating and cooling at the yucca mountain drift scale test. *International Journal of Rock Mechanics and Mining Sciences*, *45*, 1373–1389.

Rutqvist, J., Wu, Y., Tsang, C., & Bodvarsson, G. (2002). A modeling approach for analysis of coupled multiphase fluid flow, heat transfer, and deformation in fractured porous rock. *International Journal of Rock Mechanics and Mining Sciences*, *39*, 429–442.

Saad, Y. (2003). *Iterative methods for sparse linear systems.* SIAM.

Sánchez, M., Arroyo, M., & Olivella, S. (2004). Thermo-hydro-mechanical modelling of low permeability media using a double-porosity formulation..

SANDIA. (2013). *Deep borehole disposal research: Demonstration site selection guidelines, borehole seals design, and research design and development needs.* Retrieved from https://www.energy.gov/ne/downloads/deep-borehole-disposal-research-demonstration-site-selection-guidelines-borehole-seals

Schöne, F., Spörl, K., & Leiterer, M. (2017). Iodine in the feed of cows and in the milk with a view to the consumer's iodine supply. *Journal of Trace Elements in Medicine and Biology*, *39*, 202-209. Retrieved from https://www.ncbi.nlm.nih.gov/pubmed/27908415

Scott, S. M., Hu, T., Yao, T., Xin, G., & Lian, J. (2015). Graphene-based sorbents for iodine-129 capture and sequestration. *Carbon 90*, *1*(8). Retrieved from https://www.osti.gov/servlets/purl/1248954

Selvadurai, A. P. S., & Suvorov, A. P. (2017). *Thermo-poroelasticity and geomechanics.* Cambridge University Press.

Seyedi, D., & Gens, A. (2017, 05). Numerical analysis of the hydromechanical response of callovo-oxfordian claystone to deep excavations. *Computers and Geotechnics*, *85*, 275-276. doi: 10.1016/j.compgeo.2017.03.006

Shackelford, C. D., & Moore, S. M. (2012). Fickian diffusion of radionuclides for engineered containment barriers: Diffusion coefficients, porosities, and complicating issues. *Engineering Geology*, *252*(152), 133-147.

Shukla, A., Singh, A. K., & Singh, P. (2011). A recent development of numerical methods for solving convection-diffusion problems. *Applied Mathematics*, *1*, 1-12. doi: https://pdfs.semanticscholar.org/8a9b/7ba5370db0788cf9f199e8969d22237f35b8.pdf

SKB. (2019). *About SKB.* Retrieved from https://www.skb.com/skb-swedish-nuclear-fuel-and-waste-management-company/ (Last accessed 31 May 2019)

SMU Geothermal Laboratory. (2011). *Geothermal map of north america.* Retrieved from https://www.smu.edu/-/media/Site/Dedman/Academics/Programs/Geothermal-Lab/Graphics/SMUHeatFlowMap2011_CopyrightVA0001377160_jpg.jpg?la=en

Sosnovsky, E., Baglietto, E., Keijers, S., van Tichelen, K., de Souza, T. C., Doolaard, H., & Roelofs, F. (2015). Cfd simulations to determine the effects of deformations on liquid metal cooled wire wrapped fuel assemblies. In *16th international topical meeting on nuclear reactor thermal hydraulics (nureth-16)* (pp. 2747–2761). Chicago, Illinois.

Stroud, M. (2012). *Wasteland: the 50-year battle to entomb our toxic nuclear remains.* Retrieved from https://www.theverge.com/2012/6/14/3038814/yucca-mountain-wipp-wasteland-battle-entomb-nuclear-waste

Swedish Nuclear Fuel and Waste Management Company (SKB). (2009). *Swedish radiation safety authority recommends approval of the spent fuel repository.* Retrieved from http://www.mynewsdesk.com/skb/pressreleases/swedish-radiation-safety-authority-recommends-approval-of-the-spent-fuel-repository-2493057

Swift, P. (2017). *Recent developments in disposal of high-level radioactive waste*

and spent nuclear fuel. Retrieved from https://www.energy.gov/sites/prod/files/2017/11/f46/Peter20Swift20PRACoP20201720final.pdf

Szántó, Z., Svingor, E., Molnár, M., Palcsu, L., & I. Futó, Z. S. (2002, 01). Diffusion of 3h, 99tc, 125i, 36cl and 85sr in granite, concrete and bentonite. *Journal of Radioanalytical and Nuclear Chemistry, 252*(1), 133-138.

TerraPower. (2013). *Twr technology: Preparing nuclear energy for global growth.* Retrieved from https://terrapower.com/productservices/twr

TerraPower. (2019). *About the traveling wave reactor.* Retrieved from https://terrapower.com/uploads/docs/About_the_Traveling_Wave_Reactor.pdf

Tezduyar, T. E., Park, Y. Y. J., & Deans, H. A. (1987). Finite element procedures for time-dependent convection-diffusion-reaction systems. *INTERNATIONAL JOURNAL FOR NUMERICAL METHODS IN FLUIDS, 7*, 1013-1033. doi: https://www.tafsm.org/PUB_PRE/jALL/j9-IJNMF-DRD2.pdf

Toprak, E., Olivella, S., & Pintado, X. (2016, 05). Thm modelling of engineered barriers for spent fuel isolation..

US Department of Energy. (2014). *Interagency review needed to update u.s. position on enriched uranium that can be used for tritium production.* Retrieved from https://www.gao.gov/assets/670/666505.pdf

Winterle, J., Pauline, R., & Ofoegbu, G. (2011). *Regulatory perspectives on deep borehole disposal concepts* (Tech. Rep.). U.S. Nuclear Regulatory Commission.

Witherspoon, P. A., & Degerman, O. (1978). *Swedish-american cooperative program on radioactive waste storage in mined caverns program summary, technical project report no. 01.* (Tech. Rep.). Lawrence Berkeley Laboratory.

Witherspoon, P. A., & deMarsily, G. (1991). *Introduction. in: Geological problems in radioactive waste. a world wide review.* (Tech. Rep.). Lawrence Berkeley Laboratory.

World Nuclear Association. (2019a). *Comparison of lifecycle greenhouse gas emissions of various electricity generation sources.* Retrieved from http://www.world-nuclear.org/uploadedFiles/org/WNA/Publications/Working_Group_Reports/comparison_of_lifecycle.pdf

World Nuclear Association. (2019b). *Comparison of lifecycle greenhouse gas emissions of various electricity generation sources.* Retrieved from http://www.world-nuclear.org/uploadedFiles/org/WNA/Publications/Working_Group_Reports/comparison_of_lifecycle.pdf

World Nuclear Association. (2019c). *Uranium and depleted uranium.* Retrieved from https://www.world-nuclear.org/information-library/nuclear-fuel-cycle/uranium-resources/uranium-and-depleted-uranium.aspx (Last accessed 14 September 2019)

World Nuclear Association. (2019d). *Uranium and depleted uranium.* Retrieved from https://www.world-nuclear.org/information-library/nuclear-fuel-cycle/uranium-resources/uranium-and-depleted-uranium.aspx (Last accessed 14 September 2019)

World Nuclear Association. (2019e). *What is uranium? how does it work?* Retrieved from https://www.world-nuclear.org/information-library/nuclear-fuel-cycle/introduction/what-is-uranium-how-does-it-work.aspx (Last accessed 14 September 2019)

Xia, Y., Plummer, M., Podgorney, R., & Ghassemi, A. (2016). An assessment of some design constraints on heat production of a 3d conceptual egs model using an open-source geothermal reservoir simulation code. In *Forty-first workshop on geothermal reservoir engineering stanford university, stanford, california, february 22-24, 2016 sgp-tr-209* (p. 1-5). Stanford, California.

Zoback, M. D. (2015). *Reservoir geomechanics.* Cambridge University Press.